INFORMATION TO USERS

This manuscript has been reproduced from the microfilm master. UMI films the text directly from the original or copy submitted. Thus, some thesis and dissertation copies are in typewriter face, while others may be from any type of computer printer.

The quality of this reproduction is dependent upon the quality of the copy submitted. Broken or indistinct print, colored or poor quality illustrations and photographs, print bleedthrough, substandard margins, and improper alignment can adversely affect reproduction.

In the unlikely event that the author did not send UMI a complete manuscript and there are missing pages, these will be noted. Also, if unauthorized copyright material had to be removed, a note will indicate the deletion.

Oversize materials (e.g., maps, drawings, charts) are reproduced by sectioning the original, beginning at the upper left-hand corner and continuing from left to right in equal sections with small overlaps.

Photographs included in the original manuscript have been reproduced xerographically in this copy. Higher quality 6" x 9" black and white photographic prints are available for any photographs or illustrations appearing in this copy for an additional charge. Contact UMI directly to order.

Bell & Howell Information and Learning
300 North Zeeb Road, Ann Arbor, MI 48106-1346 USA
800-521-0600

MEASUREMENT AND COMPUTATION OF THERMAL STRESSES IN INJECTION MOLDING OF AMORPHOUS AND CRYSTALLINE POLYMERS

by

Yalda Farhoudi

A Thesis Submitted to the Faculty of Graduate Studies
and Research in Partial Fulfillment of the
Requirements for the Degree of
Doctor of Philosophy

Department of Chemical Engineering
McGill University
Montreal, Canada

ABSTRACT

An integrated experimental and theoretical study of the residual thermal stresses has been carried out. The final stress profiles along the thickness were measured in an amorphous and a semi-crystalline injection molded polymer using the layer removal technique. The two materials exhibited drastically distinct residual profiles. Furthermore, processing parameters such as melt and coolant temperatures, pressure history, and mold thickness were found to modify the profiles.

In order to elucidate the findings, two models were derived. The two-dimensional free mold shrinkage model was developed to provide a rapid estimation of thermal stresses and the main features of their profile. A more complex model was developed by integrating the stress analysis with the simulation of the complete injection molding cycle by McKam. This model accounts for the fountain flow effect, the crystallization, and the PVT behavior of the material. With the help of the model predictions, explanations were provided for the occurrence of various regions in the residual stress profiles. Transitions or reversal of the regions under variable conditions or material properties were observed to be mainly determined by the ratio of the thermal to the pressure effects. Using these concepts, practical conclusions were drawn for controlling the residual stresses.

As an alternative for optimization of injection molding with respect to residual stresses, inverse methods were developed to calculate the pressure history or the initial temperature distribution required to produce a prescribed residual stress distribution. These methods were tested using direct solutions with added errors and experimental stress data.

RESUMÉ

On a mené une étude expérimentale et théorique des contraintes thermiques résiduelles. On a utilisé la méthode du pelage de couche pour mesurer la répartition des contraintes résiduelles dans l'épaisseur des polymères amorphes et semi-cristallins injectés. On a obtenu des profils complètement différents dans les deux types de polymères. En outre, on a trouvé que les conditions d'injection comme la température initiale, la température de refroidissement et l'évolution de la pression, ainsi que l'épaisseur du moule influencent les contraintes résiduelles.

Nous avons formulé deux modèles pour mieux comprendre les résultats expérimentaux. Le modèle 2-D avec retrait libre dans le moule a été formulé pour un calcul rapide des contraintes résiduelles. Un modèle plus complexe a été formulé en intégrant l'analyse des contraintes avec la simulation du cycle complet de l'injection par McKam. Ce modèle tient compte de l'éffet de l'écoulement en fontaine, de la cristallisation et du comportement PVT du matériau. Nous avons fournis des explications pour l'existence des zones différentes dans les profils des contraintes résiduelles. On a constaté que les changements et la transitions de ces zones par suite de modifications des conditions d'injection et des propriétés du matériau peuvent être déterminer en examinant la proportion de l'éffet thérmique et l'éffet de la pression. Ces concepts nous ont conduits à des conclusions pratiques pour controler les contraintes résiduelles.

Afin d'optimiser le procédé d'injection par rapport aux contraintes résiduelles, on a alternativement formulé des méthodes inverses pour calculer le champs de la pression ou le profil de la température initiale qui produirait une répartition précrite ou désirable des contraintes résiduelles. On a testé ces méthodes avec la solution du problème directe additionée d'erreures, ainsi qu'avec des contraintes expérimentales.

ACKNOWLEDGMENTS

I wish to express my gratitude to the following people and organizations that have contributed to the completion of this work.

Firstly, I am especially grateful of my research director, Professor M.R.Kamal for his continuous guidance and encouragement throughout this project.

Also, I wish to thank:

- Professor A.D.Rey for his helpful advices and suggestions,
- the staff of the Chemical Engineering Machine Shop: Alain Gagnon, Charles Dolan, and Walter Greenland, for their assistance with the equipment,
- François Koran for his constant support, friendship, and for always being there,
- Rabih Nehme, Sleiman Bassila and Tareq Al Ahmad for carrying out parts of the experiments,
- Dr. Richard Laifook, for his help in the experiments and fruitful discussions,
- Imad Ansari, for his friendship and his help with McKam,
- My friends in the Polymer group, especially Mazen Samara for his continuous friendship and support, Paula Wood-Adams and Marie-Claude Heuzey,
- Lei Wang for his assistance in the computer lab.,
- Jean Dumont and Michael Harrington for their assistance in the purchase of equipment,
- Pat Fong and Anne Prihoda for their help in the Graduate Office,
- the Natural Science and Engineering Research Council of Canada (NSERC), Fonds pour la Formation de Chercheurs et l'Aide a la Recherche (FCAR), and McGill University for financial support.

Last but not least, I am grateful to my family, especially my parents for their unconditional love and support.

TABLE OF CONTENTS

LIST OF FIGURES

LIST OF TABLES

NOMENCLATURE

UPPER CASE LETTERS

$\mathbf{A}$	matrix relating strain and displacement
Biot	Biot number
C_p	specific heat
$\mathbf{D}$	matrix relating the elastic stress and strain
D_e	Deborah number
E	elastic modulus
E_a	elastic modulus of amorphous part
E_c	elastic modulus of crystalline part
$\mathbf{F}$	force vector per unit volume
$\mathbf{F}_b$	body force vector per unit volume
G_s	shear modulus
ΔH_f	heat of fusion of a 100% crystalline material
ΔH_m	measured heat of fusion of a sample
$\mathbf{I}$	unit tensor
K	non-isothermal crystallization rate constant
K_b	bulk modulus
K_{max}	maximum non-isothermal crystallization rate constant
M_i	components of the moment
$\mathbf{P}$	force per unit area vector
P	pressure
P_s	pressure at the instant of solidification (solidification pressure)
R	dissipative function
$\mathbf{R}$	vector of residual
T	temperature
T_a	ambiant temperature
T_c	coolant temperature

T_g	glass transition temperature
T_i	initial temperature
T_m	melt temperature
T_M	boundary temperature
T_s	solidification temperature
V	specific volume
X_c	absolute mass fraction crystallinity
X_{cv}	absolute volume fraction crystallinity
X_R	relative mass fraction crystallinity
X_∞	ultimate mass fraction crystallinity
Z	isothermal crystallization rate constant

LOWER CASE LETTERS

a	thermal diffusivity
a_T	shift function for time-temperature superposition
b	half-thickness of a sample
f	free energy per unit volume
f_0	free energy per unit volume in the absence of deformation
h	heat transfer coefficient
k	heat conductivity
m	consistency index in the power law relation
n	refractive index tensor
n	power law index for viscosity
n_a	Avrami exponent
t_p	characteristic process time
q	heat flux vector
u	displacement vector
v	velocity vector
$\dot{\mathbf{v}}$	acceleration vector

z_s	position of the solid-melt interface in the thickness direction z

GREEK LETTERS

α_l	linear thermal expansion coefficient
α_v	volumetric thermal expansion coefficient
β	pressure coefficient of viscosity
ε	strain tensor
ε	emissivity
ε_P	pressure strain
ε_T	thermal strain
$\dot{\varepsilon}$	strain rate tensor
δ	second order unit tensor
δ	shrinkage
δ_f	final shrinkage
δ_s	shrinkage at solidification
ϕ	deflection
γ_{ij}	shear components of strain
$\dot{\gamma}$	shear rate
η	shear viscosity
κ_i	components of the curvature vector
λ_i, i=1,2,..	regularization parameters
λ_R	relaxation time
ρ	density
ρ_a	density of the amorphous phase
ρ_c	density of the crystalline phase
σ	stress tensor
σ_t	total stress tensor
σ_B	Stefan-Boltzmann constant

τ_{ij}	shear components of stress
υ	Poisson ratio
ϖ	vorticity tensor
ζ	elongational or dilatational viscosity
ξ	modified time scale for time-temperature superposition

ABREVIATIONS

B	bottom
CMS	constrained mold shrinkage
C	center of cavity
DSC	differential scanning calorimeter
E	near the end of cavity
FMS	free mold shrinkage
FQ	free quenching
G	near the gate
HDPE	high density Polyethylene
PC	Polycarbonate
PMMA	Polymethyl-methacrylate
PP	Polypropylene
PS	Polystyrene
T	top
1-D	one-dimensional
2-D	two-dimensional

Chapter 1

INTRODUCTION

Polymeric materials exhibit a broad range of properties compared to more traditional materials such as metals and glasses. As a result, polymers exhibit a versatility that makes them useful in a variety of applications. Their primary asset is their low density, resulting in relatively high specific strength and stiffness. Polymeric materials may be classified according to their mechanical response at elevated temperatures. Thermoplastics soften when heated and harden when cooled. These processes are reversible, as long as the temperature is lower than the degradation temperature of the material. Thermosetting polymers become permanently hard when heat is applied. They do not soften upon subsequent heating because covalent crosslinks are formed between adjacent molecular chains. The "plastic" deformable state, achieved by thermoplastic polymers at elevated temperatures, and possessed by thermosetting polymers before being chemically "set", makes it possible to shape them into a variety of products, some of which are of great geometrical complexity (1).

Polymer processing methods are used to shape polymeric raw materials and convert them into finished products. Some of the most important polymer processing methods are: screw extrusion, injection molding, film blowing, blow molding, calendering, compression molding, and thermoforming. As organic polymers are replacing inorganic materials in many applications, there is an increasing demand for controlling the properties of polymeric products. The ultimate goal is to optimize the processing conditions in order to achieve desired product performance characteristics. The main subject of this thesis is related to one of the aspects of this performance: the dimensional precision and dimensional stability of the final part. These aspects are closely associated

with the distribution of residual stresses, relaxation of the stresses, and aging behavior of the material.

This chapter is an introduction to relevant subjects and a review of the present state of research concerning residual stresses in injection molding.

1.1. INJECTION MOLDING

Injection Molding is the most widely used process for shaping polymeric materials into complex-shaped products. This method has the advantage of manufacturing molded parts economically in large quantities with little or practically no finishing requirements. Injection molding evolved from metal die casting. As a result of the high viscosity of polymers, the melt can not be poured into the mold as in the case of metals. The polymer melt is injected into the mold cavity by applying large forces on it with a plunger. Once the mold is filled, solidification starts. An additional amount of melt must be packed into the mold in order to compensate for the shrinkage due to cooling. Fig.1.1 shows a schematic of the injection molding machine.

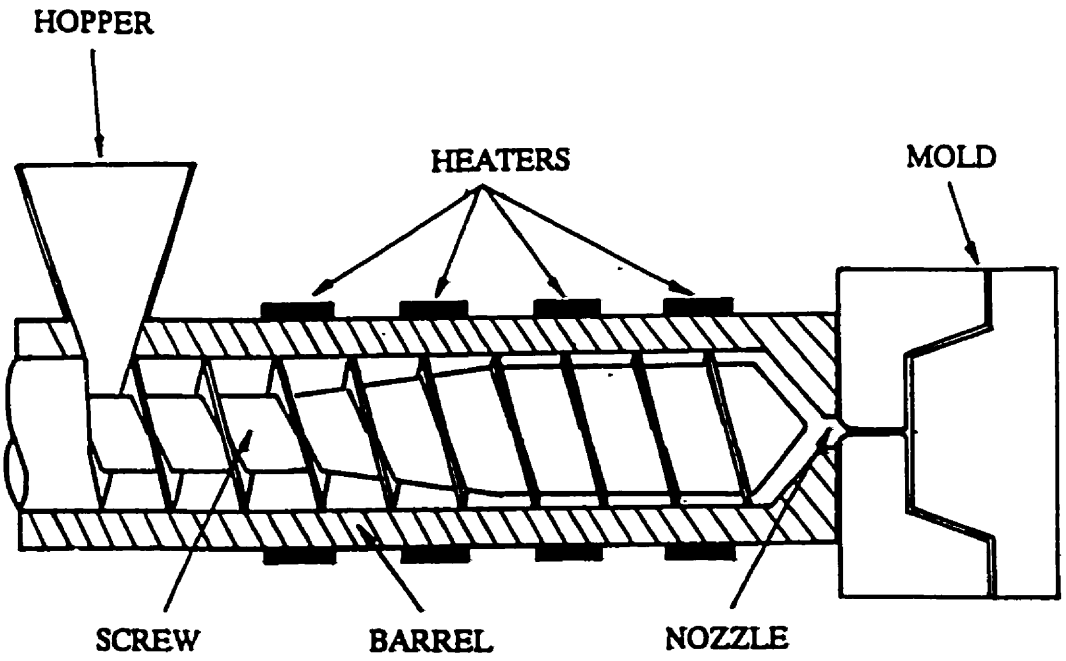

Fig.1.1. Schematic of an injection molding machine (2)

Present injection machines are mostly of the reciprocating screw type shown in Fig.1.1. The screw rotates, driven by a motor, to convey the polymer pellets or powder towards the mold. The combination of external heaters located strategically along the screw barrel and mechanical work, causes the melting and homogenization of the resin. Subsequently, the screw moves axially to pump the melt through the nozzle into the runners, the gate, and the cavity (filling stage) and maintains the melt under high pressure during the holding time (packing stage). During packing, additional melt is injected into the cavity to offset the contraction due to cooling and solidification. Later, the material inside the gate solidifies, thus isolating the mold from the injection unit. As the melt inside the mold cools, the pressure drops gradually (cooling stage). Finally, the solidified part is ejected from the mold. Fig.1.2 is a schematic representation of the gate pressure history at different stages of a typical injection molding cycle.

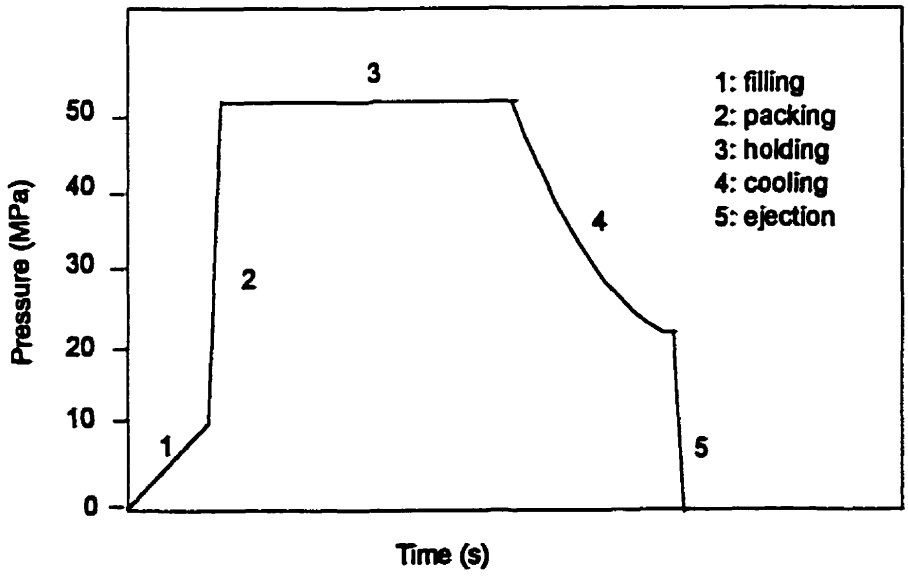

Fig.1.2. Schematic of gate pressure at different stages of injection molding

The ultimate properties of the molded products depend to a large extent on the processing conditions and the properties of the polymeric material. Some of the problems frequently encountered in injection molded parts are associated with dimensional irregularities and instabilities such as shrinkage, and warpage and they are closely related

to residual stresses. Some other problems associated with residual stresses are the impact resistance (related to the surface stress) and the long term deformation of the article as a result of stress relaxation or creep. Therefore, the study of residual stresses, their distribution in the sample, and their development during processing are of great practical importance. Presently, the prevention and remediation of the defects arising from residual stresses in the molded articles are essentially based on experience and trial and error. Computer simulation of the process and theoretical estimation of residual stresses allow us to take the first steps in predicting and preventing these problems prior to molding. Such simulations can reduce the cost and duration of process optimization and are therefore of great economical interest to industry. On the other hand, the experimental determination of the distribution of the residual stresses and other properties of the molded part are important for the development of the simulation programs and verification of the predictions.

1.2. RESIDUAL STRESSES

Residual stresses are part of the stresses generated in the sample during the molding process that remain after it is ejected from the mold and has cooled down to ambient temperature. In order to obtain adequate predictions of residual stresses, the complete injection molding history must be considered. Residual stresses in injection molded parts are known to have two different origins and are accordingly classified into two principal types: flow stresses and thermal stresses.

1.2.1. Flow Stresses

During the filling stage of injection molding, the polymer melt undergoes high strain rates. As a result, shear and extensional stresses are introduced in the sample. Shear stresses are generated throughout the melt during filling. The extensional stresses are mainly caused by the "fountain flow" at the melt front where hot melt from the core moves toward the cold surface of the mold and solidifies. The extensional stresses are also developed in expansion and contraction regions in the mold. First and

second normal stress differences are due to the viscoelastic nature of the polymer melt and its large relaxation times (3).

It is difficult to measure flow stresses directly. However, since flow stresses are associated with molecular orientation, frozen-in birefringence may be used as an indirect method to measure flow stresses, as discussed in section I.2.3.

1.2.2. Thermal Stresses

During the packing and cooling stages of injection molding, the sample is cooled rapidly inside the cavity until complete solidification. Due to the low thermal conductivity of polymers, an inhomogeneous temperature distribution is generated in the sample with a large temperature gradient across the thickness. As a result of cooling, the material tends to contract. Since the temperature is not uniform, the drop in temperature and thus the extent of the corresponding contraction are different for different elements of the sample. Due to the continuity of the body, the deformation of each element is restrained by adjacent ones, thus generating tensile and compressive stresses. Since the elastic properties and relaxation characteristics vary significantly with temperature during solidification, these stresses persist and remain as residual thermal stresses. Thermal stresses may also be generated during the filling stage where, depending on processing conditions, a thin solid layer of polymer is formed as a result of contact with the cold mold wall.

Flow and thermal stresses in injection molding are coupled, but the nature of this coupling is very complex (3). In injection molding, a large part of flow stresses relax, since the relaxation is faster at the high temperatures that prevail in the filling stage. Residual thermal stresses are usually one order of magnitude larger than residual flow stresses (4). However, particularly in the rapidly solidified skin layer, the flow stresses and the orientation of polymeric chains become frozen, affecting the properties of the polymer and thus the thermal stresses. Therefore, a complete analysis of residual stresses should include all the stages of injection molding and should account for flow stresses as well.

It is possible to isolate thermal stresses experimentally by cooling the sample in a quiescent constrained, free quenching experiment, where the residual stresses consist only of thermal stresses (5).

In the following sections, we review literature reports regarding the experimental and theoretical investigations of residual stresses.

1.2.3. Experimental Methods

Experimental methods used for determination of residual stresses have been extensively reviewed in reference (6). The most important techniques are hole drilling, stress relaxation, layer removal, and birefringence.

Hole drilling:

In this case, drilling a hole in the sample disturbs the equilibrium of the stress field. Deformations are recorded on the surface using strain gauges located around the hole. The small change in the strain $\Delta\varepsilon$, for a small increase in the depth of the hole is related to the average residual stress σ in the layer corresponding to this depth, using the following equation:

$$\sigma = \frac{E(\Delta\varepsilon)}{K_1 + \upsilon K_2} \tag{1.1}$$

where E and υ are the elastic modulus and the Poisson ratio, respectively. The two parameters K_1 and K_2 must be obtained from calibrating specimens with a known stress field. The hole drilling method has not received much attention in the polymer literature. The main difficulties of this method include attachment of strain gauges to the surface, calibration of the system, and introduction of machining stresses due to drilling (3).

Stress relaxation:

The stress relaxation method is based on the fact that the rates of creep and relaxation in a specimen depend on the level of residual stresses. The following power-law equation is used for stress relaxation:

$$\dot{\sigma} = -EB\sigma^n \tag{1.2}$$

If there is a residual stress in the sample, the stress is replaced by an effective stress obtained by subtracting the residual stress σ_r, from σ. Equation (1.2) becomes:

$$\dot{\sigma} = -EB(\sigma - \sigma_r)^n \tag{1.3}$$

By solving this equation and eliminating the time, the residual stress may be found by plotting the relaxation curve $\left(\frac{d\sigma}{d\,lnt}\right)$ versus σ. The main disadvantage of this method is the difficulty in measuring the residual stresses at different positions in the thickness direction (3).

Layer removal method:

The most widely used technique for the measurement of residual stresses is the layer removal method, where thin layers are removed from the molded sample, as shown in Fig.1.3, thus disturbing the existing equilibrium of forces.

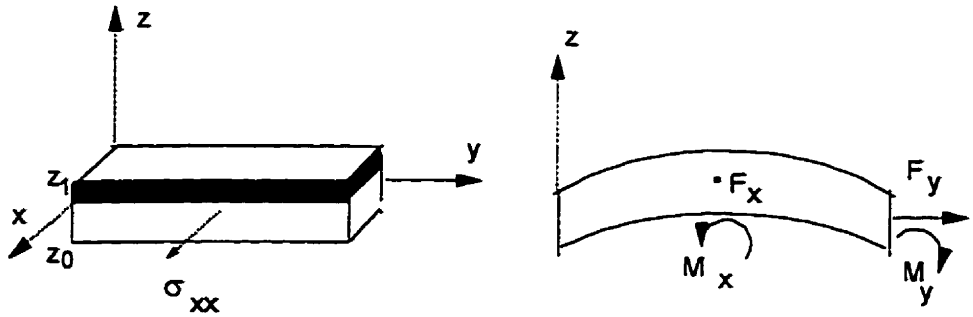

Fig.1.3. Bending moments and forces caused by removing a layer

To re-establish the equilibrium, the remaining sample warps to the shape of a circular arc. The forces and the moments associated with this deformation are equal and opposite to those of the residual stresses (7). In the case of pure bending of a flat plate, the resulting curvatures in the x and y directions, κ_x and κ_y, respectively, may be related, for a linearly elastic and isotropic material, to the bending moment M_X necessary to prevent bending, using the following equation:

$$M_x(z_1) = \left[-\frac{E}{12(1-\upsilon^2)}\right](z_0 + z_1)^3\left[\kappa_x(z_1) + \upsilon\kappa_y(z_1)\right] \tag{1.4}$$

where z_0 and z_1 are coordinates of the initial and the new upper surfaces, respectively; E is the Young's modulus, ν is the Poisson ratio, and the negative sign is used since the curvature occurs on removal of the applied moment. z_0 may be replaced by the half-thickness of the initial sample. Relating the moment M_x to the stress σ_x and assuming $\sigma_x = \sigma_y$ and $\kappa_x = \kappa_y$, the stress at z_1 may be obtained after some mathematical manipulation as follows (7):

$$\sigma_x(z_1) = \sigma_y(z_1) = -\frac{E}{6(1-\nu)}\left[(z_0+z_1)^2 \frac{d\kappa_x(z_1)}{dz_1}\right. \tag{1.5}$$

$$\left. +4(z_0+z_1)\kappa_x(z_1) - 2\int_{z_1}^{z_0}\kappa_x(z)\,dz\right]$$

In this simplified case, only one component of the curvature, κ_x, needs to be measured.

This technique is based on linear elasticity. Therefore, it must be applied to viscoelastic materials such as polymers with great care. When a layer is removed from the surface of a polymeric sample, the magnitude of the curvature increases with time until it reaches some equilibrium value. The deformation caused by the moment induced by removing a layer consists of an instantaneous elastic component and a time-dependent creep. Only the elastic component must be used in applying the Treuting and Read method. Since the creep phenomenon occurs slowly, if the curvature is measured within the first few minutes after layer removal, we obtain mostly the elastic response of the material and the use of the above mentioned method to calculate the residual stresses is adequate(3, 8, 9). Siegmann et al. (10) have however an opposite opinion. They believe that the specimen must be allowed to achieve its equilibrium configuration. In their opinion, three days should elapse between removal of the layer and curvature measurements. As a consequence of this difference in the experimental procedure, Siegmann et al. (10) obtained residual stresses in free quenched polymethyl metacrylate (PMMA) that were 55% higher than those measured by So and Broutman (11) for the same quenching conditions.

Another problem encountered is the relaxation of residual stresses. At temperatures far below the glass transition temperature of the polymer, the stress relaxation may be neglected (12, 13).

The method of Treuting and Read (7) is applicable to isotropic materials with constant Young's modulus. However, due to their molecular orientation, the modulus of injection molded polymers varies in the thickness direction. It was shown that this variation does not have a significant effect on the calculated stress profile (14).

It is important, when using the layer removal method, that the machining does not introduce additional stresses in the specimen. Otherwise, the measured stresses are different from the residual stresses induced in the processing. Measurement of stresses in annealed free quenched or compression molded samples, where the thermal stresses are removed, is a good test to evaluate the effect of machining on the stresses (3,9).

Birefringence:

The velocity of a beam of light is decreased when it is transmitted by an isotropic, uniform, non-absorbing medium. The ratio of the velocity of light in a vacuum compared to that in the medium is the refractive index n of the medium. The refractive index in a material point of a transparent birefringent medium can be represented by a second order tensor or geometrically by an ellipsoid, the so-called indicatrix (5). The axes of this refractive index ellipsoid represent the preferential directions of the medium, their lengths are equal to the refractive index for the respective directions of polarization. The birefringence is determined from the axes of the ellipse obtained by intersecting the indicatrix with the plane perpendicular to the direction of the propagation of light. If this cross section becomes a circle, no birefringence is observed. In glassy polymers and polymer melts, the application of stresses leads to birefringence. The use of birefringence to infer the components of the stress depends upon the validity of a "stress-optical relation". This relation is expressed as the proportionality between the components of the refractive index and stress tensors, as follows:

$$n^d = n - I\bar{n} = C\sigma^d = C(\sigma - IP) \qquad (1.6)$$

where $\mathbf{n}^d$ and σ^d are the deviatoric refractive index tensor and the deviatoric Cauchy stress tensor, respectively. I is the unit tensor, P is the hydrostatic pressure, and $\bar{n}$ (trace of the tensor n) is the average refractive index that may be related to the density. The stress-optical coefficient C is, in general, a temperature dependent polymer property. In

the polymer melt, stress leads to molecular orientation and the anisotropy of the chains may be observed macroscopically as birefringence. When the melt is cooled below its glass transition or melting temperature without complete stress relaxation, this anisotropy can become frozen in.

In injection molding, flow stresses are developed above the glass transition and melting temperature of the polymer. In this region, the linear stress-optical rule relating the stress and the birefringence is usually valid. For polystyrene (PS), the stress-optical sensitivity in the glassy state is 400 times lower than in the molten state (5). Therefore, the contribution of the thermal stresses, generated mostly below the glass transition temperature, to the birefringence can be neglected compared to the contribution of flow stresses. The residual birefringence may thus be used to determine the residual flow stresses in injection molded parts. Most birefringence studies of residual stresses have employed polystyrene (PS).

1.2.4. Measured Residual Stresses

The residual stresses are greatly affected by the conditions under which the sample is cooled and other processing conditions. Three principal cases may be distinguished : free quenching, constrained quenching, and injection molding.

Free quenching:

In free quenching, the sample is rapidly cooled with no constraint, external force or applied pressure. Residual stresses in freely quenched parts consist only of thermal stresses and were found to have a parabolic distribution along the thickness (3, 5, 9, 10,15, 16). So and Broutman (11) were the first to apply the layer removal method developed for metals, to polymeric materials. They measured the residual stresses in freely quenched polymethyl methacrylate (PMMA) and polycarbonate (PC). In all cases of free quenching, a maximum compressive stress and a maximum tensile stress were observed on the surface and in the core of the sample, respectively. It was found that an increase in the quenching temperature causes a lowering of the magnitude of the stresses.

Constrained quenching:

In constrained quenching, the deformation of the sample due to cooling is restrained by a complex geometry, adhesion to or friction with the surface of the wall, or by an applied pressure. This situation occurs in compression and injection molding. In free quenching, however, flow stresses are absent. Mandell et al. (17) measured residual stresses in polysulfone sheets quenched between two aluminum sheets using the layer removal method. They found a parabolic stress profile similar to the case of free quenching. Wimberger-Friedl (5) found that in the presence of wall adhesion, the level of stresses decreases significantly compared to free quenching. In fact, wall adhesion induces tensile stress on the surface of the sample, much in the same way as pressure in injection molding.

Fig.1.4. shows the radial stress build up versus the dimensionless thickness z/d calculated by Wimberger-Friedl (5) for the free quenching (solid lines) and constrained quenching (broken lines) of a polycarbonate disk of diameter d, from 160°C to 60°C. Elasticity was assumed and the time from the beginning of the quench is indicated in seconds.

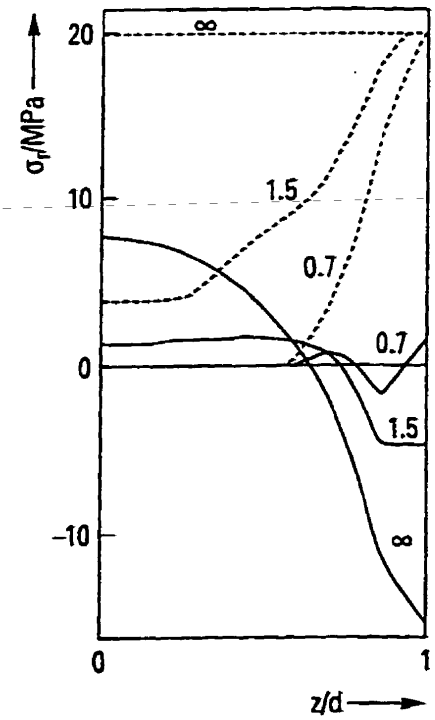

Fig.1.4. Residual stresses calculated for free and constrained quenching (5)

Injection molding:

Experimental determination of residual stresses in injection molded part has been performed previously by several workers (3, 9, 10, 18). In injection molding, the polymer is cooled while it is pressed against the mold walls by the packing pressure. Moreover, the residual stresses consist of flow stresses and thermal stresses. Unlike quenched samples, the molecules in a molded part are oriented and as a result, mechanical properties and stresses are anisotropic. Molding conditions have a significant effect on the final stress profile. In most cases, injection molded polystyrene (PS) and polycarbonate (PC) samples exhibit a stress profile with three distinct regions. A tensile region on the surface is followed by a compressive region and finally a tensile region in the core (3, 5, 9, 19, 20). Isayev (3) and Menges (18) found a compressive surface stress with a subsurface maximum compressive stress. In some cases, a parabolic profile similar to free quenching was reported (3). Variation of processing conditions can change the profile from one to the other. Siegmann (13) obtained the residual stress profile for modified poly(ethylene oxide) (Noryl) and the evaluated effects of melt temperature, mold temperature, holding pressure, and injection rate on the magnitude and shape of the profile. In most cases, a two region profile similar to free quenching was obtained. However, by changing the injection rate and the holding pressure a two region free quenching profile with reversed stresses or a three zone profile was observed. Coxon and White (21, 22) reported the residual stress distribution for high density polyethylene (HDPE) and aged polypropylene (PP) to be compressive at the surface and tensile in the core. For HDPE, they obtained a subsurface compressive maximum. For molded PP samples stored at room temperature for 8 to 10 months, they found a significant reduction of residual stresses. Pham et al. (23) measured the residual stresses in injection molded polycarbonate rectangular bars using the layer removal method, assuming the transverse curvature to be zero. They investigated the effects of molding conditions and location relative to the gate on the final stress profile. They found that the profile in regions close to the end of the cavity was compressive on the surface and tensile in the core and variation of the mold temperature and the injection speed did not affect it significantly. For regions close to the gate, low mold temperatures and high injection speeds reversed the profile so that tensile and

compressive stresses were observed in the skin and core, respectively. Thompson and White (24) studied the effect of aging and annealing at both uniform and non-uniform temperatures on the residual stress profiles and warpage of polystyrene (PS), polypropylene (PP), and glass-fiber-filled PP. The sources of distortion of the molded part were divided into two classes: non-uniformities in the molding and an external temperature gradient or prolonged loading of the article after molding. The effect of different molding conditions, cyclic loading, annealing, and prolonged storage on the fatigue behavior and aging of injection molded PC bars was investigated by Iacopi & White (25).

Molecular orientation gives rise to birefringence and is usually created by flow-induced stresses during molding operation. Birefringence has been frequently used for the assessment of molecular orientation in polymeric specimens (5, 26, 27, 28, 29).

1.2.5. Theoretical Calculation of Residual Stresses

Flow stresses:

Flow stresses are developed mainly in the filling and packing stages of the injection molding process. The governing equations: the continuity, the momentum, and the energy equations are solved to obtain the filling pattern and the velocity, pressure, and temperature fields at different times. Various rheological constitutive equations have been used to solve this problem. In earlier works, the problem was simplified to a flow between two parallel plates and a generalized non-isothermal Newtonian constitutive equation was used (30). To extend the analysis to the packing stage, the compressibility of the polymer was accounted for (31, 32, 33). Kamal and Lafleur analyzed all the stages of injection molding for a viscoelastic and semi-crystalline polymer (34, 35, 36). Kamal et.al. (37) included the fountain flow effect in injection molding simulations. Flow-induced normal stresses may be obtained from the components of the viscoelastic stress tensor. Investigations by Isayev and Hieber (38) and Isayev (27) show the potential capabilities of the Leonov' s constitutive equation (39) to predict flow stresses and birefringence in polystyrene samples. Compressibility effects, an important feature of the packing stage,

were included in Leonov's model by Stickforth (40). In one approach to calculate flow stresses, the flow kinematics was derived using a generalized Newtonian model. The flow kinematics is then used as input for the viscoelastic equation to calculate the flow stresses (4). In another approach called the direct approach, the viscoelastic behavior of the material is taken into account to calculate the flow kinematics (41). Baaijens (41) compared these methods and concluded that there is good agreement between the two approaches but the former method is more cost effective. The calculations of Baaijens (41) also show that a substantial portion of flow stresses arise after the end of the filling stage of injection molding before the gate freeze-off. This is due to the fact that as a result of the drop in temperature, small shear rates may introduce considerable normal stresses in the sample. Fig.1.5 shows the first normal stress difference N_1 (N_1 is the difference between the stresses in the flow and transverse directions) calculated by Baaijens (41), along the thickness of an injection molded polycarbonate strip, using two different methods. The initial and mold temperatures were 320°C and 80°C, respectively.

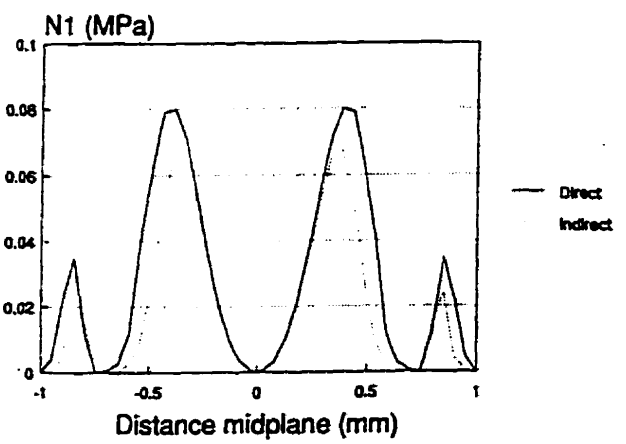

Fig.1.5. Residual flow stresses calculated in a polycarbonate sample (41)

Thermal stresses:

The transient temperature field calculated from the transient energy equation and a constitutive equation relating the components of the stress and deformation must be used to calculate the stresses. It has been shown that the stress field has little effect on the energy equation (42). Initial theoretical calculations of thermal stresses were aimed at

quenching of inorganic glasses. Bartenev (43, 44) developed a model assuming a thermoelastic response for the glass. He assumed that above T_g the glass is plastic and internal stresses are absent, and below T_g the glass is elastic with internal stresses unrelaxed. This theory was shown to predict closely the experimental residual stresses for glass quenched relatively slowly from temperatures well above T_g (43). Later, Indenbom (45) criticized Bartenev's model because it only took into account the temperature gradient in the solidifying layer and ignored the state of the layers that are already solid. He proposed that the total strain in the x-z plane (y being the thickness) is uniform across y and is composed of an elastic strain, a plastic strain, and a thermal contraction strain. The final stress calculated according to Indenbom's model showed better agreement with experiments, especially for the higher cooling rates. Aggarwala and Saibel (46) developed a theory based on a four-parameter viscoelastic constitutive model. They used it to calculate the residual stresses in a Maxwell material with a temperature-dependent thermal expansion coefficient. They assumed the viscosity coefficient to be zero above T_g and infinite below T_g . As pointed out by Isayev et al. (3), this model corresponds to Inbendom's model if the thermal expansion coefficient is assumed temperature-independent. Muki and Sternberg (47) developed a viscoelastic model for calculation of thermal stresses in the case of cooling of a slab with no lateral strain. They used a time and temperature-dependent modulus. Later, Lee et al. (48) modified their approach by assuming an infinite slab with no lateral constraint. Their nonisothermal constitutive equations for the deviatoric and spherical parts of the stress-strain fields were linear viscoelastic and purely elastic, respectively.

Struik (16) modified the theory of Aggarwala and Saibel (46) by neglecting viscoelasticity (time effects in the elastic behavior) and volume relaxation (time effects in the thermal expansion). Also, the properties such as the thermoelastic constants and heat conduction parameters were assumed constant below and above T_g , only changing discontinuously at T_g . Reasonable agreement was observed between the theoretically predicted and experimentally measured surface stresses for quenched sheets of PMMA.

In attempts to calculate thermal stresses in injection molded parts, many developed free quenching models, thus neglecting the effect of melt pressure, interaction of the

sample with the mold wall, and complex mold geometries. Rigdahl (49) used a finite-element formulation assuming that the residual thermal stresses arise from a complete restriction of the thermal contraction. The expression $\sigma = E\alpha\Delta T$ from elasticity theory was coupled with the transient temperature field obtained from solving the energy equation. Kabanemi and Crochet (50) used the finite element technique for a three-dimensional stress analysis assuming viscoelastic behavior.

It was shown experimentally that in many cases, the residual stress profile in an injection molded sample is different from the well-known parabolic profile of free quenching. This suggests that other effects present in injection molding must be taken into account in the calculation of stresses. Two models were developed by Titomanlio et al. (51) and Brucato et al. (52), using thermoelasticity but including the effect of pressure. In the first model, the sample is allowed to shrink inside the mold, while in the second model, the shrinkage is completely restrained inside the mold. These models capture the frequently reported three-zone stress profile with surface tensile stress for PS, suggesting that such a surface stress is caused by pressure. These models, however, tend to overestimate the residual stresses. It must be noted that in the constrained shrinkage model (52), the residual stress is merely caused by pressure.

Boitout et al. (53) calculated the residual thermal stresses using a thermoelastic equation taking into account the effect of mold deformation and gate freezing time. They found that these parameters have a large influence on the final stresses.

Denizart et al. (54) calculated the residual thermal stresses with a three-dimensional thermoelastic, temperature dependent finite element method for PS and PP injection molded discs. They studied numerically the effect of packing pressure, anisotropy in the thermoelastic parameters, and temperature gradient between the upper and lower parts of the mold. Their results agreed qualitatively with their warpage measurements and were found useful in understanding shrinkage in more complex geometries such as a box-shaped part.

Rezayat and Stafford (55) first modified Titomanlio's model (51) by including an analysis of cooling of the part after ejection by convection and radiation. After evaluating the residual stresses, they computed the displacements and the deformed shape by a finite

element analysis. They found that the most noticeable effect of air cooling was the change in the magnitude of the displacements while the deformed shape remained the same. Later, they calculated the thermal stress and the displacements during the packing and cooling stages of injection molding by using a thermo-viscoelastic constitutive equation for the deviatoric part of the stress and the strain and an elastic equation for the dilatational part (56). The analysis was especially appropriate for fiber reinforced plastics because they used a transversely isotropic material matrix and also assumed the only non-zero component of strain to be in the thickness direction.

Baaijens (41) and Douven (4) calculated the thermal stresses for PS and PC injection molded samples using a linear thermo-viscoelastic model obtained from a linearization of the compressible Leonov model. The effect of pressure was implemented through the continuity equation and an equation of state relating pressure, density, and temperature. The residual thermal stress distribution, calculated by Baaijens (41) is shown in Fig.1.6. The initial and mold temperatures were 320°C and 80°C, respectively. Examination of Fig.1.5 and Fig.1.6 shows that the flow stresses are much smaller than the thermal stresses.

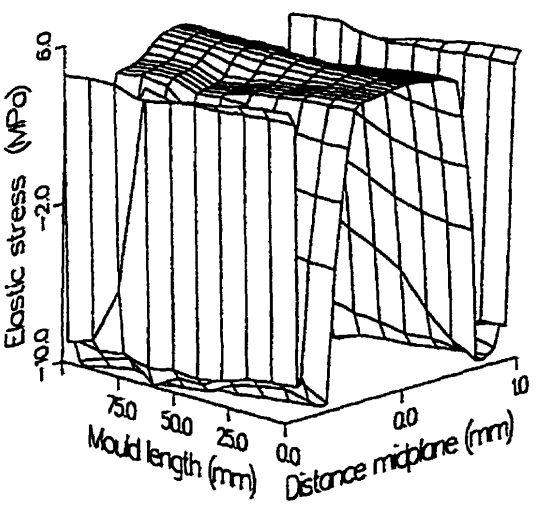

Fig.1.6. Residual thermal stresses calculated in a polycarbonate sample (41)

Fig.1.7 presents the measured and calculated residual stresses in a PS injection molded sample (4). Although the shape and the regions of compression and tensile stresses were qualitatively predicted by this model, the predicted thermal stresses were generally larger than those measured (4).

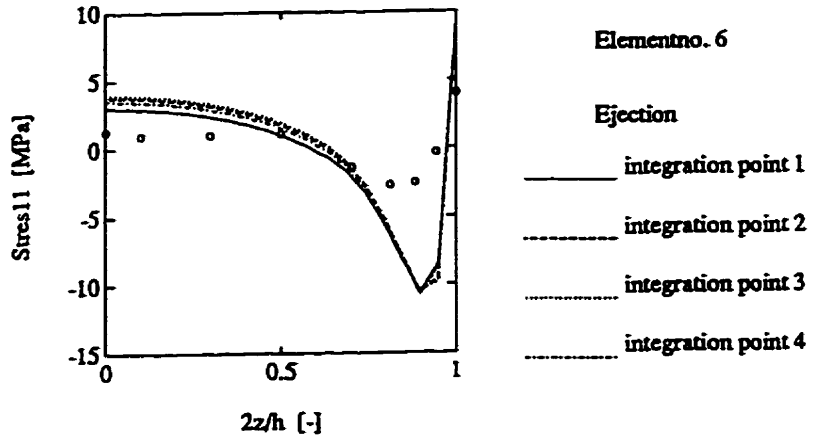

Fig.1.7. Residual stresses measured and calculated in PS injection molded samples; the initial and mold temperatures were 200°C and 55°C (4)

Baaijens took into account the elasticity of the mold and found that, in this case, the calculated pressure decay at the end of injection molding cycle is slower (41).

Bushko and Stokes (57) formulated a one-dimensional viscoelastic model, taking into account the effects of packing pressure and added mass of material during the packing stage. Using simulations with this model, they investigated extensively the effect of processing and boundary conditions on predicted shrinkage and residual stresses (58, 59, 60, 61). The results were not compared with experimental data. Santhanam (62) used a similar approach but he did not allow for the extra material entering the cavity during packing. Model predictions were then compared with experimentally measured stresses reported by Crouthamel (63). The model overpredicted the stress in most cases. Depending on the molding conditions, different boundary conditions gave better results.

Ghoneim and Hieber (64) investigated, qualitatively, the effect of density relaxation on the residual stress profile in a one-dimensional post-molded polystyrene

part. They found that density relaxation (viscoelastic material behavior in dilatation) plays an important role in the development of residual stresses in injection molding.

Jansen and Titomanlio (65, 66) used a simple elastic model to derive expressions for residual stresses and in-mold shrinkage for injection molding with shrinkage and with hindered shrinkage during solidification. They defined the pressure number N_p as the ratio of maximum pressure strain (positive) and the thermal strain (negative). The in-plane and thickness actual shrinkages depend on N_p. They also concluded that the friction between the polymer and the mold wall can be dominant and prevent length shrinkage until pressure drops to a few MPa. Jansen (67) conducted a comprehensive analysis of residual stresses and warpage by deriving analytical expressions for the solidified layer thickness, free quenching stress, and formation pressure (pressure at the time of solidification) using Titomanlio's model (51, 52).

Most of the previous theoretical studies on residual stresses have been conducted on amorphous polymers, in order to avoid the effect of crystallinity on stresses. For a semi-crystalline polymer, the effect of heat of crystallization, change in the material properties with crystallinity, and the shrinkage due to crystallization must be taken into account. Chapman et al. (68) proposed a model to predict the residual stress in semi-crystalline thermoplastic composite laminates. Free quenching was assumed. It was found that crystallinity causes an increase in the magnitude of residual stresses.

1.3. INVERSE MODELING

The common approach for the analysis of plastics processing operations relies on obtaining a direct solution of the relevant equations of change. In a directly-posed or well-posed problem, the domain and boundaries of the problem, the governing and constitutive equations, the boundary and initial conditions, and the material properties are known. A problem in which any of this information is not available is considered to be an inverse problem. Some experimental information is usually used to obtain the unknowns. In other words, in inverse problems, inputs or sources are determined from observed responses or outputs (69).

Optimization of a process such as injection molding with respect to a final property of the molded part, such as the residual stress profile, is an inverse problem of great importance. This problem was considered in the present thesis, and it was treated using both direct and inverse methods.

One approach to solve inverse problems is to assume the unknown information, solve the direct problem, and iterate until the solution agrees with the experimental observations. This method involves a large number of iterations and in each iteration the direct problem must be solved. An alternative approach is the inverse formulation to obtain the unknown information as the solution. The difficulties associated with inverse problems are : non-existence, non-uniqueness, and instability of the solution (70). A combination of the two approaches may also be used.

Inverse formulation or inverse modeling has gained growing attention in various fields of science and engineering. It has been applied to geophysics for inversion of reflection seismic data to discover oil fields, and for inversion of gravity, electromagnetic, and resistivity data (71). Significant work has been done on inverse heat conduction problems, where a time-dependent surface temperature, heat flux, or heat transfer coefficient is calculated using interior temperature measurements. One of the earliest papers on inverse heat conduction was published by Stolz (72), in which he addressed the calculation of heat transfer rates during quenching of bodies of simple finite shape. Beck (73), starting in 1961, and Alifanov (74) have had a major influence on the analysis of inverse heat conduction problems. Hensel (75) presented a detailed review of the literature on inverse heat conduction in his thesis. He also provided a methodology to solve the multi-dimensional transient nonlinear inverse problem of heat conduction with an unknown surface condition using temperature measurements from sensors inside a solid body. Both finite element and finite difference methods were used and the effects of measurement errors, number and location of the sensors, and regularization parameters were discussed.

Several methods have been suggested to deal with the non-uniqueness and instability of the inverse solution. It was suggested by Flach and Ozisik (76) that a requirement for uniqueness is that the total number of measurements be equal to or

exceed the number of unknown parameters. To control oscillations in the estimated solution, stabilizing techniques such as digital filtering and regularization may be used (77, 78).

In the processing of polymeric materials, several inverse problems of practical importance arise. An example is the estimation of the shape of the extruder die that produces an extrudate with prescribed shape. Cohen (79) used inverse formulation together with the method of characteristics to obtain the extruder die profile required to obtain uniform flow with a prescribed total flux. He dealt with the problem of non-uniqueness by imposing the additional constraint of minimal pressure drop. Legat and Marchal (80) presented a numerical scheme to solve this problem for complex geometries by means of an implicit Newton-Raphson iterative technique.

In injection molding, the operating conditions such as the pressure and the temperature distribution history affect the final properties and thus the quality of the molded product. The residual stress profile in the part is not exempt from this. Kang et al. (81) used a least-squares methodology to obtain the optimum time history of mold-wall temperature that produces an injection molded part with minimum residual stress distribution. The method was not tested with actual experimental data.

In the present thesis, inverse formulation is used to estimate the pressure history or the initial melt temperature distribution required to generate a specified residual stress profile (82). The one dimensional models developed by Titomanlio et al. (51) and Brucato et al. (52) were used in the inverse formulation.

1.4. OBJECTIVES AND OUTLINE OF THESIS

In spite of a large number of experimental and theoretical investigations on residual stresses, the subject is far from being completely resolved. The stress profiles reported by various researchers are not always consistent and do not seem to be well understood. The influence of the molding conditions on the stresses is not clear, since reported data are sometimes contradictory. Most previous experimental and theoretical studies have been conducted on amorphous polymers. A large number of polymeric materials widely used in industry are semi-crystalline. Therefore, a thorough analysis of

the coupling effect of crystallization and residual stress is of large practical interest. The inverse approach for the optimization of the injection molding process with respect to the residual stresses in the product has not yet been explored.

The main objective of the present thesis was to expand the existing knowledge on the generation of thermal stresses and to combine theoretical and experimental findings to obtain a practical tool for controlling them. This goal was achieved by:

- developing a thermoelastic model for calculation of residual stresses and to evaluate the effects of various parameters on them, considering only the packing and cooling stages of injection molding.
- using the above model to assess the most important parameters that determine the shape and magnitude of residual stresses.
- developing inverse methods in combination one-dimensional stress models to calculate the unknown pressure history or initial temperature distribution required to generate a prescribed residual stress profile.
- linking the thermoelastic model with the simulation of the complete injection molding cycle using the package McKam©, developed at McGill.
- investigating the effect of crystallinity on residual stresses using McKam©.
- measuring the distribution of residual stresses along the thickness, in polystryrene (amorphous) and polyethylene (semi-crystalline) samples, injection molded under well-defined processing conditions.
- investigating and providing explanations for the effect of various molding conditions and crystallization on the stress profile, combining the experimental and theoretical results.
- based on these findings, developing procedures for optimizing the injection molding process with respect residual stresses.

This thesis is organized in the following way:

In the first part of Chapter 2, general theoretical definitions and concepts are presented. In the second part of this chapter, the procedure for direct calculation of thermal stresses and inverse calculation of an unknown pressure history or initial temperature profile is described.

Chapter 3 consists of the characterization of materials and the description of the machines and experimental procedures involved in the measurement of residual stresses and crystallinity in injection molded samples.

The experimental and theoretical results are presented, compared, and discussed in Chapter 4. This chapter also includes the results of the inverse formulations.

Finally, Chapter 5 includes the main conclusions of the thesis, some recommendations for future continuation of this work, and claims for contribution to knowledge.

1.5. SUMMARY OF CHAPTER 1

Injection molding is the most widely used process for manufacturing plastics parts with complex shapes. It mainly consists of 3 stages: filling, packing, and cooling. The ultimate properties of the molded part depend, to a large extent, on its morphology and the distribution of orientation, residual stress, and crystallinity. These, in turn, are determined by the material properties and the molding conditions. This thesis is mainly concerned with residual stresses.

Residual stresses may be classified into flow-induced and thermally-induced stresses. The most important technique used to measure residual stresses is the layer removal technique based on disturbing the equilibrium of the stress field by successively removing thin layers from the surface of the sample.

The residual stress profile in free quenched samples is parabolic with compressive stress on the surface and tensile stress in the core. In injection molded parts, various profiles have been observed for different material and molding conditions. The differences, compared to free quenching, have been attributed to the effects of pressure, mold geometries, wall adhesion, and the presence of flow stresses.

Optimization of a process with respect to an output or a property of the final product represents an inverse problems which may be solved by inverse formulation, a new approach in polymer processing.

Chapter 2

CALCULATION OF THERMAL STRESSES

In this chapter, the basic theory of thermal stresses is described in the general form. Subsequently, the obtained equations are simplified for special cases using appropriate simplifying assumptions. Finally, the inverse problem of estimating the processing conditions that generate a prescribed residual stress profile is considered.

2.1. INTRODUCTION

During the injection molding process, a highly viscous thermoplastic flows into a cavity of complex geometry and cools until it is solidified. The rheological behavior of the material is usually a strong function of temperature and pressure, both changing rapidly during the process. As the mold is filled with the polymer, layers of the melt closer to the walls start to solidify. The large time-dependent deformation rates cause a non-homogeneous orientation in the melt that leads to a highly anisotropic product, especially in the case of fiber-filled composites. As the polymer cools and solidifies, its specific volume is decreased and additional material is pushed into the cavity due to the high packing pressure in order to compensate for the volume shrinkage. Thermal stresses are generated as a result of the restriction of part of this shrinkage. This restriction is due to the non-homogeneity of the shrinkage and the continuity of the body. The aim of this chapter is to formulate the development of these thermal stresses and to calculate them in an injection molded part.

2.2. GENERAL THEORETICAL ASPECTS

When a material is subjected to a force, either it moves as a whole (translational or rotational motion) or its particles move relative to each other. The latter is called deformation. Upon application of the force, the thermodynamic equilibrium is disturbed inside the material and rearrangements take place to bring it back to equilibrium. In any real material, these rearrangements take a finite time. The required time may be short or long, depending on the material. If the changes occur so rapidly that this time is negligible compared to the time scale of the experiment, the material is considered purely viscous. As a result, in a purely viscous material all the energy required to produce the deformation is dissipated as heat and the deformation is not reversible. If the rearrangements of the molecules of the material take infinite time, the material is called purely elastic. In a purely elastic material, the energy of deformation is stored and may be recovered completely when the forces are released. In intermediate cases, the deformation may consist of a recoverable (elastic) and a permanent part (viscous). The behavior of the material may be formulated by a constitutive equation which is independent of the size or the shape of the body and of the type of force and deformation, and only depends on its material nature (83). The first relevant constitutive equation was formulated by Hooke, stating that the extension of a stretched spring is proportional to the force applied to it. In order to be independent of the geometry and type of the deformation, a constitutive equation should not be expressed in terms of force and displacement but rather in terms of the stress tensor and the strain tensor or the strain rate tensor.

2.2.1. The Strain Tensor

The shape and volume of a body change under the influence of an applied force. Let us consider the position of a point in a body defined by the vector **r** with components $x_1=x$, $x_2=y$, and $x_3=z$ in a coordinate system, as shown in Fig. 2.1.

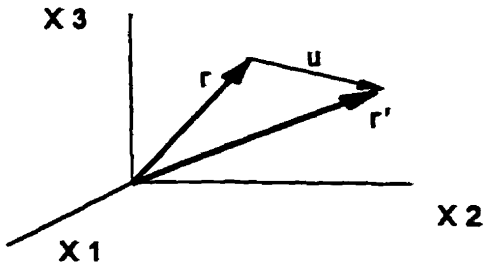

Fig.2.1. Displacement of the position vector under deformation

When the body is deformed, the position vector changes to r' with components x_i'. The displacement of this point due to the deformation is given by the vector $u = r' - r$. The components of **u** are given by:

$$u_i = x_i' - x_i \tag{2.1}$$

The vector **u** is called the displacement vector.

When a body is deformed, the distance between its points changes. The strain tensor or the displacement gradient tensor relates the distance between two points in the deformed body to that in the undeformed body. If the change in a distance in the body is small compared to the distance itself, the strain is small. For small strains or deformations, free of translation or rotation, the symmetric second order strain tensor is given by:

$$\varepsilon_{ij} = \frac{1}{2}\left(\frac{\partial u_i}{\partial x_j} + \frac{\partial u_j}{\partial x_i}\right) \tag{2.2}$$

while the antisymmetric tensor

$$\frac{1}{2}\left(\frac{\partial u_i}{\partial x_j} - \frac{\partial u_j}{\partial x_i}\right) \tag{2.3}$$

represents the rigid body rotation and is called the rotation tensor.

The components on the main diagonal of the strain tensor are called normal strains and represent extension, the off-diagonal components are called shear strains and denote shear deformation. It may be shown that the trace of the strain tensor (the sum of the diagonal components) gives the relative change in volume due to deformation (84) :

$$\frac{V - V_0}{V_0} = \varepsilon_{11} + \varepsilon_{22} + \varepsilon_{33} \tag{2.4}$$

The time derivative of the strain tensor is the rate of deformation tensor given by:

$$\dot{\varepsilon}_{ij} = \frac{1}{2}\left(\frac{\partial v_i}{\partial x_j} + \frac{\partial v_j}{\partial x_i}\right) \tag{2.5}$$

where :

$$v_i = \dot{u}_i = \frac{du_i}{dt} \tag{2.6}$$

is the velocity and $\frac{\partial v_i}{\partial x_j}$ is the velocity gradient tensor.

2.2.2. The Stress Tensor

In a body that is not deformed, the arrangement of the molecules corresponds to a state of thermal equilibrium. This means that if some portion of the body is considered, the resultant of the forces acting on that portion is zero. When a deformation occurs, the arrangement of the molecules changes and the body is not in its original equilibrium state anymore. The surrounding material exerts forces on the surface of each element that tend to return the body to its equilibrium state. These forces are proportional to the surface of the element and the force per unit area is called the stress. If F_i is the force vector exerted per unit volume, the second order stress tensor σ_{ij} is related to F_i by the following expression (84) :

$$F_i = \frac{\partial \sigma_{ij}}{\partial x_j} \tag{2.7}$$

where the indicial notation (summation over repeated index) has been used. The stress tensor is symmetric due to the balance of internal angular momentum. Therefore, it has six independent components instead of nine. The diagonal components are the normal stresses and the components with differing indices are called the shear stresses. The sign convention found in most textbooks and followed throughout this thesis, is that a tensile stress is positive. Equation (2.7) is a force balance and the equations of equilibrium for a deformed body are derived from this equation by letting $F_i = 0$, as follows:

$$\frac{\partial \sigma_{ij}}{\partial x_j} = 0 \tag{2.8}$$

If there are body forces (such as the gravity force) acting throughout the body and whose magnitudes are proportional to the volume of the element, equation (2.8) becomes:

$$\frac{\partial \sigma_{ij}}{\partial x_j} + F_{bi} = 0 \tag{2.9}$$

where $\mathbf{F_b}$ is the body force per unit volume. The external forces applied to the surface of the body appear in the boundary conditions of the equilibrium equations. If **P** is an external force per unit area acting on the surface of the body and **n** is a unit vector along the outward normal to the surface, we have:

$$\sigma_{ij} n_j = P_i \tag{2.10}$$

This is the condition that must be satisfied at each point on the surface of a body in equilibrium. If all parts of the body are not in static equilibrium, equation (2.9) takes the more general form :

$$\frac{\partial \sigma_{ij}}{\partial x_j} + F_{bi} = \rho \dot{v}_i \tag{2.11}$$

where ρ is the density and $\dot{v}_i$ is the acceleration in the x_i direction.

To calculate the strains or displacements in a body, equation (2.9) or (2.11) must be solved. To this end, however, a constitutive equation is needed to relate the stress and the strain. The simplest relation between the stress and the strain is a linear relation. Experiment has shown that linear relations may be assumed to be obeyed in the limit of infinitesimally small elastic deformations. In the general case, this linear relationship may be expressed as:

$$\sigma_{ij} = C_{ijkl}\, \varepsilon_{kl} \tag{2.12}$$

where **C** is the fourth order modulus tensor with 81 components. In purely elastic deformations, these components are material constants known as elastic coefficients. Due to the symmetry of the stress and strain tensors and their relation with the Helmholtz free energy, only 21 independent constants are required. Introduction of various degrees of symmetry in the material reduces further the number of material constants required to describe its behavior (85). Isotropic materials possess only two elastic constants.

3.2.3. Elastic behavior

From thermodynamics of deformation, the components of the stress tensor may be obtained by differentiating the free energy f with respect to the strain at constant temperature, as follows (84):

$$\sigma_{ij} = \left(\frac{\partial f}{\partial \varepsilon_{ij}}\right)_T \tag{2.13}$$

The free energy f for small deformations and small changes in the temperature of an isotropic body may be expressed as:

$$f(T) = f_0(T) - K_b\alpha_v(T - T_0)\varepsilon_{kk} + G_s(\varepsilon_{ij} - \tfrac{1}{3}\delta_{ij}\varepsilon_{kk})^2 + \tfrac{1}{2}K_b\varepsilon_{kk}^2 \tag{2.14}$$

where K_b and G_s are the bulk modulus and the shear modulus, respectively and α_v is the volumetric coefficient of thermal expansion; f_0 is the free energy in the absence of deformation; T_0 is a reference temperature at which the body is stress-free in the absence of external forces and δ is the second order unit tensor. If the body is at a temperature T different from T_0 then it will be deformed even if there is no external force, due to thermal expansion. Using equation (2.13), we can obtain the resulting stress by differentiating the free energy:

$$\sigma_{ij} = -K_b\alpha_v(T - T_0)\delta_{ij} + K_b\varepsilon_{kk}\delta_{ij} + 2G_s(\varepsilon_{ij} - \tfrac{1}{3}\delta_{ij}\varepsilon_{kk}) \tag{2.15}$$

The first term on the right-hand-side denotes the stress caused by the change in the temperature, the second is due to an isotropic deformation such as compression, and the last terms is the result of pure shear. In fact, the trace of the last term is zero meaning that there is only change in the shape of the body and no change in its volume. The above expression provides the stress tensor in terms of the strain tensor for an isotropic elastic body. To obtain the formula that expresses the strain tensor in terms of the stress tensor, we take the trace of the equation (2.15) and solve for the trace of strain.. Since the trace of the last term is zero, we find :

$$\varepsilon_{kk} = \frac{\sigma_{kk}}{3K_b} + \alpha_v(T - T_0) \tag{2.16}$$

Replacing in equation (2.15) and solving for ε_{ij} we obtain:

$$\varepsilon_{ij} = \frac{\sigma_{kk}}{9K_b}\delta_{ij} + \frac{1}{2G_s}\left(\sigma_{ij} - \frac{1}{3}\sigma_{kk}\delta_{ij}\right) + \frac{\alpha_v}{3}(T - T_0)\delta_{ij} \tag{2.17}$$

In the case of the isothermal simple extension of a rod along the z-direction due to a tensile force per unit area of magnitude p, the zz-component of the stress tensor may be obtained from the boundary condition as: $\sigma_{zz} = p$. From the general expression (2.17) the non-zero strains are given by:

$$\varepsilon_{xx} = \varepsilon_{yy} = -\frac{1}{3}\left(\frac{1}{2G_s} - \frac{1}{3K_b}\right)p \quad , \quad \varepsilon_{zz} = \frac{1}{3}\left(\frac{1}{3K_b} + \frac{1}{G_s}\right)p \tag{2.18}$$

The component ε_{zz} gives the increase in the length of the rod. The coefficient of p, $\frac{1}{3}\left(\frac{1}{3K_b} + \frac{1}{G_s}\right)$, is called the coefficient of extension and its reciprocal is called the modulus of extension or Young's modulus E. Therefore, the Young's modulus is related to the shear and bulk moduli, as follows:

$$E = \frac{9K_bG_s}{(3K_b + G_s)} \tag{2.19}$$

The components ε_{xx} and ε_{yy} give the relative compression of the rod in the transverse direction. The ratio of the negative transverse compression to the longitudinal extension $\frac{-\varepsilon_{xx}}{\varepsilon_{zz}}$ is called the Poisson ratio υ and is derived from equation (2.18), as follows:

$$\upsilon = \frac{(3K_b - 2Gs)}{2(3K_b + G_s)} \tag{2.20}$$

The relative increase in the volume of the rod is $p/3K_b$.

Expanding equation (2.15), the components of stress and strain are related for an elastic and homogeneous deformation, as follows:

$$\sigma_{xx}=\frac{E}{(1+\upsilon)(1-2\upsilon)}\left[(1-\upsilon)\varepsilon_{xx}+\upsilon\left(\varepsilon_{yy}+\varepsilon_{zz}\right)-\tfrac{1}{3}(1+\upsilon)\alpha_v\left(T-T_0\right)\right]$$

$$\sigma_{yy}=\frac{E}{(1+\upsilon)(1-2\upsilon)}\left[(1-\upsilon)\varepsilon_{yy}+\upsilon\left(\varepsilon_{xx}+\varepsilon_{zz}\right)-\tfrac{1}{3}(1+\upsilon)\alpha_v\left(T-T_0\right)\right] \qquad (2.21)$$

$$\sigma_{zz}=\frac{E}{(1+\upsilon)(1-2\upsilon)}\left[(1-\upsilon)\varepsilon_{zz}+\upsilon\left(\varepsilon_{yy}+\varepsilon_{xx}\right)-\tfrac{1}{3}(1+\upsilon)\alpha_v\left(T-T_0\right)\right]$$

$$\tau_{xy}=\frac{E}{1+\upsilon}\gamma_{xy}\quad,\quad \tau_{zx}=\frac{E}{1+\upsilon}\gamma_{zx}\quad,\quad \tau_{yz}=\frac{E}{1+\upsilon}\gamma_{yz}$$

where the shear components of the stress and strain are denoted by τ and γ, respectively.

The above equations may be rewritten in the following way:

$$\begin{pmatrix}\sigma_{xx}\\ \sigma_{yy}\\ \sigma_{zz}\end{pmatrix}=\frac{E}{(1+\upsilon)(1-2\upsilon)}\begin{pmatrix}1-\upsilon & \upsilon & \upsilon\\ \upsilon & 1-\upsilon & \upsilon\\ \upsilon & \upsilon & 1-\upsilon\end{pmatrix}\begin{pmatrix}\varepsilon_{xx}-\varepsilon_T\\ \varepsilon_{yy}-\varepsilon_T\\ \varepsilon_{zz}-\varepsilon_T\end{pmatrix} \qquad (2.22a)$$

and

$$\begin{pmatrix}\tau_{xy}\\ \tau_{zx}\\ \tau_{yz}\end{pmatrix}=\frac{E}{(1+\upsilon)}\begin{pmatrix}1 & 0 & 0\\ 0 & 1 & 0\\ 0 & 0 & 1\end{pmatrix}\begin{pmatrix}\gamma_{xy}\\ \gamma_{zx}\\ \gamma_{yz}\end{pmatrix} \qquad (2.22b)$$

where ε_T is $\frac{1}{3}\alpha_v\left(T-T_0\right)$, α_v is the volumetric thermal expansion coefficient, as before.

Plane strain case:

The two-dimensional state of plane strain is defined as one in which the displacement component in one direction (in this case z) is negligible and thus assumed to be zero (86). Consequently, from the definition of strain, equation (2.2), the corresponding strain components are:

$$\varepsilon_{zz}=\varepsilon_{yz}=\varepsilon_{zx}=0 \qquad (2.23)$$

If we replace $\varepsilon_{zz}=0$ in the equations giving the strain components in terms of stress components (2.17), we obtain for σ_{zz} :

$$\sigma_{zz} = \upsilon\left(\sigma_{xx} + \sigma_{yy}\right) - E\varepsilon_T \tag{2.24}$$

Eliminating σ_{zz} in equation (2.17), equation (2.21) for the plane strain case becomes:

$$\sigma_{ij} = \frac{E\upsilon}{(1+\upsilon)(1-2\upsilon)}\varepsilon_{kk}\delta_{ij} + \frac{E}{(1+\upsilon)}\varepsilon_{ij} - \frac{E}{1-2\upsilon}\varepsilon_T\delta_{ij} \tag{2.25}$$

Equation (2.25) may be expressed in matrix notation as follows:

$$\begin{pmatrix}\sigma_{xx}\\ \sigma_{yy}\\ \tau_{xy}\end{pmatrix} = \frac{E}{(1+\upsilon)(1-2\upsilon)}\begin{pmatrix}1-\upsilon & \upsilon & 0\\ \upsilon & 1-\upsilon & 0\\ 0 & 0 & 1-2\upsilon\end{pmatrix}\begin{pmatrix}\varepsilon_{xx}\\ \varepsilon_{yy}\\ \gamma_{xy}\end{pmatrix} - \frac{E}{(1-2\upsilon)}\begin{pmatrix}\varepsilon_T\\ \varepsilon_T\\ 0\end{pmatrix} \tag{2.26}$$

Plane Stress Case:

The second alternative to have a two-dimensional system in a thermoelastic analysis is plane stress.

In the plane stress case, we have:

$$\sigma_{xz} = \sigma_{yz} = \sigma_{zz} = 0 \tag{2.27}$$

Substituting (2.27) in the general thermoelastic equations (2.17), we obtain for the strains:

$$\begin{aligned}\varepsilon_{xz} &= \varepsilon_{yz} = 0\\ \varepsilon_{zz} &= -\frac{\upsilon}{E}\left(\sigma_{xx} + \sigma_{yy}\right) + \varepsilon_T\end{aligned} \tag{2.28}$$

The stress-strain relationship (2.21) now becomes (42):

$$\sigma_{ij} = \frac{E\upsilon}{(1+\upsilon)(1-\upsilon)}\varepsilon_{kk}\delta_{ij} + \frac{E}{(1+\upsilon)}\varepsilon_{ij} - \frac{E}{1-\upsilon}\varepsilon_T\delta_{ij} \tag{2.29}$$

or in matrix notation:

$$\begin{pmatrix}\sigma_{xx}\\ \sigma_{yy}\\ \tau_{xy}\end{pmatrix} = \frac{E}{(1+\upsilon)(1-\upsilon)}\begin{pmatrix}1 & \upsilon & 0\\ \upsilon & 1 & 0\\ 0 & 0 & 1-\upsilon\end{pmatrix}\begin{pmatrix}\varepsilon_{xx}-\varepsilon_T\\ \varepsilon_{yy}-\varepsilon_T\\ \gamma_{xy}\end{pmatrix} \tag{2.30}$$

2.2.4. Viscous Behavior

In elastic bodies, it is assumed that the deformation is reversible. This is due to the fact that the level of free energy in the deformed body remains constant as long as the external force is not changed. In a viscous fluid, when the deformation disturbs the existing equilibrium, irreversible processes take place immediately to bring the body back to equilibrium. The free energy is, thus, dissipated as the molecules transit from the initially raised energy level (deformed state) to the final equilibrium state. Consequently, if the applied force is removed no strain energy is left to return the body to its initial state.

If we have a mechanical system whose motion involves the dissipation of energy, this motion can be described by the usual equations of motion, taking into account the dissipative forces or frictional forces which are linear functions of the rate of the motion (velocity) (84).

In order to derive a constitutive equation for viscous fluids, we consider the dissipative function R which describes the internal friction and must be zero for a translation or rotation and in the absence of friction (84). This means that it must depend not on the velocity itself but on its gradients and contain only combinations of the derivatives of the velocity that vanish for pure rotation, as follows:

$$\dot{\varepsilon}_{ij} = \frac{1}{2}\left(\frac{\partial v_i}{\partial x_j} + \frac{\partial v_j}{\partial x_i}\right) \tag{2.31}$$

As mentioned before (equation (2.5)), the tensor $\dot{\varepsilon}_{ij}$ is the symmetric part of the velocity gradient tensor and is called the rate of deformation tensor (87). The antisymmetric part of the velocity gradient is called the vorticity tensor and is given by:

$$\omega_{ij} = \frac{1}{2}\left(\frac{\partial v_i}{\partial x_j} - \frac{\partial v_j}{\partial x_i}\right) \tag{2.32}$$

The dissipative function R must then be a quadratic function of the velocity gradient tensor and its most general form is (84):

$$R = \frac{1}{2}\eta_{iklm}\dot{\varepsilon}_{ik}\dot{\varepsilon}_{lm} \tag{2.33}$$

The fourth order tensor η_{iklm} is the viscosity tensor. Equation (2.33) is analogous to the expression for free energy of an elastic crystal (84), here the viscosity tensor replaces the

elastic modulus tensor. Various symmetries in the material reduce the number of independent components of the viscosity tensor. For an isotropic body, equation (2.33) may be written in the following form:

$$R=\eta\left(\dot{\varepsilon}_{ij}-\frac{1}{3}\delta_{ij}\dot{\varepsilon}_{kk}\right)^2+\frac{1}{2}\xi\,\dot{\varepsilon}_{kk}^{\,2} \tag{2.34}$$

where η and ξ are the shear and the dilatational viscosity coefficients, respectively. The dilatational viscosity is zero for ideal, monoatomic gases; for incompressible materials, $\varepsilon_{kk}=0$. Therefore, the dilatational viscosity is of no importance in these two limiting cases (88). In analogy to the elastic stress, the dissipative or viscous stress tensor σ_{ij} is defined in the general case by:

$$\sigma_{ij}=\frac{\partial R}{\partial\dot{\varepsilon}_{ij}}=\eta_{ijkl}\,\dot{\varepsilon}_{kl} \tag{2.35}$$

For an isotropic body, we have:

$$\sigma_{ij}=2\eta\left(\dot{\varepsilon}_{ij}-\frac{1}{3}\delta_{ij}\dot{\varepsilon}_{kk}\right)+\xi\,\dot{\varepsilon}_{kk}\,\delta_{ij} \tag{2.36}$$

The stress tensor is symmetric for materials with no preferred direction other than that imposed by the deformation. This is a consequence of the principle of conservation of angular momentum for isotropic materials (87).

Two important types of flow, present in most processes, are shear flow and elongational flow. In a shear flow, the rate of deformation tensor has the form:

$$\dot{\varepsilon}=\frac{1}{2}\begin{pmatrix}0 & \dot{\gamma} & 0\\ \dot{\gamma} & 0 & 0\\ 0 & 0 & 0\end{pmatrix} \tag{2.37}$$

where $\dot{\gamma}$ is the shear rate. The shear rate $\dot{\gamma}$ is in fact the second invariant of $\dot{\varepsilon}$ ($\dot{\gamma}=\sqrt{\dot{\varepsilon}:\dot{\varepsilon}}$). In the simple shear flow between parallel plates, shown in Fig.2.2, the shear rate is dv_x/dy.

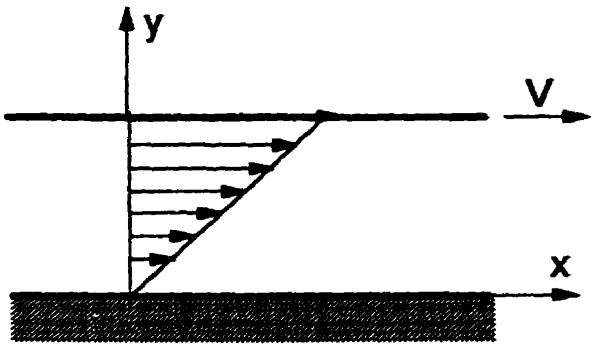

Fig.2.2. Simple shear flow between parallel plates

The stress tensor in shear flow is given in the general case by:

$$\sigma = \begin{pmatrix} P+\sigma_{11} & \tau_{12} & 0 \\ \tau_{12} & P+\sigma_{22} & 0 \\ 0 & 0 & P+\sigma_{33} \end{pmatrix} \tag{2.38}$$

where P is the isotropic pressure. The quantities of experimental interest are the shear stress and the normal stress difference as follows (88):

Shear stress: τ_{12}

Primary normal stress difference: $\sigma_{11}-\sigma_{22}$

Secondary normal stress difference: $\sigma_{22}-\sigma_{33}$

In many polymer processes such as fiber spinning, blow molding, thermoforming and others, the major mode of deformation is elongation. In elongational flows, the rate of deformation tensor is given by:

$$\dot{\varepsilon} = \begin{pmatrix} \dot{\varepsilon}_{11} & 0 & 0 \\ 0 & \dot{\varepsilon}_{22} & 0 \\ 0 & 0 & \dot{\varepsilon}_{33} \end{pmatrix} \tag{2.39}$$

Examples of uniaxial, biaxial, and planar elongations are shown in Fig.2.3.

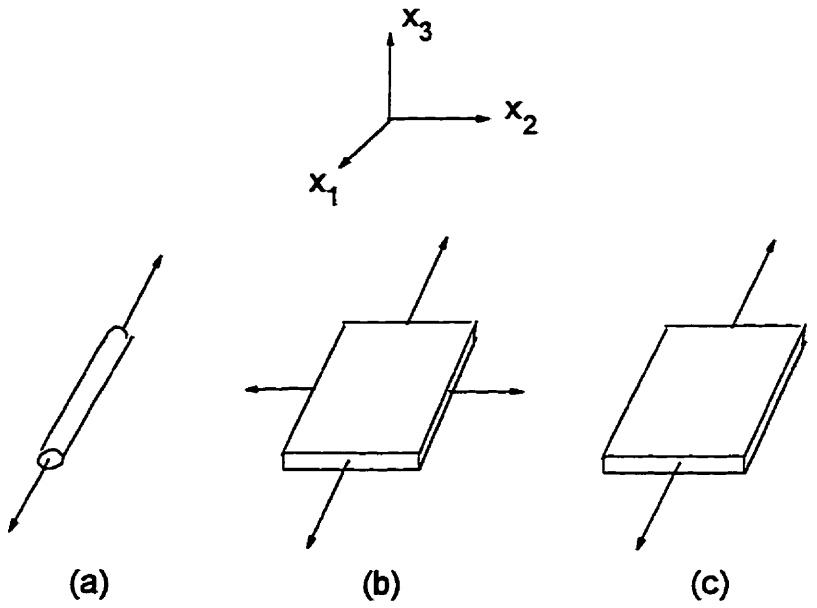

Fig.2.3.Uniaxial (a), biaxial (b), and planar (c) elongational flow

The stress tensor in elongational flow is given by:

$$\sigma=\begin{pmatrix}\sigma_{11} & 0 & 0\\ 0 & \sigma_{22} & 0\\ 0 & 0 & \sigma_{33}\end{pmatrix} \tag{2.40}$$

A viscous fluid that follows equation (2.36) with constant viscosity coefficients is called a Newtonian fluid. The viscosity of a Generalized Newtonian fluid depends on the deformation. For most polymer melts, the viscosity depends on the rate of deformation, temperature, and pressure. Fig.3.1 in Chapter 3 shows the variations of the shear viscosity of the polystyrene sample used in the present study with the rate of shear and temperature. In a simple shear flow, for instance, the shear viscosity for a Generalized Newtonian fluid may be expressed as a function of the shear, the temperature, and the pressure: $\eta=\eta(\dot{\gamma},T,P)$. The temperature and pressure dependence of viscosity are normally factored out and approximated by exponential functions, as follows:

$$\eta(\dot{\gamma},T,P)=exp\left(\frac{E_a}{R}\left(\frac{1}{T}-\frac{1}{T_0}\right)\right)exp\left(\beta\left(P-P_0\right)\right)\eta(\dot{\gamma},T_0,P_0) \tag{2.41}$$

where T_0 and P_0 are the reference temperature and pressure, respectively; E_a is the activation energy, R is the gas constant, and β is the pressure coefficient. Most polymers are shear thinning. This means that their viscosity decreases with increasing the rate of deformation. The Power Law model is a simple model that accurately represents the shear thinning region in the viscosity versus strain rate curve. However, it neglects the Newtonian plateau observed at small strain rates. The dependence of the viscosity on the shear rate may be expressed using a Power Law model, given by:

$$\eta = m(T,P)\,\dot{\gamma}^{n-1} \tag{2.42}$$

where m is referred to as the consistency index and n is the Power Law index. The temperature and pressure dependence of the viscosity are included in the consistency index. The shear thinning behavior corresponds to $n < 1$. According to equation (2.42), the viscosity is infinite at zero rate of deformation. This leads to an erroneous result in problems where there is a region of zero shear rate, such as the center of a tube.

A model that fits the whole range of strain rates is the Carreau-Yasuda model that contains five parameters:

$$\frac{\eta-\eta_0}{\eta_0-\eta_\infty} = \left[1+|\lambda\dot{\gamma}|^a\right]^{(n-1)/a} \tag{2.43}$$

Some materials such as polymer emulsions and slurries exhibit a no-flow region below a certain yield stress τ_y. The Bingham Fluid model represents their behavior, as follows:

$$\begin{aligned} \tau \le \tau_Y \qquad & \eta = \infty \quad or \quad \dot{\gamma} = 0 \\ \tau \ge \tau_Y \qquad & \eta = \mu_0 + \frac{\tau_Y}{\dot{\gamma}} \end{aligned} \tag{2.44}$$

where τ is the magnitude of the deviatoric (zero trace) stress tensor.

2.2.5. Viscoelastic Behavior

Viscoelastic materials exhibit an elastic behavior in fast deformations and a viscous behavior in slow deformations. A useful parameter, often used to estimate the elastic effects during flow, is the Deborah number, De, defined by (89):

$$De = \frac{\lambda_R}{t_P} \tag{2.45}$$

where λ_R is the relaxation time of the material and t_P is a characteristic process time. A Deborah number of zero represents a viscous fluid and an elastic solid has an infinite Deborah number. As De becomes larger than one, the molecules of the material do not have enough time to relax and rearrange during the deformation. Therefore, when the deformation ceases, the material returns to its initial configuration. Polymer melts are viscoelastic fluids and show elastic and viscous behavior when deformed. Examples of their elastic behavior are: rod climbing in a rotating shaft (Weissenberg effect), irregularities during extrusion such as extrudate swell and melt fracture, the possibility of forming a tubeless siphon (87). Fig.2.4 shows some of these phenomena.

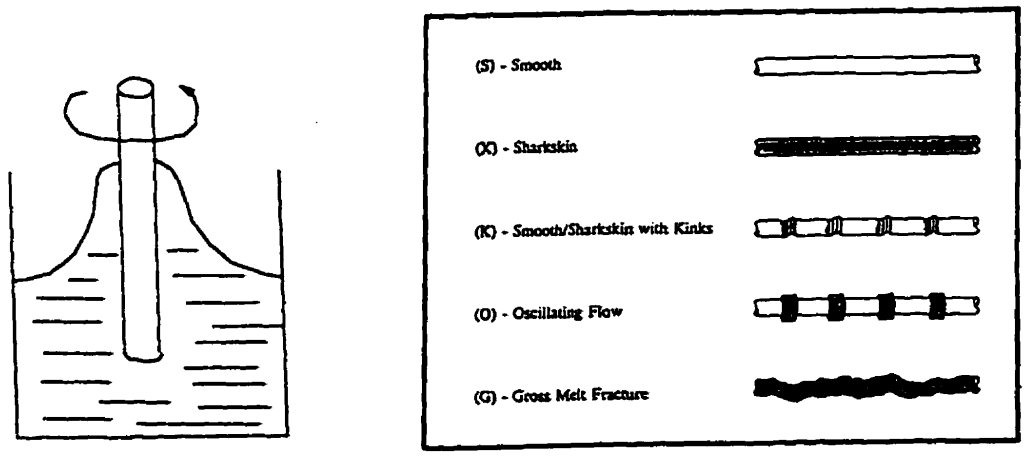

(a) rod climbing (b) extrudate distortions

Fig.2.4. Examples of elastic behavior of polymer melts

When the deformation stops in viscoelastic fluids, the stresses relax in the course of time so that after a sufficiently long time, almost no internal stress remains in them. This time depends on the applied temperature and pressure. For small deformations, a linear viscoelastic theory may be used to describe the behavior of these materials. Various combinations of elastic and viscous elements have been used to approximate the behavior of polymers. The most common one is the Maxwell model that consists of a spring and a dashpot, as shown in Fig.2.5.

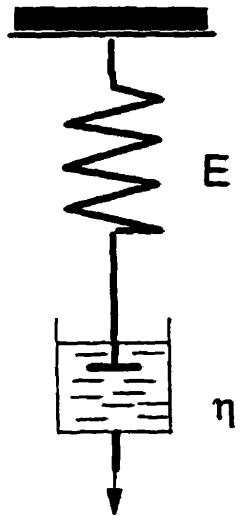

Fig.2.5. Schematic diagram of the Maxwell model

For homogeneous, linear, and at most orthotropic materials (materials possessing three mutually orthogonal planes of symmetry), the general linear constitutive equations (2.12) may be simplified and expressed in the Cartesian coordinates as two uncoupled equations, as follows (57):

$$\begin{bmatrix}\sigma_{xx}\\ \sigma_{yy}\\ \sigma_{zz}\end{bmatrix}=\begin{bmatrix}L_{11} & L_{12} & L_{13}\\ L_{12} & L_{22} & L_{23}\\ L_{13} & L_{23} & L_{33}\end{bmatrix}*\begin{bmatrix}\varepsilon_{xx}-\varepsilon_{T_x}\\ \varepsilon_{yy}-\varepsilon_{T_y}\\ \varepsilon_{zz}-\varepsilon_{T_z}\end{bmatrix} \tag{2.46a}$$

and

$$\begin{bmatrix}\tau_{xy}\\ \tau_{yz}\\ \tau_{zx}\end{bmatrix}=\begin{bmatrix}L_{44} & 0 & 0\\ 0 & L_{55} & 0\\ 0 & 0 & L_{66}\end{bmatrix}*\begin{bmatrix}\gamma_{xy}\\ \gamma_{yz}\\ \gamma_{zx}\end{bmatrix} \tag{2.46b}$$

Equations (2.46a) and (2.46b) may be written in vectorial form, as follows:

$$\sigma=L_1*(\varepsilon-\varepsilon_T) \tag{2.47a}$$

$$\tau=L_2*\gamma \tag{2.47b}$$

The fourth order tensor **C** defined in the general equation (2.12), is replaced here by the second order tensors $\mathbf{L}_1$ and $\mathbf{L}_2$. The components of $\mathbf{L}_1$ and $\mathbf{L}_2$ represent the moduli of the polymer and are in general time-dependent. The general linear operator * will be specified below. In equations (2.46) and (2.47), the shear deformation is denoted by γ. The vector

ε in equation (2.47a) is the actual or observed (65) deformation. This equation shows that the normal thermal stresses are zero if the thermal strain ε_T is equal to ε (no restriction on the thermal deformation).

Many thermoplastics behave as thermo-rheologically simple viscoelastic materials. This means that the stress in a given fluid element depends only on the deformation history of that element and not the deformation history of the neighboring elements (88). For these materials, the time-temperature superposition principle together with appropriate shift factors may be used to describe the behavior over a wide range of temperature and pressure, by a single master-curve at some reference state. For such a material, the linear operator * in equations (2.47a) and (2.47b) may be defined as:

$$\sigma = \int_0^t L_1(\xi(t)-\xi(t'))\, d(\varepsilon(t')-\varepsilon_T(t')) \qquad (2.48a)$$

$$\tau = \int_0^t L_2(\xi(t)-\xi(t'))\, d\gamma(t') \qquad (2.48b)$$

where the modified time scale $\xi(t)$ is defined by:

$$\xi(t) = \int_0^t \frac{1}{a_T}\, dt \qquad (2.49)$$

a_T is the temperature-dependent shift function, often characterized by the WLF equation, as follows:

$$Log\, a_T = -\frac{c_1(T-T_0)}{c_2+T-T_0} \qquad (2.50)$$

c_1 and c_2 are material constants, and T_0 is the reference temperature corresponding to the temperature of the master-curve. The pressure dependence of the shift factor may be incorporated, as follows (4):

$$T_0(P) = T_0(0)+sP \quad , \quad c_2(P) = c_2(0)+sP \qquad (2.51)$$

where s is a constant. It must be noted that since the temperature and pressure are space-dependent, the components of L_1 and L_2 depend on space, as well.

Bushko and Stokes (57) suggested to write the tensor L_1 in the following general form:

$$L_I = \sum_{a=1}^{M} A^a\, L_I^a \qquad (2.52)$$

The value of M and the form of the matrix A^n and the function L_1^n determine the class of material that is considered. For example, for an isotropic material, M=2, L_1^1 is the shear modulus G_s, L_1^2 is the bulk modulus K_b, and :

$$A^1 = \frac{2}{3}\begin{bmatrix} 2 & -1 & -1 \\ -1 & 2 & -1 \\ -1 & -1 & 2 \end{bmatrix} \quad , \quad A^2 = \begin{bmatrix} 1 & 1 & 1 \\ 1 & 1 & 1 \\ 1 & 1 & 1 \end{bmatrix} \qquad (2.53)$$

For a viscoelastic material, G_s and K_b are the time-dependent relaxation moduli.

In polymer processing, mass, momentum, and energy transfer occur simultaneously. In order to analyze these processes quantitatively, we must follow the changes in these properties with time and position and relate them to the final properties of the produced article. One way to determine the distribution of these properties at different times is to ignore the molecular nature of matter and view it as a continuum. The balance equations may then be used to state mathematically the physical laws of conservation of mass, momentum, and energy.

2.2.6. Balance Equations

In deriving the balance equations, the assumption is made that the points over which they hold are large enough to be characterized by properties averaged over a large number of molecules so that there is no discontinuity from point to point. It is also assumed that locally the molecules can establish equilibrium very fast (1).

The Equation of Continuity

The equation of continuity deals with the principle of the conservation of mass. If we apply it to a stationary volume element ΔV over which a fluid of density $\rho(x_i, t)$ is flowing with a velocity $v(x_i, t)$, the principle of conservation of mass may be expressed as follows:

Rate of mass accumulation in ΔV = Rate of mass transferred into ΔV - Rate of mass transferred out of ΔV

In terms of density and velocity, the application of the above balance produces the equation of continuity, as follows:

$$\frac{\partial \rho}{\partial t} = -(\nabla . \rho v) = -div(\rho v) \tag{2.54}$$

where 'div' is the operator defined by:

$$\nabla . v = \frac{\partial v_x}{\partial x} + \frac{\partial v_y}{\partial y} + \frac{\partial v_z}{\partial z} \tag{2.55}$$

in Cartesian coordinates. For an incompressible material, the density is constant and the equation of continuity becomes:

$$\nabla . v = 0 \tag{2.56}$$

The Equation of Motion

The equation of motion denotes the conservation of momentum and is inferred from Newton's second law. Momentum is a vector. Therefore, the equation of motion is a vectorial equation that has three components in the three spatial directions. Momentum can be transported by two mechanisms. The first is convection due to the bulk flow of the fluid, and the momentum flux (momentum per unit area per unit time) associated with it is given by ρvv. The second mechanism is due to intermolecular forces and the momentum flux associated with it is the total stress tensor σ_t. The ij component of τ_t represents the flux of the j-component of the momentum in the i-direction. The equation of motion, also called Cauchy's equation may be expressed as:

$$\frac{\partial}{\partial t}\rho v = -(\nabla . \rho vv) - (\nabla . \sigma_t) + \rho g \tag{2.57}$$

In deriving equation (2.57), the conservation of momentum in the control volume and the divergence theorem of Gauss are used. The total stress tensor σ_t consists of two parts: the dynamic or extra stress tensor σ associated with flow and the isotropic pressure P, as follows:

$$\sigma_t = P\delta + \sigma \tag{2.58}$$

where δ is the second order unit tensor. In the absence of flow, P is identical to the thermodynamic pressure and is related to the density and temperature. Therefore, the contribution of pressure is incorporated in the momentum equation through the isotropic part of the total stress tensor σ_t . Flow produces non-equilibrium conditions. Furthermore,

the incompressibility assumption is generally used in solving some problem processing problems such as mold filling in injection molding. As a result of these two points, the meaning of P is not completely clear in the above situations. No difficulty arises, however, since the pressure gradient is solved for. It must be noted that in the absence of flow, equation (2.57) reduces to the equilibrium equation (2.9).

The Equation of Energy

Following the same procedure as for the conservation of mass and momentum, we can derive an equation for the rate of change of kinetic and internal energy. The resulting energy equation may be expressed as follows (1):

$$\rho\frac{DU}{Dt}=-(\nabla.q)-P(\nabla.v)-(\sigma:\nabla v)+\dot{S} \qquad (2.59)$$

where U is the specific internal energy (per unit mass), q is the heat flux vector, and $\dot{S}$ is a thermal energy (per unit volume per unit time) source term. The term $P(\nabla.v)$ is the reversible rate of internal energy increase per unit volume by compression, and the term $(\sigma:\nabla v)$ is the irreversible rate of energy increase per unit volume by viscous dissipation. In non-isothermal problems, the energy equation and the equation of motion are coupled through the viscous dissipation term and the temperature dependence of viscosity and must be solved simultaneously. In equation (2.59) the operator $\frac{D}{Dt}$ is the substantial derivative and is defined by:

$$\frac{D}{Dt}=\frac{\partial}{\partial t}+v.\nabla \qquad (2.60)$$

It corresponds to the change of a variable with time as measured by a viewer that moves with the particle velocity (Lagrangian point of view). The time derivative $\frac{\partial}{\partial t}$ on the other hand, is evaluated at any fixed position in space (Eulerian point of view).

The mechanism of transfer of heat between two particles depends on the character of the matter between and surrounding them. There are three modes of heat transfer: conduction, radiation, and convection.

Between two particles of a solid body that are at different temperatures, heat is only transferred by conduction. This is a process that takes place at the molecular and atomic levels. The conduction heat flux vector may be related to the temperature gradient using the following general form of Fourier's equation:

$$q_i = -k_{ik} \frac{\partial T}{\partial x_k} \tag{2.61}$$

where the second order tensor **k** is the thermal conductivity tensor of the material. For an isotropic material, it is a scalar and simply called thermal conductivity k. In the latter case the heat flux vector is parallel to the vector of gradient of temperature $\frac{\partial T}{\partial x_k}$. The Fourrier law of conduction may be derived from the thermodynamics of irreversible processes, first formulated by Onsager (85).

Heat transfer may also take place by electromagnetic radiation. All bodies emit radiant electromagnetic energy at a rate which is found to be dependent on the fourth power of the absolute temperature of the body. When this radiant energy reaches another body, it may be either transmitted, reflected, or absorbed. The terms transmissivity, reflectivity, and absorptivity denote the corresponding fractions of the incident energy. The sum of these fractions is equal to unity. For most engineering opaque materials, the transmissivity is negligible and the limiting case of unit absorptivity and zero reflectivity is the ideal case of black body. The total radiant energy emitted in unit time from unit area of a non-black body is its emissive power, given by:

$$W = \varepsilon \sigma_B T^4 \tag{2.62}$$

where σ_B is the Stefan-Boltzmann constant, ε is the emissivity, and T is the temperature in Kelvin. The emissivity ε of a surface is the ratio of the emissive power of the surface to that of a black body. If two surfaces forming part of a structure are separated by a non-absorbing medium (vacuum or gas), radiant energy may be transferred between them.

Heat transfer in a fluid takes place by conduction, convection, and radiation. Convection occurs when the fluid is in motion. In this case, the rate of heat transfer increases since portions of the fluid at different temperatures can be brought closer. For heat convection from a fluid to a solid, the heat flux at the solid surface may be written as:

$$q = h.\Delta T \tag{2.63}$$

where h is the heat transfer coefficient and ΔT is the temperature difference between the fluid and the solid. If the motion of the fluid is due to the density variations in the fluid caused by a non-uniform temperature distribution, the process is called free or natural convection. If the motion is due to any other cause, the convection is said to be forced. In general, heat transfer by free convection is quite small.

Basically, two types of flow can occur near the surface of the solid: laminar or turbulent. In laminar flow, the fluid moves mainly in layers parallel to the surface, whereas in turbulent flow the fluid particles have random motions in all directions such that mixing of the fluid layers occurs. The heat transfer at the surface takes place by molecular conduction in the fluid layers adjacent to the surface in both cases. Turbulent motion has the effect of steepening the temperature gradient in the fluid near the surface, thereby increasing the heat transfer rate. The heat transfer coefficient h is not a constant and varies considerably with conditions in the flow.

In addition to the balance equations, the solution to many polymer processing problems requires an equation of state relating the pressure, the specific volume, and the temperature. For example in injection molding, as the cavity is being filled with polymer melt, the applied pressure increases to overcome the increasing resistance to flow. Once the mold is completely filled, a large packing pressure is applied through the gate to compensate for volumetric shrinkage due to cooling and phase change. As a result, different portions of the polymer solidify under variable pressure. The local density of the material is greatly affected and an equation of state is needed to calculate these changes. The gate area may solidify before the part is completely solid. In this case the molten core material is cut of from the applied pressure and the P-V-T relationship is used to calculate the density and pressure at each point as a function of time. The pressure and its variations are found to have a great influence on residual stresses and the crystallinity distribution in the product. Some P-V-T equations of state are briefly discussed in the next section.

2.2.7. Pressure-Volume-Temperature Relations

Two approaches can be used for the formulation of an equations of state. The first is experimental, yielding empirical equations obtained from curve fitting of the data. The second approach is to obtain the equation of state from a knowledge of the intermolecular force field. Then statistical mechanics averages are taken over molecular variables to obtain macroscopic quantities.

The Spencer and Gilmore equation is an empirical equation as given below:

$$(P+\pi)(V-\omega)=RT \tag{2.64}$$

where P is the pressure, π is an 'internal pressure', V is the specific volume, ω is the specific volume at 0 K, and R is the ideal gas constant.

Another frequently used empirical equation of state is the Tait equation expressed as follows:

$$V(T,P)=V_0(T)\left[1-C\,ln\left(1+\frac{P}{B(T)}\right)\right] \tag{2.65}$$

where V_0 is the specific volume at atmospheric pressure, C is a constant ($C \cong 0.0894$), and B is a temperature dependent material parameter. Usually, the regions below and above T_g or T_m (for amorphous or semi-crystalline polymers) are fitted with different parameters.

In the processing of crystallizable polymers, due to a non-uniform temperature distribution resulted from simultaneous effect of large cooling or heating rates and the release of heat of crystallization, the degree of crystallinity varies from one point to the other in the final product. The final mechanical properties of the part are largely influenced by the microstructure and the extent of crystallinity. The process modeling of crystallizable polymers must therefore be coupled with information about the kinetics of crystallization. This is the subject of the following section.

2.2.8. Crystallization Kinetics

The rate of crystallization of pure polymers depends on two processes: nucleation and crystal growth (1). Nucleation rates are high at low crystallization temperatures, where chains have low energy levels. High crystallization temperatures favor rapid crystal

growth rates. This is due to the fact that the melt viscosity decreases at high temperatures, thus increasing the chain mobility and the rate of growth of the crystals. It is expected, then, that the rate of crystallization has a maximum at some crystallization temperature between the melt temperature T_m and the glass transition temperature T_g.

The generalized Avrami equation has been used to describe the kinetics of crystallization of polymers under isothermal conditions, as follows:

$$X_R(t,T) = \frac{X_c(t)}{X_\infty} = 1 - exp\left(-Z(T)\, t^{n_a}\right) \tag{2.66}$$

where $X_R(t,T)$ is the relative crystallinity at time t, $X_c(t)$ is the absolute crystallinity at time t, X_∞ is the ultimate absolute crystallinity, Z is the isothermal crystallization rate constant containing the nucleation and growth rates, and n_a is the Avrami exponent. In polymer processing operations, the temperature varies with time and position, and crystallization occurs under non-isothermal conditions. Nakamura et al. (90) obtained the following equation for these conditions based on the assumption that the growth of a crystal ceases when it impinges on a neighboring one (37):

$$X_R(t) = 1 - exp\left[-\left(\int_0^t K(T)dt\right)^{n_a}\right] \tag{2.67}$$

where n_a is the Avrami exponent determined from the isothermal crystallization data, and K(T) is related to Z(T) as follows:

$$K(T) = [Z(T)]^{\frac{1}{n_a}} \tag{2.68}$$

The rate of crystallization is strongly dependent on temperature and molecular orientation in the polymer through K. The rate constant K is zero above T_m and below T_g and exhibits a maximum K_{max} in the intermediate region. The relative degree of crystallization X_R is controlled by the maximum rate constant K_{max} and the increment of time the polymer spends in the vicinity of this maximum, therefore the cooling rate dT/dt, as follows:

$$X_R \propto \frac{K_{max}\,\Delta T}{(dT/dt)_{T_{max}}} \tag{2.69}$$

The temperature dependence of the rate constant is determined from experimental measurements, as explained later in Chapter 3.

The pressure has been found to have a large effect on the rate constant of crystallization. According to He (91), a doubling of pressure from 100 to 200 MPa causes an increase in K equivalent to five orders of magnitude. Such a change is very significant, especially during the packing stage of injection molding.

2.3. CALCULATION PROCEDURE

In the previous section, the balance equations and constitutive equations were briefly reviewed. In this part, we make use of these equations to develop a methodology for calculation of thermal stresses in injection molded amorphous and semi-crystalline polymers. To calculate the evolution of thermal stresses in the solidifying material, we must solve the energy equation to obtain the temperature distribution history, and the equilibrium equations for the stresses. We also need the pressure history in the cavity from experimental measurements or from calculations, a constitutive equation relating the stresses with the strains, the kinetics of crystallization to calculate the evolution of the degree of crystallinity in the material as it solidifies in the mold, and a P-V-T equation of state for pressure calculations. The volume change in the polymer due to variations of temperature, pressure, and degree of crystallinity is the main driving force for generation of thermal stresses and may be inferred from the P-V-T data. A realistic calculation of temperature, pressure, crystallinity, and density distribution throughout the sample must be coupled with a complete simulation of flow and heat transfer in all the stages of injection molding. This has been done using the package McKam© developed at the Department of Chemical Engineering of McGill University and introduced in later sections.

2.3.1. Strain and P-V-T

The generation of thermal stresses in polymer processing is closely related to the P-V-T behavior of the polymers. In injection molding, especially during packing and cooling, the specific volume of the material changes non-uniformly as a result of non-uniform variations in temperature, pressure, and crystallinity. If the material is free to

deform, an infinitesimal change dV in its specific volume leads to a deformation corresponding to the linear strain $\frac{dV}{3V}$ and no stress is generated. Since the temperature, pressure, and crystallinity fields are usually not uniform, the change in volume varies from one point to another and is thus partly restricted by adjacent elements. This restriction gives rise to stresses if the material is 'solid' enough or if the molecular relaxation time is sufficiently large for a viscoelastic material. The effects of variations of temperature, pressure, and crystallinity on the specific volume may be expressed as:

$$\frac{dV}{V}=\frac{1}{V}\left(\frac{\partial V}{\partial T}\right)_{P,X_c}dT+\frac{1}{V}\left(\frac{\partial V}{\partial P}\right)_{T,X_c}dP+\frac{1}{V}\left(\frac{\partial V}{\partial X_c}\right)_{T,P}dX_c \qquad (2.65)$$

The coefficient of the first term on the right-hand-side, $\frac{1}{V}\left(\frac{\partial V}{\partial T}\right)_{P,X_c}$ is the volumetric thermal expansion coefficient α_v and $-\frac{1}{V}\left(\frac{\partial V}{\partial P}\right)_{T,X_c}$ is the compressibility κ of the material. The term $\frac{1}{V}\left(\frac{\partial V}{\partial X_c}\right)_{T,P}$ denotes the change of the volume due to crystallization. Fig.2.6 shows a simplified sketch of a typical P-V-T diagram for a semi-crystalline polymer.

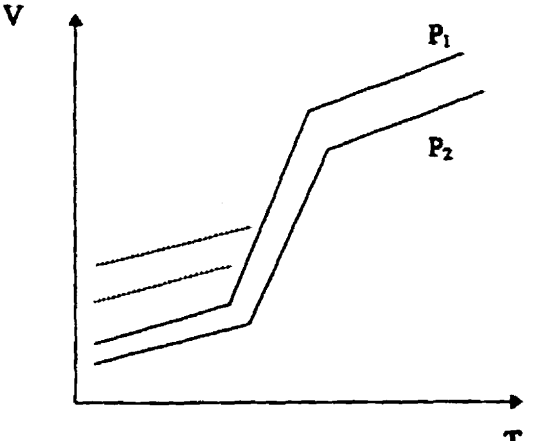

Fig.2.6. Schematic of a P-V-T diagram for a semi-crystalline polymer

For a constant pressure, the specific volume decreases as the material is cooled. During crystallization, a sharp drop in volume is observed due to the lower volume of the growing crystalline phase. An increase in the pressure leads to a lower specific volume at

a constant temperature ($P_2 > P_1$). The solid lines in Fig.2.6. represent schematically isobars in a typical P-V-T experiment. In most cases, however, especially close to the glass transition and crystallization regions, the behavior of the material is no longer uniquely determined by the equilibrium P-V-T diagram alone but also by the time and rate of heating and cooling and in general, by the entire thermal history (1). The solid lines in Fig.2.6 correspond to a specific rate of cooling. For a higher cooling rate, the specific volume of the solid increases as shown by the broken lines. Information about the non-equilibrium behavior of the material or its structural relaxation are usually not available, and the equilibrium P-V-T data are used in practice.

If the specific volume of an isotropic material changes by dV during the time dt, the infinitesimal linear strain may be expressed in terms of the specific volume V or the density $\rho = 1/V$, as follows:

$$d\varepsilon_{T_x} = d\varepsilon_{T_y} = d\varepsilon_{T_z} = d\varepsilon_T = \frac{1}{3}\frac{dV}{V} = \frac{1}{3}dLnV = -\frac{1}{3}dLn\rho \qquad (2.71)$$

ε_T is the diagonal linear thermal strain vector and, in the general case and if calculated from equation (2.71), it contains the effect of variations in temperature, pressure, or degree of crystallinity of the material on its specific volume. In an isotropic material all the components of ε_T are equal and denoted by the scalar ε_T. If we integrate equation (2.71) over a finite time increment Δt during which the specific volume changes from V_1 to V_2 and the density changes from ρ_1 to ρ_2, the total linear strain $\Delta\varepsilon_T$ is given by:

$$\Delta\varepsilon_T = \frac{1}{3}Ln\left(\frac{V_2}{V_1}\right) = \frac{1}{3}Ln\left(\frac{\rho_1}{\rho_2}\right) \qquad (2.72)$$

The change in the thermal strain may also be expressed as:

$$\Delta\varepsilon_T = \int_{T_1}^{T_2} \alpha_l(T,P,X_c)\,dT \qquad (2.73)$$

where α_l is the linear thermal expansion coefficient which is generally variable with pressure, temperature, and degree of crystallinity. In a reactive system, α_l depends on the degree of conversion or cure, as well. Equation (2.72) is equivalent to equation (2.73) and allows us to use directly the fitted P-V-T data instead of first calculating and fitting the thermal expansion coefficient from these data. As mentioned in section 2.2.7., however, most equations of state do not provide a good fit in the phase transition regions.

Furthermore, they do not include the effect of cooling rate. A suggested methodology to account for these effects in semi-crystalline polymers is described below.

The density in the solidified material may be obtained using the rule of mixtures and the calculated degree of crystallinity, as follows (1):

$$\rho = X_{cv}\rho_c + (1 - X_{cv})\rho_a \tag{2.74}$$

where X_{cv} is the volume fraction crystallinity related to the mass fraction crystallinity X_c through the following expression:

$$X_{cv} = X_c \cdot \frac{\rho}{\rho_c} \tag{2.75}$$

ρ is the density of the semi-crystalline material; ρ_c and ρ_a are the densities of the crystalline and the amorphous phases, respectively . ρ_c is found in the literature and ρ_a may be inferred by extrapolating the melt density (from PVT data) to the desired temperature. Combining equations (2.74) and (2.75), the following expression is obtained to relate the density to the mass fraction crystallinity X_c :

$$\rho = \frac{\rho_a \rho_c}{\rho_c + X_c(\rho_a - \rho_c)} \tag{2.76}$$

Note that the degree of crystallinity calculated by McKam© is a mass fraction crystallinity.

The disadvantage of this method is that any error involved in the crystallinity calculations is incorporated in the density of the solid obtained by this method.

2.3.2. Pressure Strain

Solidification of the polymer melt in injection molding may start during filling, but mainly occurs in the packing and cooling stages. During these stages, two phases are present in the cavity as shown in Fig.2.7.

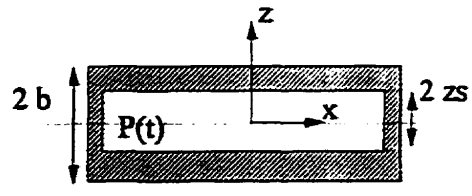

Fig.2.7. Solidification under pressure in the mold

A very high pressure is applied to the melt through the nozzle to add more material into the cavity and compensate for the shrinkage due to cooling and solidification. At the solid-melt interface, the melt applies a normal force equal to the instantaneous value of pressure to the solidifying material. The effect of this force is to counteract the volume decrease in this element by expanding it. This strongly affects thermal stresses and must be taken into account. The pressure effect is incorporated in the calculations by adding to ε_T in equation (2.46a) and (2.47a), a pressure strain ε_P induced by the packing pressure. Following a procedure similar to the calculation of the thermal strain in equations (2.71) and (2.72), the pressure strain in a solidifying element may be expressed as:

$$\Delta\varepsilon_P = -\frac{1}{3}Ln\left(\frac{V(P_s,T_s)}{V(0,T_s)}\right) = -\frac{1}{3}Ln\left(\frac{\rho(0,T_s)}{\rho(P_s,T_s)}\right) \tag{2.77}$$

where T_s is the solidification temperature and P_s is the melt pressure at the time of solidification (solidification pressure). It may be verified from equation (2.77) that $\Delta\varepsilon_P$ is positive since the density increases with increasing pressure, while the thermal strain is negative in cooling. The melt pressure varies with time during solidification. Therefore, different elements of the sample solidify under different pressure strains. As a consequence, we expect the pressure history to have an influence on the final thermal stress profile. In fact, it is observed experimentally in the present work that this influence is quite significant.

2.3.3. Strain-Displacement and Compatibility

As mentioned in section 3.2.1., for small deformations, the strain is given by:

$$\varepsilon_{ij} = \frac{1}{2}\left(\frac{\partial u_i}{\partial x_j} + \frac{\partial u_j}{\partial x_i}\right) \tag{2.2}$$

Equation (2.2) consists of six equations for the six independent components of the strain in terms of the three components of displacement. These equations are not necessarily satisfied for large deformations.

By eliminating the displacements in strain-displacement relations, we obtain the compatibility equations for the strains (92). Only if the strain components satisfy the compatibility equations, there exists displacement components that are solutions of (2.2). If the problem is formulated in terms of the displacements, i.e., if the variables to be calculated are the displacement components, the strains are derived from the calculated displacements and automatically satisfy the compatibility equations.

2.3.4. Equilibrium Equations

If the body is in equilibrium, the stresses must satisfy the equilibrium equations in three directions, given in vectorial form by equations (2.9) as follows:

$$\frac{\partial \sigma_{ij}}{\partial x_j} + F_{bi} = 0 \tag{2.9}$$

The three equilibrium equations in terms of the components of the stress tensor are obtained by expanding equation (2.9), as follows:

$$\begin{aligned}
&\frac{\partial \sigma_{xx}}{\partial x} + \frac{\partial \tau_{xy}}{\partial y} + \frac{\partial \tau_{xz}}{\partial z} + F_{bx} = 0 \\
&\frac{\partial \tau_{yx}}{\partial x} + \frac{\partial \sigma_{yy}}{\partial y} + \frac{\partial \tau_{yz}}{\partial z} + F_{by} = 0 \\
&\frac{\partial \tau_{zx}}{\partial x} + \frac{\partial \tau_{zy}}{\partial y} + \frac{\partial \sigma_{zz}}{\partial z} + F_{bz} = 0
\end{aligned} \tag{2.78}$$

where the normal and shear components of the stress are denoted by σ_{ij} and τ_{ij}, respectively; $\mathbf{F_b}$ is the body force per unit volume. The stresses in equation (2.78) are replaced in terms of the strains using an appropriate constitutive equation, as explained in the next section. Furthermore, the strain-displacement relations (2.2) are used to eliminate the strains leading to three equations for the three unknown components of displacement. These equations may be solved simultaneously with appropriate boundary conditions. The boundary conditions may be restrictions on the components of displacement or their gradients (stresses or strains) at the boundaries. Once the above equations are solved, the strains and the stresses may be calculated from the displacements.

2.3.5. Thermoelastic 3-D and 2-D Stress-Strain Relationships

We first develop a general three-dimensional stress analysis formulation. For an isotropic and elastic body, the components of the matrix of moduli L_1 and L_2 are constants and the linear constitutive equations given by equations (2.46) and (2.47) reduce to equation (2.22) in section 2.2.3, as follows:

$$\begin{pmatrix}\sigma_{xx}\\ \sigma_{yy}\\ \sigma_{zz}\end{pmatrix}=\frac{E}{(1+\upsilon)(1-2\upsilon)}\begin{pmatrix}1-\upsilon & \upsilon & \upsilon\\ \upsilon & 1-\upsilon & \upsilon\\ \upsilon & \upsilon & 1-\upsilon\end{pmatrix}\begin{pmatrix}\varepsilon_{xx}-\varepsilon_T\\ \varepsilon_{yy}-\varepsilon_T\\ \varepsilon_{zz}-\varepsilon_T\end{pmatrix} \tag{2.22a}$$

and

$$\begin{pmatrix}\tau_{xy}\\ \tau_{zx}\\ \tau_{yz}\end{pmatrix}=\frac{E}{(1+\upsilon)}\begin{pmatrix}1 & 0 & 0\\ 0 & 1 & 0\\ 0 & 0 & 1\end{pmatrix}\begin{pmatrix}\gamma_{xy}\\ \gamma_{zx}\\ \gamma_{yz}\end{pmatrix} \tag{2.22b}$$

Equations (2.22a) and (2.22b) may be written in a more concise form, as follows:

$$\sigma=D.(\varepsilon-\varepsilon_T) \tag{2.79}$$

where σ, ε, and ε_T are the vectors containing the stress, strain, and thermal strain components, respectively. The matrix **D** relates the stress and the strain as given by equations (2.22a) and (2.22b) in an elastic body.

If u, v, and w are the displacements in x, y, and z directions, respectively, the strains may be related to the displacements using equation (2.2), in the following way:

$$\begin{bmatrix}\varepsilon_{xx}\\ \varepsilon_{yy}\\ \varepsilon_{zz}\\ \gamma_{xy}\\ \gamma_{yz}\\ \gamma_{zx}\end{bmatrix}=\begin{bmatrix}\frac{\partial}{\partial x} & 0 & 0\\ 0 & \frac{\partial}{\partial y} & 0\\ 0 & 0 & \frac{\partial}{\partial z}\\ \frac{\partial}{\partial y} & \frac{\partial}{\partial x} & 0\\ 0 & \frac{\partial}{\partial z} & \frac{\partial}{\partial y}\\ \frac{\partial}{\partial z} & 0 & \frac{\partial}{\partial x}\end{bmatrix}.\begin{bmatrix}u\\ v\\ w\end{bmatrix} \tag{2.80}$$

If the displacement vector is denoted by e and the matrix relating the strains and displacements by **A**, equation (2.80) may be written as:

$$\varepsilon = A.e \tag{2.81}$$

It may be verified that the equilibrium equations (2.78) may be expressed in vectorial form using the transpose of the matrix **A** in equation (2.81), as follows:

$$A^T \cdot \sigma + F = 0 \tag{2.82}$$

Replacing the stresses from equation (2.79), equation (2.82) becomes:

$$A^T \cdot \left[D \cdot \left(\varepsilon - \varepsilon_T \right) \right] + F = 0 \tag{2.83}$$

Finally, eliminating the strain ε using equation (2.81), the following vectorial equation is obtained for the displacements:

$$\left(A^T \cdot D \cdot A \right) \cdot e = -F + A^T \cdot D \cdot \varepsilon_T \tag{2.84}$$

The second term on the right-hand-side of the equation (2.84) is analogous to a thermal load.

The two-dimensional plane strain and plane stress cases may be derived similarly: In the plane stress case, we have: $\sigma_{xy} = \sigma_{yy} = \sigma_{yz} = 0$. The constitutive equation (2.22) reduces to equation (2.30) derived in section 2.2.3., as follows:

$$\begin{pmatrix} \sigma_{xx} \\ \sigma_{zz} \\ \tau_{xz} \end{pmatrix} = \frac{E}{(1+\upsilon)(1-\upsilon)} \begin{pmatrix} 1 & \upsilon & 0 \\ \upsilon & 1 & 0 \\ 0 & 0 & 1-\upsilon \end{pmatrix} \begin{pmatrix} \varepsilon_{xx} - \varepsilon_T \\ \varepsilon_{zz} - \varepsilon_T \\ \gamma_{xz} \end{pmatrix} \tag{2.30}$$

The strain-displacement relationship in the two-dimensional case becomes:

$$\begin{bmatrix} \varepsilon_{xx} \\ \varepsilon_{zz} \\ \gamma_{xz} \end{bmatrix} = \begin{bmatrix} \dfrac{\partial}{\partial x} & 0 \\ 0 & \dfrac{\partial}{\partial z} \\ \dfrac{\partial}{\partial z} & \dfrac{\partial}{\partial x} \end{bmatrix} \cdot \begin{bmatrix} u \\ w \end{bmatrix} \tag{2.85}$$

Following the same procedure as for the 3-D analysis, we obtain two equations for the two unknown components of the displacement u and w. These equations may be expressed in vectorial form as shown in equation (2.84), where **A** and **D** may be inferred from equations (2.30) and (2.85) for the plane stress case.

In the plane strain case, we have: $\varepsilon_{xy}=\varepsilon_{yy}=\varepsilon_{yz}=0$. The formulation is the same as the plane stress, only the constitutive equations are given by equation (2.26) derived in section 2.2.3., as follows:

$$\begin{pmatrix}\sigma_{xx}\\ \sigma_{zz}\\ \tau_{xz}\end{pmatrix}=\frac{E}{(1+\upsilon)(1-2\upsilon)}\begin{pmatrix}1-\upsilon & \upsilon & 0\\ \upsilon & 1-\upsilon & 0\\ 0 & 0 & 1-2\upsilon\end{pmatrix}\begin{pmatrix}\varepsilon_{xx}\\ \varepsilon_{zz}\\ \gamma_{xz}\end{pmatrix}-\frac{E}{(1-2\upsilon)}\begin{pmatrix}\varepsilon_T\\ \varepsilon_T\\ 0\end{pmatrix} \quad (2.26)$$

In this case, equation (2.84) becomes:

$$\left(A^T\cdot D\cdot A\right)\cdot e=-F+3K_b\left(A^T\cdot\varepsilon_T\right) \quad (2.86)$$

where K_b is the bulk modulus given by:

$$K_b=\frac{E}{3(1-2\upsilon)} \quad (2.87)$$

The effect of packing pressure is incorporated as explained earlier in section 2.3.2. The isotropic pressure strain is added to the thermal strain at the time of solidification. The pressure strain may be obtained using directly the P-V-T data and equation (2.77). For an elastic material, equation (2.17) may be used to derive the linear strain due to pressure in the melt, as follows: Since this strain is normal and isotropic, we have: $\varepsilon_{xx}=\varepsilon_{yy}=\varepsilon_{zz}$ and the normal stresses in the melt are equal to -P where P is the instantaneous pressure. The minus sign is consistent with the negative sign conversion for a compressive stress. The thermal contraction in the solidifying material may be neglected since above the solidification temperature the material relaxes rapidly and the thermal contraction does not lead to significant stresses. If we substitute in equation (2.17) we obtain for the pressure strain, induced in the solidifying element:

$$\varepsilon_P=\frac{P}{3K_b}=\frac{(1-2\upsilon)}{E}P \quad (2.88)$$

where (1-2υ)/E is the compressibility of the elastic solid material. The strain induced in the solidifying element, by increasing the pressure from zero to P_s (solidification pressure) is given by:

$$\Delta\varepsilon_P=\frac{(P_s-0)}{3K_b}=\frac{(1-2\upsilon)}{E}P_s \quad (2.89)$$

The pressure strain is added to the thermal strain at the instant of solidification. Bushko and Stokes considered $\Delta\varepsilon_P$ as a reference strain in the melt.

The boundary conditions used for the stress analysis are zero force (free displacement) at the mold walls. At the moving boundary made of the solid-melt interface, the stress normal to the boundary (σ_{zz}) is equal to the pressure P(t).

2.3.6. Two-dimensional Free Mold Shrinkage Model (2-D FMS)

Injection molding of a polymer sample in a thin rectangular mold is considered as shown in Fig. 2.8.

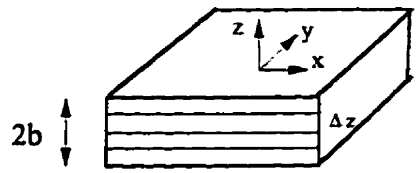

Fig.2.8. Geometry for the 2-D FMS model

In this simplified model, only the packing and cooling stages of injection molding are considered. The velocities are neglected and the energy equation is solved with the assumption that the main temperature gradient is in the thickness direction z. The temperature field inside the cavity and the transient position of the solid-melt interface are obtained from the solution of this equation with appropriate boundary conditions. For an amorphous polymer, the glass transition temperature T_g is used to find the interface. In a semi-crystalline polymer, an average solidification temperature T_s or the degree of crystallinity may be used for this purpose. If the thermal properties are assumed constant, the energy equation given by equation (2.59) simplifies to:

$$\rho C_P \frac{\partial T}{\partial t} = k \frac{\partial^2 T}{\partial z^2} + \rho \Delta H_f \frac{dX_C}{dt} \qquad (2.90)$$

where ρ, C_P , and k are the density, specific heat, and heat conductivity of the material, respectively. ΔH_f is the heat of crystallization and $\frac{dX_C}{dt}$ is the rate of crystallization. Due to symmetry, half the thickness is considered and the thermal boundary conditions are as follows:

$$T(z)=T_i \quad at \quad t=0$$
$$\frac{\partial T}{\partial z}=0 \quad at \quad z=0 \qquad (2.91)$$
$$-k\frac{\partial T}{\partial z}=h(T-T_c) \quad or \quad \frac{\partial T}{\partial z}=-\frac{Biot}{b}(T-T_c) \quad at \quad z=b$$

where Biot =hb/k is the dimensionless Biot number, h is the heat transfer coefficient between the sample and the coolant, b is half the thickness of the mold, and T_c is the coolant's temperature. In an alternative approach, the heat of crystallization is included in the variations of the specific heat C_p. In this case, the second term on the right-hand-side of equation (2.90) is omitted (35).

For a semi-crystalline polymer, equation (2.90) together with boundary conditions (2.91) are coupled with an equation describing the kinetics of crystallization, as explained later in section 2.3.9 (McKam©). In the absence of crystallization and for constant properties, the last term in the right-hand-side of equation (2.90) (the source term) is omitted. An analytical solution exists for equation (2.90) in this case, given by:

$$\frac{T-T_c}{T_i-T_c}=2\sum_{m=1}^{\infty}exp\left(-\frac{\beta_m{}^2 at}{b^2}\right)\cdot\frac{\beta_m{}^2+Biot^2}{\left(\beta_m{}^2+Biot+Biot^2\right)}cos\left(\beta_m z/b\right) \qquad (2.92)$$

where $a=\frac{k}{\rho C_p}$ is the thermal diffusivity of the material and the eigenvalues β_m are the positive roots of the equation $\beta tan\beta = Biot$ (93). Once the temperature field and the position of the solid-melt interface are obtained, the thermal strain is calculated using equation (2.73) with a constant α_l and the pressure strain is obtained from equation (2.89). It must be noted that in the stress calculations by this model, the experimentally measured pressure was used. The solidification pressure P_s varies with space and is obtained for each element from the time of solidification of this element and the pressure at this time. The pressure strain is added to the thermal strain upon solidification.

Assuming a plane strain case, equation (2.86) is solved at each time step for the displacement e during this time, assuming no body forces (F=0) and using the Galerkin finite element technique. The changes in strains and stresses are calculated using equations (2.85) and (2.26). The procedure continues until all the elements of the sample have reached the final ambient temperature. The total displacements, strains, and stresses are

then obtained by adding up their incremental changes (integrating) over time. It must be noted that for the geometry shown in Fig.2.12, the non-zero components of stress and strain are the xx, zz, and xz components and the non-zero displacements are u and w (the x and z components). The numerical technique is discussed in more detail below.

2.3.7. McKam©

In this model, the full injection molding cycle is considered and the velocity, temperature, pressure, and crystallinity fields are calculated by the McKam© package.

The injection molding process involves injecting the molten polymer into the cavity (filling), then maintaining a high pressure to add more material into the mold (packing). Packing is to compensate for the volume shrinkage due to cooling. Finally the material is cooled until it solidifies and takes the shape of the cavity (cooling). Mathematical modeling of injection molding presents several challenges. It involves transient non-isothermal flow of non-Newtonian and viscoelastic polymer melts with simultaneous solidification. Furthermore, the free surface is moving continuously through channels and molds of complex geometries. In order to solve the relevant equations, simplifying assumptions must be made. Various models differ in these assumptions and in the method of solution.

McKam© employs the Finite-Volume Method (FVM) for discretizing the conservation equations (94). FVM is used together with the Boundary Fitted Curvilinear Coordinate transformation (BFCC) with the dependent variables in the momentum balance being the covariant velocity components. McKam© is based on the so-called 21/2-D analysis that employs a 2-D flow analysis (x-y plane) and a 3-D (including the thickness direction z) heat transfer analysis. In the advancing front region during filling, the rapidly moving melt at the midplane in the thickness direction, spills out to the mold wall to form the surface of the molded part at that location (1). Thus, in the front region the central core decelerates in the flow direction as it acquires a velocity component in the thickness direction. This phenomenon is called the fountain effect and its incorporation is critical for the description of the temperature field, both near the flow front and near the mold wall, and for determination of the surface quality and morphology. In particular, the evolution

of crystallinity is strongly influenced by the fountain flow (37). The BFCC technique is used to transform the physical domain and implement finite difference to solve the resulting partial differential equations. The properties of the material are allowed to change with time and space.

The viscoelastic nature of the melt may be taken into account in this package with the use of the White-Metzner equation. In the present work, however, to simplify the analysis, non-isothermal Power-law or WLF-Carreau constitutive equations are employed. The Nakamura model (90) is used to couple the kinetics of crystallization with the energy equation. The empirical Tait equation of state (95) is implemented to describe the P-V-T behavior of PS and HDPE with appropriate constants.

A schematic representation of the geometry of the rectangular mold cavity considered throughout this thesis is shown in Fig.2.9. The continuity and the momentum equations (2.54 and 2.57) are solved in McKam© and coupled with the energy equation (2.59) through the temperature dependence of the viscosity. The Nakamura equation (2.67) is solved in its differential form:

$$\frac{DX_c}{Dt} = X_\infty n_a K(T)\left(1-X_R\right)\left[ln\left(\frac{1}{1-X_R}\right)\right]^{\left(\frac{n_a-1}{n_a}\right)} \qquad (2.93)$$

simultaneously with the balance equations, where

$$\frac{DX_c}{Dt} = \frac{\partial X_c}{\partial t} + u\frac{\partial X_c}{\partial x} + v\frac{\partial X_c}{\partial y} + w\frac{\partial X_c}{\partial z} \qquad (2.94)$$

and X_R is the relative crystallinity given by: X_c / X_∞. The initial condition for the degree of crystallization in equation (2.93) is zero crystallinity at time zero. However, in order to avoid a zero initial rate of crystallization, a very small value of say 10^{-15} must be arbitrarily assumed for the initial crystallinity (96).

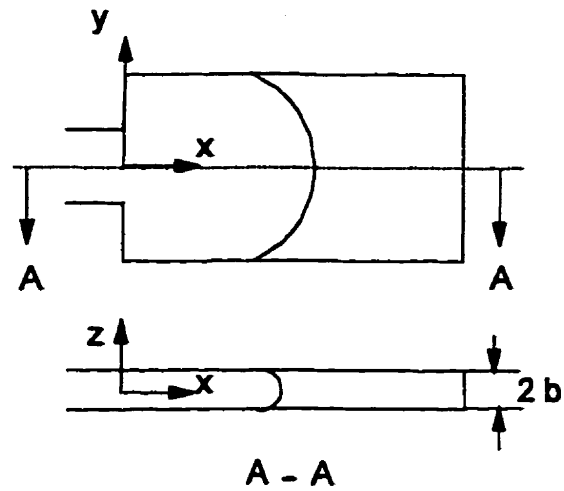

Fig.2.9. The mold cavity geometry

In this model, the stresses are obtained as in the 2-D FMS model (section 2.3.8). The thermal stresses are assumed to be generated during the packing and cooling stages. During packing, the pressure is held at a high value until the end of holding time when the nozzle pressure goes to zero or the material in the gate solidifies and the melt pressure in the cavity starts decaying as the material cools according to its P-V-T behavior. If the nozzle pressure goes to zero before the gate freezes, the pressure in the cavity may cause some back-flow. The material may be added or removed from the cavity during packing and before the sealing of the gate.

The temperature dependence of the thermal properties, the P-V-T behavior and the crystallization kinetics have an important impact on the calculated temperature and pressure fields and thus on thermal stresses. These factors are taken into account in this model. The crystallization kinetics is coupled with the energy balance equation through the heat of crystallization in the source term.

The Young modulus E of a semi-crystalline polymer is calculated using a simple rule of mixture from the crystalline modulus E_c and the amorphous modulus E_a (97), as follows:

$$E = X_{cv} E_c + (1 - X_{cv}) E_a \qquad (2.95)$$

2.3.8. Numerical Techniques for Stress Analysis

At each time t, the set of two coupled second order partial differential equations (PDE) given by equation (2.86) with **F=0** is solved for the displacements u and w. These two equations may be expanded to give:

$$(1-\upsilon)\frac{\partial^2 u}{\partial x^2}+\upsilon\frac{\partial^2 w}{\partial x\partial z}+(1-2\upsilon)\left(\frac{\partial^2 u}{\partial z^2}+\frac{\partial^2 w}{\partial x\partial z}\right)=\alpha_t(1+\upsilon)\frac{\partial \Delta T}{\partial x}+\frac{(1+\upsilon)(1-2\upsilon)}{E}\frac{\partial P_s}{\partial x}$$

$$\upsilon\frac{\partial^2 u}{\partial x\partial z}+(1-\upsilon)\frac{\partial^2 w}{\partial z^2}+(1-2\upsilon)\left(\frac{\partial^2 u}{\partial x\partial z}+\frac{\partial^2 w}{\partial x^2}\right)=\alpha_t(1+\upsilon)\frac{\partial \Delta T}{\partial z}+\frac{(1+\upsilon)(1-2\upsilon)}{E}\frac{\partial P_s}{\partial z} \qquad (2.96)$$

where the linear thermal expansion coefficient α_t has been assumed constant and the last term on the right-hand-side is added to each element at the instant of solidification. Galerkin finite element method is used to solve these equations numerically.

In the finite element method, the domain is divided into subdomains commonly referred to as finite elements. The unknown functions are represented within each element by an interpolating polynomial which is continuous, along with its derivatives to a specified order within the element. Generally, the interpolating function is of lower order continuity between elements than within an element (98). One approach to derive the finite element formulation is the Method of Weighted Residuals (MWR). The Galerkin method is a special case of MWR.

In the method of weighted residuals, the unknown function u is replaced by a finite series approximation $\hat{u}$, as follows:

$$u \approx \hat{u} = \sum_{j=1}^{N} U_j \varphi_j \qquad (2.97)$$

The set of functions φ_j are chosen to be polynomials that satisfy certain boundary conditions imposed on the problem and can be defined over both the time and space domain. These functions are called shape functions, basis functions, or interpolation functions. U_j's are undetermined coefficients. Substitution of $\hat{u}$ into the PDE results in a residual R. The objective is to select the coefficients U_j's in such a way as to minimize this residual. To generate N equations for the N unknown coefficients, a weighting function w_i

is introduced. Setting the integral of each weighted residual to zero yields N independent equations, as follows:

$$\int_t \int_V R.w_i dV\, dt = 0 \qquad i = 1,2,.....,N \tag{2.98}$$

The Galerkin method results when the weighting function is chosen to be the basis function. Thus we have:

$$\int_t \int_V R.\varphi_i dV\, dt = 0 \qquad i = 1,2,.....,N \tag{2.99}$$

The theory and details of the finite element method are elaborated by many authors (98, 99, 100).

In the present work, bilinear basis functions and rectangular elements were used. Numerical integration was perform by Gaussian quadrature. The initial code was taken from the following reference (101) and was modified to include solidification, the thermal and the pressure "loads", and other aspects specific to this problem.

The problem of thermal stresses may be further simplified in some simple one-dimensional and limiting cases. Some of these cases are now considered to provide more insight into the problem.

2.3.9. Free Quenching (FQ)

When a body is cooled under no applied load or restriction to its deformation, the process is called free quenching (FQ). The linear thermal strain $\Delta\varepsilon_T$ for a temperature drop of ΔT and a constant linear thermal expansion coefficient α_l is given by:

$$\varepsilon_T = \alpha_l \Delta T \tag{2.100}$$

As mentioned before, thermal stresses are caused by simultaneous effect of non-uniform temperature distribution, continuity of the body, and significant changes in properties. Let us consider the one-dimensional free quenching of an amorphous polymer melt where the temperature gradient is large in the thickness direction z, compared to x and y directions (see Fig.2.8). As a result of symmetry, only half the thickness is considered. Solidification starts from the surface and proceeds layer by layer towards the core until all the sample has solidified. Equation (2.90) reduces in this case to:

$$\rho C_p \frac{\partial T}{\partial t} = k \frac{\partial^2 T}{\partial z^2} \tag{2.102}$$

The analytical solution of equation (2.102) and the boundary condition in equation (2.91) is given by equation (2.92). The evolution of the position of the solid-melt interface $z=z_s$ is obtained by replacing T in the solution (2.92) by the solidification temperature T_s of the polymer. The material is assumed to be elastic and the elastic modulus of the melt is negligible compared to the modulus of the solid polymer. Due to symmetry, the resulting thermal strains and stresses in the x and y directions are identical. The normal strain $\varepsilon_{xx} = \varepsilon_{yy} = \varepsilon$ may be obtained from equation (2.17), (2.19), and (2.20), as follows:

$$\varepsilon = \frac{1}{E}\left\{(1+\upsilon)\sigma_{xx} - \upsilon\left(\sigma_{xx}+\sigma_{yy}+\sigma_{zz}\right)\right\} + \varepsilon_T \tag{2.102}$$

ε is the actual or observable shrinkage in the part. The generated thermal stresses are $\sigma_{xx}=\sigma_{yy}=\sigma$. In free quenching, $\sigma_{zz}=0$. Using equation (2.102) and the above considerations, the increment of thermal stress generated in the layer z during the time Δt is given by:

$$\Delta\sigma(z,t) = \left(\frac{E}{1-\upsilon}\right)\left[\Delta\varepsilon(t) - \Delta\varepsilon_T(z,t)\right] \tag{2.103}$$

If the sample is assumed to maintain its shape without bending, ε is independent of z (51). The final residual stress distribution is obtained by adding up $\Delta\sigma$'s up to the time when the temperature in the sample has reached the final temperature everywhere. Equation (2.103) may be integrated along the thickness of the solidified part of the sample to obtain:

$$\int_{z_s}^{b} \Delta\sigma(z,t)dz = \left(\frac{E}{1-\upsilon}\right)\left[\Delta\varepsilon(t)(b-z_s) - \int_{z_s}^{b} \Delta\varepsilon_T(z,t)dz\right] \tag{2.104}$$

where z_s is the position of the solid-melt interface at time t. In the absence of external loads, the equilibrium of forces requires that:

$$\int_{z_s}^{b} \Delta\sigma(z,t)dz = 0 \tag{2.105}$$

Replacing equation (2.105) into (2.104) and rearranging, the actual shrinkage at time t is obtained, as follows:

$$\Delta\varepsilon(t) = \frac{\int_{z_s}^{b} \Delta\varepsilon_T(z,t)dz}{(b - z_s)} \qquad (2.106)$$

where Δ refers to the change with respect to the previous time step. Equation (2.106) shows that in this special case, the actual shrinkage during a time step Δt is equal to the average thermal strain in the solidified layers. Fig.2.10 shows the evolution of the thermal stress distribution during free quenching of a polystryrene sample with an initial temperature of T_i= 235°C and a constant surface temperature T_M=20°C, as calculated from equations (2.103) and (2.106). An infinite Biot number was used (equivalent to a constant surface temperature).

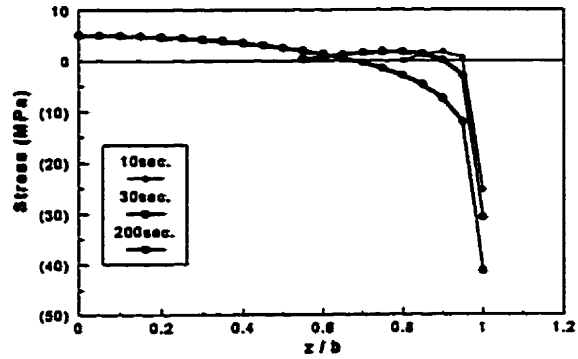

Fig.2.10 Evolution of free quenching thermal stresses

The stress distribution obtained from this simple model is, as reported in many experimental studies (3), compressive on the surface and tensile in the core of the sample. The simplified cooling model of Struik (16) may be used to understand these observations: When the layers close to the surface solidify, the layers in the core are still molten. The molten layers do not exhibit a resistance against the contraction of the surface layers because of the negligible value of the melt modulus. When the core solidifies and contracts, the solidified surface layers impose a constraint on its shrinkage. Consequently, at the end of cooling, the core is under tensile stress and the surface under compressive stress. It must be noted that in the absence of such a large variation in the modulus, the final sample would be stress-free.

Using some approximations, Struik obtained an analytical expression for the final stress distribution in terms of the reduced stress $S(z)=\frac{\sigma(z)}{A(T_g-T_M)}$ where $A=\frac{\alpha_l E}{1-\upsilon}$ and a Biot boundary condition was used on the surface (z=b). T_M and T_g are the wall and the glass temperatures, respectively. This expression and the details of its derivation are given on pages 247-249 of reference (16). Subsequently, Struik obtained simple expressions for the following cases:

The mid-plane stress (z=0):

$$S(0)=\frac{\sigma(0,t=\infty)}{A(T_g-T_M)}=1-\frac{\sin\beta_1}{\beta_1} \tag{2.107}$$

Very low Biot number:

$$S(z)=\frac{\sigma(z,t=\infty)}{A(T_g-T_M)}=\frac{1}{6}Biot\left[1-3\left(\frac{z}{b}\right)^2\right] \qquad Biot<<1 \tag{2.108}$$

The surface stress and very large Biot (z=b):

$$S(b)=\frac{\sigma(b,t=\infty)}{A(T_g-T_M)}=0.06-\frac{1}{2}\ln(Biot) \qquad Biot>>1 \tag{2.109}$$

In equation (2.107), β_1 is the first root of the equation $\beta\tan\beta=Biot$.

2.3.10. Constrained Mold Shrinkage (CMS)

Let us assume that the quenched sample considered above is inside a mold and its shrinkage is completely constrained due to the geometry of the mold or due to friction between the surfaces of the sample and the mold wall. In this case that we will call Constrained Mold Shrinkage (CMS), the shrinkage of the surface layer is prevented in the first stage of cooling and thus the surface is under tension. In the second cooling stage, the core cools from the same initial to final temperature as the surface layer did during the first stage. The total thermal contractions on the surface and in the core are identical and completely restricted. The resulting stress is thus uniform. When the product is ejected (as in injection molding), the constraints are removed, the actual shrinkage is uniform and, as a consequence, the final product is stress-free (5, 52, 67). The tensile stress before

ejection is usually quite large, therefore the viscoelastic stress relaxation effects are expected to be more important. As a result, small stresses will remain in the part (5).

In the case of injection molding, the polymer melt is solidified under high applied pressure. If viscoelasticity is neglected and it is assumed that, as in case of constrained quenching, the shrinkage of the sample is completely prevented in the mold, the resulting residual stress will be entirely due to pressure variations. Following Brucato et al. (52), let δ_f be the final shrinkage when the sample has reached the ambient temperature T_s outside the mold. δ_f is the sum of the strain given by equation (2.102) and the pressure strain given by equation (2.89). Since the thickness is much smaller than the other two dimensions, the stress in the thickness direction z may be neglected and we have: $\sigma_{xx}=\sigma_{yy}=\sigma$ and $\sigma_{zz}=0$. Replacing in equation (2.102), we obtain:

$$\delta_f = \frac{1-\upsilon}{E}\sigma(z)+\varepsilon_T+\frac{1-2\upsilon}{E}P_s(z) \tag{2.110}$$

where the total thermal strain $\varepsilon_T = \int_{T_s}^{T_e}\alpha_l(T)\,dT$ is independent of z. Integrating equation (2.110) over half-thickness of the sample and making use of the equilibrium of stresses, the following expression is obtained for the total shrinkage δ_f:

$$\delta_f = \varepsilon_T+\frac{1-2\upsilon}{E}\int_0 P_s(Z)\,dZ \tag{2.111}$$

where Z=z/b is the dimensionless distance from the midplane of the sample. Replacing in equation (2.110), we obtain:

$$\sigma(Z)=\left(\frac{1-2\upsilon}{1-\upsilon}\right)\left[\int_0 P_s(Z)\,dZ-P_s(Z)\right] \tag{2.112}$$

Therefore, the CMS stresses may be calculated from equation (2.112). The above equation shows that the stresses do not depend on the modulus in this case. As pointed out by Jansen (67), the reason is that we have assumed the modulus E to be temperature-independent. As a result, the modulus of a layer that just solidified is equal to the average modulus. It may be seen from equation (2.112) that, in this case, if there is no pressure or if the solidification pressure is the same for all layers, the sample will be stress-free.

2.3.11. One-Dimensional Free Mold Shrinkage (1-D FMS)

If the sample is allowed to shrink inside the mold, the resulting residual stresses are due to simultaneous thermal and pressure effects. Titomanlio et al. (51) developed a simple model to calculate the stress in this case. The procedure is similar to the case of free quenching. However, the pressure enters in the stress-strain equations and in the integration along the thickness since the pressure force must be in equilibrium with the resultant internal stresses (67). Equation (2.102) may be used to calculate the stress $\Delta\sigma(z,t)$ generated in each layer between the solidification time and the instant t. In this case, σ_{zz}= -P. Since the stress at the time of solidification is zero, $\Delta\sigma(z,t)= \sigma(z,t)$. Each layer solidifies at a different time, therefore, the shrinkage during this time period is different for each layer and is given by $\delta(t) - \delta_s(z)$, where $\delta(t)$ and $\delta_s(z)$ are the shrinkages of the sample at time t and at the instant of solidification of layer z, respectively. The thermal strain $\varepsilon_T(z,t)$ for a constant thermal expansion coefficient is $\alpha_l[T(z,t)-T_s]$. The effect of pressure is implemented as the solidification pressure strain $\varepsilon_p(z)$ (see equation (2.89)). The generated stress in a layer z is proportional to $\delta(t)- \delta_s(z)-(\varepsilon_T(z,t)-\varepsilon_p(z))$. Replacing in and rearranging equation (2.102), the stress in the layer z and at time t is given by:

$$\sigma(z,t)=\left(\frac{E}{1-\upsilon}\right)\left[\delta(t)-\delta_s(z)-\varepsilon_T(z,t)+\varepsilon_P(z)-\frac{\upsilon}{E}P(t)\right] \qquad (2.113)$$

Equation (2.116) may be integrated along half-thickness of the solid sample to give:

$$\delta(t)(b-z_s)+\int_{z_s}^{b}\eta(z)dz=\frac{P(t)}{E}(z_s-2\upsilon z_s+\upsilon b)+\int\varepsilon_T(z,t)dz \qquad (2.114)$$

where $\eta(z)=\varepsilon_p(z)-\delta_s(z)$ and the following force balance between the melt pressure and internal stresses has been used:

$$\int_{z_s}^{b}\sigma(z,t)dz=P(t).z_s+interactions\ with\ mold\ edges \qquad (2.115)$$

The edge interactions are neglected since if the sample shrinks, they are zero, and otherwise the mold prevents the deformation (δ=0).

Writing equation (2.113) for the melt next to the solidifying layer z at time t (ε_T=0 and $\delta=\delta_s$) , we obtain the compressive (negative) pressure strain, as follows:

$$\varepsilon_p(z) = \frac{2\upsilon - 1}{E} P(t) \qquad (2.116)$$

which is equal and opposite to the pressure-induced strain in the solidifying layer (see equation (2.89)).

The evolution of stresses may be calculated using equations (2.113-2.116) above (51). In the case of no applied pressure, this model reduces to free quenching (equation (2.104)) and in case of very large pressure or friction that prevents shrinkage in mold, the final stress profile is equivalent to equation (2.112).

Fig.2.11 (same as 4.82) compares the experimentally measured stresses (18) with the CMS and 1-D FMS stress profiles. Fig.2.11 also shows the estimated pressure history during injection molding of polystyrene with uniform initial melt temperature of 235°C and mold temperature of 20°C. Menges et al. (18) did not report the exact pressure-time profile. The profile shown in Fig.2.11 was suggested by Titomanlio et al. (51) using the reported values of maximum pressure and holding time. The comparison with the predictions of the two models suggests that in this experiment the shrinkage of the sample was constrained in the mold and the stresses are mostly due to pressure. It is difficult, however, to comment on the predicted surface stresses since data are not provided close enough to the surface. The simplified models described in section 2.3.12 (CMS) and section 2.3.13 (1-D FMS) are used.

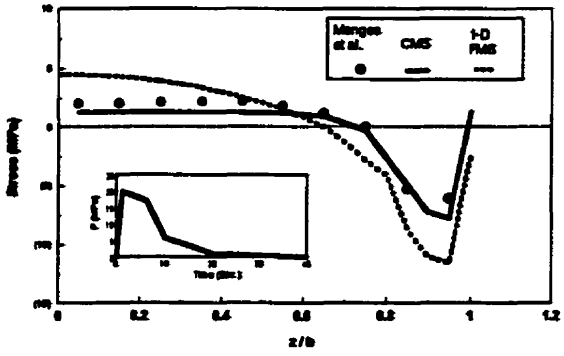

Fig.2.11. Residual stress profiles measured (18) and calculated using different models for PS and conditions I in Table 2.1.

So far, we have discussed direct models to calculate thermal stresses from a set of known processing conditions. The problem of optimization of the injection molding

process with respect to residual stresses may be handled by using the above direct models in conjunction with trial and error. The alternative approach of inverse formulation has also been employed in this thesis and is the subject of the next section.

2.4. INVERSE FORMULATION

2.4.1. General Aspects

The inverse formulation is used to estimate the processing conditions required to achieve prescribed product properties, in this case, the residual stress distribution. Thus, in the statement of the problem, the distribution of residual stresses is given as a starting point, and the inverse formulation is employed to provide information regarding the processing conditions. In this manner, the inverse formulation may be used as a tool for process optimization, design, and control. The analysis is applicable to the injection or compression molding process.

2.4.2. Unknown Pressure History

The cooling and solidification of polystyrene with conditions of Menges et al. (18) is considered. This conditions are listed in Table 2.1. below as I. The mold surface temperature and the initial uniform temperature of the melt are known. The pressure history that is required to generate a prescribed residual stress distribution needs to be calculated.

Constrained Mold Shrinkage (CMS)

As mentioned in section 2.3.12., the sample is not allowed to shrink while inside the mold in this case. Half of the sample, b, is divided into N equal layers of dimensionless thickness, $\Delta Z=\Delta z/b$. The final stress profile is related to the pressure history through equation (2.112) above. Equation (2.112) may be expressed as:

$$\sigma_i = \left(\frac{1-2\upsilon}{1-\upsilon}\right)\left[\sum_{j=1}^{N} P_j \, \Delta Z_{ji} - P_i\right] \qquad (2.117)$$

where σ_i and P_i are the stress and the solidification pressure in the layer i, respectively. If all the layers have the same thickness ΔZ, the term $\sum_{j=1}^{N} P_j \Delta Z_j$ becomes $\Delta Z_i \cdot \sum_{j=1}^{N} P_j$ and is identical for different layers. In this problem the vector $\underline{P}$ is unknown and must be calculated using a known residual stress distribution $\underline{\sigma_e}$. The stress distribution may be prescribed or obtained from experimental data. Replacing this stress into equation (2.117) results in a residual R as follows:

$$R_i = \sigma_{e_i} - \left(\frac{1-2\upsilon}{1-\upsilon}\right)\left[\Delta Z_i \sum_{j=1}^{N} P_j - P_i\right] \tag{2.118}$$

In order to calculate the pressure history, we must find P_i's so that the residuals R_i vanish. Then the pressure history P(t) may be found by knowing the transient position of the solid-melt interface $z_s(t)$ and eliminating z. We need at least N equations for the N unknown P_i's. Using a multi-dimensional Variable Metric method (102), the sum of the squared residuals $\sum_{i=1}^{N} R_i R_i$ is minimized with respect to P_i. As a result, N equations are obtained for N unknown P_i's. The pressure history is obtained as the solution of the minimization.

1-D Free Mold Shrinkage (1-D FMS)

In this case, the sample is allowed to shrink inside the mold. It is assumed that the final residual stress profile and the total shrinkage are known or prescribed and the unknown pressure history is then calculated using the following methodology.

Equation (2.113) may be written for the final time, as follows:

$$\sigma_f(z) = \left(\frac{E}{1-\upsilon}\right)\left[\delta_f + \eta(z) - \varepsilon_{T_f} - \frac{\upsilon}{E} P_f\right] \tag{2.119}$$

where $\sigma_f(z)$ is the known final stress profile, δ_f is the final shrinkage of the part, and ε_{Tf} is given by $\alpha_l (T_f - T_s)$, T_f being the final uniform temperature of the sample. The final pressure P_f is the pressure at the instant before ejection of the sample and is assumed zero as a first guess. When the pressure history is calculated from the inverse model, the final pressure is corrected, if necessary, and a new iteration starts with the new value of P_f. The

final shrinkage δ_f may be determined experimentally. $\eta(z)$ is calculated in the N layers from equation (2.119). To calculate the pressure, we start from t=0 (z_s=b) and march forward in time until complete solidification (z_s=0). At each time t, we calculate the pressure P(t) and the shrinkage $\delta(t)$ from equations (2.114) and (2.116). Combining these two equations and rearranging, the following expressions are obtained in terms of the dimensionless Z=z/b:

$$\delta(t)=\left(\frac{2\upsilon-1}{\upsilon-1}\right)\left\{\left[\frac{Z_s(t)-2\upsilon Z_s(t)+\upsilon}{2\upsilon-1}\right]\eta(Z_s)-\int_{Z_s}^{1}\eta(Z)dZ+\int_{Z_s}^{1}\varepsilon_T(Z,t)dZ\right\} \quad (2.120)$$

$$P(t)=\left(\frac{E}{2\upsilon-1}\right)\left[\delta(t)+\eta(Z_s)\right] \quad (2.121)$$

Note that, at the time of solidification of Z_s, we have: $\delta(t)=\delta_s(Z_s)$ and thus in equation (2.116) $\varepsilon_p(Z_s)=\delta(t)+\eta(Z_s)$.

The position of the solid-melt interface z_s (t) must be obtained at time t by solving the energy equation, as in the forward model. Once P(t) and $\delta(t)$ are calculated, the stress distribution at time t may be obtained from equation (2.113).

2.4.3. Unknown Initial Melt Temperature Profile

In this example, cooling of a polymer melt in the mold is considered as above. The goal is to obtain the temperature profile in the cavity at the end of filling that results in a prescribed residual stress distribution. The shrinkage is assumed to be prevented in the mold, therefore, the CMS model is used. An initial temperature profile $T_i(z)$ is assumed as an initial guess to solve equation (2.102) together with equation (2.103). The position of the solid-melt interface may be obtained from equation (2.104). The procedure is similar to the calculation of the pressure history using the CMS model. In this case, the residual R_i is formed as in equation (2.121). The initial temperature is assumed to be constant in one layer. The sum of squared residuals $\sum_{i=1}^{N} R_i R_i$ is minimized with respect to the initial temperatures at different layers T_i's. The derivative $\frac{\partial P}{\partial T_i}$ is needed in the

minimization procedure. It is replaced by $\frac{\partial P}{\partial t}.\frac{\partial t}{\partial T_i}$, since P depends on T_i through time t. The term $\frac{\partial P}{\partial t}$ may be calculated from the known pressure history P(t) and $\frac{\partial t}{\partial T_i}$ is obtained, for each solidifying layer z, from the temperature distribution history given by equation (2.92), by replacing the temperature T by the solidification temperature T_s. As before, a multi-dimensional Variable Metric method (102) was employed.

In subsequent testing of this method, it was found that the stresses have a low sensitivity to the initial temperature distribution and the minimization leads to multiple local solutions. In order to deal with the problem of non-uniqueness and obtain a physically acceptable temperature profile, we imposed some physical constraints and used regularization to narrow the solution domain. The imposed constraints required that the initial temperature be larger than the solidification temperature everywhere and that the temperature decrease as the mold wall is approached from the core of the sample. These constraints may not be valid in some actual cases. For example, if the flow of the polymer melt is slow enough in the filling stage, a thin layer of the polymer close to the surface may cool below T_s. Also, due to viscous heating, some points between the core and the mold wall may have a higher temperature than the midplane. In regularization, constraints are imposed on the magnitude of the inverse solution, its first, second,... derivative depending on the order of regularization. To this end, a term or several terms are added to the squared sum of residuals; each term is multiplied by a coefficient λ_i, i=0,1,2,... called the regularization parameters. For up to second order spatial regularization on the whole domain z=0 to z=b, the objective function S to be minimized becomes:

$$S = \int_0^b R^2 dz + \lambda_0 \int_0^b T_i^2 dz + \lambda_1 \int_0^b \left(\frac{\partial T_i}{\partial z}\right)^2 dz + \lambda_2 \int_0^b \left(\frac{\partial^2 T_i}{\partial z^2}\right)^2 dz \qquad (2.122)$$

2.4.4. Testing the Inverse Methods

The first test for an inverse solution is to use the solution of the direct model as the prescribed residual stress profile and compare the obtained pressure history with the pressure history used in the first place for the direct problem. This is a test for the

numerical minimization procedure. Subsequently, random errors are added to the prescribed stress profile to simulate experimental errors. An important criterion for the performance of an inverse method is its sensitivity to errors. The final test is the use of experimental data. The experimental conditions and properties used for testing are listed in Table 2.1. as I (18) and II (4).

	I	II
Poisson ratio, υ	0.35	0.33
Elastic modulus, E (MPa)	2000	2000
Thermal diffusivity, a (m^2/s)	6.13×10^{-8}	6.13×10^{-8}
Coefficient of linear thermal expansion, α_l (K^{-1})	7×10^{-5}	7×10^{-5}
Maximum pressure (MPa)	20	48
Holding time (s)	5	2.5
Mold half-thickness, b (mm)	2	1
Mold temperature (°C)	20	55
Solidification temperature (°C)	80	100

Table 2.1. Properties and conditions used for testing the inverse methods (4, 18)

2.5. SUMMARY OF CHAPTER 2

In this chapter, some theoretical aspects of calculation of thermal stresses in polymer processing were reviewed. Polymers are viscoelastic materials. In order to understand their behavior, we must understand the elastic and viscous behaviors. The constitutive equations for elastic and viscous behaviors may be derived from thermodynamics consideration and starting from the free energy and the dissipation function. Viscoelastic materials exhibit elastic behavior in fast deformations and viscous

behavior in slow deformations. The Deborah number De, may be used to estimate the elastic effects during the flow of these materials.

Balance equations are used in polymer processing to state mathematically the physical laws of conservation of mass, momentum, and energy. To model a process, these equations are coupled with constitutive equations describing the behavior of the material: rheology, P-V-T dependence, crystallization kinetics, and stress-strain relationship.

The derivation of the relevant equations for the injection molding of an amorphous and a semi-crystalline polymer and for the development of thermal stresses is introduced. Thermoelastic constitutive equation were used to relate the stress and the strain. The effect of packing pressure on stresses was discussed and incorporated. The two-dimensional plane strain case was formulated in terms of displacements. The equations were solved numerically using the Galerkin finite element technique. The stresses were obtained from the calculated displacements.

Two main versions of the model were employed: a simpler version (two-dimensional free mold shrinkage 2-D FMS) providing insight and quick estimation of stresses, and a more complex and realistic version, where stress calculations were linked with a complete simulation of injection molding by the package McKam©. Some special cases, such as free quenching (FQ), constrained mold shrinkage (CMS), and one-dimensional free mold shrinkage (1-D FMS), were discussed.

Finally, two inverse methods to calculate the pressure history or the initial temperature distribution from a prescribed residual stress profile, were presented.

Chapter 3

EXPERIMENTAL

This chapter describes the experimental aspects, including materials, equipment, and experimental procedures employed for sample preparation and the various measurements.

3.1 MATERIALS

Two resins were used in this study: Polystyrene(PS) and High Density Polyethylene (HDPE).

3.1.1. Polystyrene (PS)

The polystyrene resin, STYRON 685D, was supplied by Dow Chemical Canada Inc. Some of its properties are given below.

Rheology:

The viscosity versus shear rate data for three different temperatures were provided by Dow Chemical Canada Inc. These data were fitted to the Carreau-WLF equation (89), as follows:

$$\eta = \frac{K_1 a_T}{\left[1 + K_2 |\dot{\gamma}| a_T\right]^{K_3}} \tag{3.1}$$

where η is the shear viscosity, $\dot{\gamma}$ the shear rate, and a_T is the temperature shift factor. The temperature dependence of a_T is given below:

$$\ln a_T = \frac{8.86\left(K_4 - K_5\right)}{101.6 + K_4 - K_5} - \frac{8.86\left(T - K_5\right)}{101.6 + T - K_5} \tag{3.2}$$

K_i's, i=1,..,5 are material dependent constants and their values for Styron 685D are listed in Table 3.1.

	K_1 (Pa.s)	K_2 (s)	K_3	K_4 (°C)	K_5 (°C)
Styron 685D	2165.71	0.068	0.76	244.01	203.0

Table 3.1. Carreau-WLF constants for Styron 685 D

The viscosity data and the fitted curves are presented in Fig.3.1. It must be noted that, in order to obtain a more appropriate fit, we must have data in a broader range of shear rate and temperature.

Pressure-Volume-Temperature:

The P-V-T data for this material were measured using a GNOMIX PVT Apparatus available in the Chemical Engineering Department. This apparatus measures the volume change of the polymer at various temperatures caused by an applied pressure. A hydrostatic pressure of silicone oil is produced by a motorized pump. This pressure is transmitted to the sample by a flexible bellows. The deflection of the bellows is a measure of volume change.

The temperature was varied from 30°C to 200°C and the pressure from 10 to 200 MPa. The sample was kept at each temperature for a complete pressure scan. The procedure was repeated for the next temperature. The holding time for each pressure was 60 s.

The Tait equation was used to fit the PVT data for PS, as follows (4):

$$V(P,T) = \left(A_0 + A_1 T\right)\left(1 - 0.0894 \ln\left(1 + \frac{P}{B(T)}\right)\right) \tag{3.3}$$

T is the temperature in °K and B(T) is given by:

$$B(T) = B_0 \exp\left(-B_1 T\right) \tag{3.4}$$

T in equation (3.4) is in °C. The pressure dependence of the glass transition temperature T_g is given by:

$$T_g(P) = T_g(0) + s_1 P + s_2 P^2 \tag{3.5}$$

A_0, A_1, B_0, B_1, s_1, and s_2 in equations (3.3-3.5) are constants and their values for Styron 685D are given in Table 3.2.

The PVT data and the fitted curves are shown in Fig.3.2. As may be seen in this figure, the data are fitted well with the Tait equation except in the glass transition region.

Styron 685 D	melt	glass
A_0 (m^3/kg)	7.631×10^{-4}	8.888×10^{-4}
A_1 (m^3/kg.K)	5.846×10^{-7}	2.486×10^{-7}
B_0 (Pa)	$2.3058 \times 10^{+8}$	$3.30298 \times 10^{+8}$
B_1 ($°C^{-1}$)	3.7911×10^{-3}	3.1068×10^{-3}
T_g (0) (°C)	100	100
s_1 (K/Pa)	6.135×10^{-7}	6.135×10^{-7}
s_2 (K/Pa^2)	-1.457×10^{-13}	-1.457×10^{-13}

Table 3.2. Tait parameters for Styron 685 D

Heat Capacity:

Data for the temperature dependence of heat capacity were taken from reference (4). Note that these data are given for PS 678 E from Dow Chemical. The following equation was proposed to fit the data:

$$C_P = C_{P1} + C_{P2}\left(T - C_{P5}\right) + C_{P3}\ tanh\left(C_{P4}\left(T - C_{P5}\right)\right) \qquad (3.6)$$

T is the temperature in °K and the constants C_{pi}, I=1,..,4 are given in Table 3.3.

	C_{p1} (J/kg.K)	C_{p2} (J/kg.K)	C_{p3} (J/kg.K)	C_{p4} (J/kg.K)	C_{p5} (J/kg.K)
PS 678 E	1730	2.1	172	0.155	359

Table 3.3. The fit parameters for heat capacity of PS678E

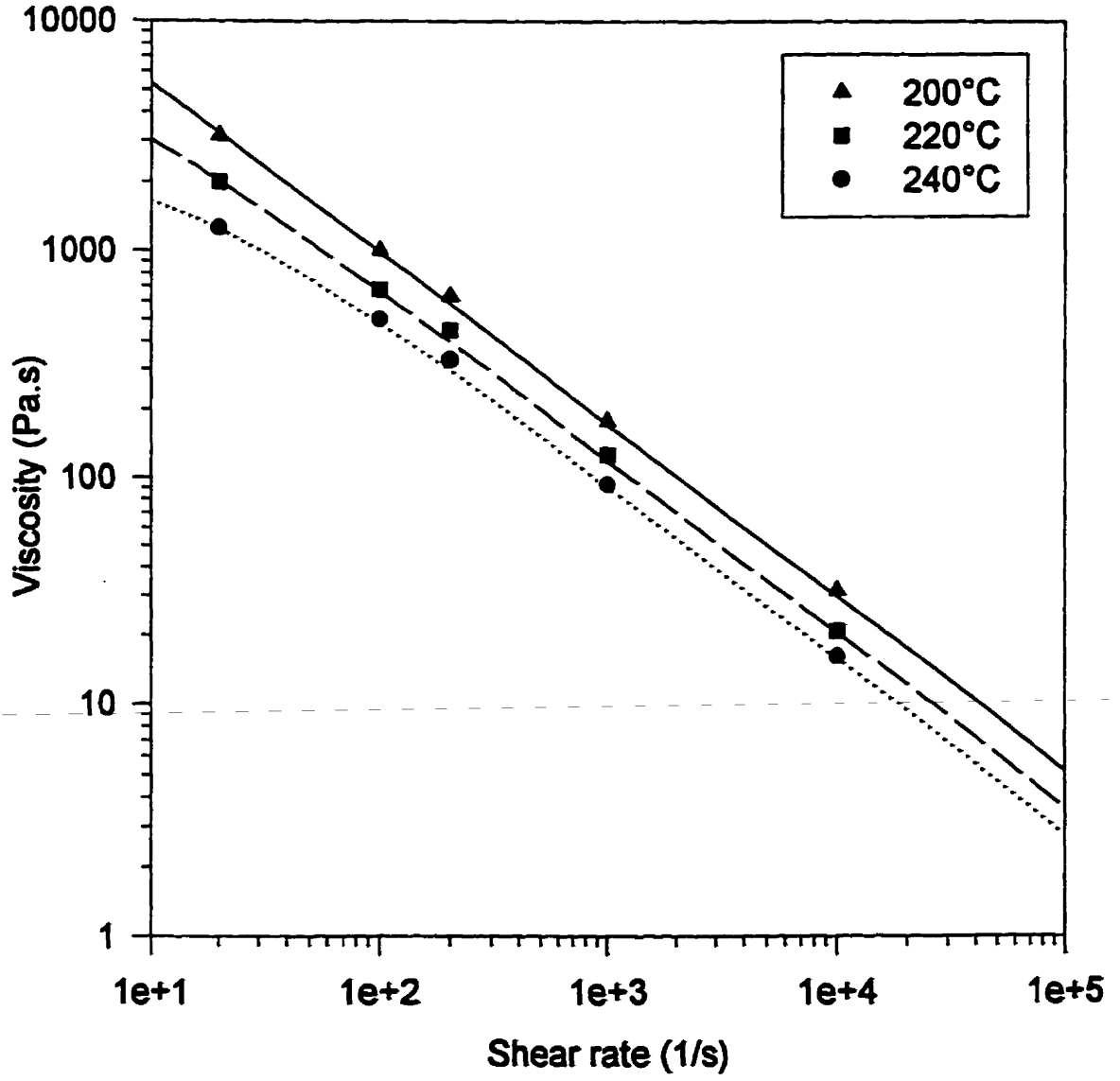

Fig.3.1.Viscosity data for Styron 685D fitted with with Carreau-WLF equation

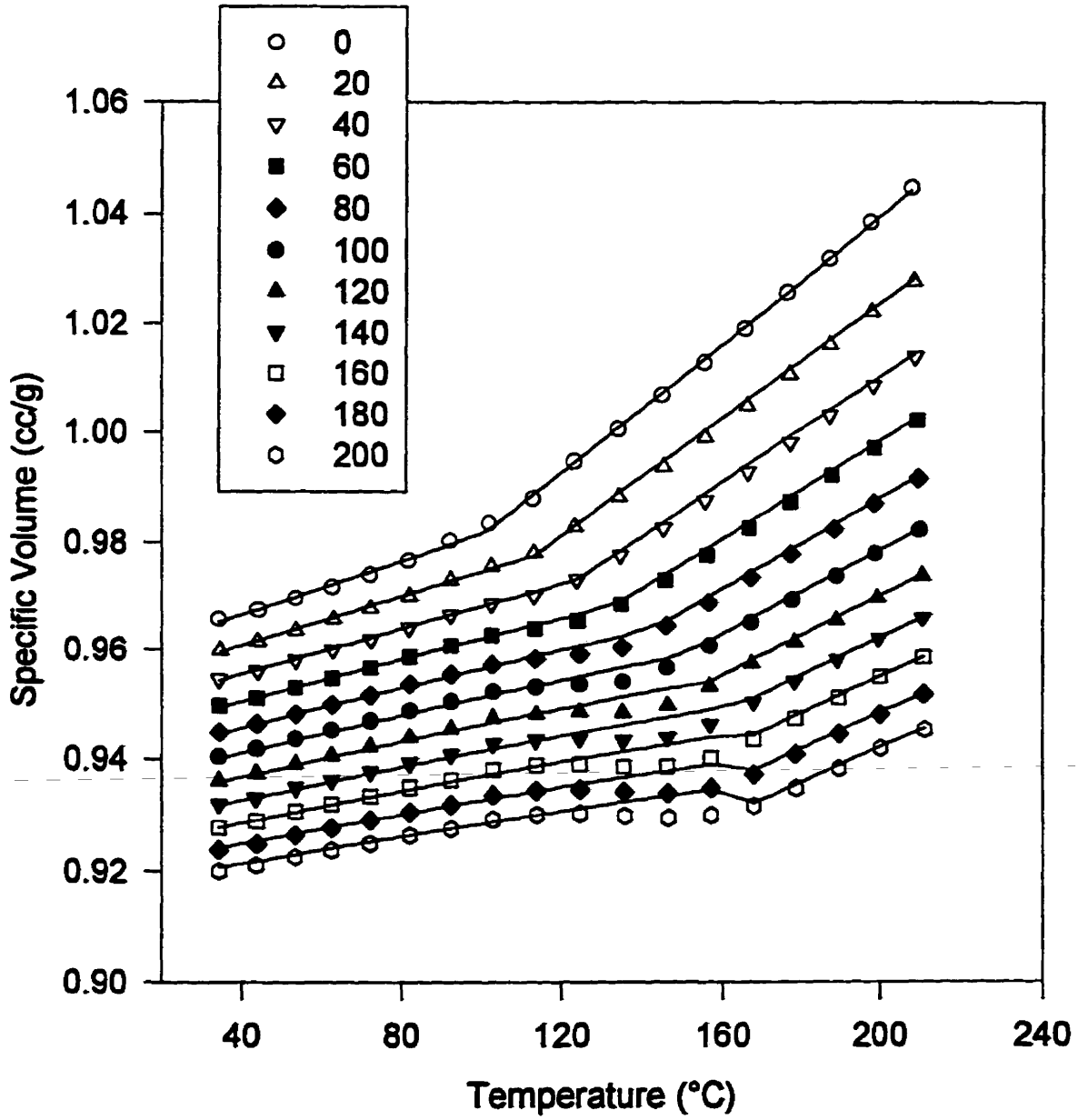

Fig.3.2. Experimental (symbols) and fitted (lines) specific volume versus temperature for different pressures in MPa (Styron 685D fitted with Tait equation)

Thermal Conductivity:

The thermal conductivity for this material was provided by Dow Chemical. As illustrated in Fig.3.3, the data were fitted by a second order polynomial as shown below:

$$k = k_0 + k_1 T + k_2 T^2 \qquad (3.7)$$

T is the temperature in °K and the constants are given in Table 3.4.

	k_0 (W/(m.K))	k_1 ((W/(m.K^2))	k_2 ((W/(m.K^3))
Styron 685 D	0.1006	2.51×10^{-4}	-2.5×10^{-7}

Table 3.4. Fitting constants for thermal conductivity of Styron 685 D

Other Properties:

The measured value of the elastic modulus at ambient temperature was 2300 MPa. The values used for the Poisson ratio υ and the linear thermal expansion coefficient α_l were 0.35 and 7×10^{-5} K^{-1}, respectively. Some other properties of Styron 685 D provided by the company are listed in Appendix I.

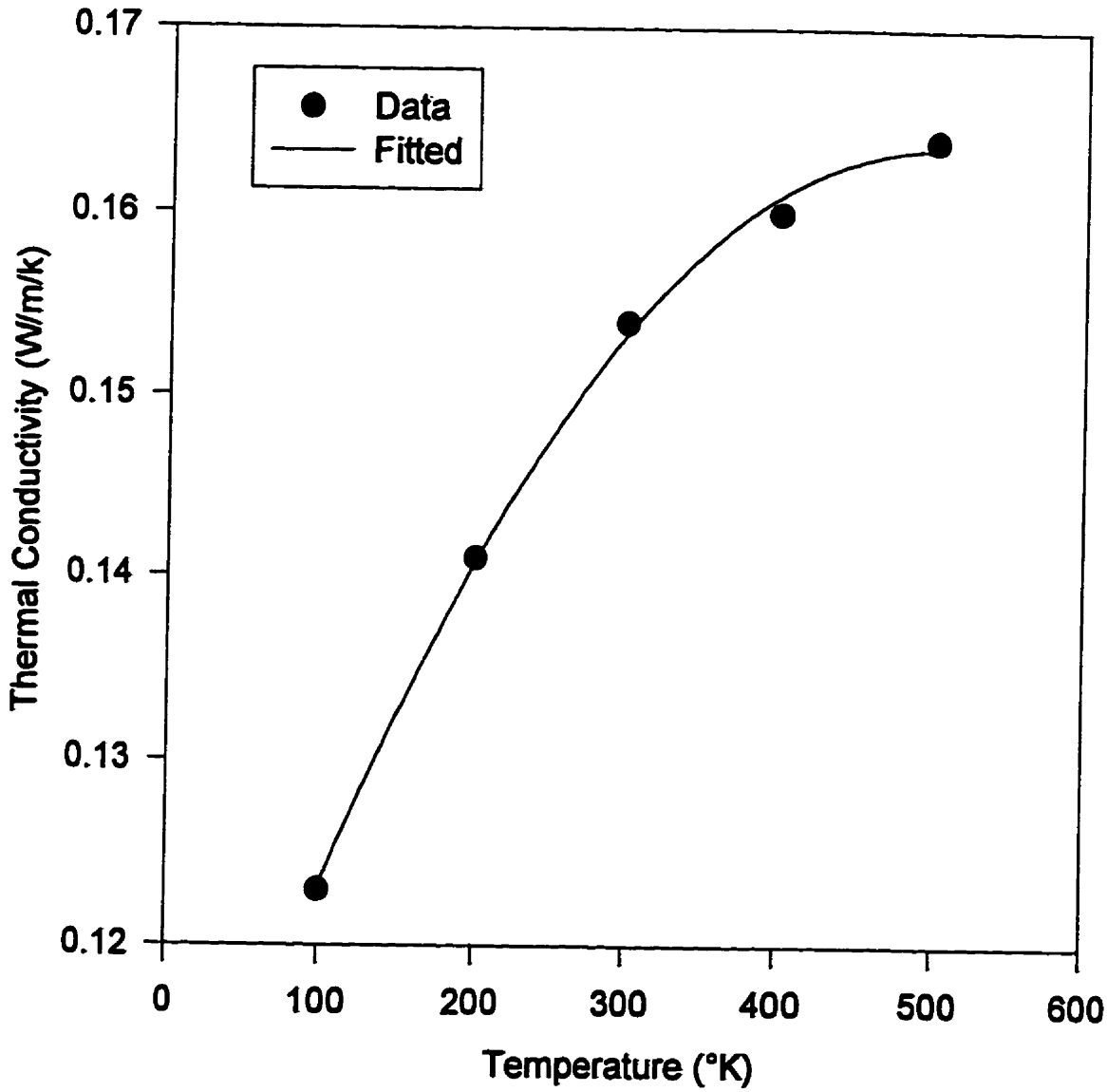

Fig.3.3. Temperature dependence of thermal conductivity (Styron 685 D)

3.1.2. Polyethylene (HDPE)

The Polyethylene resin was SCLAIR 2908, supplied by NOVA Chemical Inc.

Rheology:

The Arrhenius-Power law equation was used for the non-isothermal viscosity as a function of shear rate, as follows:

$$\eta = m_0 \exp\left(E_a / (RT)\right)\dot{\gamma}^{n-1} \tag{3.8}$$

where the constants m_0, E_a, and n are listed in Table 3.5.

	m_0 (Pa.s^n)	E_a/R (°K^{-1})	n
Sclair 2908	2.285	3158.2	0.75

Table.3.5. Power law parameters for Sclair 2908 (HDPE)

The viscosity data in Table 3.5 were taken from: Kamal, M.R. and Papathanasiou, T.D., Polym.Eng.& Sci., 33 (7), 410 (1993)

Pressure-Volume-Temperature:

The PVT data, obtained by Samara (103) are presented in Fig.3.4. Tait equation given by equation (3.3) was used to fit these data. Some of the fitted curves are shown in Fig.3.4. Note that V(0,T) was fitted to a second order polynomial and B(T) was fitted to second and third order polynomials. Fig.3.4. shows that the fit is not adequate for the crystallization region. Tait parameters are listed in Table 3.6.

Sclair 2908	Melt	Solid
A_0 (cm^3/g)	1.1177	1.0436
A_1(cm^3/g/C)	1.0033 x 10^{-3}	2.1014 x 10^{-5}
A_2(cm^3/g/C/C)	-6.4986 x 10^{-8}	3.9163 x 10^{-6}
B_0 (Pa)	-443.1836 x 10^{+8}	233.1217 x 10^{+8}
B_1(Pa/C)	5.4221	0.3988
B_2(Pa/C/C)	-0.0141	-5.6809 x 10^{-3}
B_3(Pa/C/C/C)	_	-2.4750 x 10^{-5}

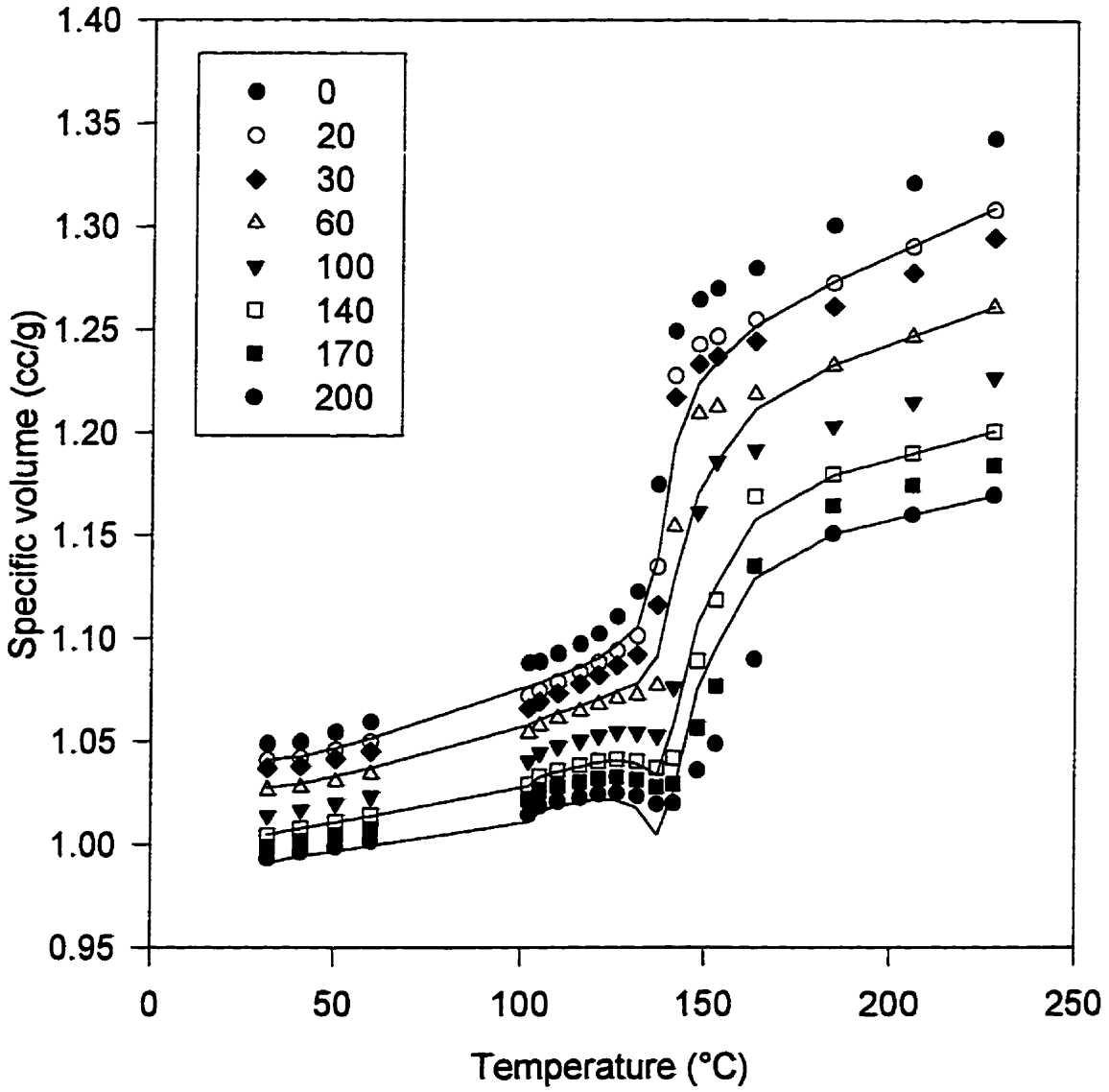

Fig.3.4. Experimental (symbols) and some fitted (lines) specific volume versus temperature for different pressures in MPa (Sclair 2908 fitted with Tait equation, data taken from Samara(103))

Crystallization Kinetics:

As mentioned in Chapter 2, Nakamura equation (2.60) was used to describe the non-isothermal kinetics of crystallization of Sclair 2908. The temperature dependence of the rate constant of crystallization K(T) was obtained from an empirical formula proposed by Ziabicki (37). According to this formula, the crystallization half-time is given by:

$$\left(\frac{1}{t_{1/2}}\right)=\left(\frac{1}{(t_{1/2})_{max}}\right)exp\left[-4\ln(2)\frac{(T-T_{max})^2}{D^2}\right] \qquad (3.9)$$

where $t_{1/2}$ is the half-time (time to reach 50 % conversion) and may be related to the isothermal Avrami rate constant z(T) as follows:

$$t_{1/2}=\left(\frac{\ln 2}{z}\right)^{1/n} \qquad (3.10)$$

n is the Avrami exponent (equation (2.59)). z_{max} , T_{max}, and D were determined experimentally by Samara (103) and are listed in Table 3.7 below. The isothermal rate constant z(T) is related to K(T) according to equation (2.61) :

$$K(T)=[z(T)]^{1/n} \qquad (2.61)$$

n	z_{max} (s^{-n})	D (°K)	T_{max} (°K)
1	10.25×10^{-2}	36.77	370.5
1.5	3.82×10^{-2}	40.91	370.5
2	1.37×10^{-2}	44.19	370.5

Table 3.7. Crystallization kinetics constants for Sclair 2908

The pressure dependence of T_{max} was fitted by the following equation (103):

$$T_{max}=97.5+0.2568P \qquad (3.11)$$

where the temperature is in °C and the pressure P is in MPa.

Specific Heat :

Samara (103) measured the specific heat (C_p) of Sclair 2908 using Differential Scanning Calorimetry. The specific heat increases linearly with temperature up to the

melting range. In this region, C_p exhibits a sharp peak and further raise in temperature causes C_p to drop back to the linear function. The linear function was found by Samara (103) by fitting the data, as follows:

$$C_p = 95 + 6.158T \tag{3.12}$$

where C_p is in J/Kg/°K and T is in °K. If C_p is calculated from this equation, the source term corresponding to the heat of crystallization must be included in the energy equation, as shown in equation (2.90). If the source term is omitted in equation (2.90), the heat of crystallization is taken into account in C_p.

Thermal Conductivity:

The temperature dependence of the thermal conductivity of Sclair 2908 was expressed by polynomials (2), as follows:

Solid: $$k = A_0 + A_1T + A_2T^2 + A_3T^3 + A_4T^4 + A_5T^5 \tag{3.13a}$$

Melt: $$k = B_0 + B_1T + B_2T^2 + B_3T^3 \tag{3.13b}$$

where k x 10^{-4} is the thermal conductivity in W/(m.°K) and T is the temperature in °C. The constants in these equations are listed in Table.3.9.

Sclair 2908	Solid	Melt
A_0	5.1528×10^{3}	
A_1	-1.1389×10^{2}	
A_2	3.6453	
A_3	-5.758×10^{-2}	
A_4	4.2367×10^{-4}	
A_5	-1.1766×10^{-6}	
B_0		-2.6526×10^{3}
B_1		0.9418×10^{2}
B_2		5.6777×10^{-1}
B_3		1.1607×10^{-3}

Table.3.8. Fitting constants for thermal conductivity of Sclair 2908

Other Properties:

The value of the average elastic modulus was taken as 971 MPa. The values used for the Poisson ratio υ and the thermal expansion coefficient α_l were 0.33 and 11 x 10^{-5} $^{o}K^{-1}$, respectively. Also, the amorphous and crystalline moduli, E_a and E_c were 430 and 5700 MPa, respectively.

3.2. Injection Molding

The resins were injection molded into rectangular plaques using a Danson Metalmec (Model 60-SR, 2-1/3 ounce, 68 ton) reciprocating screw injection molding machine. The barrel is divided into four heating zones (104). Each zone is independently heated by an electrical heating band. The temperatures are controlled within ±3°C, with respect to the set temperatures. The automatic mode of operation was used in the preparation of the moldings. Operating conditions were set using a computer that controlled the machine settings, the operation of the machine timers, and the data acquisition. Before each experiment, time intervals for recording pressure and temperature data, temperatures along the barrel and on the mold cavity surface, injection rate, and injection, cooling, and recycle times were set. Sufficient time was allowed for thermal stabilization of the unit. Polymer pellets were then fed from the hopper into the barrel where they were plasticized and conveyed through the melt reservoir section. The polymer melt was then injected into the mold cavity through the gate, where it was cooled using cooling water. As the melt solidifies, its volume decreases. More melt is sent into the cavity by applying high pressure during the packing stage. Finally, the molded part was ejected from the mold. To produce plaques with different thicknesses, two rectangular molds were used with the following dimensions: 10 cm x 6 cm x 3 mm and 10 cm x 6 cm x 1.5 mm. Each run corresponds to one set of processing conditions. In order to attain steady state and obtain a sufficient number of samples, 30 specimens were produced for each run. In order to prevent relaxation and creep in the specimens, they were stored at low temperatures (-34.8°C). Tables 3.10 and 3.11 list the processing conditions for the injection molding of PS and HDPE, respectively.

Runs	1	2	3	4	5	6	7	8
Thickness(mm)	3.0	3.0	3.0	3.0	3.0	3.0	3.0	1.5
$(P_{Nozzle})_{max}$	27	26.8	27.5	29.5	29.5	28	27.5	26
$(P_{Gate})_{max}$	19.5	18.2	23	22.5	22.9	21.4	20	23.2
$T_{coolant}$ (°C)	30	30	30	20	45	30	30	30
T_{melt} (°C)	230	210	250	230	230	230	230	250
End of holding (s)	7.0	7.0	7.0	7.0	7.0	5.0	10.0	7.0

Table.3.9. Processing conditions for injection molding of PS

Runs	1	2	3	4	5	6	7	8	9	10	11
Thickness(mm)	3.0	3.0	3.0	3.0	3.0	3.0	3.0	3.0	3.0	1.5	1.5
$(P_{Nozzle})_{max}$	30.5	30.5	30.5	30.5	30.0	31.0	31.0	26.6	30.3	30.5	32.8
$(P_{Gate})_{max}$	24.5	23.8	22.5	25.0	25.9	25.5	25.0	22.7	21.5	29.5	30.5
$T_{coolant}$ (°C)	40	20	40	50	40	40	40	40	40	40	40
T_{melt} (°C)	210	210	190	210	230	210	210	210	210	250	250
End of holding (s)	30	30	30	30	30	20	35	30	30	30	30

Table.3.10. Processing conditions for injection molding of HDPE

3.3. DETERMINATION OF RESIDUAL STRESSES

A variety of methods may be used to determine the residual stress distribution in the injection molded specimens. In this work, the layer removal technique was employed. The theory of this technique was described in detail in Chapter 2. The procedure is as follows: Specimens were cut from several positions on the injection molded plaques. They were 8.6 cm long and 5 mm wide in the longitudinal case. The distance between specimens on the plaque and the end and the sides of the cavity was 1 cm. The axes of symmetry of the specimen 2 and the cavity coincide. The distance between specimens and the gate edge is 4 mm. In the transverse case, the specimens were 5 mm wide and their

length was equal to the width of the molded plaque (6.25 cm). The distance between the gate edge and specimen 4 was 12 mm, between specimens 4 and 5 it was 33 mm, between 5 and 6, 25 mm, and finally, between 6 and the end of cavity there was a 15 mm gap. The positions were selected in order to avoid the transducer marks on the specimen. Figures 3.5a and 3.5.b show the configuration of different longitudinal and transverse specimen.

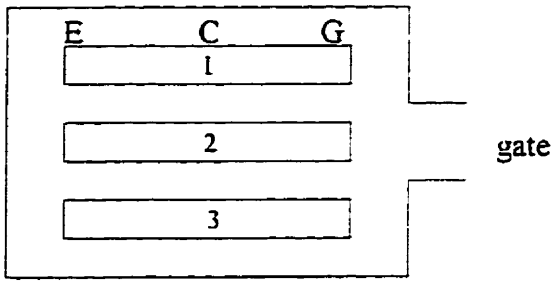

Fig.3.5a. Longitudinal locations on the side opposite to the ejectors

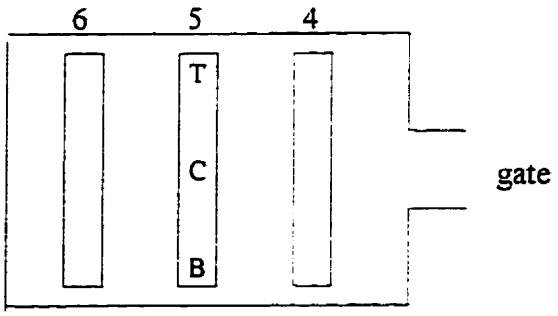

Fig.3.5b. Transverse locations on the side opposite to the ejectors

Successive layers were then removed from the surface of the specimen using a milling machine and a two- flute end-mill cutter rotating at high speed, taking care to hold the specimen flat in a precision vice during cutting to ensure uniform thickness of each layer removed. In order to be consistent, the layer is always removed from the side opposite to the ejector, and the deflection of the surface on the ejector side is measured, using an optical system. This system consists of a light source directed onto the specimen, a visualization system of macro-lens for magnification, a video camera, and a data acquisition system with computer to grab the image and to magnify the deflection of the sample. The specimen stands on two supports at the ends

and can travel horizontally relative to the camera, using a micrometer screw device connected to the system and a stationary length scale. Measurements were made in 5 mm intervals. In this way, it was possible to measure the deflection and calculate the curvature at any position along the specimen or the flow path. Unlike the mechanical methods (9), the optical method does not apply a force to the sample, causing no additional deflection.

Following Hastenberg et al. (9), the total profile was subdivided equally into three segments as shown in Fig.3.6, and the curvature and stresses were assumed to be constant within each segment. The mid-points of each segment were labeled G, C, and E denoting near the gate, center, and near the end of cavity locations, respectively.

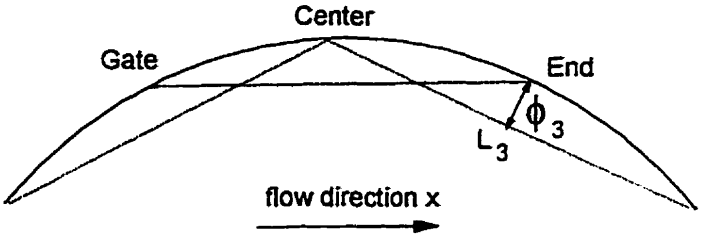

Fig.3.6. Gate, Center, and End locations in the specimen

The curvature κ can be calculated from:

$$\kappa = \frac{8\phi}{L^2 + 4\phi^2} \tag{3.14}$$

where L is the length of the chord and ϕ is the deflection (distance from chord to arc at the midpoint of the chord), as shown in Fig.3.6. The derivation of this equation is given in Appendix I. The curvature data points obtained from a segment were fitted by regression with a polynomial function. The stress distribution was calculated using the stress-curvature relation derived by Treuting and Read (7) and shown below:

$$\sigma_{xx}(z) = \frac{-E}{6(1-\upsilon)}\left\{(z+b)^2 \frac{d\kappa_x(z)}{dz} + 4(z+b)\kappa_x(z) - 2\int_z^b \kappa_x(z)dz\right\} \tag{3.15}$$

where z is the remaining distance along half of the thickness of the specimen and varies from 0 at the core to b, the specimen's half thickness. The derivative and the integral of the curvature in equation (3.15) were obtained using the fitting polynomial function.

A similar analysis was carried out on specimen cut along the cross-flow direction (transverse direction). The procedure was identical to the longitudinal one and the segments were labeled T, C, and B for top, center, and bottom, respectively.

An important source of error in this procedure is due to the viscoelastic behavior of the polymeric material. As a result, part of the internal stresses relax with time, thus modifying the residual stress profile resulting from the process. Also, the resulting curvature of the specimen increases in time, due to creep. These phenomena were more pronounced in the case of polyethylene, because of its low glass transition temperature (≈-100°C). To minimize errors due to this phenomenon, the deflection was always measured within 5-6 minutes of removing the layer. For more discussion on equation (3.15), see Appendix I.

The main sources of errors in this technique are: effect of machining, creep and relaxation, initial difference in the thickness of specimen near the gate, in the center, and near the end, thickness readings, order of the polynomial fitted to the curvature, simplifying assumptions in the stress equation, and variations of E and υ along the thickness.

3.4. DETERMINATION OF CRYSTALLINITY

For semi-crystalline polymers, crystallization must be taken into account in the simulation of the injection molding process. The distribution of the degree of crystallinity affects the calculated thermal stress profile. The degree of crystallinity is in turn affected by the processing conditions, especially the temperature and pressure histories. Other factors such as flow, orientation of polymeric chains, and the presence and orientation of fiber reinforcements also affect the distribution of crystallinity. As mentioned in the previous chapter in the development of models, a number of simplifying assumptions must be made in order to solve the relevant equations. In order to evaluate these calculations and attain a better understanding of the morphology of the molded polymer, the distribution of crystallinity was determined experimentally along the thickness of the samples.

3.4.1. Microtoming

Square specimens of 1cm x 1cm were cut from selected locations in the injection molded plaques of polyethylene, as specified in Fig.3.7. The horizontal distance between the specimens was 3 cm. The distance between position 1 and end of cavity as well as between positions 3 and the gate edge was 5 mm. Also the samples 4 and 5 were 5 mm apart from the side of cavity.

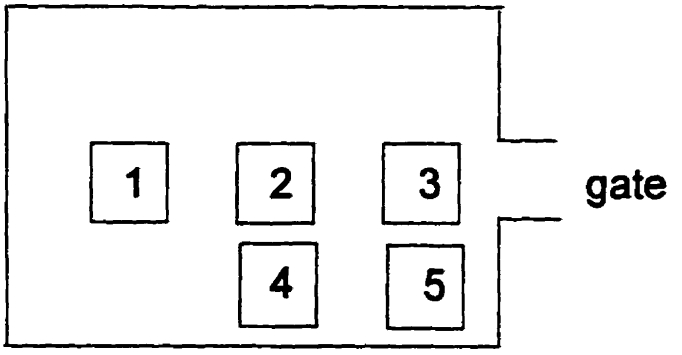

Fig.3.7. Locations of specimens cut from the molded plaque

These parts were then mounted on a Plexiglas support using a five-minute epoxy glue and allowed to settle overnight. The apparatus used to remove successive layers from the specimen in the thickness direction was the rotary microtome, built in the Chemical Engineering Department. The support was clamped to the microtome carriage and aligned with the steel blade. The carriage moved orthogonal to the blade and its velocity was set at 40 on the dial. The blade rotated at a speed indicated by the dial as 40. The thickness of each removed layer was controlled by setting the required depth using the installed Mitutoyo micrometer. Twelve successive layers were cut from half-thickness of each sample. The degree of crystallinity at seven different depths was then measured using the differential scanning calorimeter (DSC).

The main error in microtoming is in the reading of the depth of the removed layer.

3.4.2. Differential Scanning Calorimeter (DSC)

A Perkin-Elmer differential scanning calorimeter, model DSC-7 was used to carry out melting experiments. The change in the enthalpy of the specimens during melting was measured in order to determine the degree of crystallinity. The sample and reference compartments in the calorimeter were kept at identical temperature, by means of two heaters located under the sample and reference holders. Temperature data are fed into a differential amplifier. The output of the differential amplifier adjusts the differential power increment to keep both the sample and the reference at the same temperature throughout the analysis.

The microtomed specimen of known weight was encapsulated in the aluminum sample pan using a crimping press. After running the baseline for the DSC, the sealed sample pan was placed in the sample compartment and heated at a rate of 10°C/min from 50 °C to 200 °C. In a typical DSC thermogram, the power is plotted versus time, providing information about the melting range and the enthalpy of fusion of the sample. In the melting range, the curve exhibits a sharp peak corresponding to the heat of fusion. The enthalpy of fusion ΔH_m is given by the area under the curve. The weight fraction crystallinity of the sample, X_C may be calculated as follows:

$$X_C = \frac{\Delta H_m}{\Delta H_f} \tag{3.16}$$

where ΔH_m is the measured heat of fusion of the sample in J/g and ΔH_f is the theoretical heat of fusion of a 100% crystalline sample. For high density polyethylene, the latter was estimated by Dole to be 293.076 J/g (2).

Beside the errors involved in the DSC equipment, taking the average crystallinity in the microtomed layer produced some error.

3.5. SUMMARY OF CHAPTER 3

In this chapter, the rheological, thermodynamics, and mechanical characteristics of the two resins used in the present study, Styron 685 D and Sclair 2908, were presented. These resins were injection molded into thin rectangular plaques under various conditions.

The residual stress distribution along the thickness was measured at different locations in the part, using the layer removal technique.

The differential scanning calorimeter was employed to measure the degree of crystallinity in thin layers cut from the molded sample by microtoming.

Chapter 4

RESULTS AND DISCUSSION

In the first part of this chapter, the experimental and calculated results for polystyrene (PS) and high density polyethylene (HDPE) are presented and compared. Furthermore, the effect of various parameters on the final stress profile is investigated, using simulations and experiments. The results are then discussed in the second part. The objective is to understand the origin of thermal stresses and the factors influencing them, in order to predict and control the final stress profile.

4.1. RESULTS

4.1.1. Polystyrene (PS)

The residual stress profile in injection molded PS samples was measured using the layer removal technique, as explained in Chapter 3. Fig.4.1 shows a gradual increase in the deflection of a typical sample, as successive thin layers are removed from its surface. Using equation (3.14), the curvatures are calculated from the deflection curves at three locations: near the gate (G), center of cavity (C), and near the end of cavity (E). The curvatures are fitted with polynomials and used in equation (3.15) to obtain the residual stress distribution. The curvatures and the residual stress profiles corresponding to run 1 (see Table 3.10) are shown in Fig.4.2 to Fig.4.4. The nozzle and gate pressures are recorded during injection molding and are presented in Fig.4.5. The measured residual stress profiles consist of three main regions in this case: tensile (positive) stress on the surface (z/b=1) followed by a compressive (negative) region, and finally, a tensile region in the core. These three regions have been observed by other investigators for various

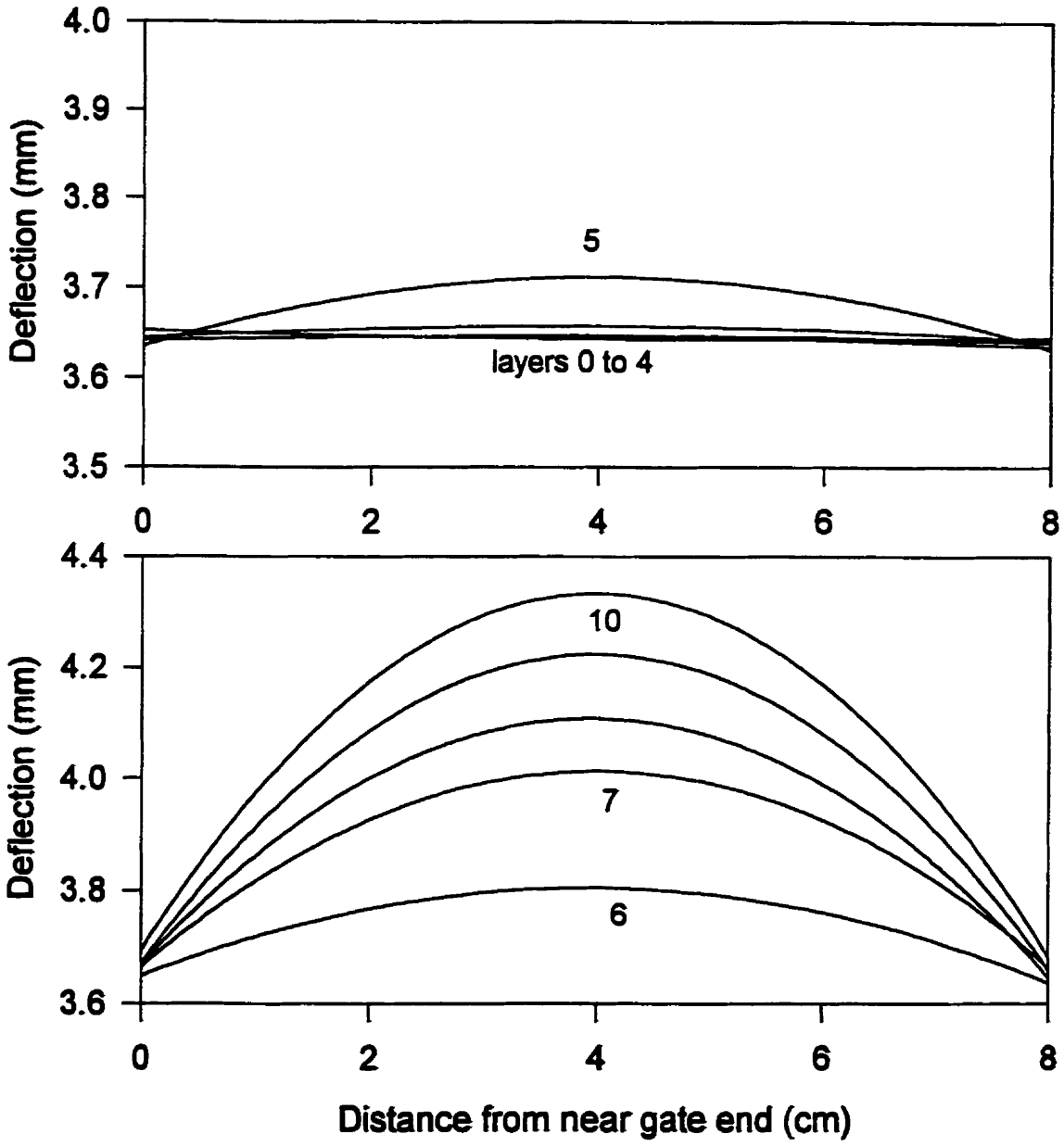

Fig.4.1. Deflection of the PS sample after removal of successive layers from its surface.

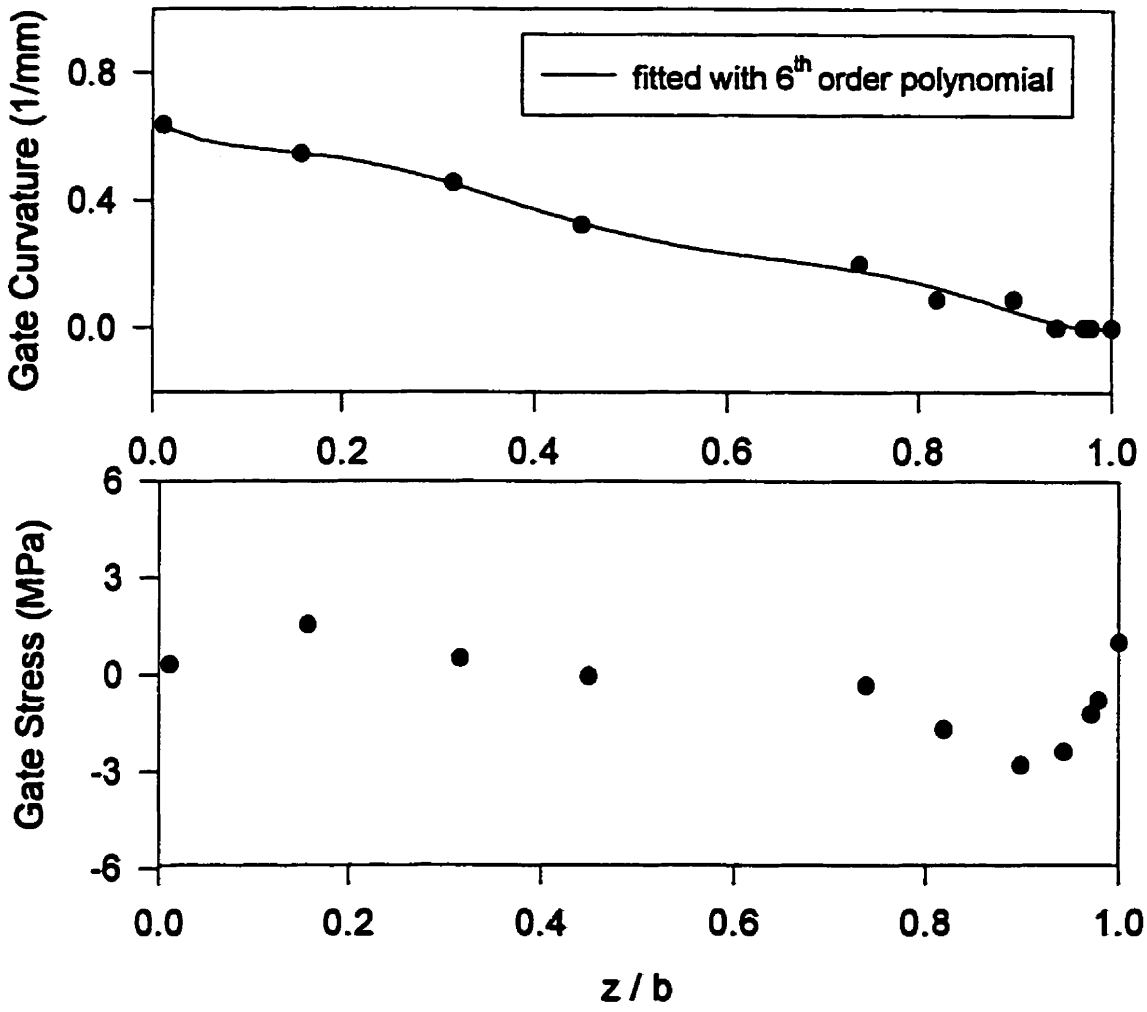

Fig.4.2.Curvature and stress profile near the gate for run 1 with PS.

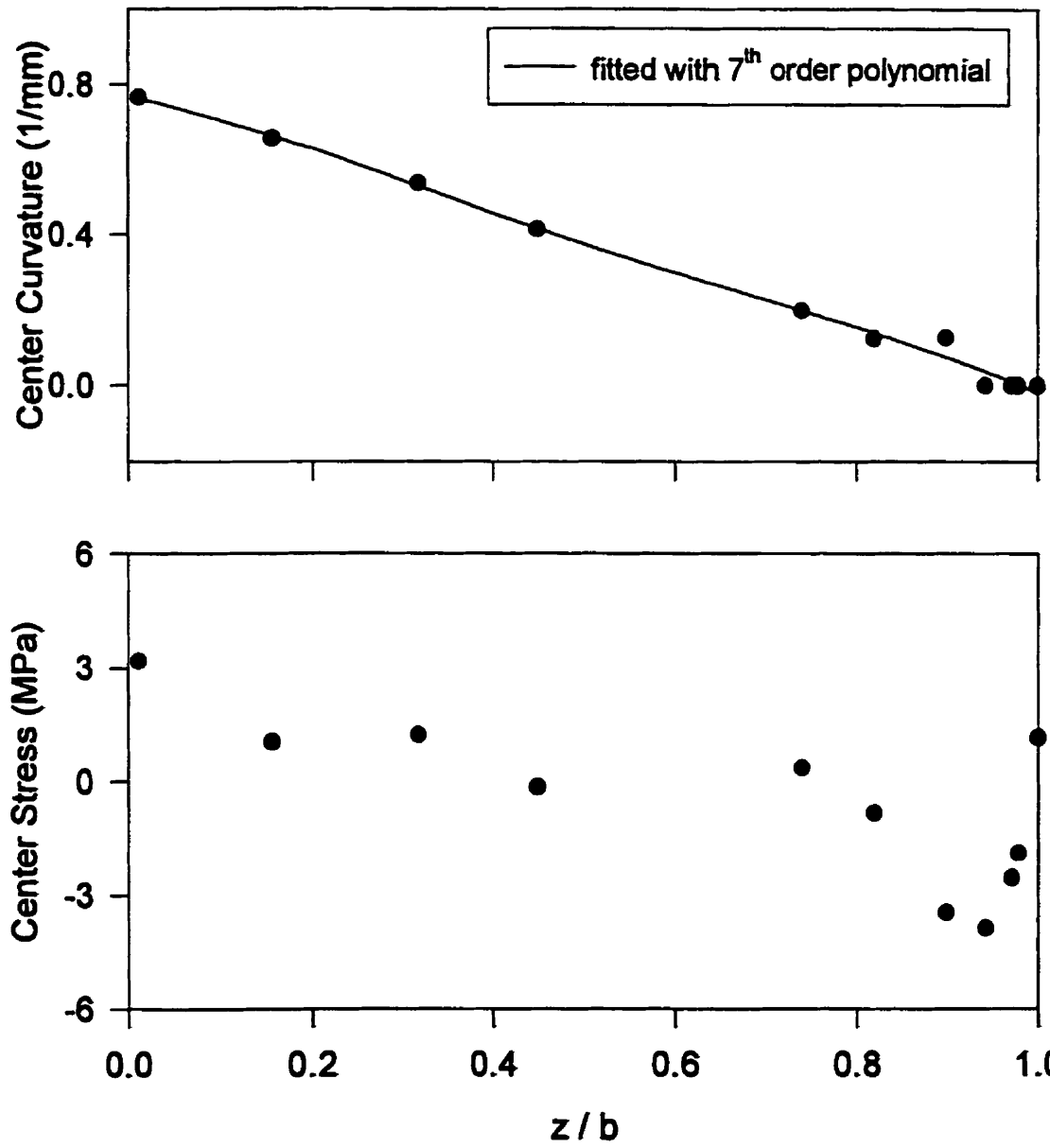

Fig.4.3.Curvature and stress profiles in the center of cavity for run 1 with PS.

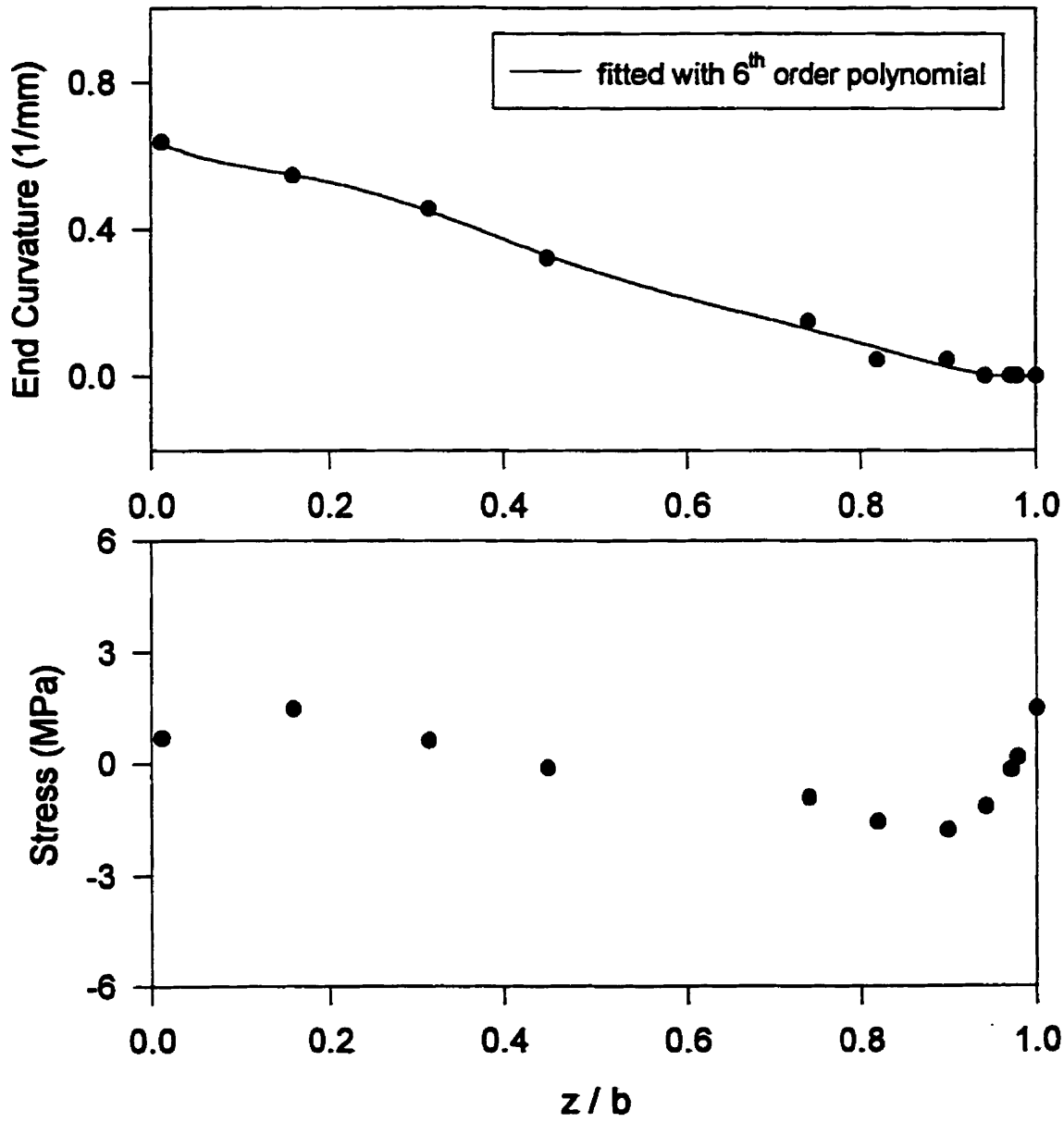

Fig.4.4.Curvature and stress profile near the end of cavity for run 1 with PS

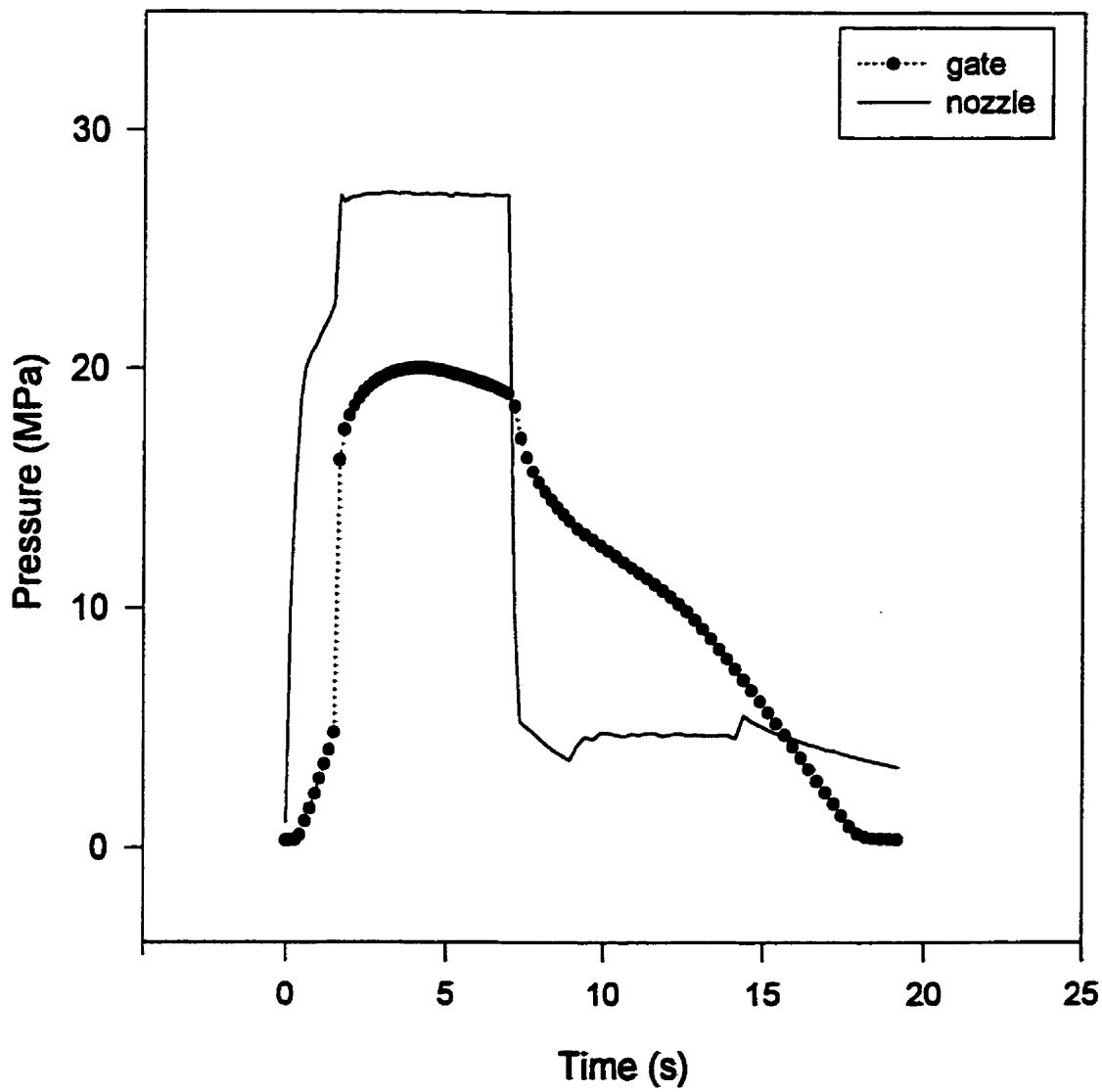

Fig.4.5. Nozzle and gate pressure histories for run 1 with PS

materials (18, 9, 19, 5, 64). In some cases, there is a compressive peak near the surface but the surface stress does not become positive (tensile) (18). Three main regions may also be distinguished in the gate pressure history, shown in Fig.4.5. During filling, the pressure increases linearly (to about 5 MPa for this run), until the mold is completely filled. Then, during packing, the pressure rapidly rises to a high value of 20 MPa. This high pressure is held until the gate freezes or the applied pressure at the nozzle is set to zero at the end of holding. At this stage, the pressure decays according to the thermodynamic properties of the material. In the case shown in this figure, the gate does not solidify completely before the end of holding.

The two-dimensional free mold shrinkage (2-D FMS) model, introduced in Chapter 2, was used to calculate the stresses for PS.

Free Quenching (FQ)

To illustrate the thermal effects in the absence of pressure, the free quenching (FQ) case is first considered. The position of the solid-melt interface is calculated using the solidification temperature of PS (T_g = 100°C) and is shown in Fig.4.6. The FQ stress profile is calculated by letting P=0 in the 2-D FMS model. The evolution of the temperature profiles and the xx component of the FQ stress in half-thickness of the sample are illustrated in Fig.4.7 to 4.10 for different Biot numbers.

For small Biot numbers (1 and 3), due to large resistance to heat transfer at the wall, the surface layer (z/b=1) takes longer to solidify whereas it solidifies instantaneously for high Biot numbers (30 and 100). For the same reason, there is a larger temperature gradient along the thickness for larger Biot numbers (Fig.4.9 and 4.10, top) compared to smaller Biot numbers (Fig.4.7 and 4.8, top), when the polymer melt cools down starting from its initial temperature (230°C). The coolant temperature is 30°C and the wall temperature is about 34°C.

As found by other investigators both experimentally and theoretically (3, 15), a compressive stress region close to the surface and a tensile region in the core may be distinguished in the FQ profiles. The surface stress seems to be more affected by

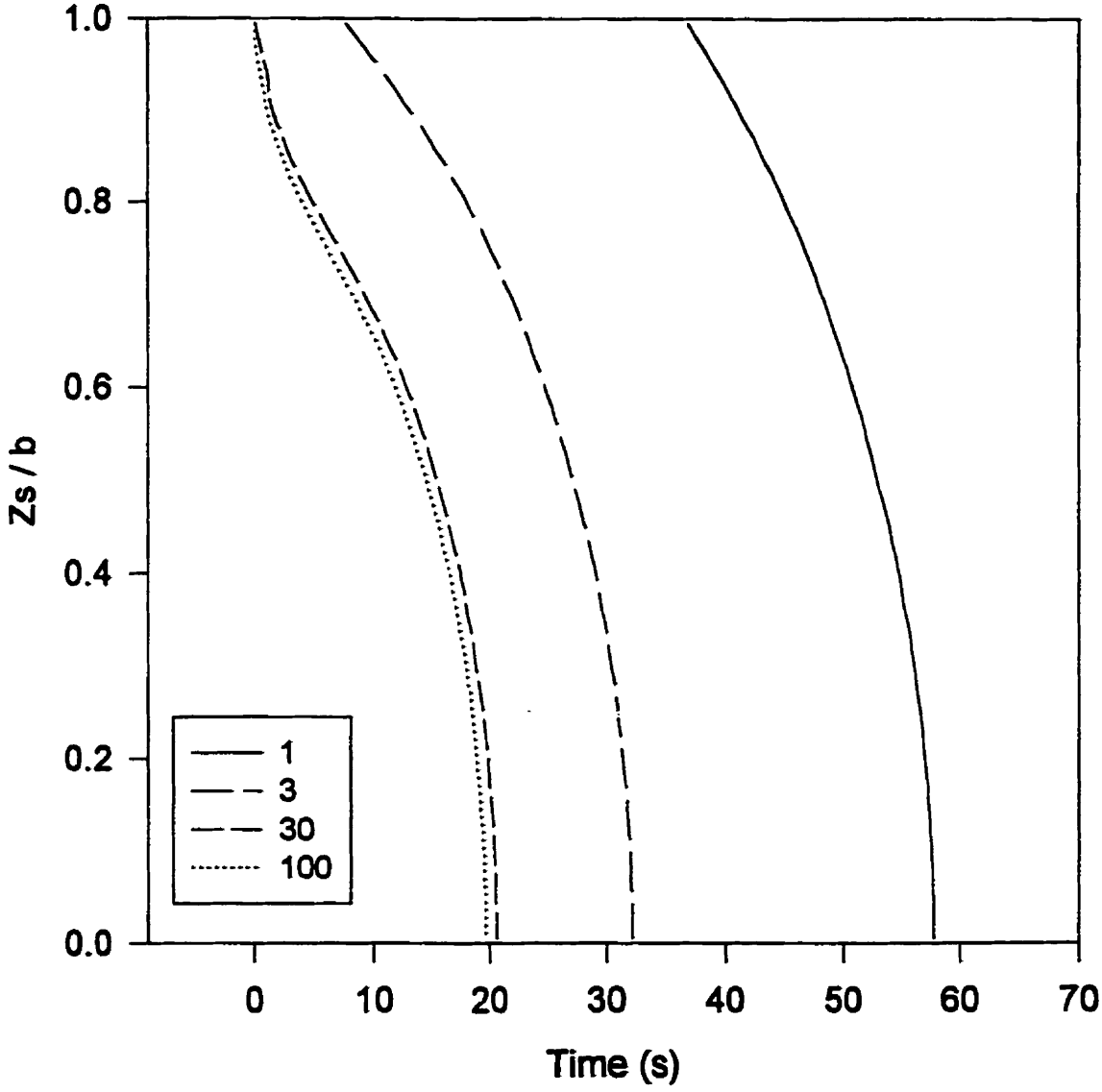

Fig.4.6.Evolution of solidification front for cooling of PS with variable Biot number (2-D FMS model, run 1)

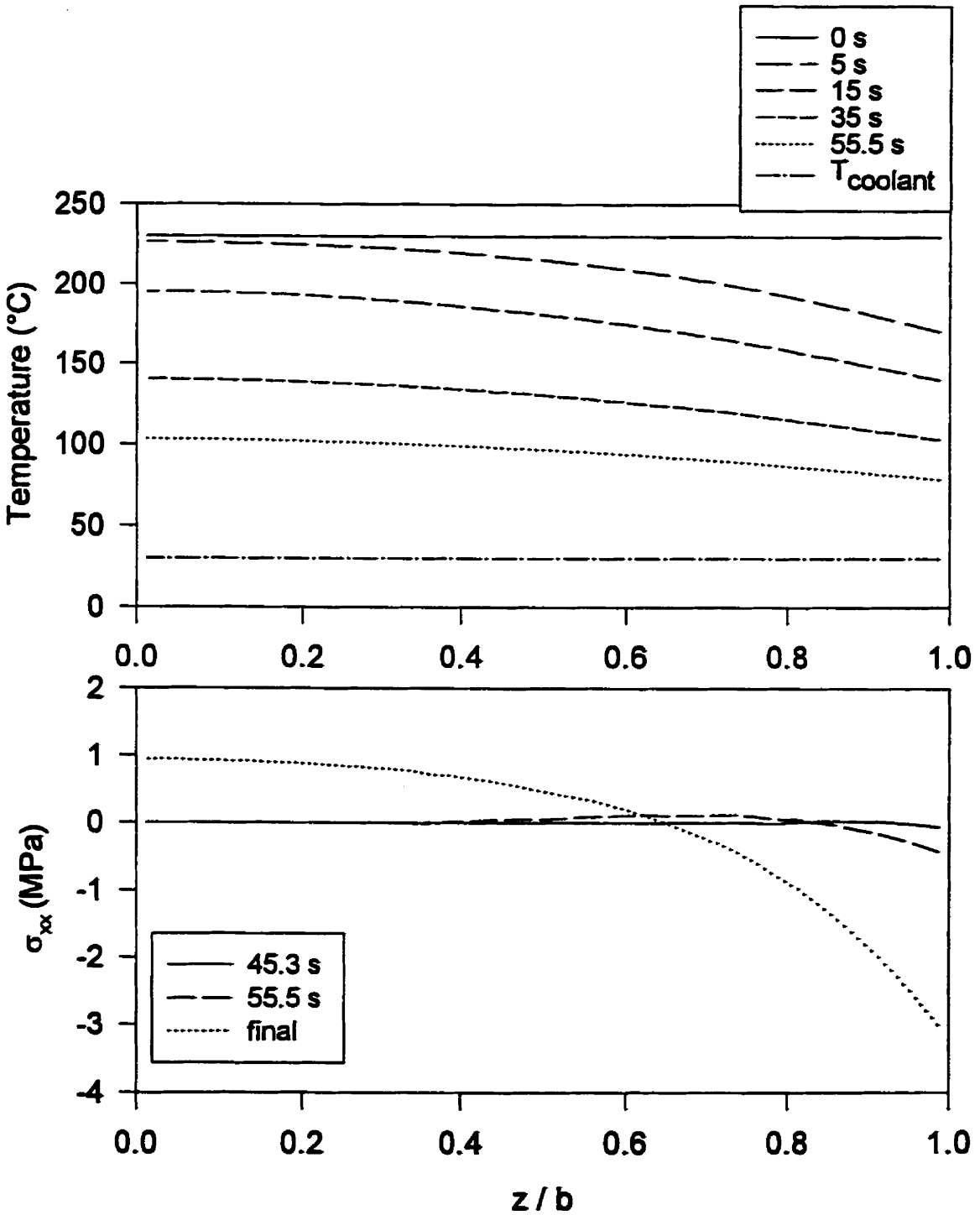

Fig.4.7.Evolution of temperature and residual stress profiles in cooling of PS using the 2-D FMS model (run 1, Biot = 1)

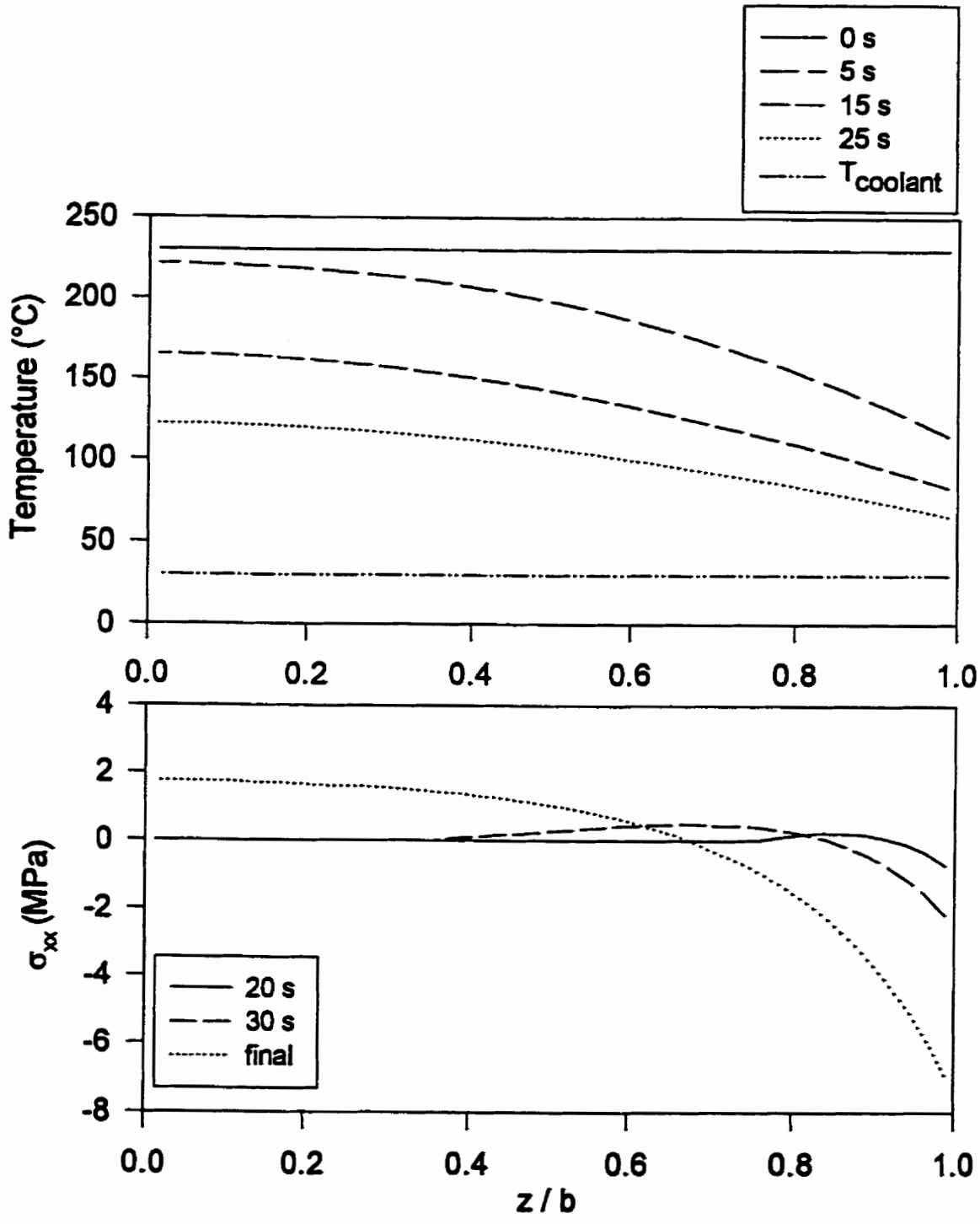

Fig.4.8.Evolution of temperature and residual stress profiles in cooling of PS using the 2-D FMS model (run 1, Biot=3)

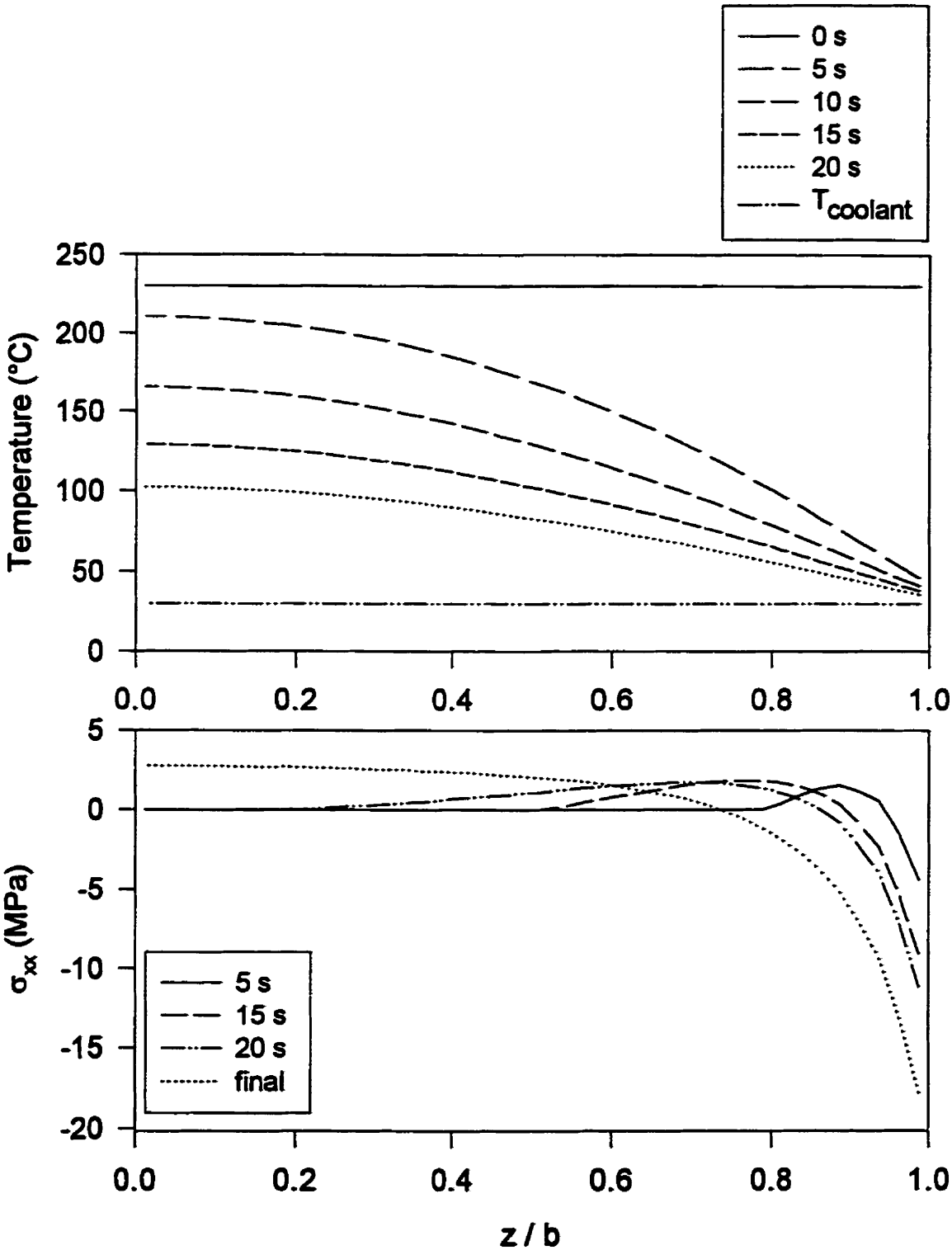

Fig.4.9. Evolution of temperature and residual stress profiles in cooling of PS using the 2-D FMS model (run1, Biot=30)

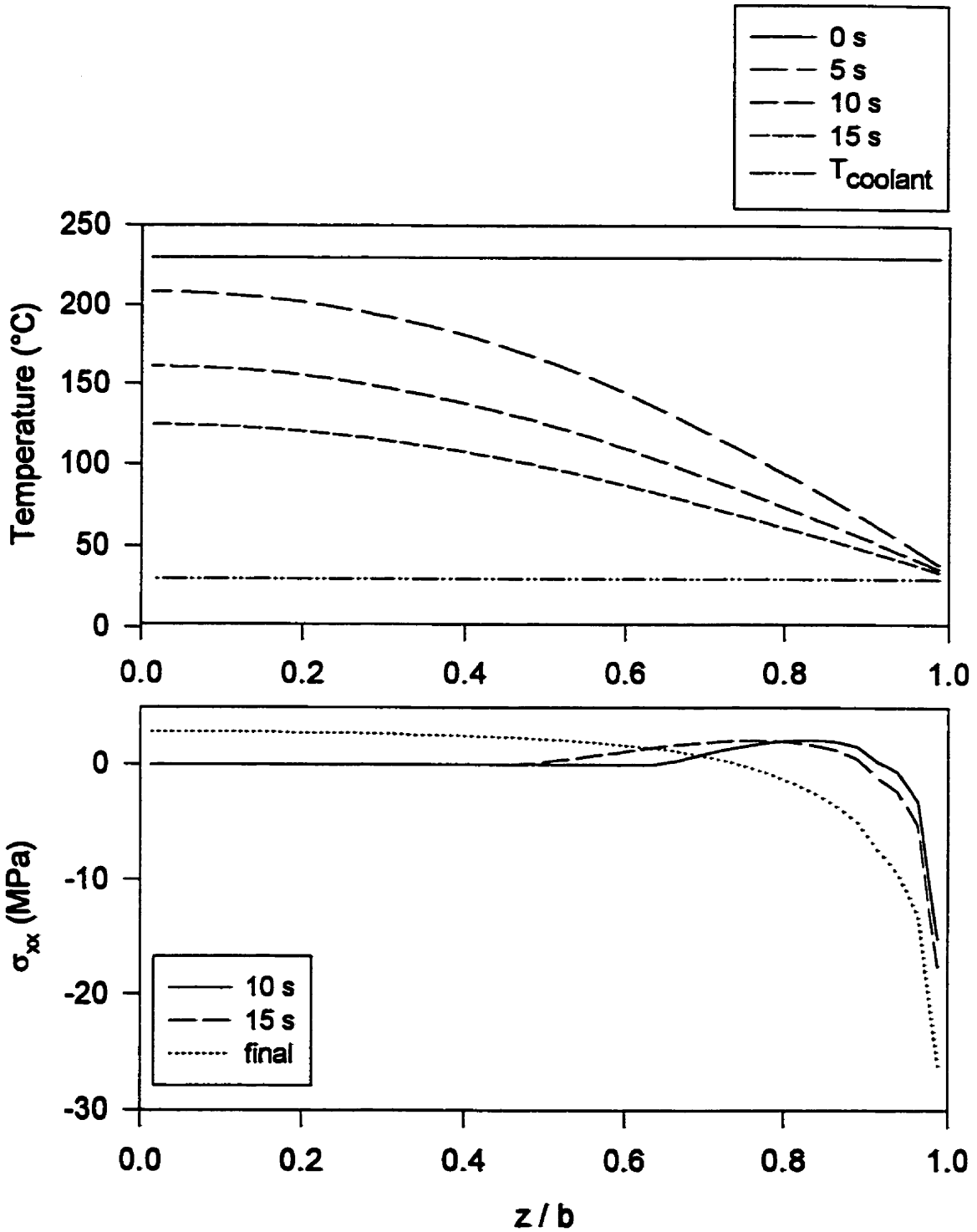

Fig.4.10. Evolution of temperature and residual stress profiles in cooling of PS using the 2-D FMS model (run1, Biot=100)

Biot number than the midplane stress. The surface stress varies from about -3.2 MPa for Biot=1 to -27 MPa for Biot=100, whereas the midplane stress changes from 0.9 to 2.8 MPa. Fig.4.11 shows the three components of the FQ stress for different Biot numbers. The top graph illustrates the increase in the magnitude of the xx-component on the surface and in the mid-plane with Biot number, as observed previously. The negative surface stress varies much more rapidly at first but levels off for high Biot numbers. As shown in the middle figure, the zz component of the stress is almost zero, except for Biot=100 and near the surface. The physical meaning of the non-zero σ_{zz} at the surface is not clear since the temperature changes only in the z direction. The bottom figure shows small shear stresses in the sample, due to the variation of shrinkage along the thickness, z.

As illustrated by Fig.4.12, all three components of the strain are negative and their magnitude increases with Biot number. The xx-component of strain has a parabolic profile, similar in shape to σ_{xx}. It is large near the surface and small in the core. The profile for the zz-component is also parabolic but its maximum magnitude is in the mid-plane. The shear deformation and the shear stress both show a maximum at $z/b \approx 0.76$. This is the point where the xx-component of the stress changes sign (see Fig.4.11).

Injection Molding:

The calculated transient position of the interface in injection molding is identical to the FQ case. The 2-D FMS model with $P \neq 0$ was used to calculate stresses in the injection molded PS sample (run 1 in Table 3.10). The resulting stresses depend on the Biot numbers as shown in Fig.4.13 and 4.14. These figures show the evolution of the stress profile for Biot number of 1, 3, 30, and 100. For Biot = 1, a parabolic profile similar to free quenching is obtained. The surface and midplane stresses are identical with the free quenching stresses shown in Fig.4.7. For larger Biot numbers, the midplane stress remains similar to free quenching. The compressive surface stress, however, rises gradually until it becomes tensile (Fig.4.13 and 4.14). Also, the zero-stress point, where the stress changes sign, shifts to lower z/b's (closer to the core) when pressure is taken into account and as the Biot number increases. It must be noted that the experimental pressure history near

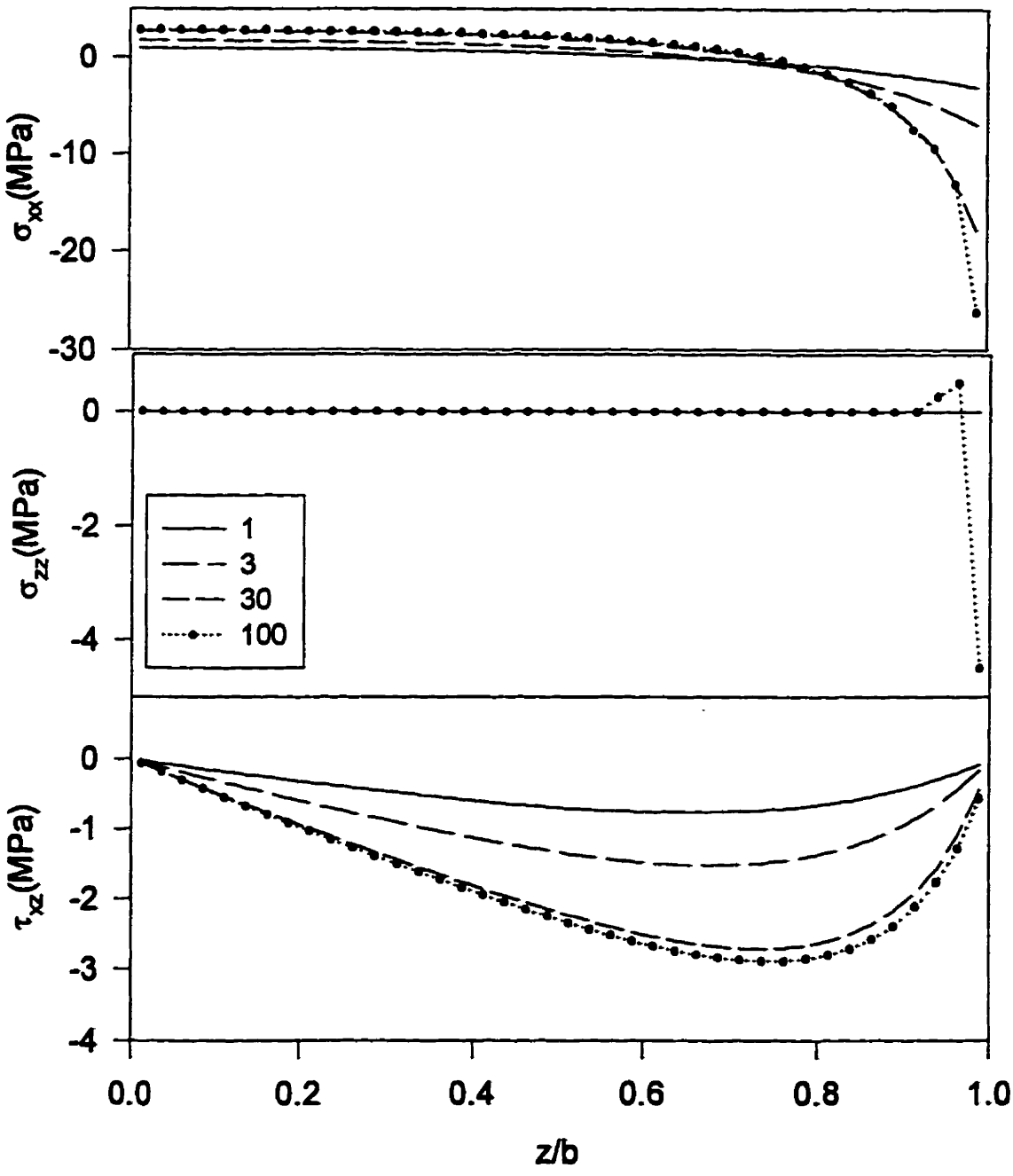

Fig.4.11 Final distribution of 3 stress components for different Biot numbers in free quenching of PS (2-D FMS, run1)

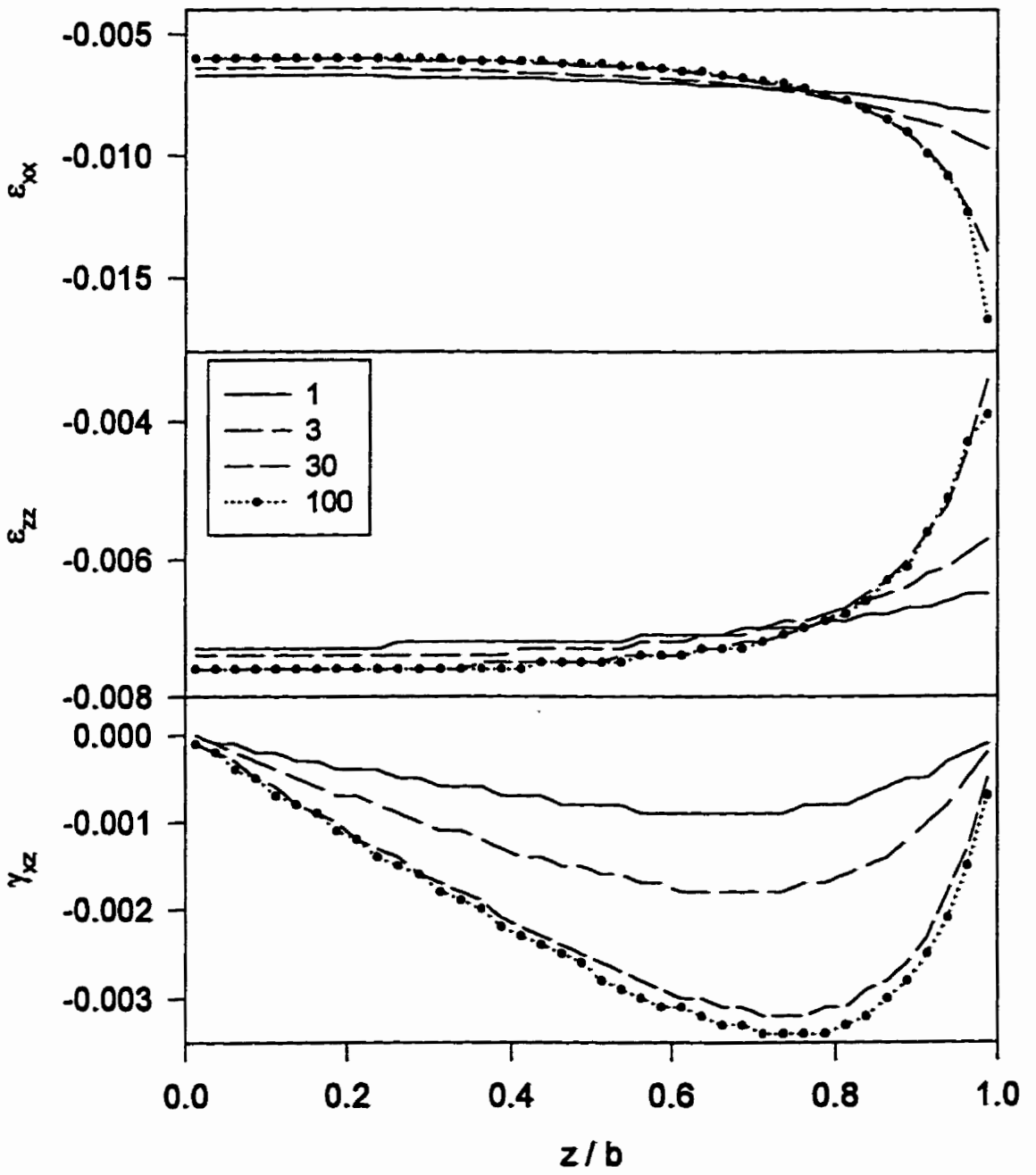

Fig.4.12.Final distribution of 3 strain components for different Biot numbers in free quenching of PS (2-D FMS, run 1)

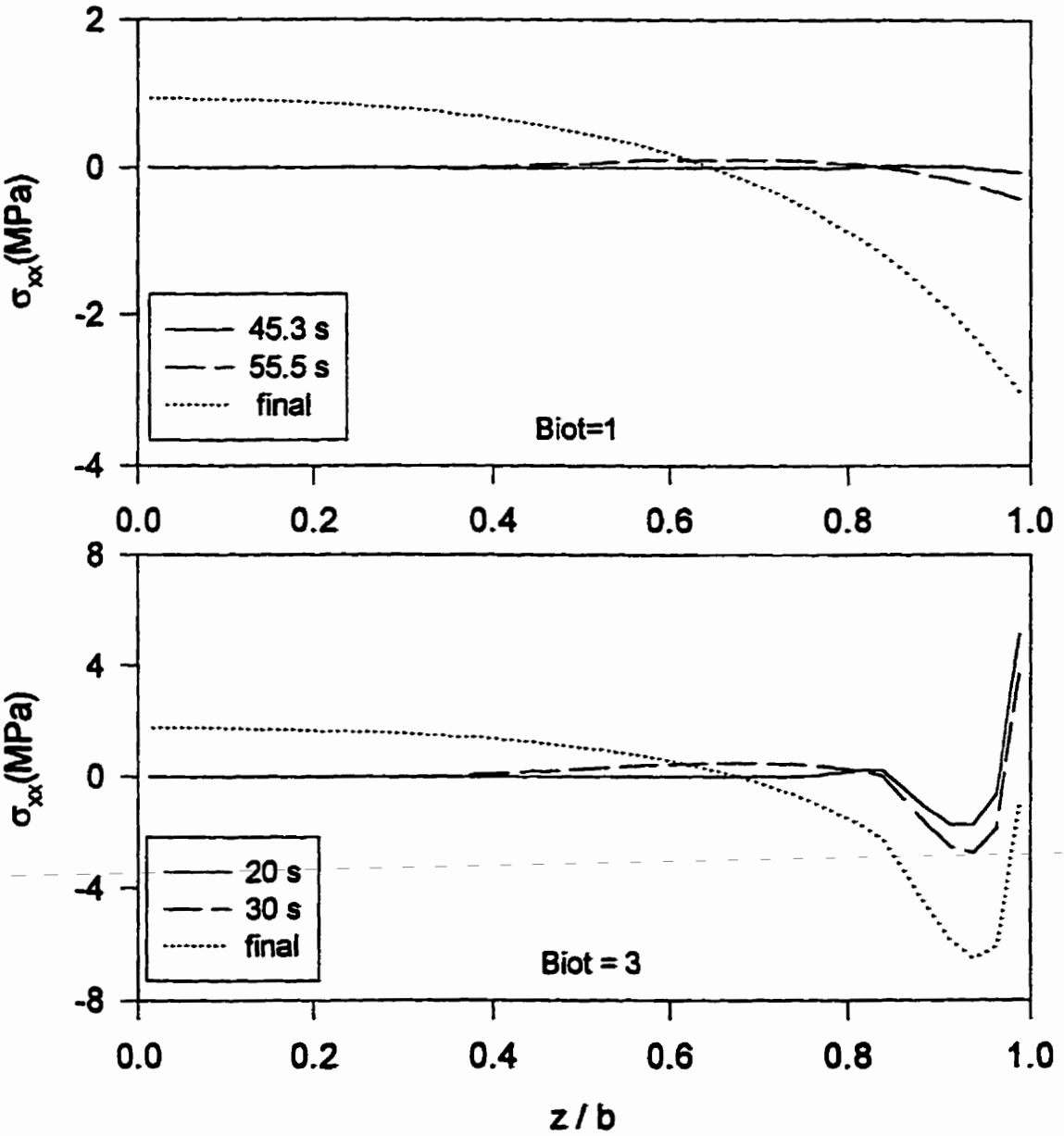

Fig.4.13.Evolution of the xx-component of stress for PS using 2-D FMS model (run 1, Biot=1, 3)

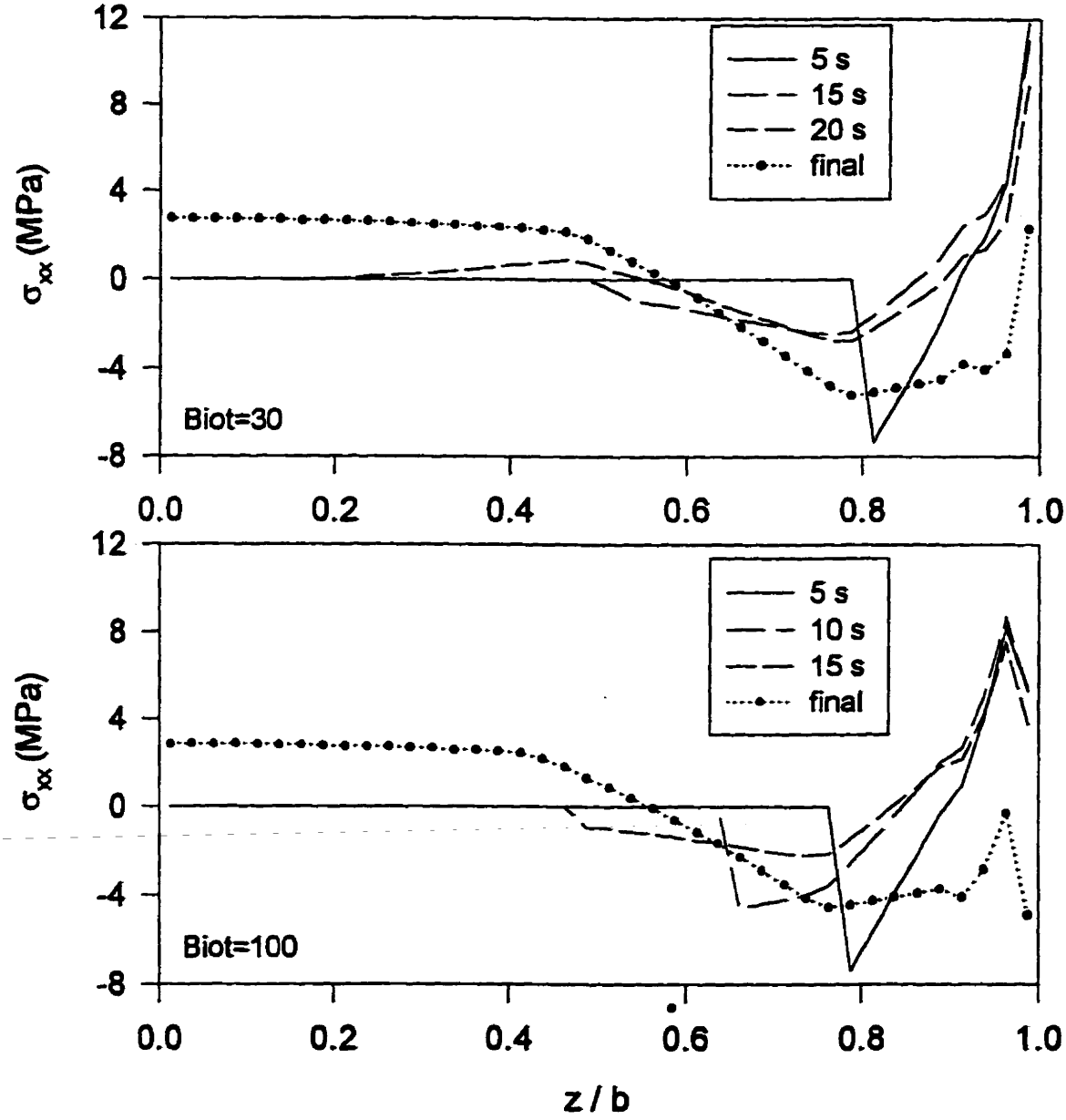

Fig.4.14.Evolution of xx-component of stress for PS using 2-D FMS model (run1, Biot=30, 100)

the gate for run 1 (Fig.4.5) was used to obtain these results. In an actual process, the pressure history does not remain constant when the Biot number, cooling rate, and other studied parameters change. This assumption is used here to better understand the effect of different parameters separately.

Fig.4.15 shows the evolution of the surface stress for different Biot numbers. For smaller Biot numbers (1 and 3), there is an induction time for the surface stress to become non-zero (solidification of the surface). Except for Biot = 1 where the surface stress decays to a final negative value, for other cases the surface stress first increases to a maximum and then decreases. Its final value depends on the Biot number: it is slightly negative for Biot=3, positive for 30, and negative for 100, as illustrated in the bottom graph. These peculiar differences in the residual stress profiles may be understood by considering the solidification pressure profiles, as in Fig.4.16. The solidification pressure $P_s(z)$ is the pressure in the melt at the time the layer z solidified. This pressure is important since the stretching force of the melt pressure on the newly formed solid layer counteracts its shrinkage (see equations (2.88) and (2.89)). In the CMS (52) it is assumed that this force prevents the shrinkage in the mold completely. Fig.4.16 shows that the solidification pressure is zero everywhere for Biot=1. Therefore, the calculated stress profile is identical to the free quenching case (see Fig.4.17,top). The reason for the zero solidification pressure is that, in this case, cooling is so slow that it takes a long time for the surface to solidify (≈55 s). As shown in Fig.4.5, the pressure reaches zero 17 s after the cycle starts. This situation is clearly not realistic since the sample would be molten when ejected from the mold. For Biot=3, P_s is large at the surface and decreases to zero at z/b=0.83. It may be seen in Fig.4.17 (bottom) that the stress profile is identical to free quenching for $0<z/b<0.83$. This corresponds to the layers with $P_s=0$ (Fig.4.16).

Fig. 4.18 compares the final FQ and injection molding stress profiles for Biot=30 and 100. The profiles are also identical in the core.

In Fig.4.19, the measured stresses for PS in run 1 are compared to the predicted values from three different models: the CMS and 1-D FMS models developed by Titomanlio et al. (51, 52), and the 2-D FMS model . All these models take the effect of pressure into account. The stresses, here and throughout this thesis, correspond to the xx-

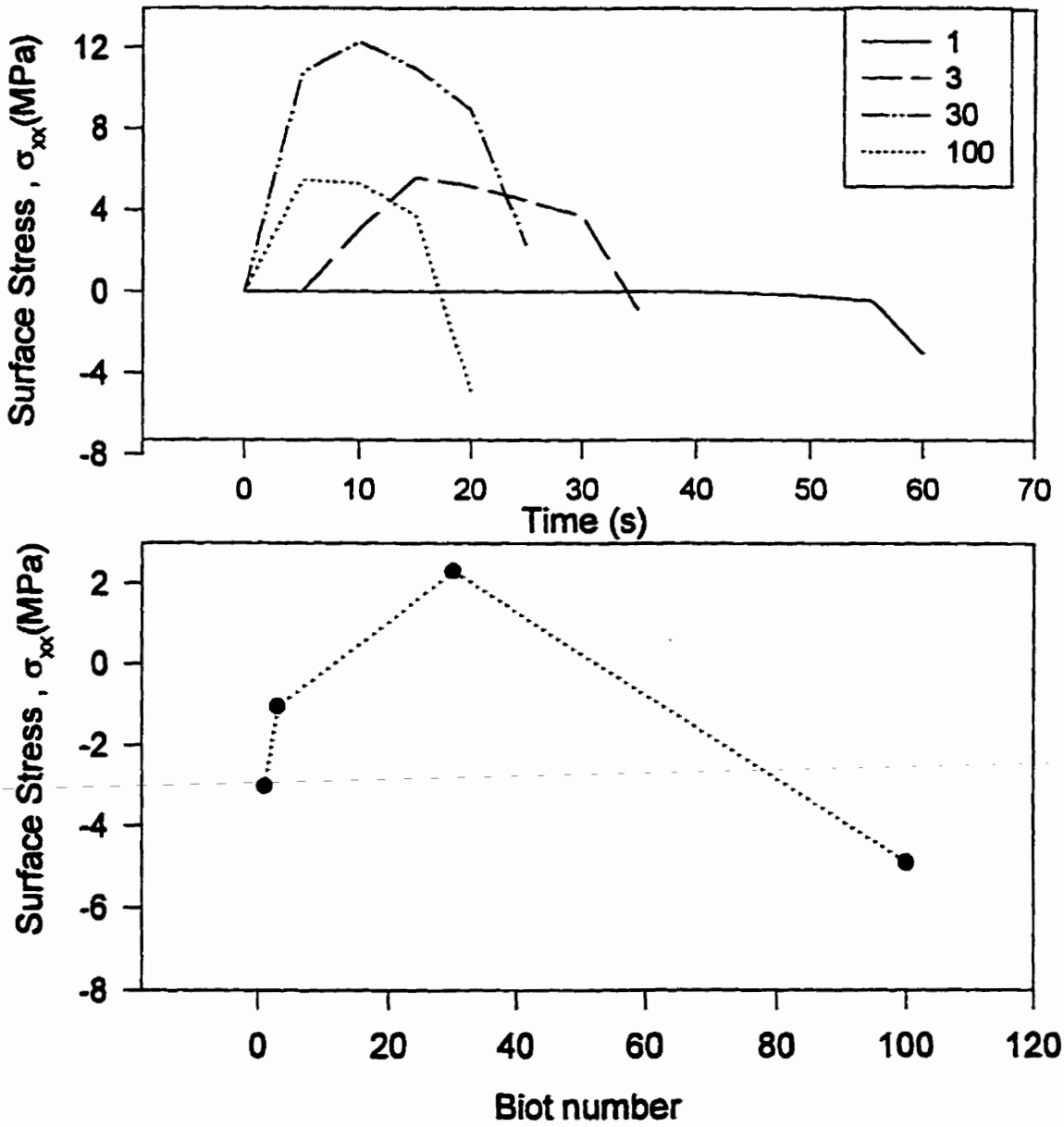

Fig.4.15.Surface stress for PS using 2-D FMS model and different Biot numbers (run1)

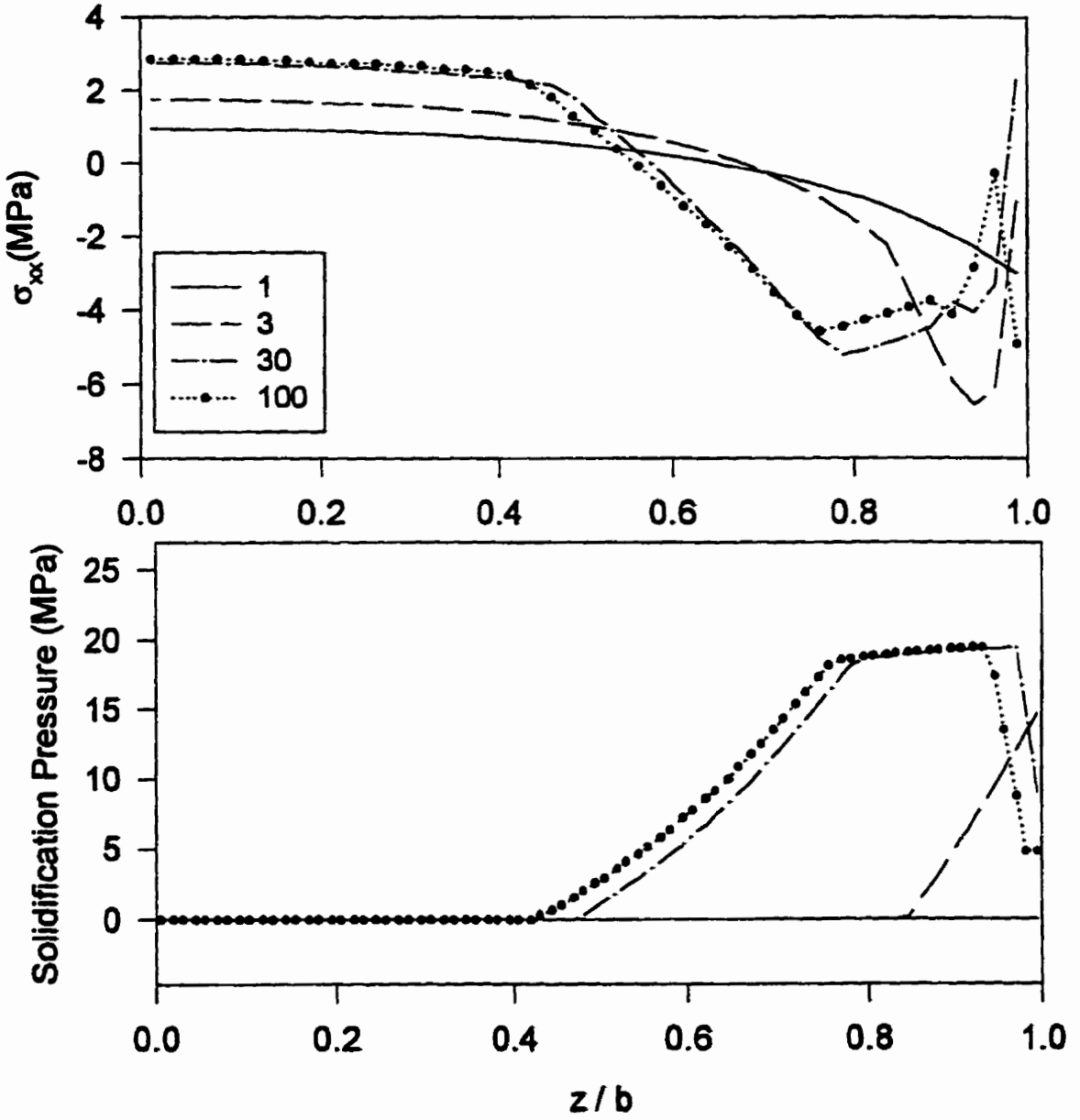

Fig.4.16.Final stress and solidification pressure profiles using 2-D FMS and different Biot (run1, PS)

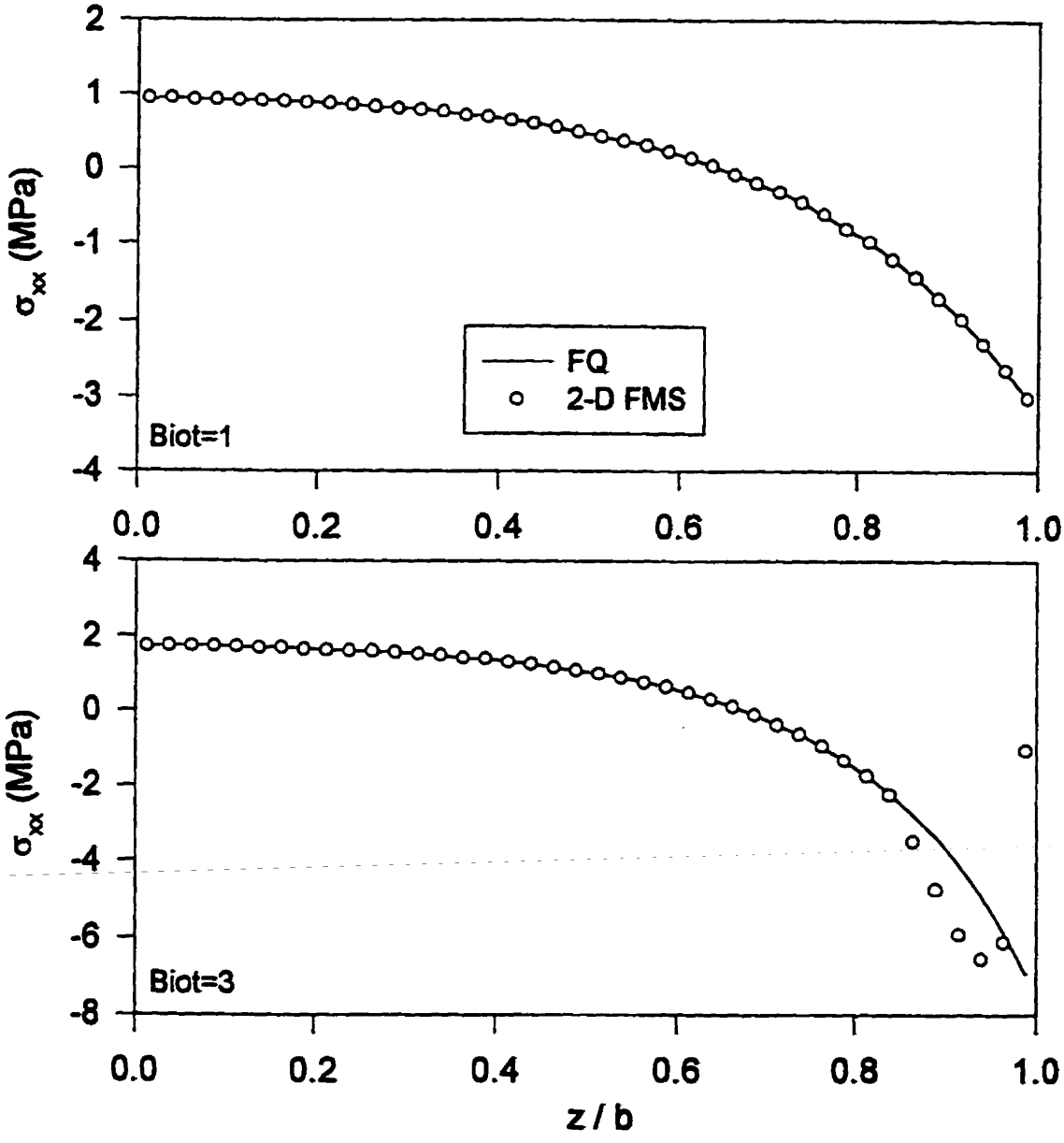

Fig.4.17.Effect of including pressure in the stress calculations using 2-D FMS model (run1, PS)

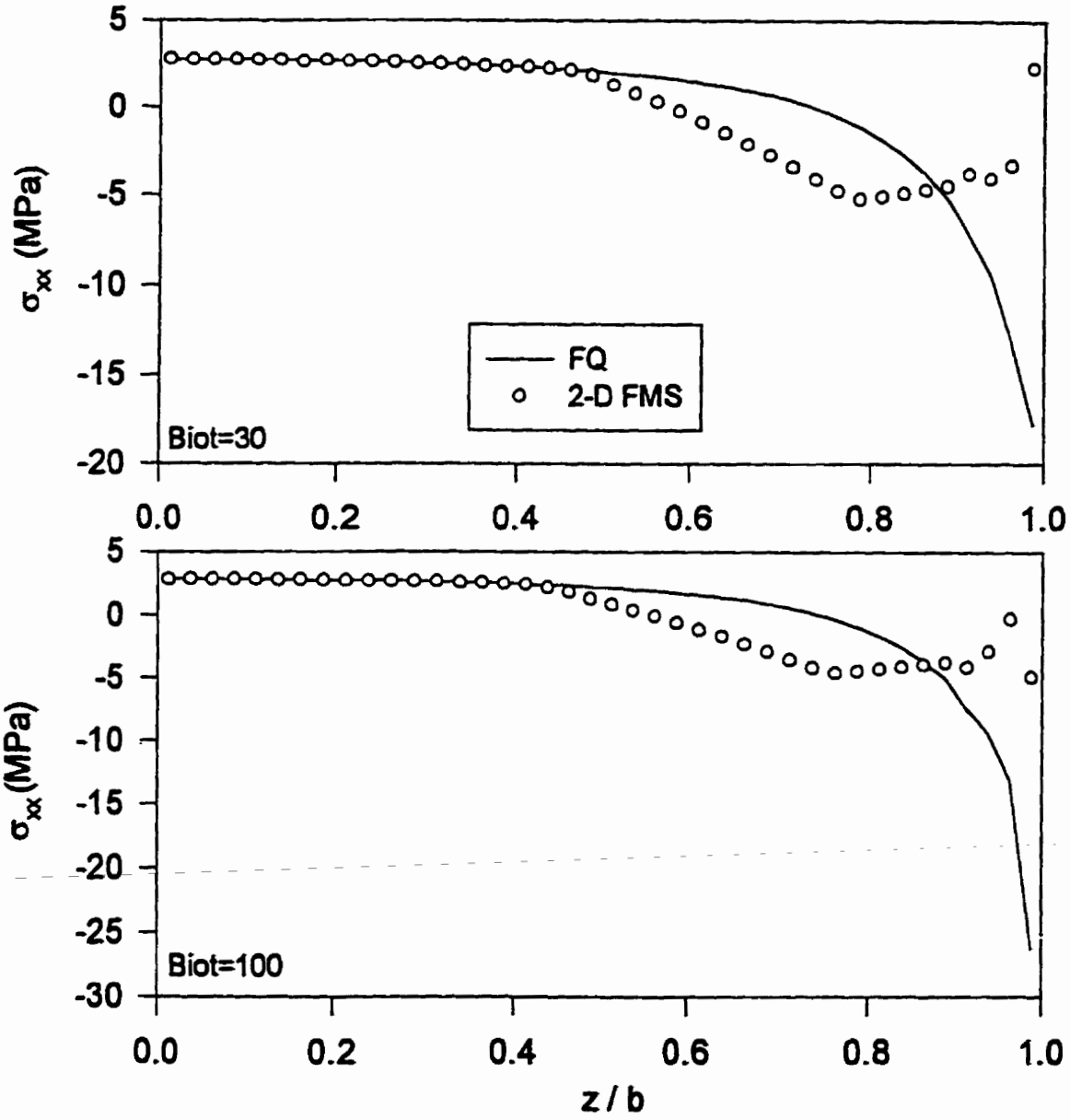

Fig.4.18.Effect of including pressure in the stress calculations using 2-D FMS model (run1, PS)

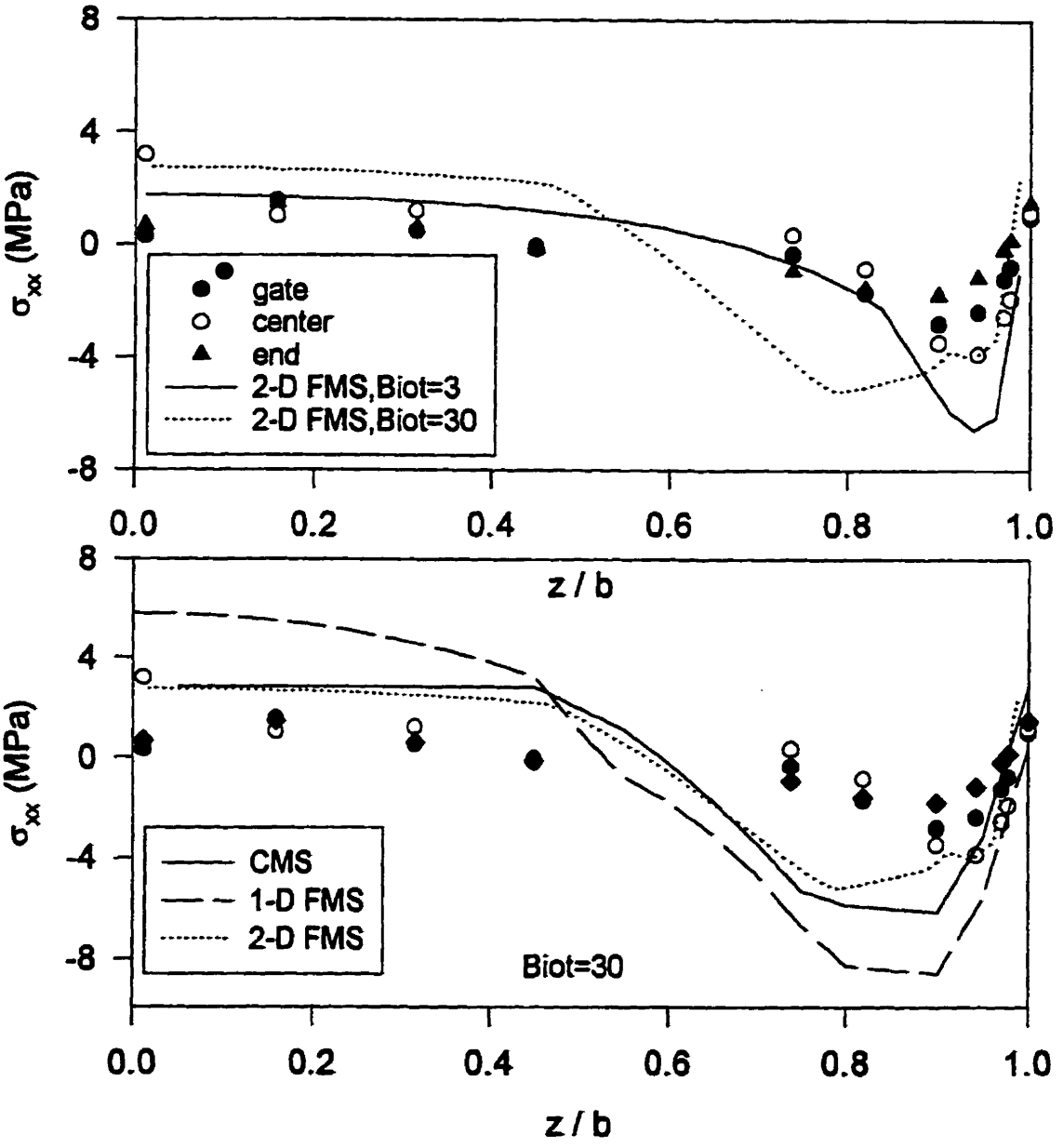

Fig.4.19.Residual stress profiles measured and calculated using different models (run 1 , PS)

component of the stress tensor, unless otherwise specified. All three models capture the surface tensile region but overpredict the maximum compressive stress. For Biot=30, all the predicted zero-stress locations are closer to the mid-plane than the experimental data. The results of the 2-D FMS model with Biot=3 seem closer to the experiments in this case, although the maximum compression is still overpredicted. Compared to other model-experiment evaluations (4, 62) and despite all the simplifications, the performance of the 2-D FMS model is good. The predictions suggest that this model might include the important parameters involved in the generation of thermal stresses.

In the following sections, the effect of various parameters on the residual stresses is investigated experimentally and theoretically.

4.1.1.1. Effect of Melt Temperature

Fig.4.20 shows the measured residual stress distributions at three locations along the flow in PS samples, injection molded with two initial melt temperatures of 230°C and 250°C. The three stress regions are observed for both cases. The surface stress is larger for T_m=250°C near the gate and in the center of cavity. It is smaller at the end location. Variation of T_m does not seem to have a significant effect in the mid-plane. The zero-stress point moves towards the core as T_m is increased. The magnitude of the compressive stress near the gate and near the end of the cavity increases when T_m is raised. In the center, this effect is reversed.

The corresponding recorded nozzle and gate pressure histories are presented in Fig.4.21(top). In order to better understand the results, the experimental gate pressure profiles were used with the 2-D FMS model to calculate the solidification pressure and the residual stress profiles in these two cases. These profiles are shown in Fig.4.21 (bottom) and Fig.4.22, respectively. As illustrated by Fig.4.21, the nozzle pressure was about 1.5 MPa higher for the high melting point case. The maximum gate pressure for this case is higher by 3 MPa. The measured and calculated stresses at the gate for these two runs are compared in Fig..4.22. The run at the higher melt temperature (250°C) leads to larger calculated tensile surface stress, lower maximum compressive stress, and lower midplane tensile stress.

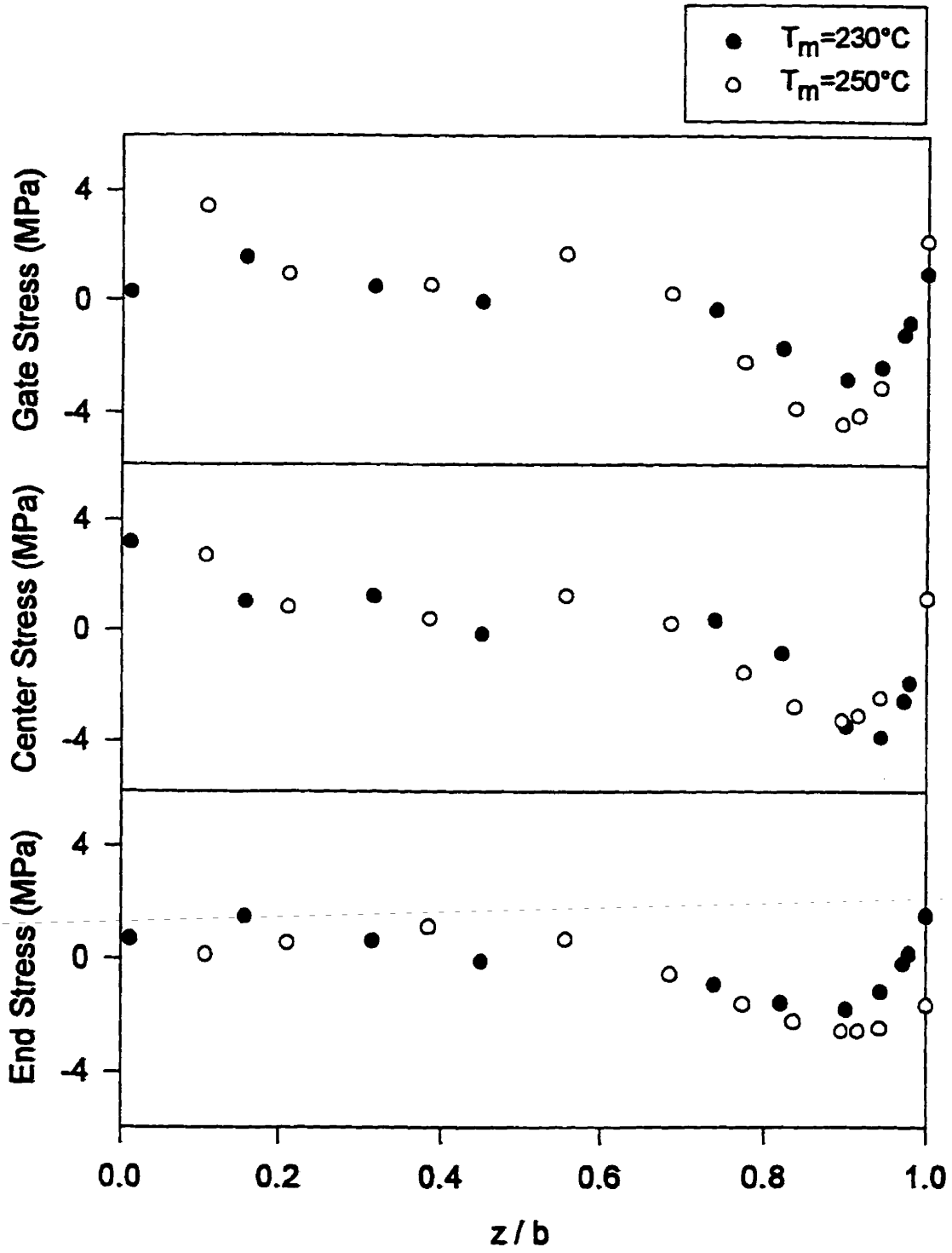

Fig.4.20.Residual stress profile for 3 locations along the flow and 2 initial melt temperatures (run1,3, PS)

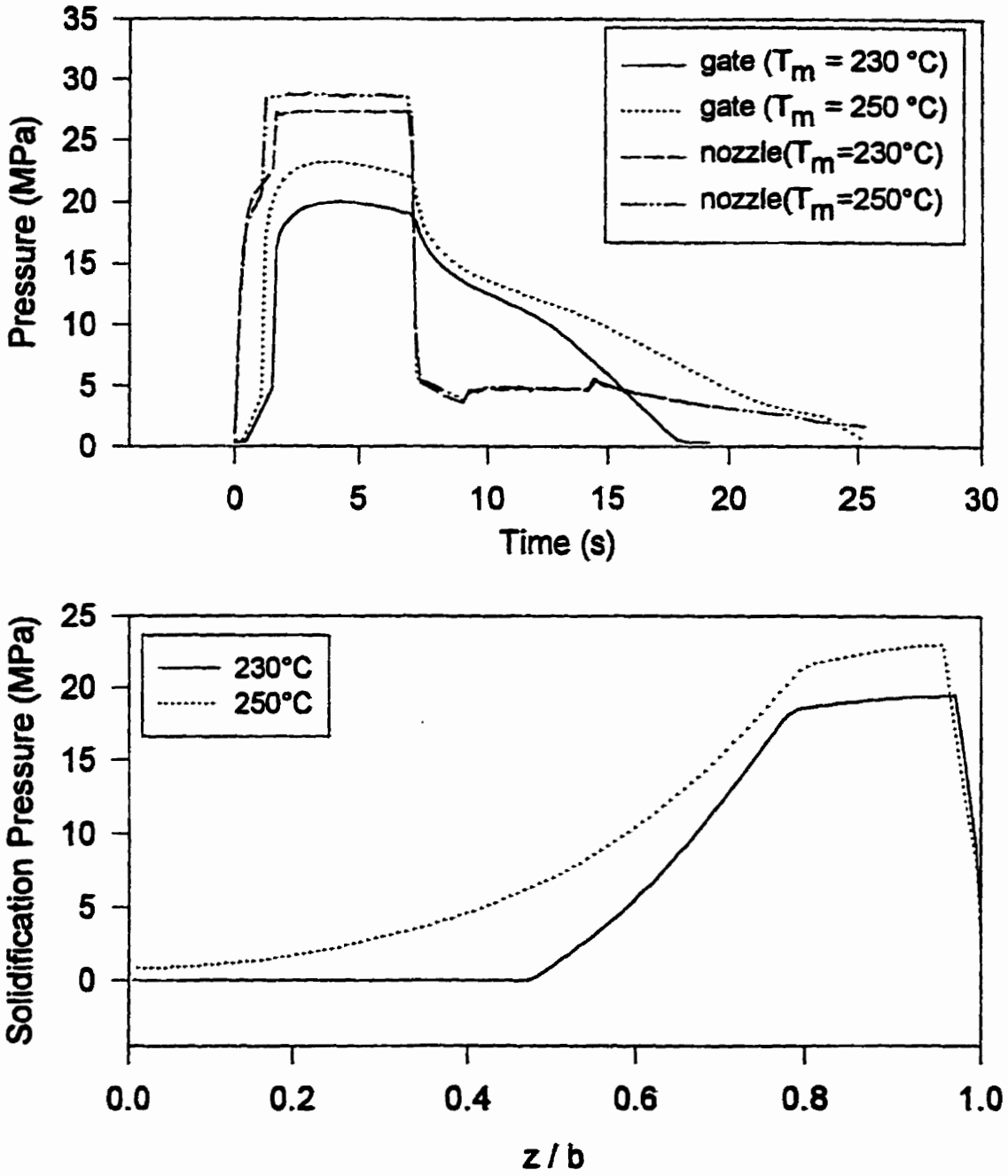

Fig.4.21.Measured pressure histories (top) and calculated solidification pressures (bottom) using 2-D FMS, for 2 melt temperatures (runs1,3,PS)

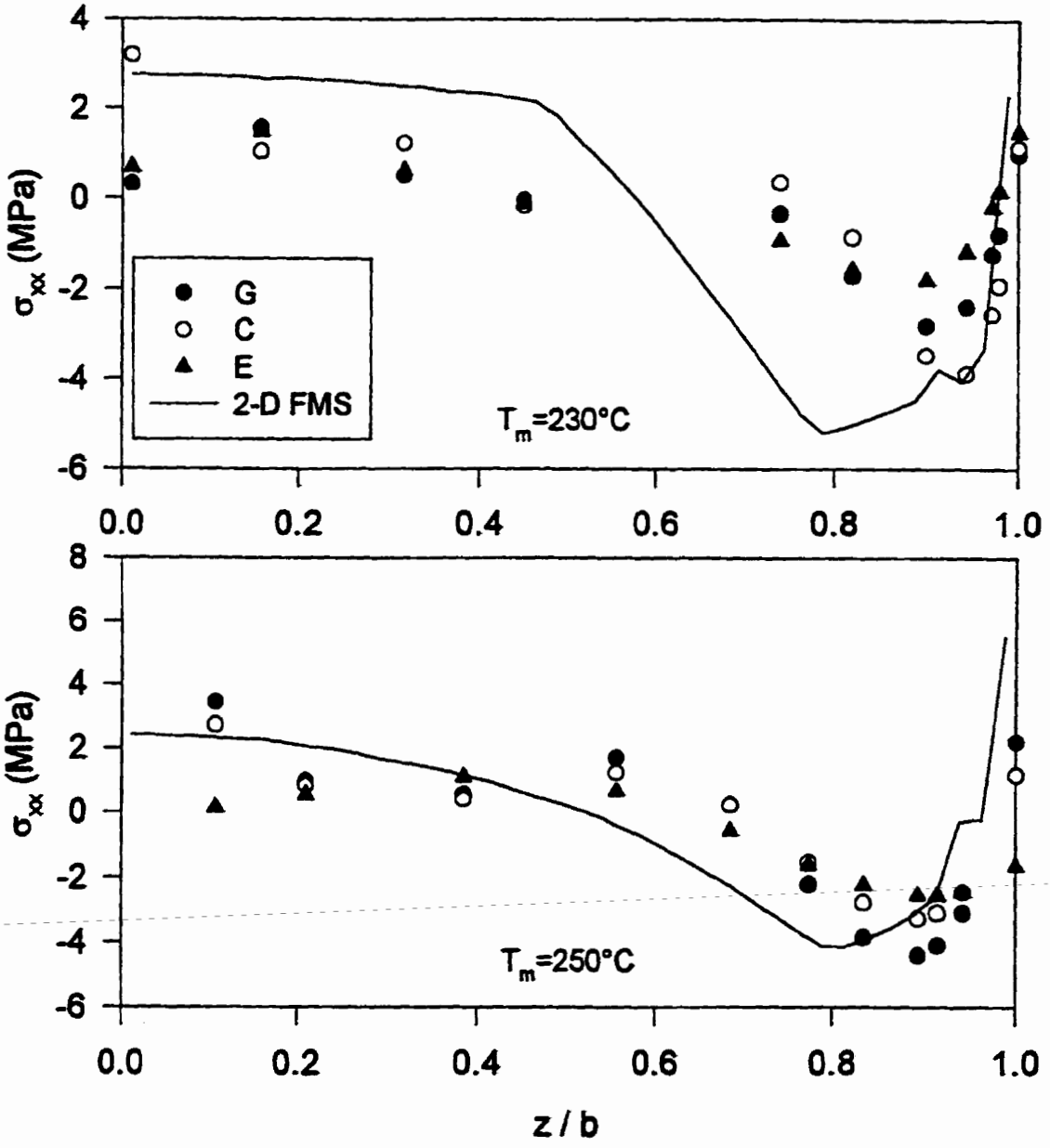

Fig.4.22. Residual stress profiles measured and calculated using 2-D FMS model for 2 melt temperatures (runs 1, 3, PS)

As mentioned above, in the experimental results, near the gate and in the center of the cavity, the larger melt temperature leads to a larger surface stress as predicted. The situation is reversed for the end location, as shown in Fig.4.20. It must be noted that, according to the calculation, the FQ stresses are independent of T_m. This is consistent with Struik's results (15). The compressive region in the center location is consistent with the model predictions. It must be noted that the melt temperatures are close to each other, and the differences in the stresses are small compared to the experimental errors (the errors associated with the stress measurements are evaluated in the polyethylene section).

In order to isolate the effect of the melt temperature on the residual stresses, the pressure history was kept constant and the residual stress profiles were calculated for three different melt temperatures, as presented in Fig.4.23. A high melt temperature leads to a higher cooling rate, thus the maximum solidification pressure extends over a smaller region as may be seen in Fig.4.23, top. The residual tensile surface stress decreases and the maximum compressive stress increases with T_m.

4.1.1.2. Effect of Holding Time

As illustrated by Fig.4.24, the surface stresses are affected substantially by the holding time (h.t.). At all three locations, a short holding time causes the surface stress to fall to a negative value and the stress profile to approach the free quenching curve. This effect seems to be weaker in the center. The runs with larger holding times (h.t.=5 s. and 8.5 s.) show small tensile stresses on the surface. However, contrary to what was expected, the surface stress is slightly lower for h.t.=5 s., near the gate and near the end of cavity. This may be associated with experimental errors, considering the scatter obtained in the curvature data for these two runs.

The actual pressure histories for different holding times are presented in Fig.4.25 (top). During packing, a high pressure is applied to the polymer melt through the nozzle. As more layers on the surface solidify, the pressure measured at the wall near the gate starts decaying slowly. This is due to the fact that the solid shell becomes thicker and the melt pressure is transferred less efficiently to the pressure transducer on the mold wall. At the end of holding, the nozzle pressure is set to zero, and the gate pressure first drops

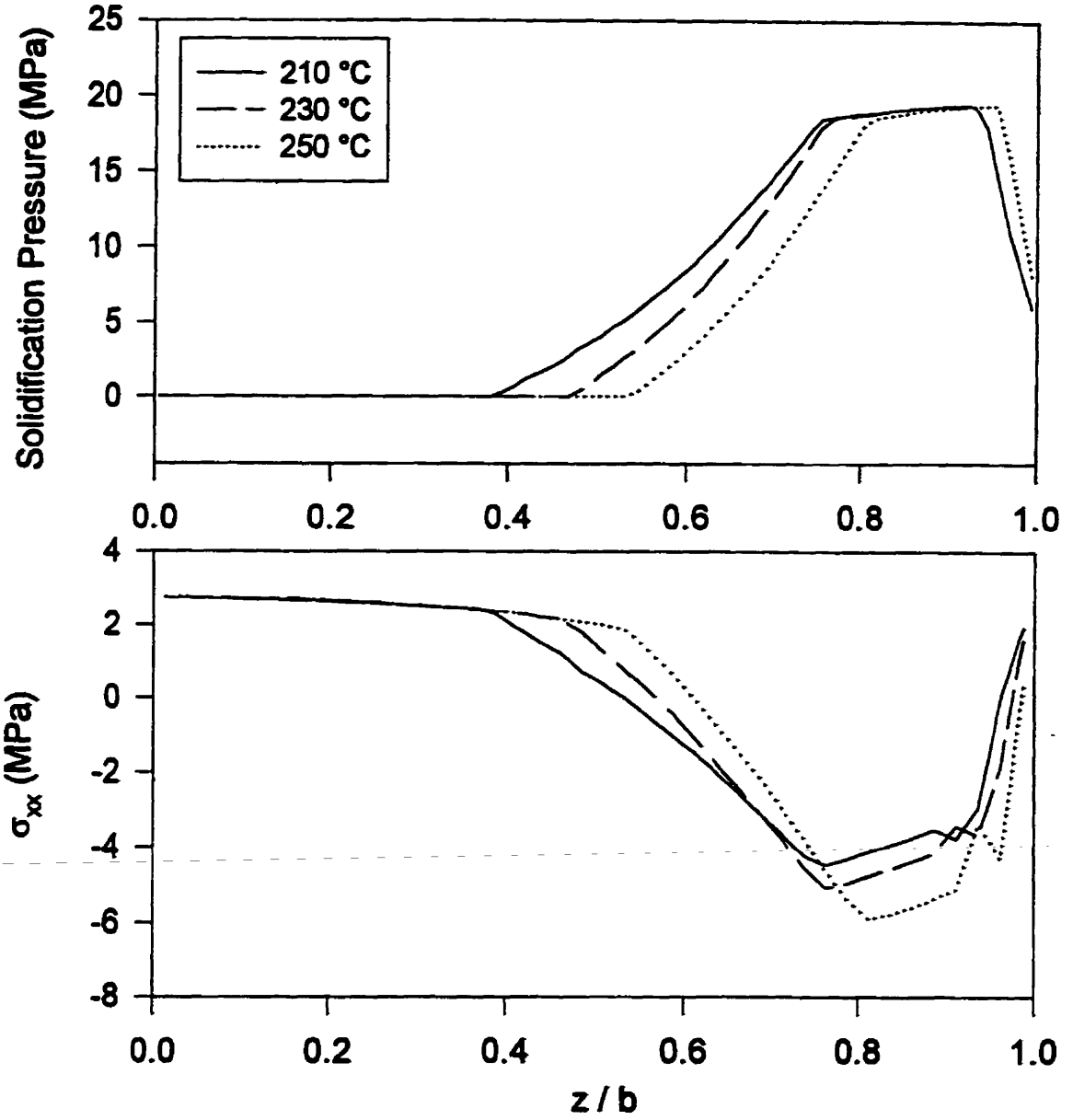

Fig.4.23.Solidification pressure and residual stress profiles for 3 melt temperatures calculated using 2-D FMS (PS, other conditions: run 1, Biot=30)

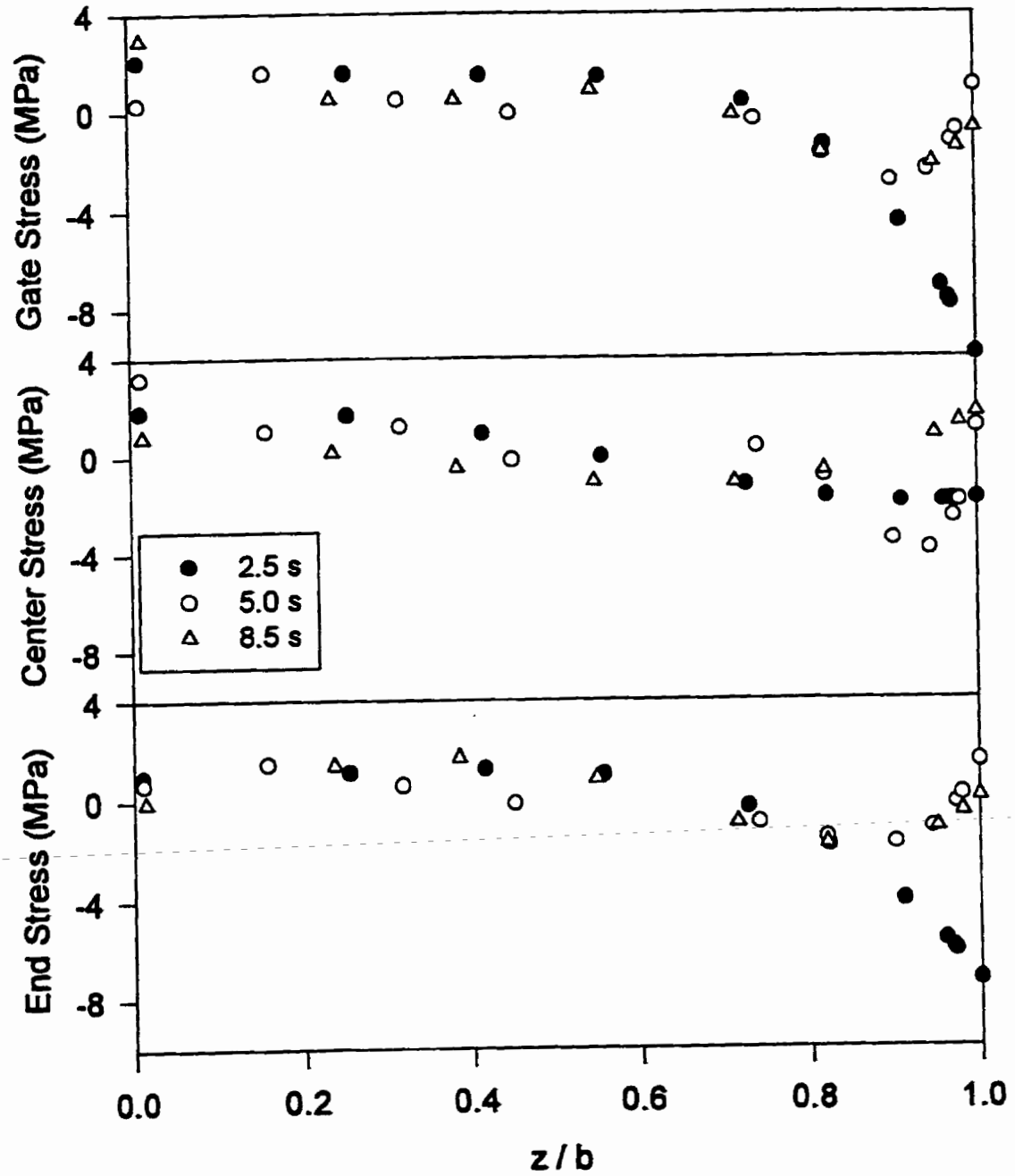

Fig.4.24.Residual stress profiles for 3 locations along the flow and 3 holding times (runs 6,1,7, PS)

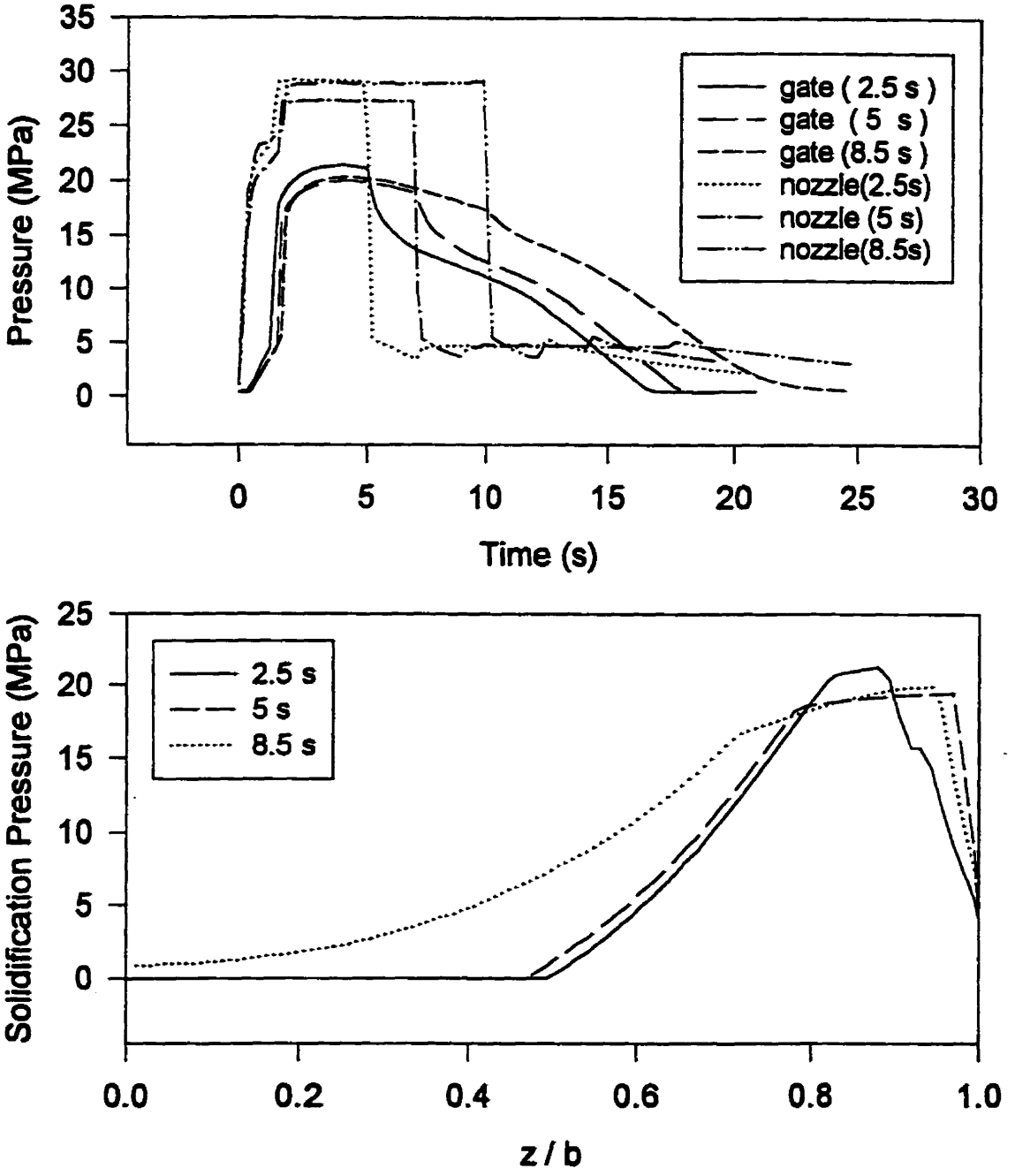

Fig.4.25.Measured pressure histories (top) and calculated solidification pressures (bottom) using 2-D FMS, for 3 holding times (runs 6,1,7, PS)

quickly then decays slowly as cooling continues. The quick drop after holding is due to the flow of some material out of the cavity once there is no more resistance to it. This back-flow is smaller for larger holding times, since more material has solidified. The maximum packing pressure near the gate for h.t.=2.5 s. is slightly higher than in the other runs.

The solidification pressure profiles near the gate are presented in Fig.4.25 (bottom). In Fig.4.26, the final stress profiles calculated by the 2-D FMS model are compared with the measured stresses for different holding times. The predictions agree well with experiments except for h.t.=2.5 s.

In Fig.4.27, the residual stresses are calculated for conditions corresponding to run 1 and for different holding times. As expected, the tensile stress on the surface increases with holding time and the compressive region becomes wider. All three stress curves join the tensile free quenching stress in the core that is identical for them.

4.1.1.3. Effect of Mold Thickness

The measured residual stress distributions for 2 different mold thicknesses are presented in Fig.4.28. In the thinner mold (1.5 mm), the temperature gradient over the thickness and, thus, the free quenching stress are higher. Consequently, a large compressive stress is added to the surface stress. The magnitude of this compressive stress is the largest near the gate and the smallest in center. The corresponding measured pressure histories and the calculated solidification pressure profiles are shown in Fig.4.29. In the case of the thin mold, the pressure near the gate starts decaying soon after it reaches the maximum packing. This is due to the rapid solidification (freezing) of the gate. The pressure eventually reaches a constant value of $\approx$ 12 MPa until ejection from the mold at which point it drops to zero. The rapid solidification of the material may be observed from Fig.4.29 (bottom). According to the calculations, the core solidifies under a high pressure corresponding to the peak of the packing pressure.

The residual stress profiles presented in Fig.4.30 are calculated using the 2-D FMS model and the corresponding recorded pressure histories (Fig.4.29). The calculated residual stress in the thin mold exhibits a negative surface stress and a small compressive

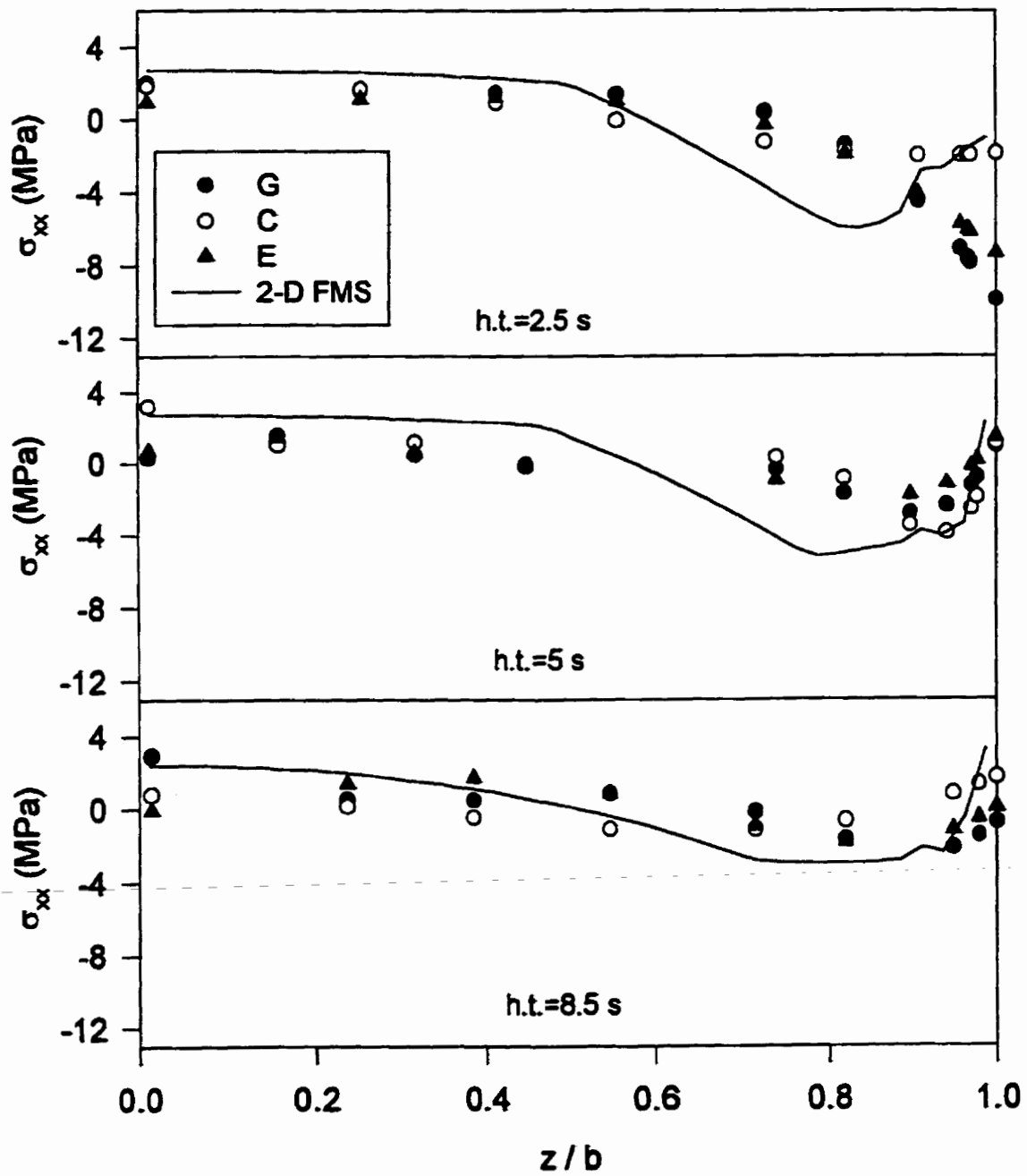

Fig.4.26. Residual stress profiles measured and calculated using 2-D FMS model for 3 holding times (runs 6, 1,7, PS)

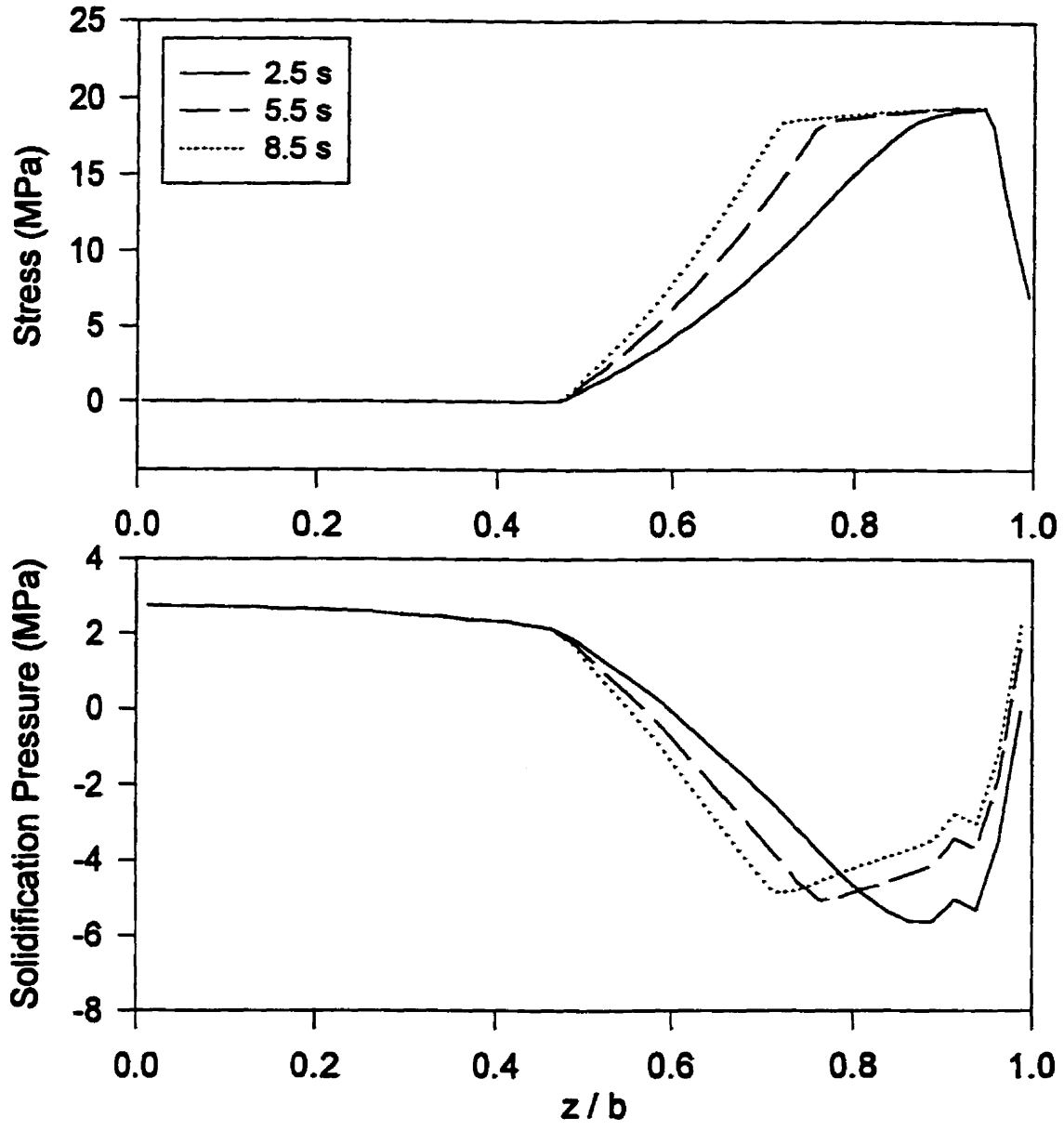

Fig.4.27.Solidification pressure and residual stress profiles for 3 holding times calculated using 2-D FMS (PS, other conditions: run 1)

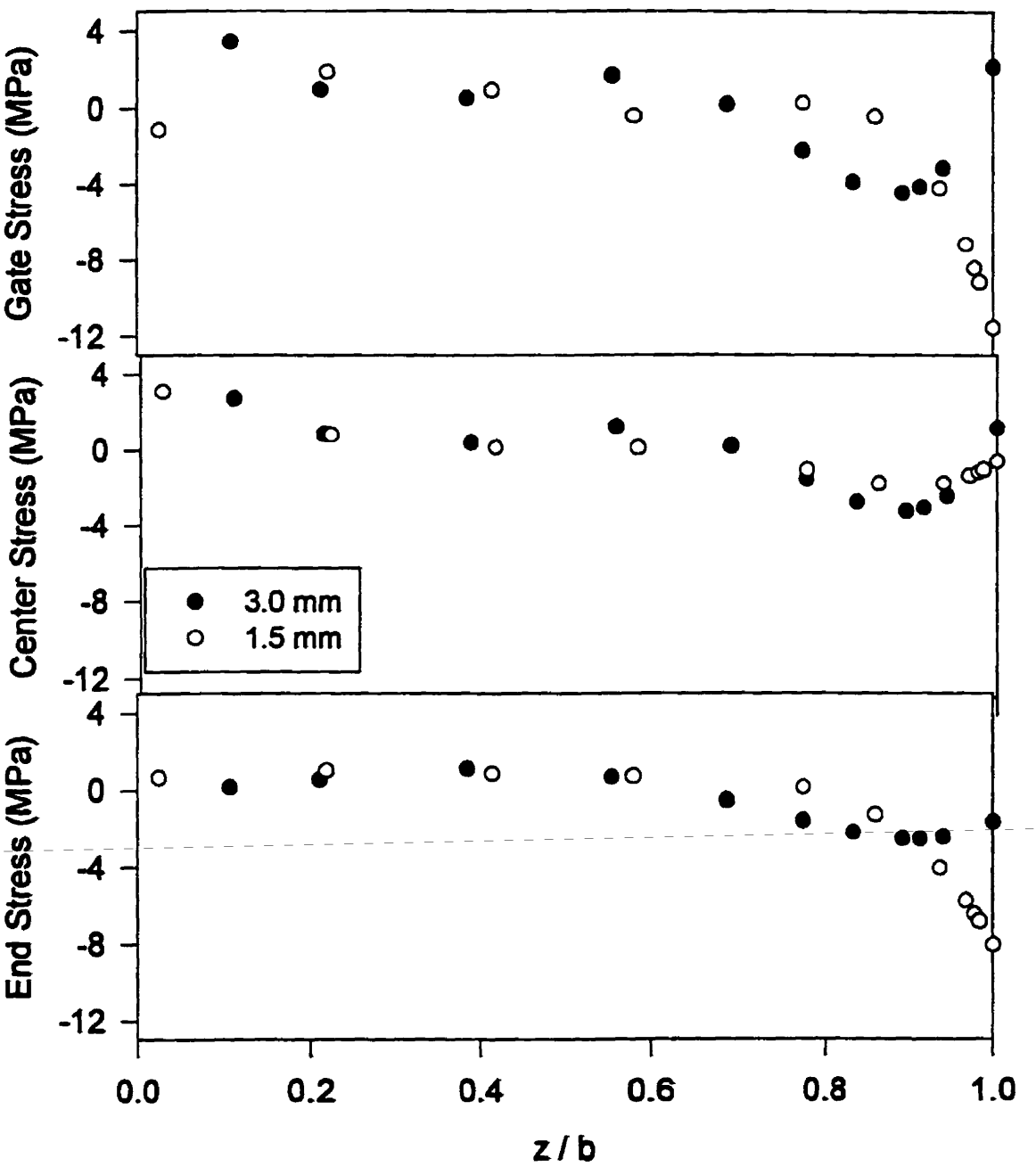

Fig.4.28.Residual stress profiles for 3 locations along the flow and 2 mold thicknesses(runs 3,8,PS)

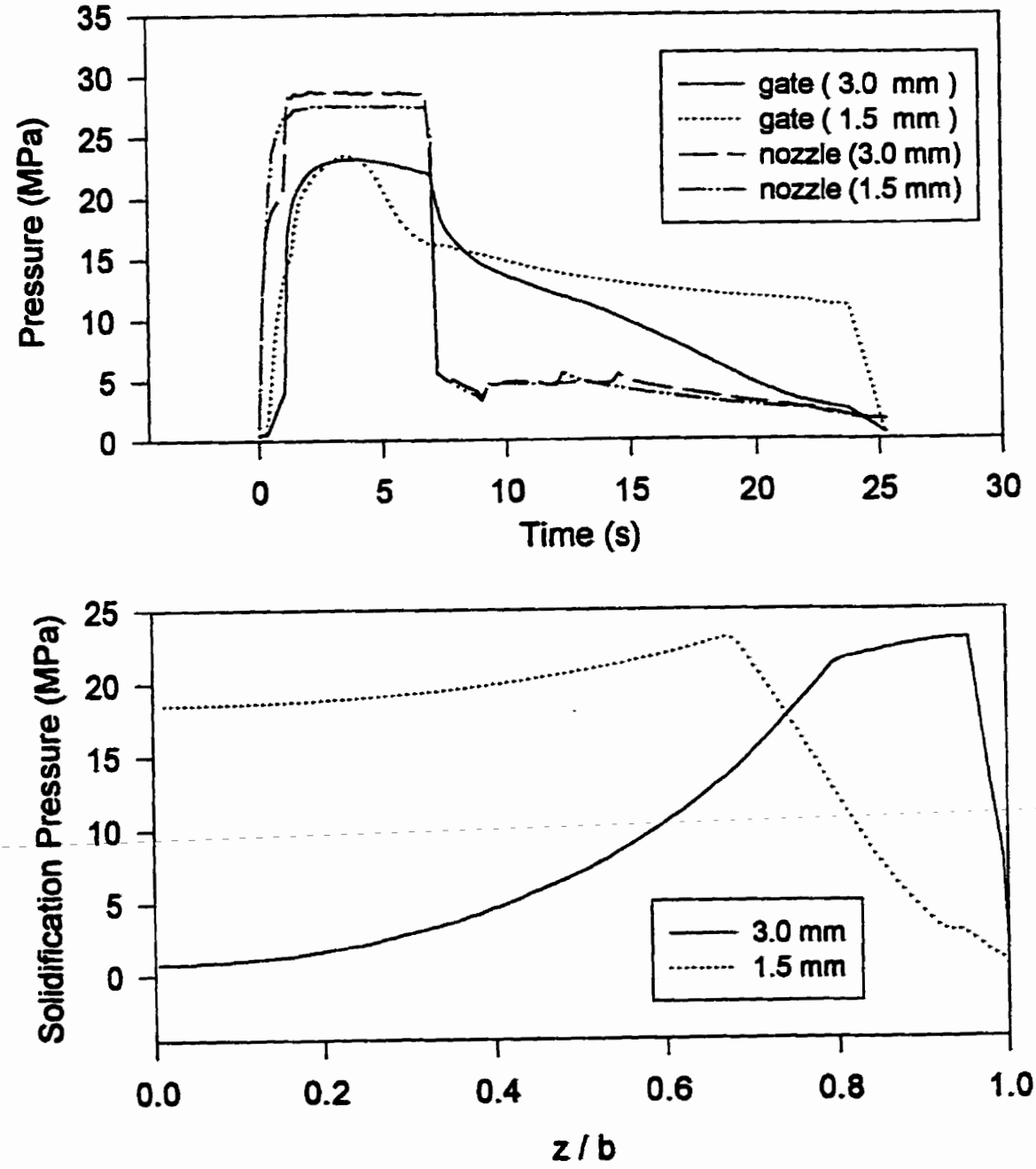

Fig.4.29.Measured pressure histories (top) and calculated solidification pressures (bottom) using 2-D FMS, for 2 mold thicknesses (runs 3,8, PS)

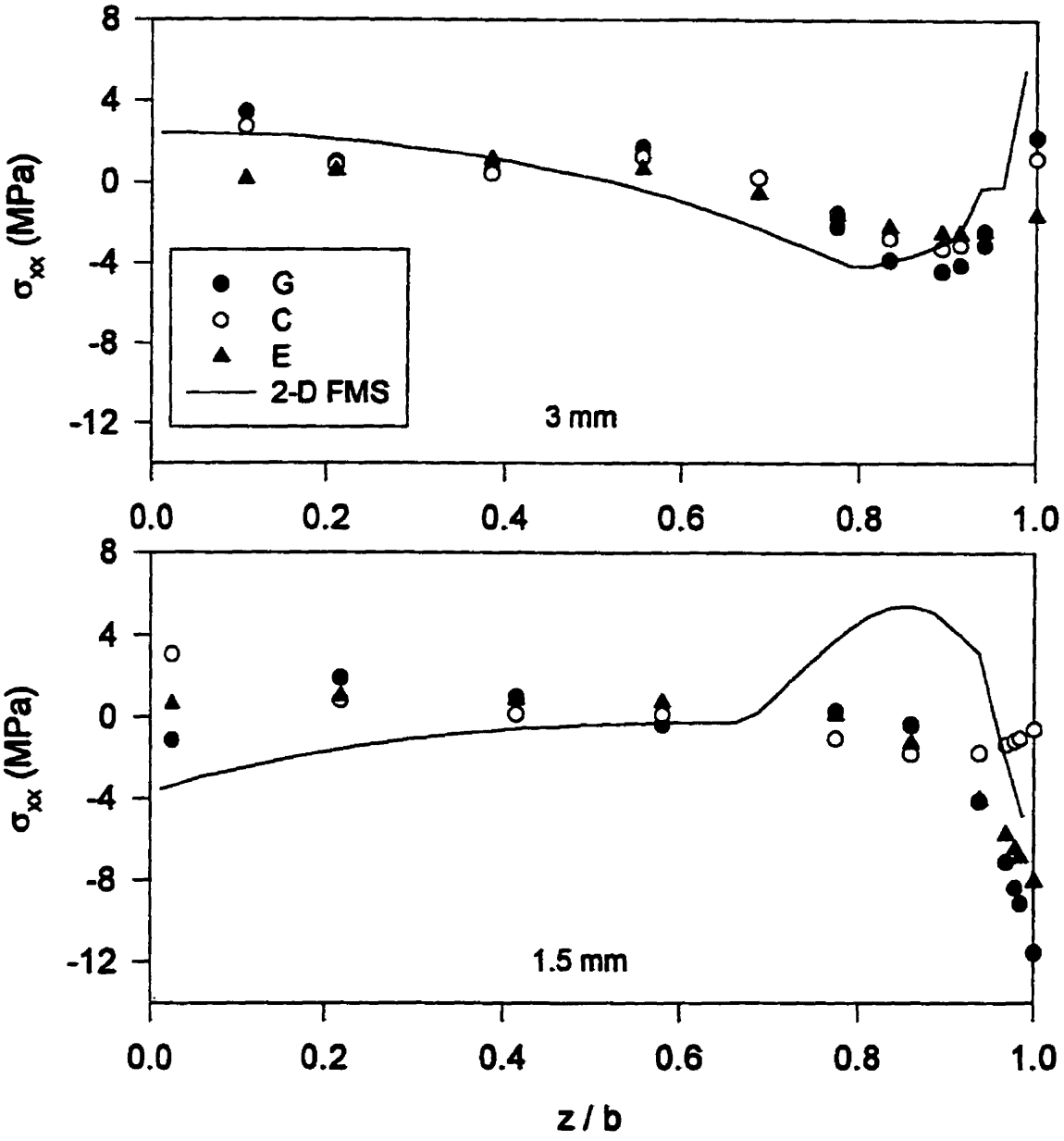

Fig.4.30.Residual stress profiles measured and calculated using 2-D FMS model for 2 mold thicknesses (runs 3,8, PS)

midplane stress similar to the experimental observation. It shows, however, a maximum in between, that is not depicted in the measurements. Fig.4.31 illustrates the effect of the mold thickness on the calculated stresses when everything else is kept constant. A definite conclusion about the effect of this parameter cannot be drawn from the trend. The issue will be clarified in the discussion section. In a real situation, the pressure history at the gate is not independent of the solidification of the material.

4.1.1.4. Effect of Packing Pressure

To study the influence of the packing pressure, the stress profiles calculated from the 2-D FMS model using 3 different packing pressures, are compared in Fig.4.32. Appropriate experimental runs to isolate this effect were not available. Increasing the magnitude of the packing pressure from 10 MPa to 40 MPa causes the surface stress to vary gradually from compressive (-9MPa) to tensile (+20MPa). An intermediate compressive region is formed and the maximum compressive stress grows for higher packing. The tensile stress at the core is not affected by the packing pressure since, as shown in Fig.4.32 (top), P_s is zero in this region for all cases.

4.1.2. Polyethylene (HDPE)

In this section, the generation of stresses is investigated in a semi-crystalline polymer: high density polyethylene (HDPE). The residual stress profile was measured in injection molded HDPE samples using the layer removal technique, as described previously. Several injection molding runs were performed, varying one parameter at a time, to the extent possible (Table 3.11). Fig.4.33 illustrates the variation of the nozzle and gate pressure with time for run 1. After the cavity is filled ($\approx$ 3 s.), a large packing pressure ($\approx$ 30 MPa) is applied at the nozzle. The pressure near the gate reaches 23 MPa, showing a pressure drop of 7 MPa with respect to the nozzle. Compared to the pressure histories measured in the runs with PS, the maximum packing region is significantly prolonged for HDPE.

In Fig.4.33, during packing, the gate pressure decreases slightly and increases again before dropping. This may be due to the competing effects of cooling and the

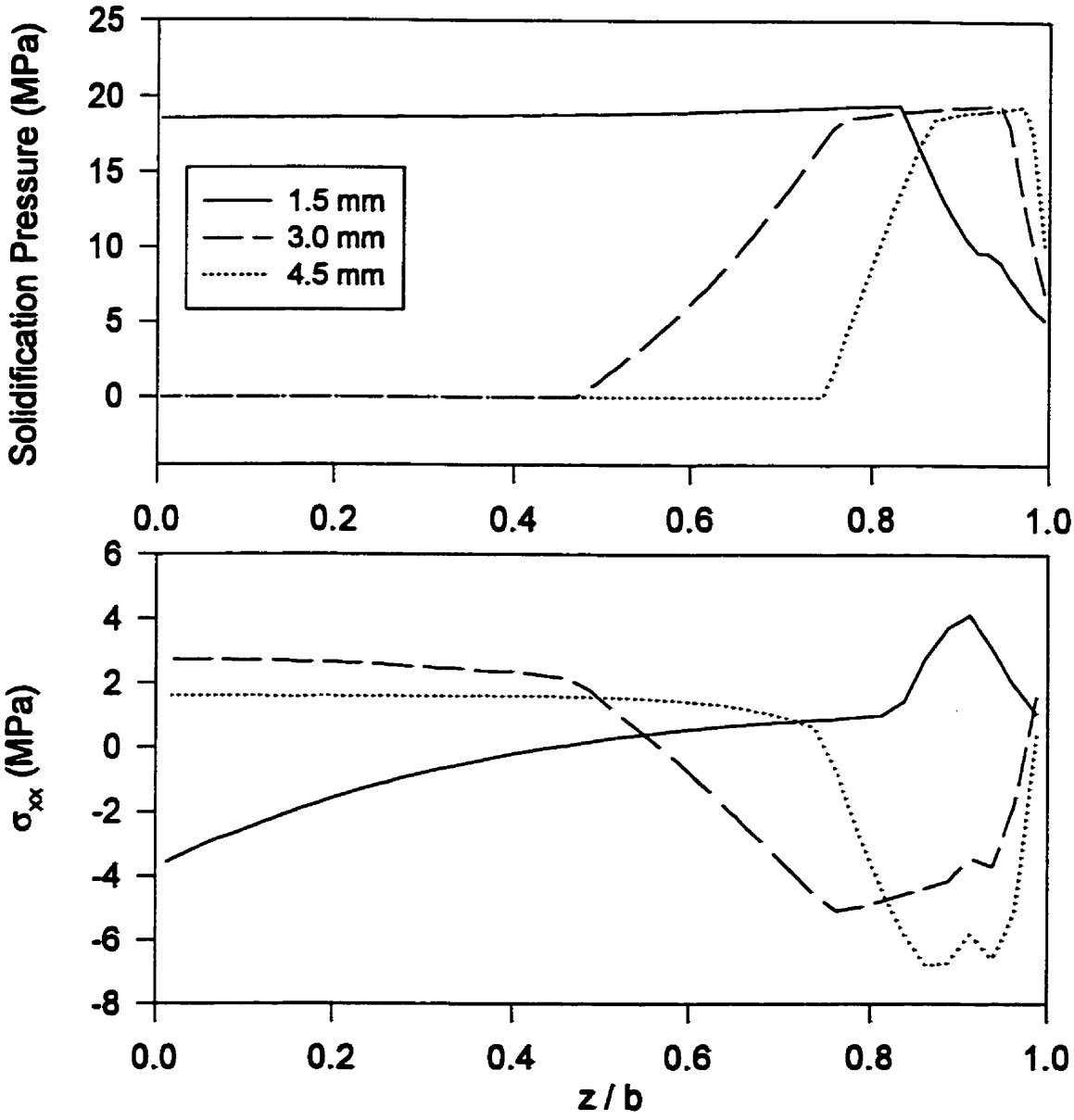

Fig.4.31.Solidification pressure and residual stress profiles for 3 mold thicknesses calculated using 2-D FMS model (PS, other conditions: run 1)

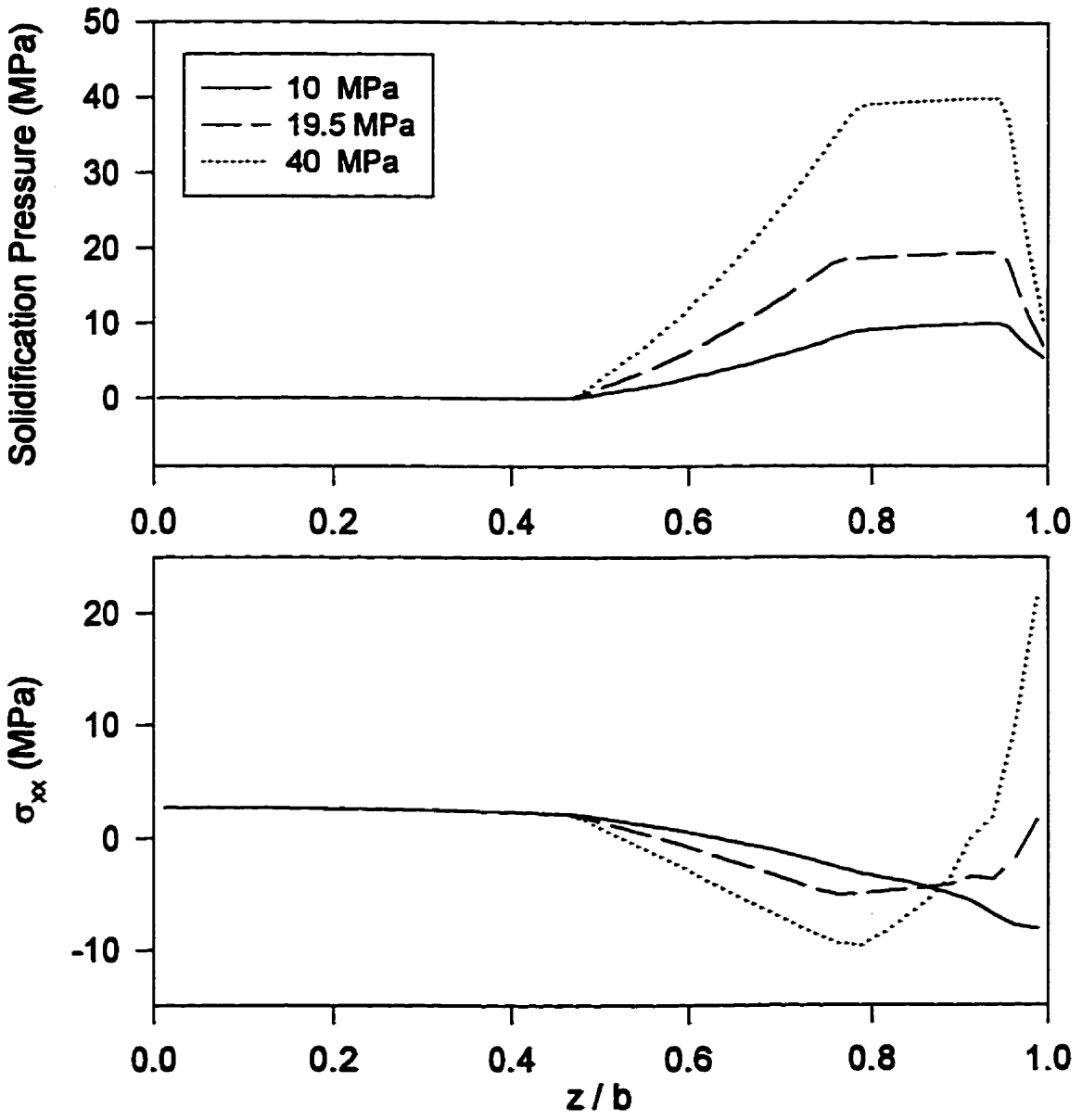

Fig.4.32. Solidification pressure and residual stress profiles for 3 packing pressures calculated using 2-D FMS model (PS, other conditions: run 1)

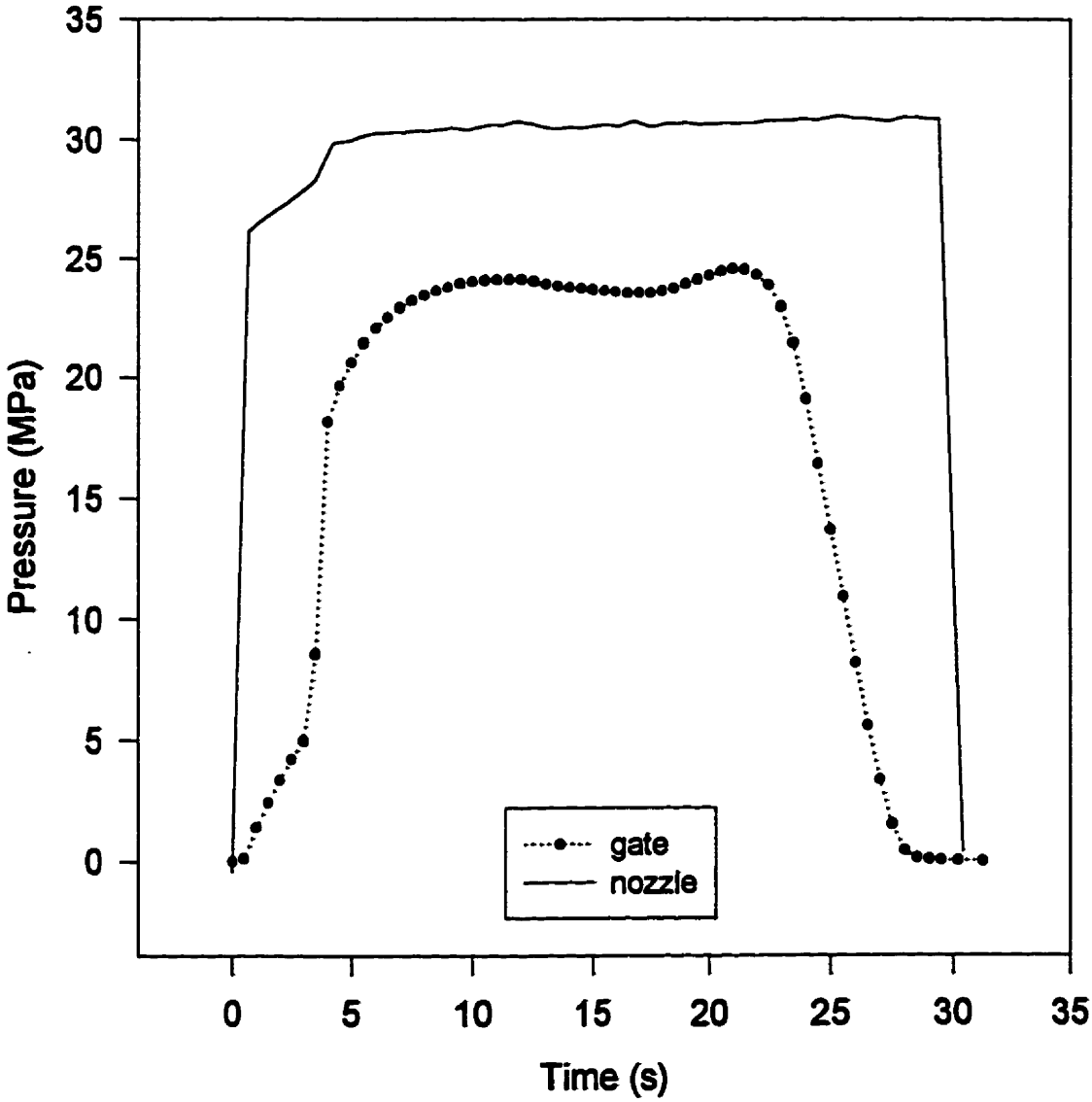

Fig.4.33.Measured gate and nozzle pressure histories for run 1 with HDPE

generated heat of crystallization. Furthermore, the gate pressure starts decaying before the nozzle pressure is removed (t ≈22 s.). This is the gate-freeze time, the time when the material in the gate completely solidifies. The melt pressure in the cavity is no more connected to the nozzle and starts decaying with temperature according to thermodynamic P-V-T relations. Note that this decay is faster in HDPE than PS. This is due to the PVT behavior of HDPE and to some extent, to its larger conductivity (≈5 times), as a result of crystallinity.

The next three figures (4.34 to 4.36) show the measured curvature and the residual stress distribution for run 1 at three different locations in the cavity. Fourth order regression was used for the curvature, and the stress profiles were calculated using equation (3.15) (7). The obtained stress profiles show large tensile stress on the surface and small compressive stress in the core of the sample. The stresses in the center (Fig.4.35) and near the end (Fig.4.36) of the cavity are very similar in this case. The surface stress is large and as the core is approached, the stress becomes compressive, goes up to nearly zero, and becomes compressive, consecutively. This fluctuation may be related to the oscillation in the maximum packing pressure, observed in Fig.4.33. The surface stress near the gate (Fig.4.34) is nearly half of its level at the other locations, and the fluctuation in the compressive zone is less pronounced.

The repeatability and the error involved in the stress measurements were evaluated by measuring the residual stresses in position 1 (Fig.3.2.a) for two samples injection molded with the conditions of run 2 (Table 3.11). The stress profiles for near the gate, in the center, and near the end of cavity are presented in Fig.4.37. All the profiles exhibit the two major regions, previously observed in run 1. The largest error is obtained on the surface, especially near the end of cavity (±3 MPa). Considering all possible sources of error in various measurement and calculation steps of the layer removal technique, the results are satisfactory. Due to a large gradient of stress on the surface, this location is more susceptible to error. It must be noted that, in order to decrease the errors, thinner layers were removed near the surface, and the data points were closer to each other in this region. The surface was also found to be especially sensitive to the regression order for the curvature. The error magnitude should be kept in mind when analyzing the

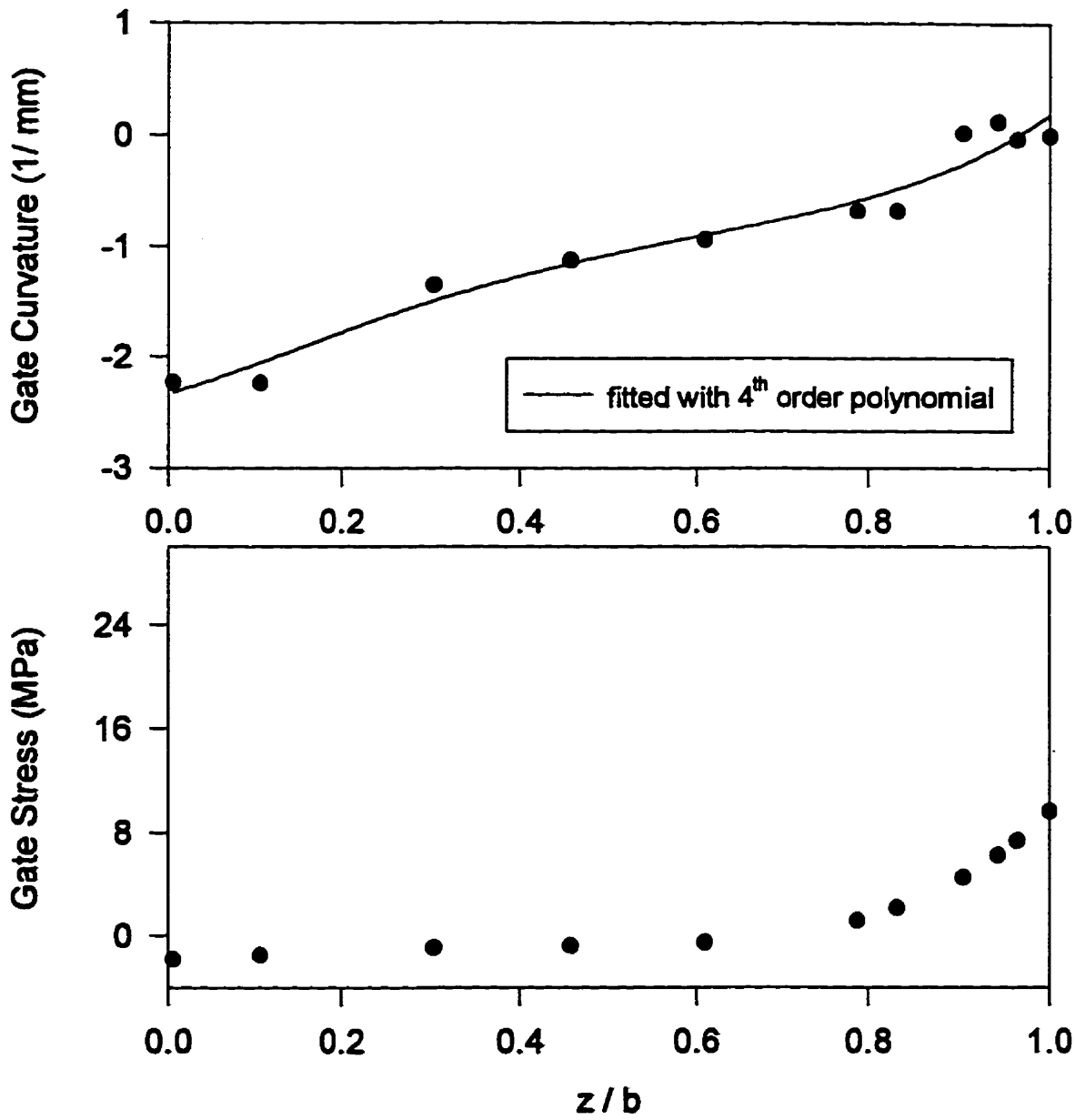

Fig.4.34.Measured curvature and stress profiles near the gate (run 1, HDPE)

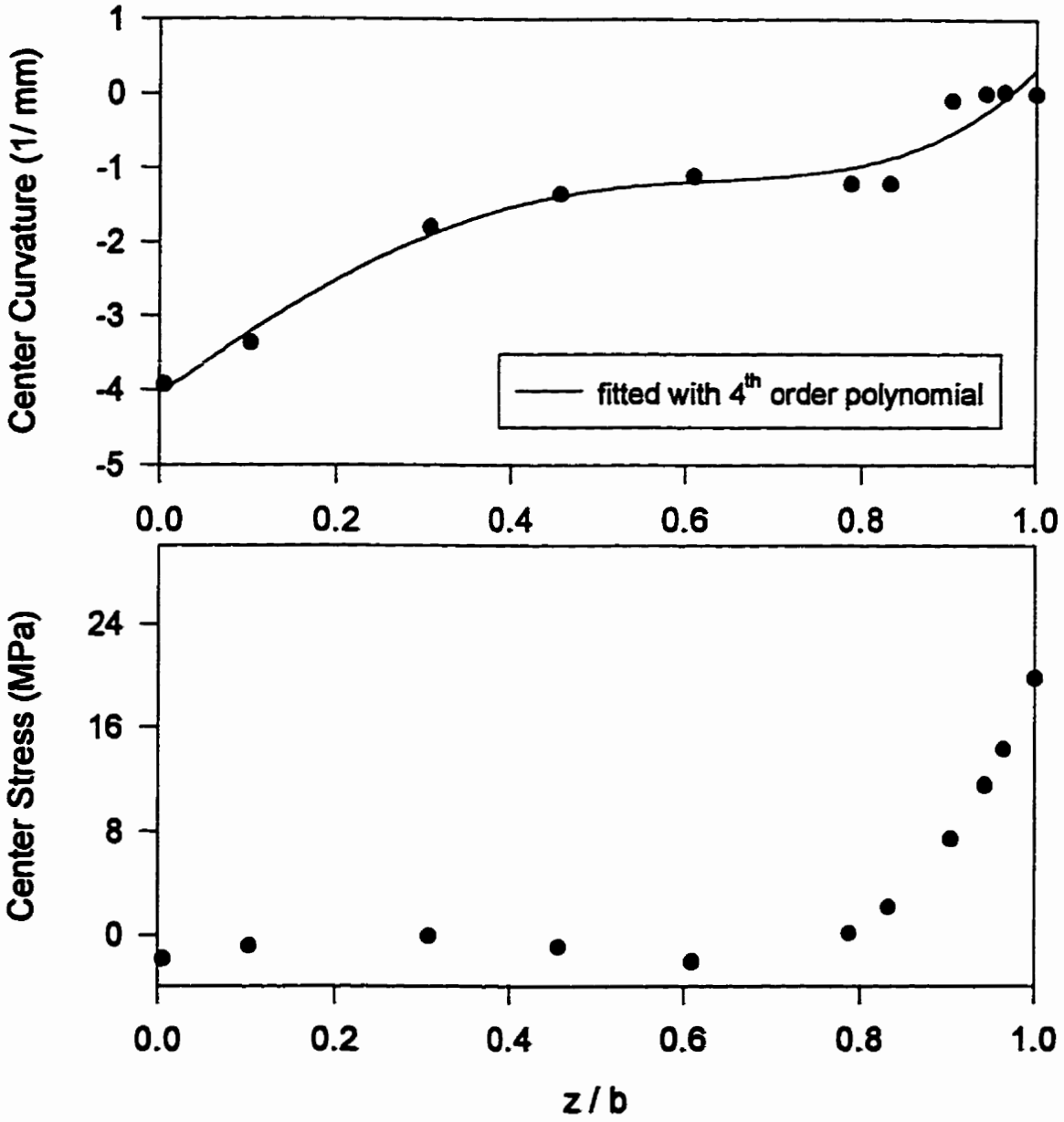

Fig.4.35.Measured curvature and stress profile in the center of cavity (run 1, HDPE)

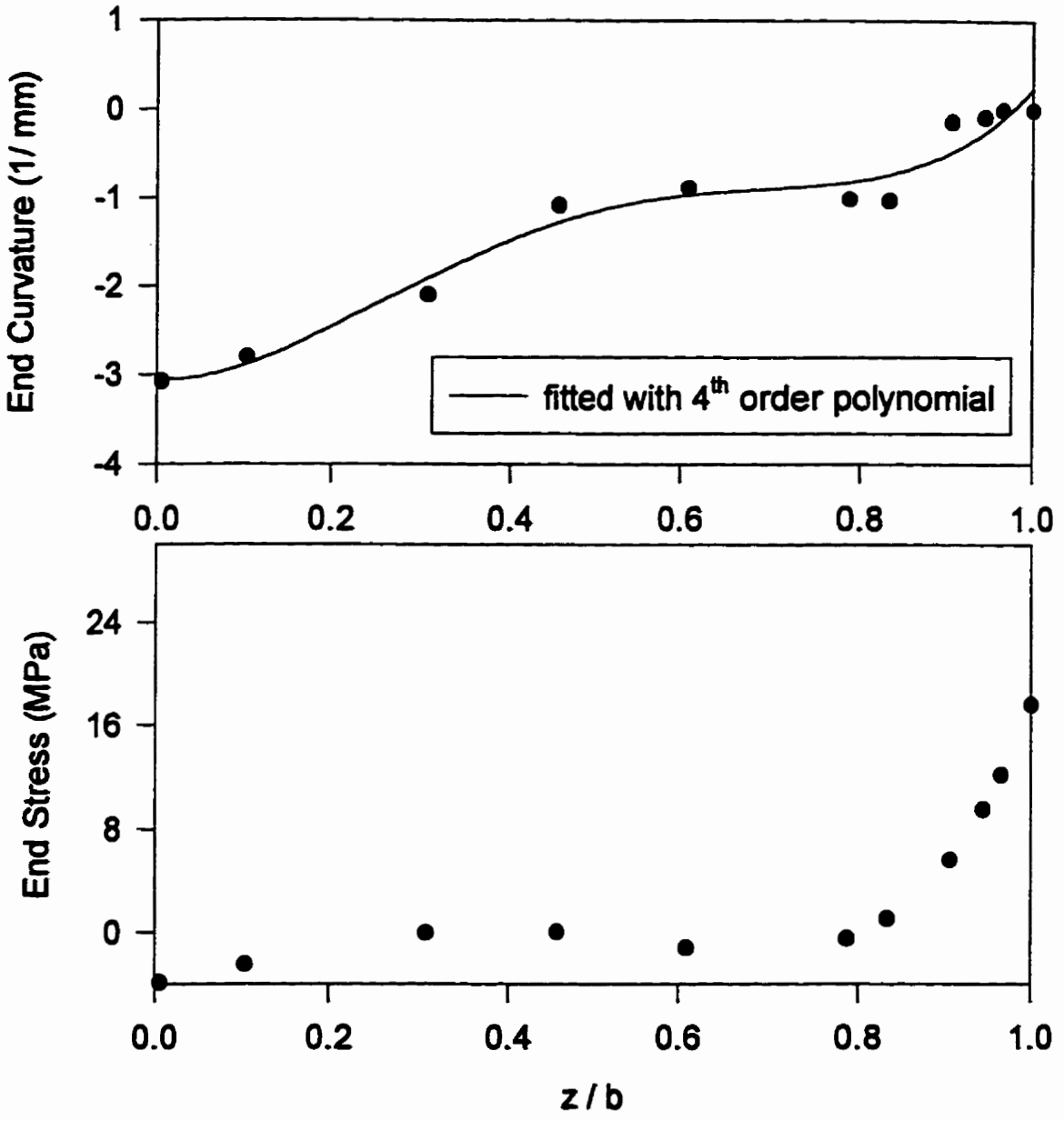

Fig.4.36.Measured curvature and stress profiles near the end of cavity (run 1, HDPE)

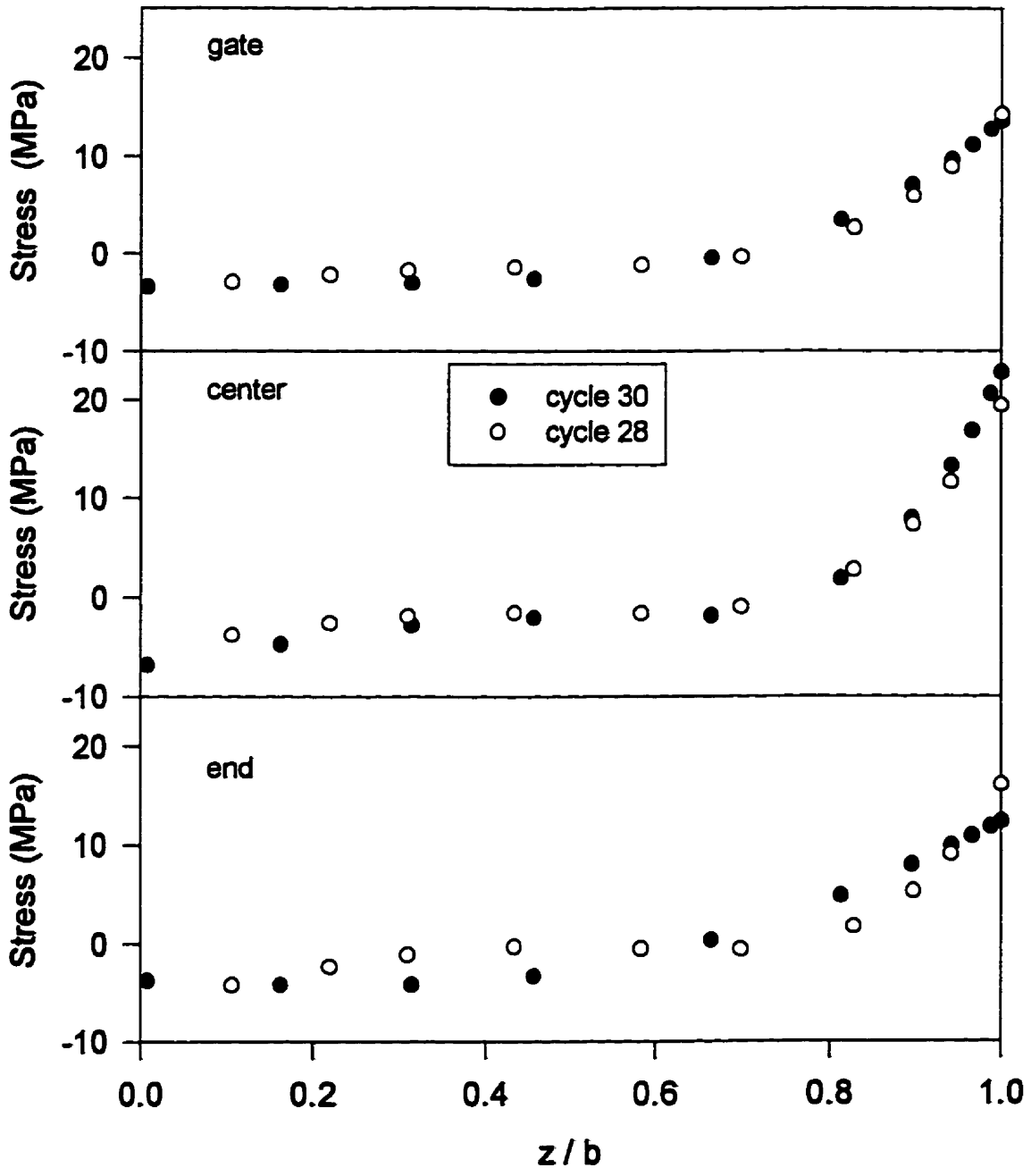

Fig.4.37. Repeatability of residual stress measurements for different positions in the mold (HDPE, run 2, position 1)

experimental stress profiles. Although these samples were taken from the same run, they correspond to different cycles (different molded plaques). Therefore, the conditions may slightly differ due to fluctuations of conditions from one cycle to the other. It must be noted that the stress profiles shown in Fig.4.37 were measured 2 weeks after molding.

Due to the viscoelastic nature of polymers, the stresses in the polymeric samples are time-dependent. Residual stresses relax and the extent of relaxation depends on their storage time, temperature, and other conditions. If the storage temperature exceeds the glass transition temperature (T_g), the stress relaxation may be significant. In Fig.4.38, the residual stresses measured 2 weeks and 6 months after injection molding are compared. They correspond to run 2, position 3 (see Table 3.11 and Fig.3.5a). The samples were stored at -34.8°C. This temperature is well above the T_g of HDPE (≈ -110°C). The surface stresses show a consistently lower value for the sample that was stored for 6 months. This difference ranges from 5 to 7.5 MPa. The mid-plane stress seems not to be affected.

4.1.2.1. Effect of Location Inside the Cavity

Fig.4.39 shows the longitudinal (xx) stress profiles measured at various locations in the cavity for run 2 (see Fig.3.5a and b for the locations). Positions 1 and 3 are expected to be similar due to symmetry. This is true except for the large surface stress in the center of cavity and in position 1 (see Fig.4.39). This, however, may be due to an error in the measured value of this stress at this position. In fact, as mentioned before, Fig.4.37 shows that the measured midplane stress for cycle 30 (used for position 1 in Fig.4.39) is larger compared to the other sample from the same run and position.

Fig.4.40 illustrates the residual stresses in the transverse directions (yy-components). In general, these stresses seem to be smaller than the longitudinal ones. This is especially true for position 6 at the end of cavity. Smaller stresses may be associated with the absence of flow stresses and a lower orientation in the transverse direction, y.

Residual stresses in HDPE samples were calculated using the 2-D FMS model and McKam©. McKam© predictions are based on a complete simulation of the injection

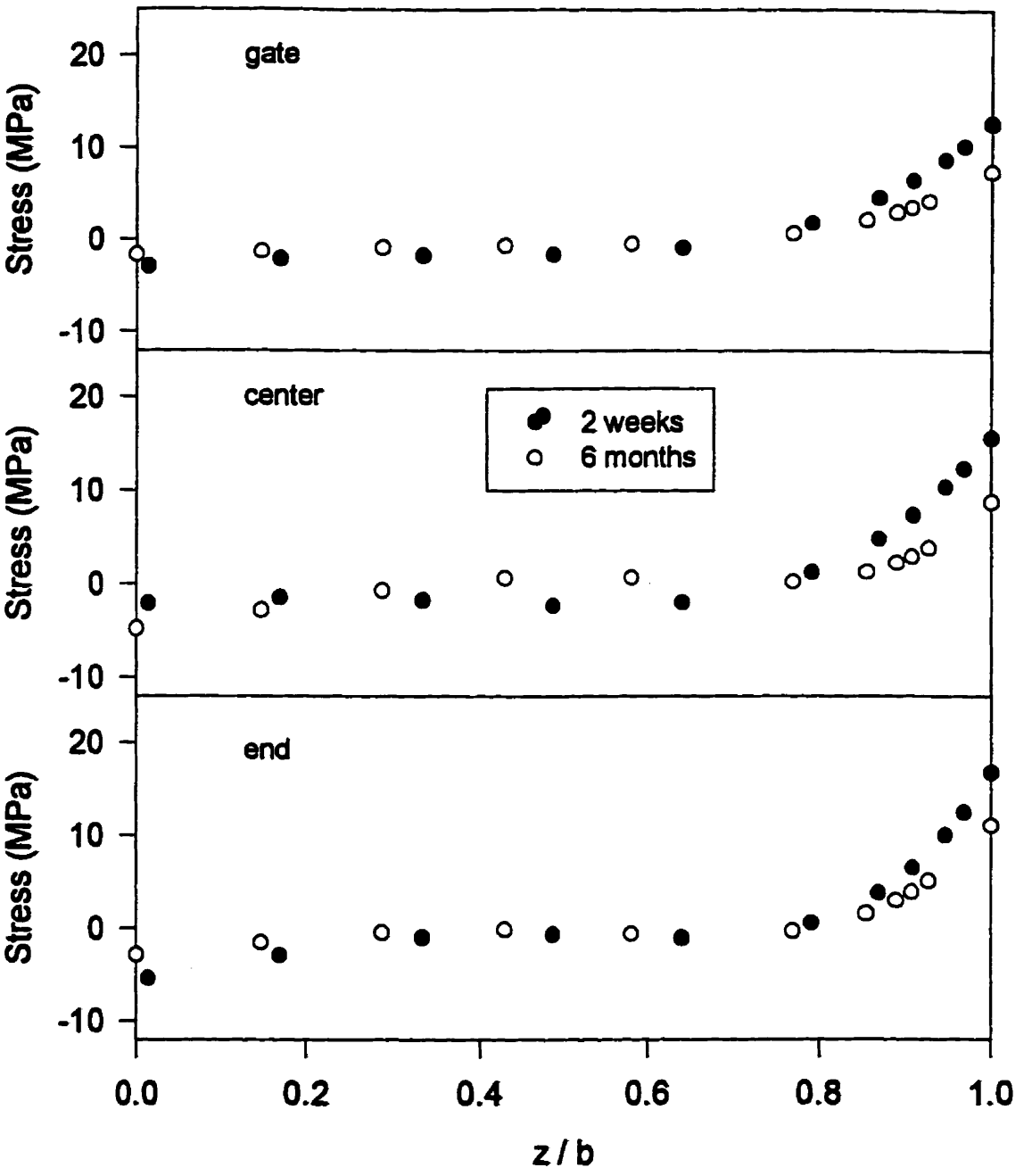

Fig.4.38.Effect of time elapsed between molding and stress measurements (HDPE, run 2, position 3)

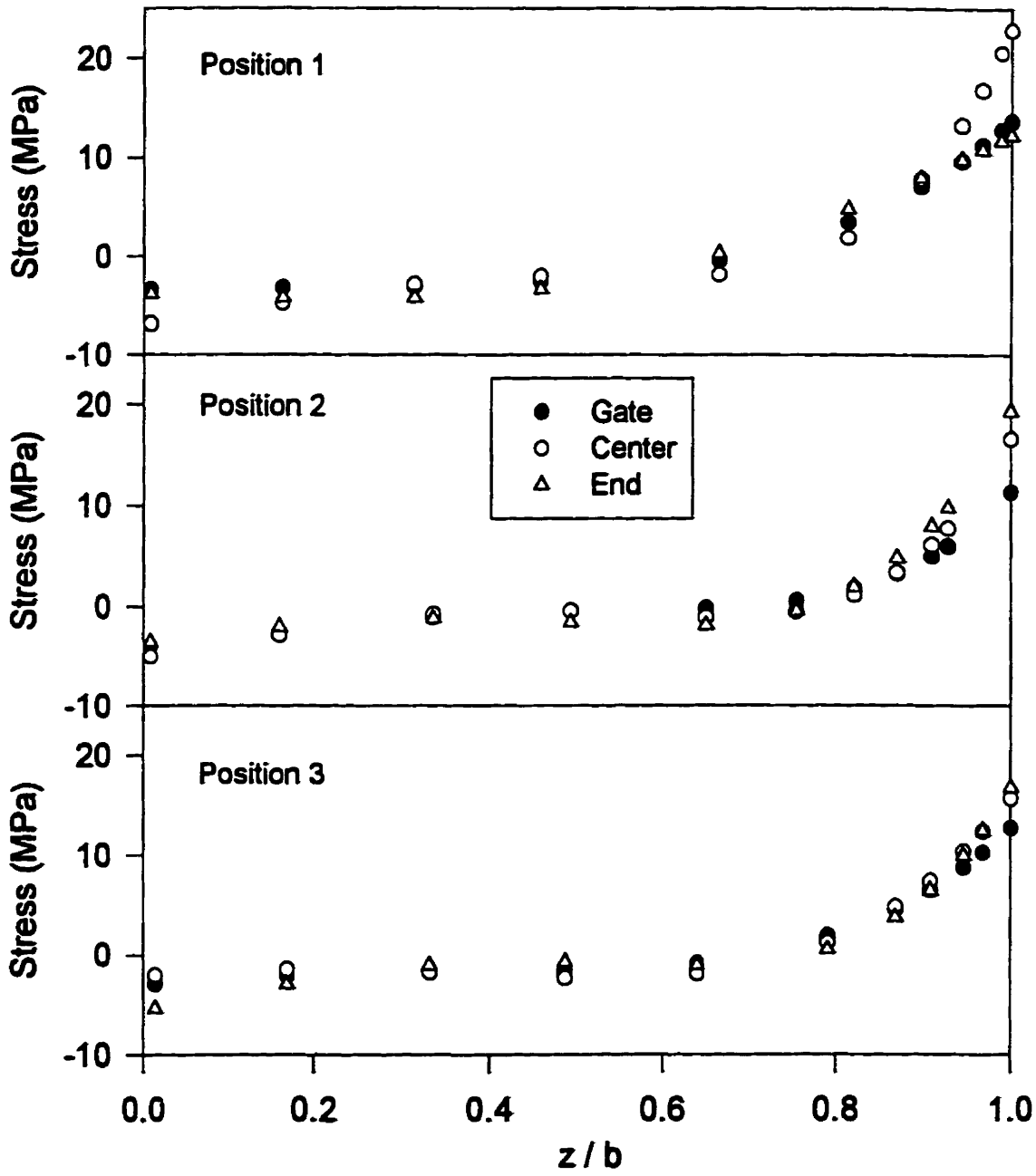

Fig.4.39.Effect of location (see Fig.3.5) in the mold on measured residual stress profiles (run 2,HDPE)

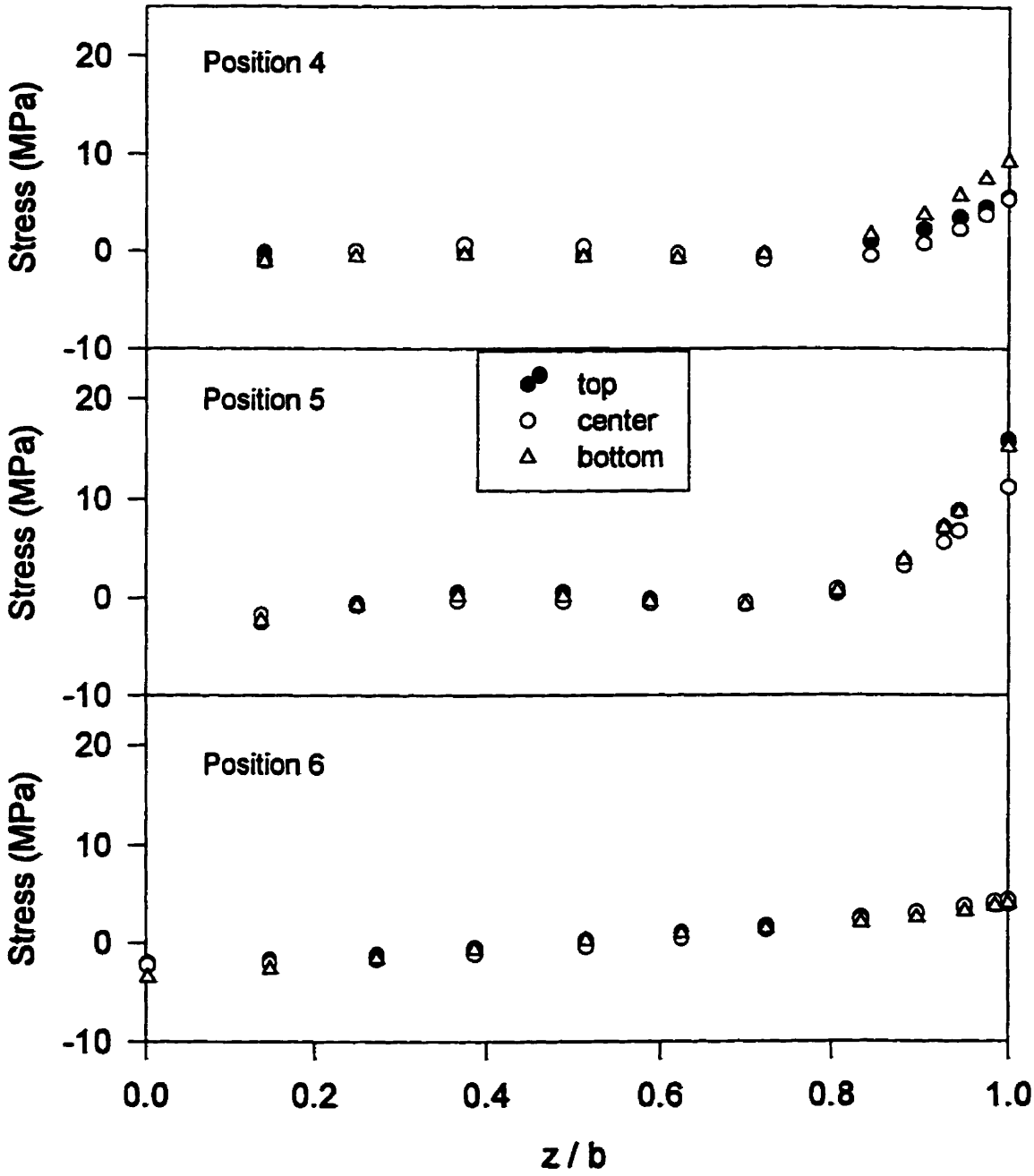

Fig.4.40.Effect of location (see Fig.3.5) in the mold on the measured residual stress profiles (run 2, HDPE)

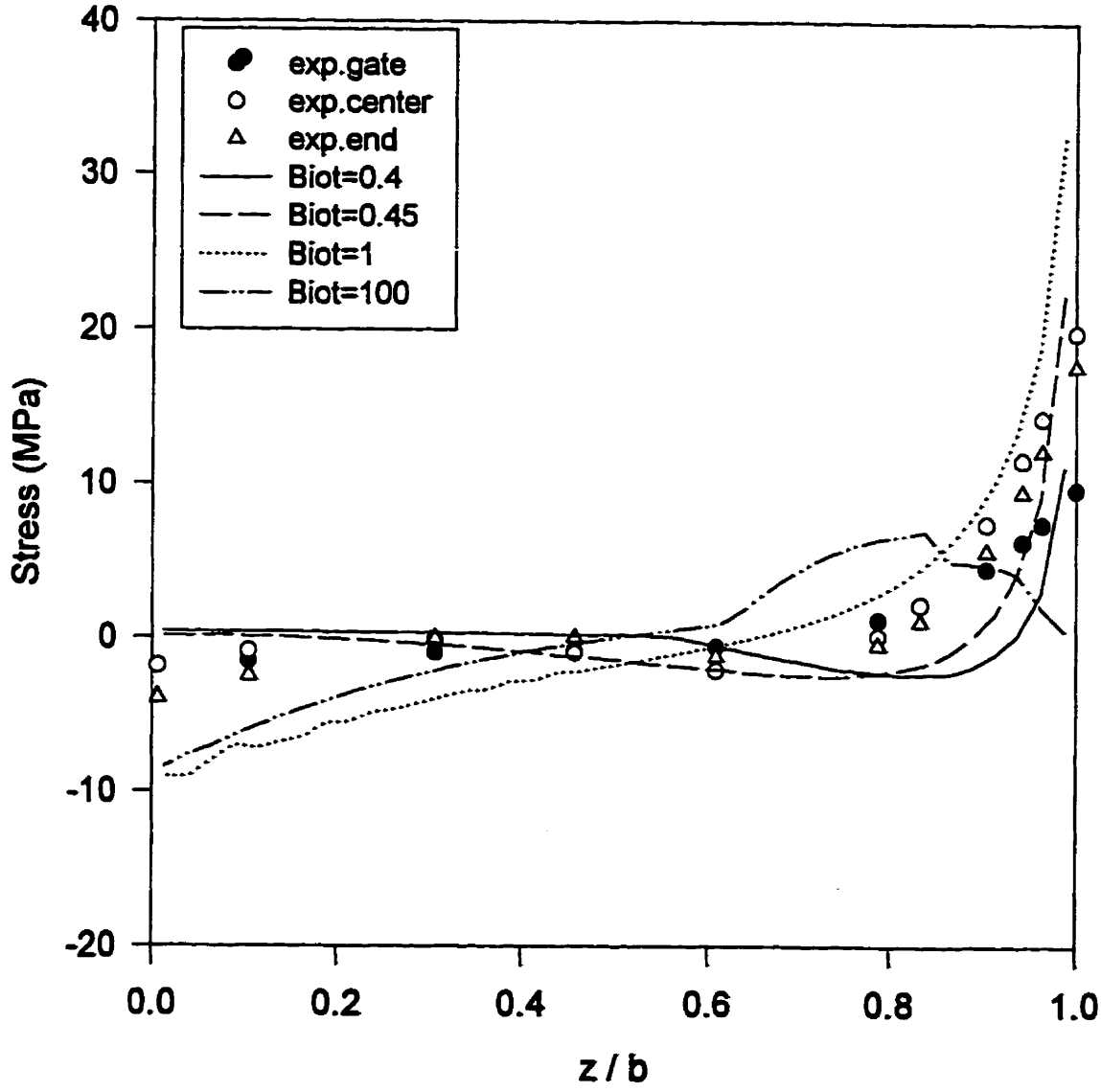

Fig.4.41.Residual stress profiles measured and calculated using 2-D FMS model (run1, HDPE)

molding process, while the 2-D FMS model is a simplified model that is useful for a quick estimation of residual stresses. Fig.4.41 shows the measured and calculated residual stress profiles for run 1, using the 2-D FMS model with 4 different Biot numbers. The experimental pressure history was used in the model and the effect of crystallinity was neglected. In spite of the above simplifications, the calculated profiles display the main features obtained in experiments: large tensile stress on the surface and small compressive or tensile stress in the core, depending on the Biot number. Crystallization is not taken into account directly. However, by using the experimental pressure histories in calculating the stresses, the main effect of crystallization, as far as thermal stresses are concerned, is included: its effect on the pressure history. The closest agreement between experiments and calculations was obtained with Biot=0.45. Therefore, this value was selected for parametric studies in later sections. In order to better understand the calculated stress profiles, they are plotted together with the solidification pressure profiles for 4 different Biot numbers in Fig.4.42 and Fig.4.43. An important observed difference between HDPE and PS results is that, due to different thermal properties, the solidification takes place faster in HDPE if crystallization is neglected. For crystallizing polymers, however, the large volume change and the heat generated due to crystallization delay the cooling and gate-freezing. This causes the plateau of high packing pressure to last longer. Although the 2-D FMS model does not include the crystallization effect, the use of the experimental pressure helps capture the main features of the residual stress profile.

The stresses calculated using McKam© and an imposed maximum pressure are shown in Fig.4.44. The general shape of the calculated profiles is consistent with the measured ones. Note that half-thickness of the sample is divided into 10 elements in McKam© and 40 elements in 2-D FMS. The surface and midplane stresses near the gate are, however, overpredicted. This may be partly due to the relaxation of stresses since they were measured 6 months after molding.

Fig.4.45 compares the measured gate pressure with the pressure histories calculated by McKam©, for run 2. The pressure during filling and the pressure decay in the final cooling stage are in good agreement with the measurements. The maximum packing pressure is, however, overpredicted, and the gate-freeze time is underpredicted.

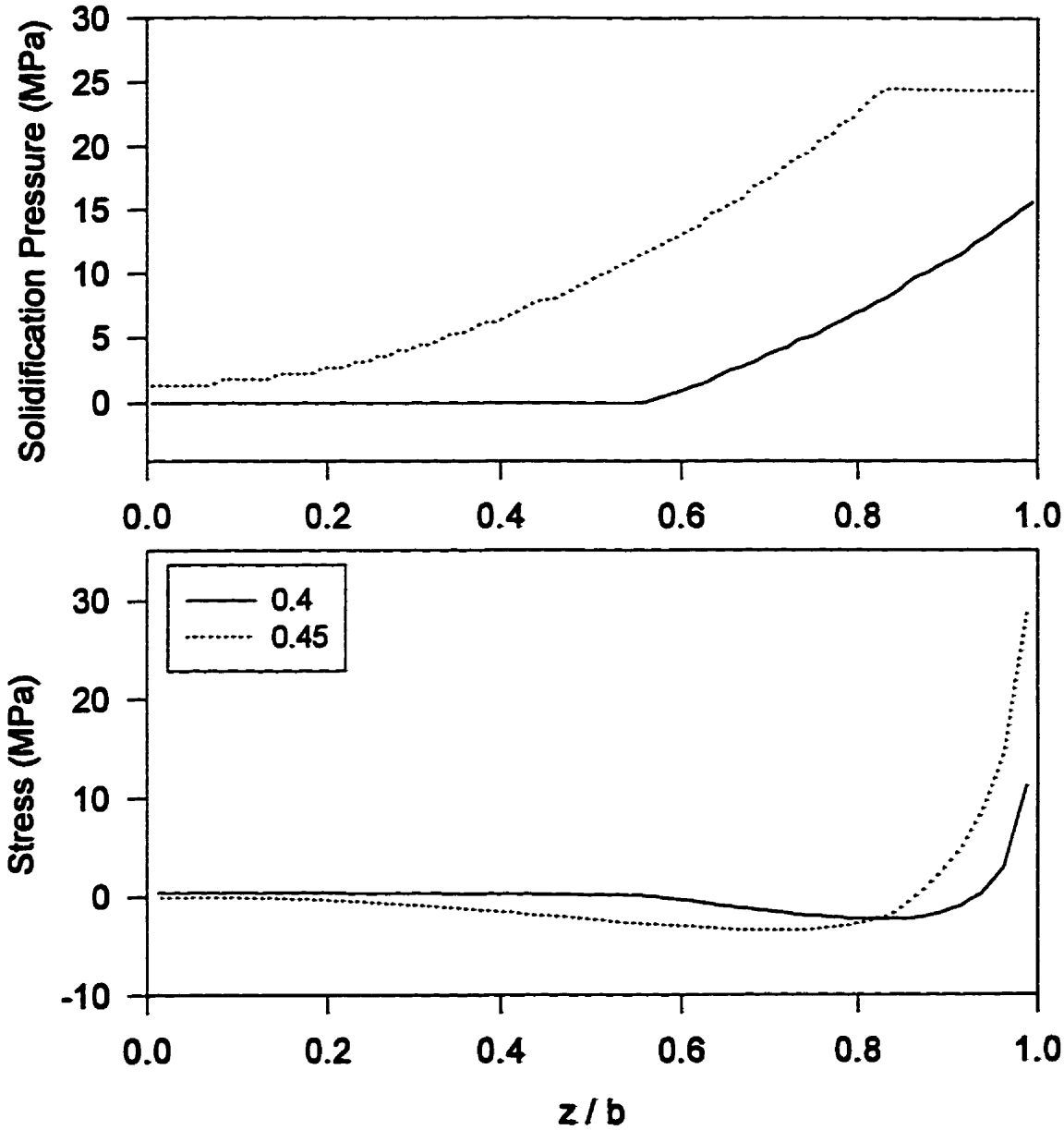

Fig.4.42.Solidifcation pressure and residual stress profiles using 2-D FMS and 2 Biot numbers (run 1,HDPE)

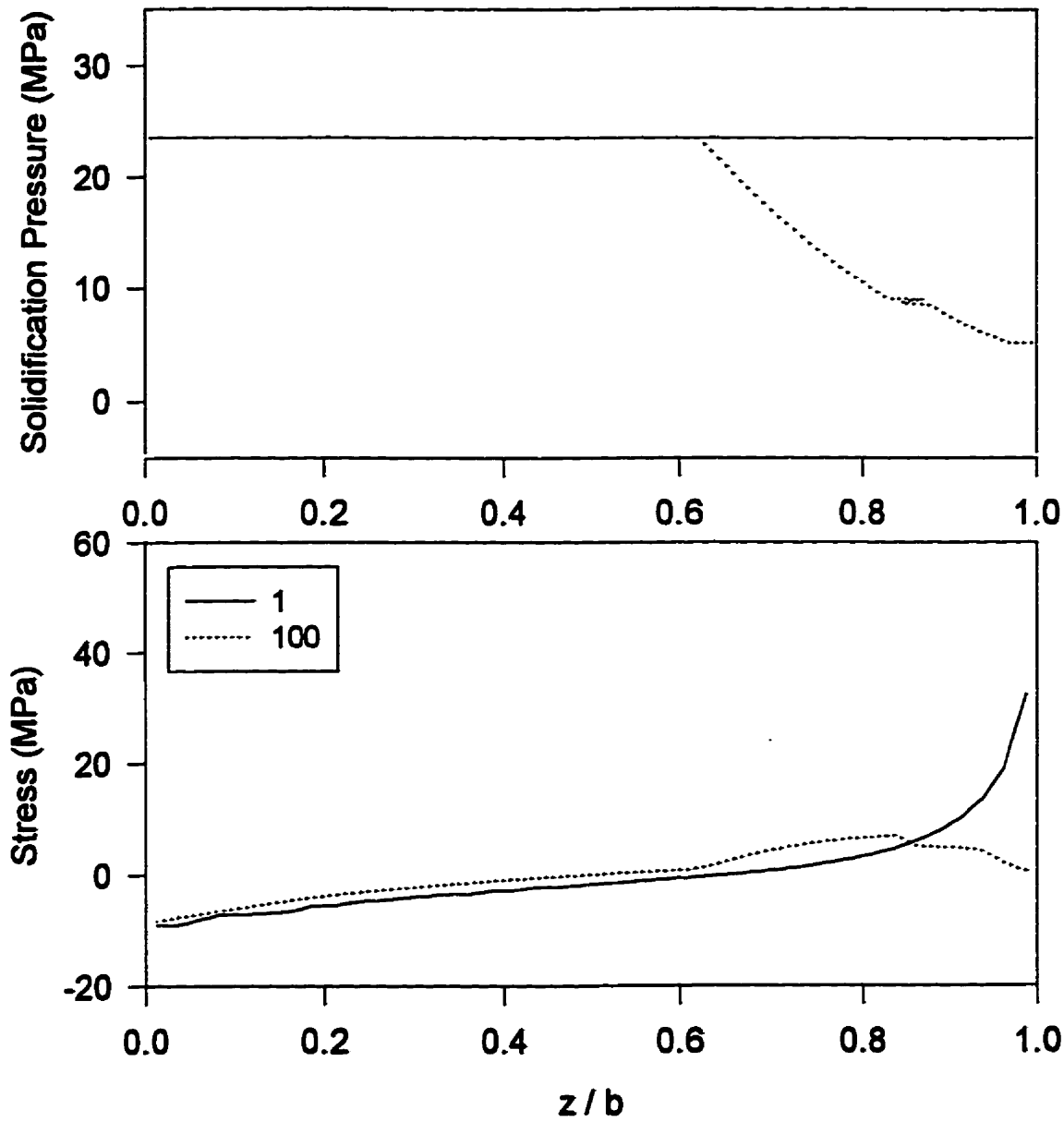

Fig.4.43.Solidification pressure and residual stress profiles using 2-D FMS and 2 Biot numbers (run 1,HDPE)

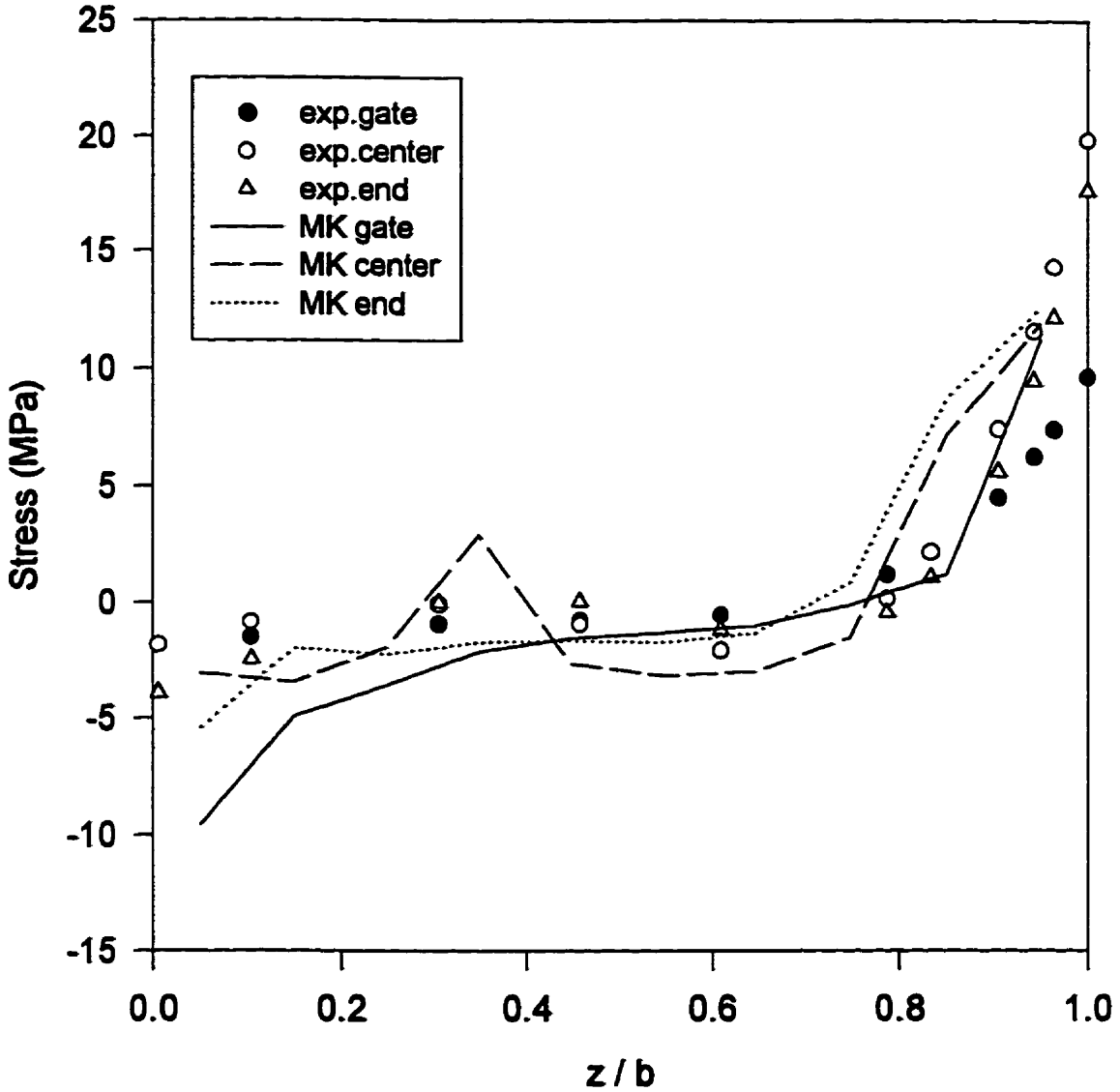

Fig.4.44.Residual stress profile at different locations, measured and calculated using McKam with imposed packing pressure (run 1,HDPE, h=600)

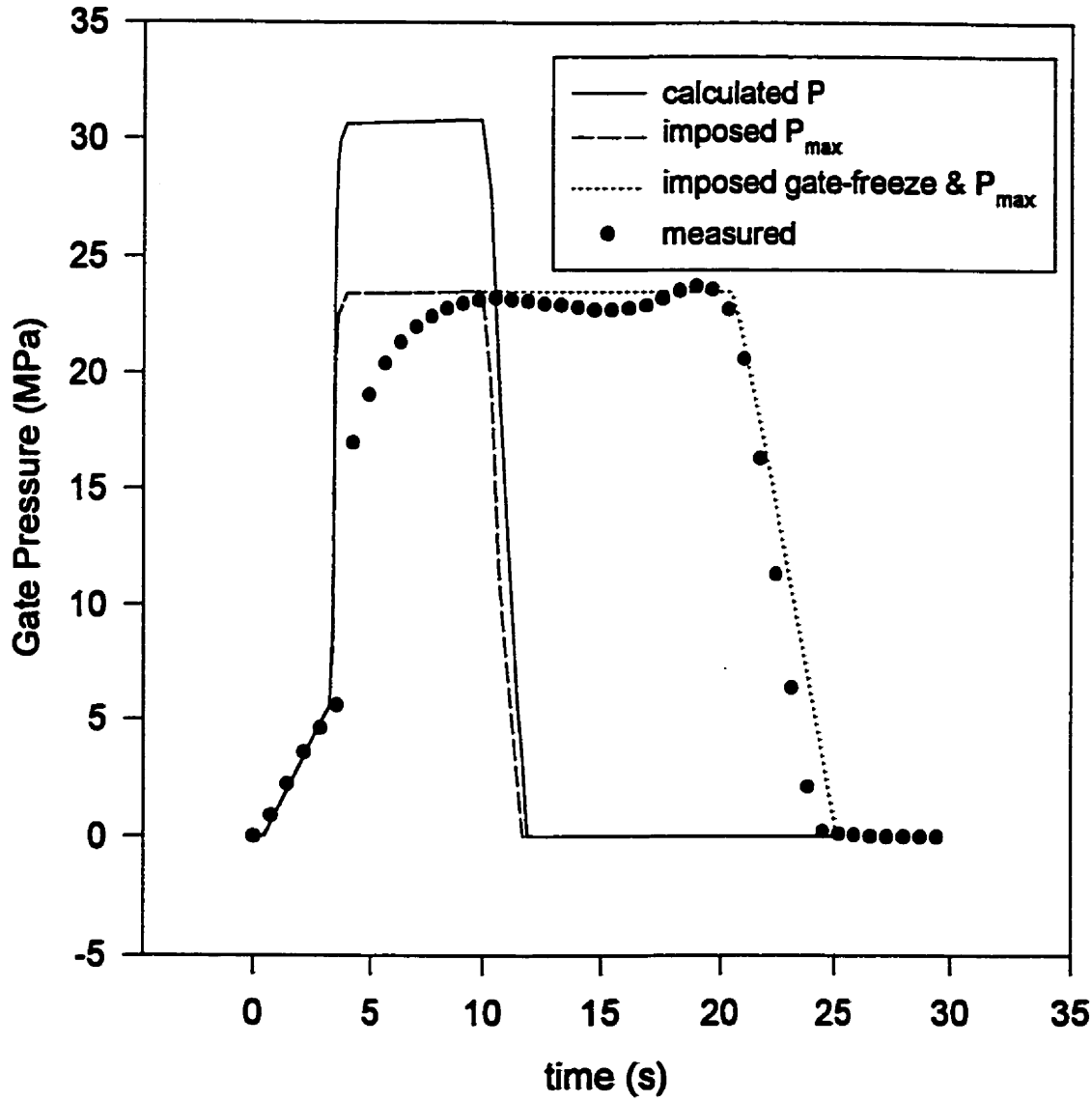

Fig.4.45. Gate pressure measured and calculated by McKam (run 2, HDPE)

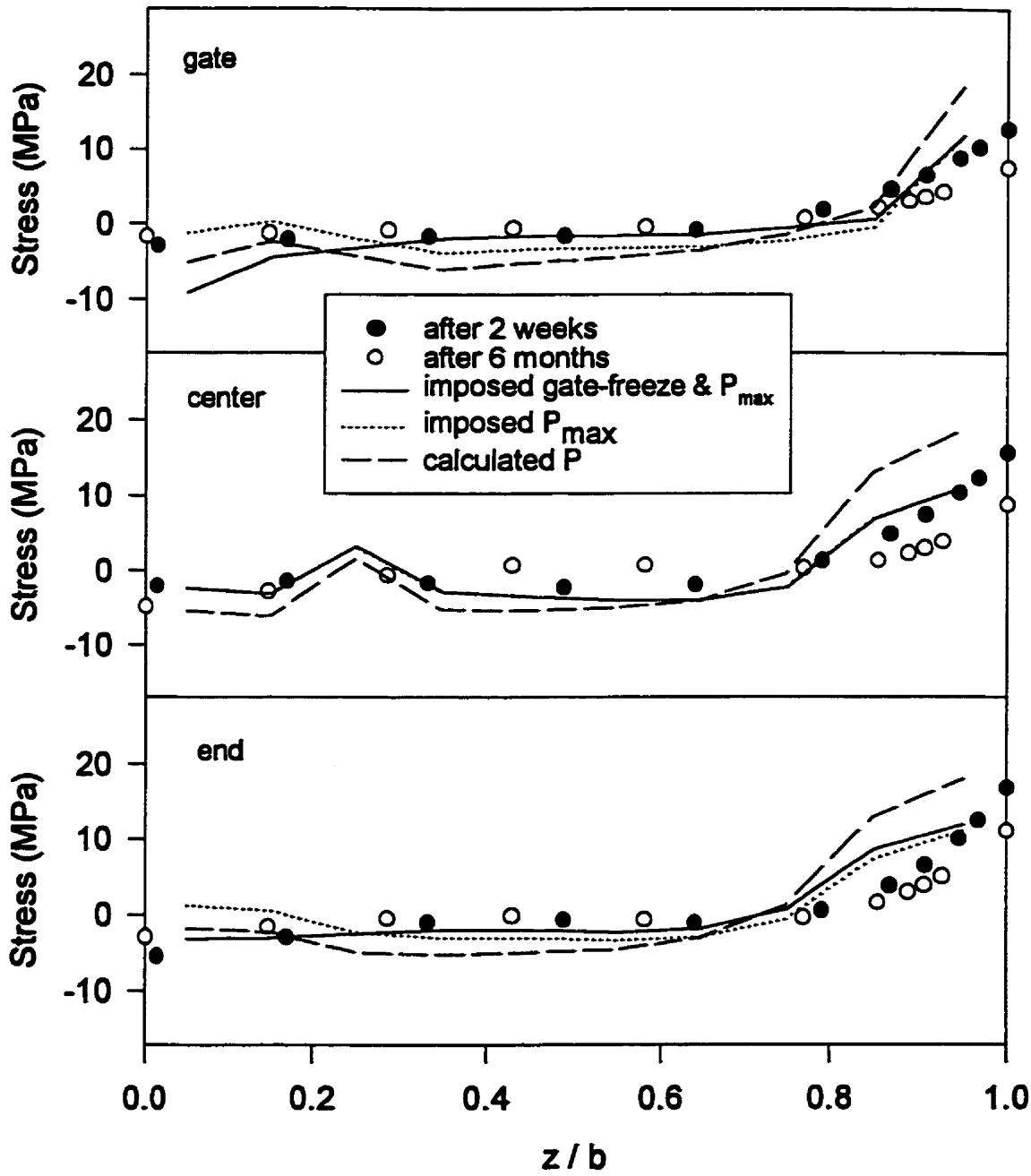

Fig.4.46.Residual stress profiles measured and calculated using McKam (run2, HDPE, position 3)

As illustrated by Fig.4.46, the stresses measured only 2 weeks after molding are in good agreement with the calculated ones if the maximum packing pressure is imposed. In the same figure, the stresses calculated using McKam© without imposing the pressure are also presented. It may be seen that the stresses in this case are much larger than the experiments. Unlike the experimental results, the pressure drop between the nozzle and the gate, calculated by McKam© is nearly zero, causing a very large cavity pressure and thus, an overprediction of residual stresses. Imposing the gate freeze-time slightly decreases the mid-plane compressive stresses.

McKam© calculates the crystallinity distribution in HDPE samples, at different stages of injection molding. In order to evaluate these calculations and the effect of crystallinity on residual stresses, the final crystallinity profiles in the molded samples were measured using DSC, as explained in Chapter 3. Fig.4.47 and 4.48 compare the measured and calculated final crystallinity distribution along the thickness of the samples, for run 2, at five different locations (see Fig.3.8) in the cavity. In most cases, the measured and the calculated crystallinities do not change drastically with thickness and are around 55 %. Consider the top graph in Fig.4.47 corresponding to the position 1 at the end of the cavity. The calculated crystallinity is about 20% on the surface (z/b=1) and grows quickly to reach a plateau of 55% as the core of the sample (z/b=0) is approached. This variation is due to the rapid cooling at the surface. The measurements for this case show a minimum crystallinity in the intermediate layers. In fact, large flow stresses can induce additional crystallization near the surface.

Crystallization in the injection molded HDPE samples is closely related to the cooling rate and thus to the evolution of the temperature distribution. On the other hand, the heat generated during crystallization affects the cooling rate. Fig.4.49 presents the temperature profiles, calculated by McKam©, for run 2, at three locations in the cavity after 5, 20, and 30 s., respectively. The value used for the heat transfer coefficient h was 600 W/(m^2.K) (average Biot number ≈3) . Fig.4.50 and 4.51 illustrate the corresponding evolution of the percent crystallinity.

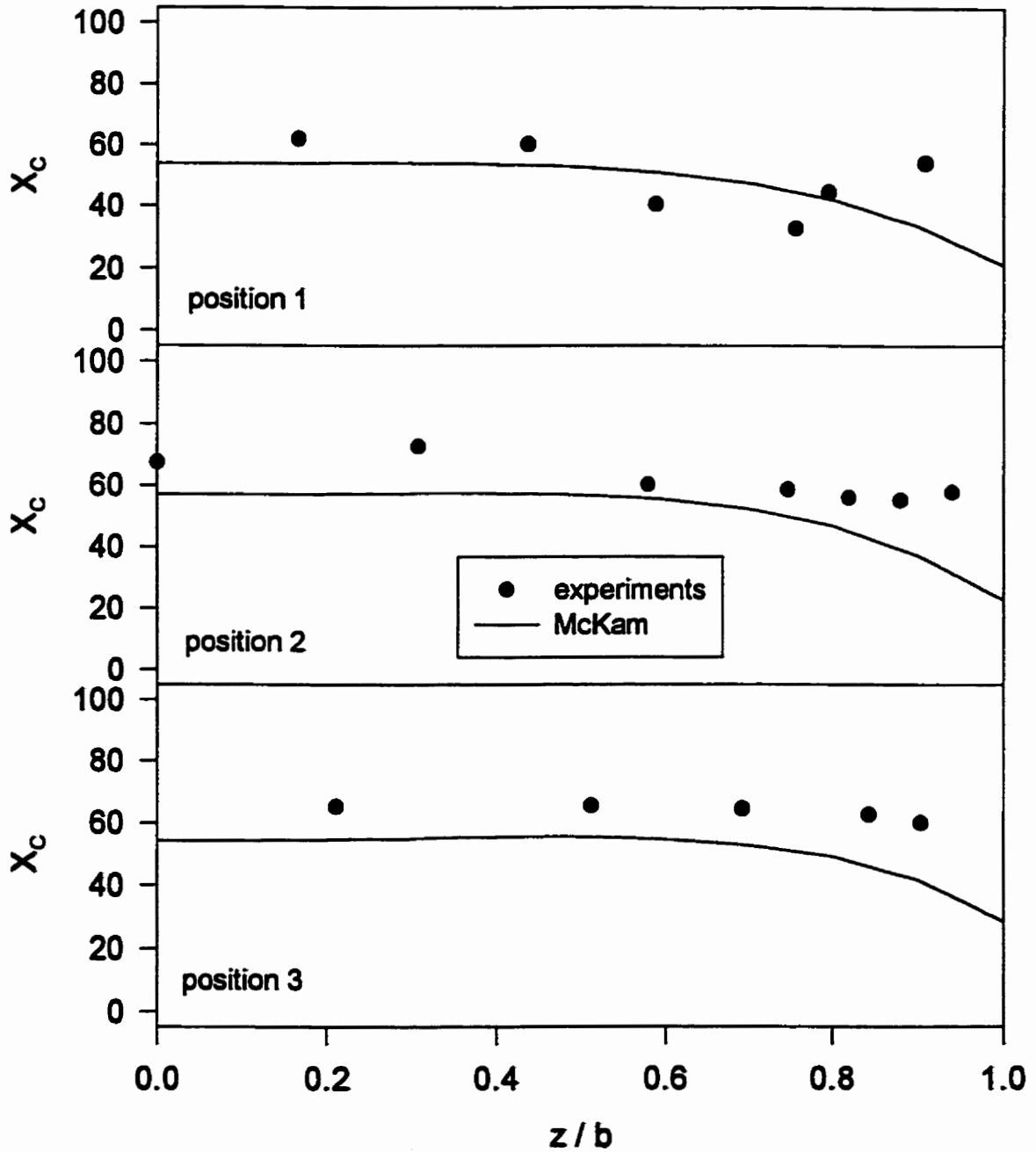

Fig.4.47.Measured and calculated percent crystallinity profiles for positions1,2,3 in Fig.3.8 (run 2,HDPE)

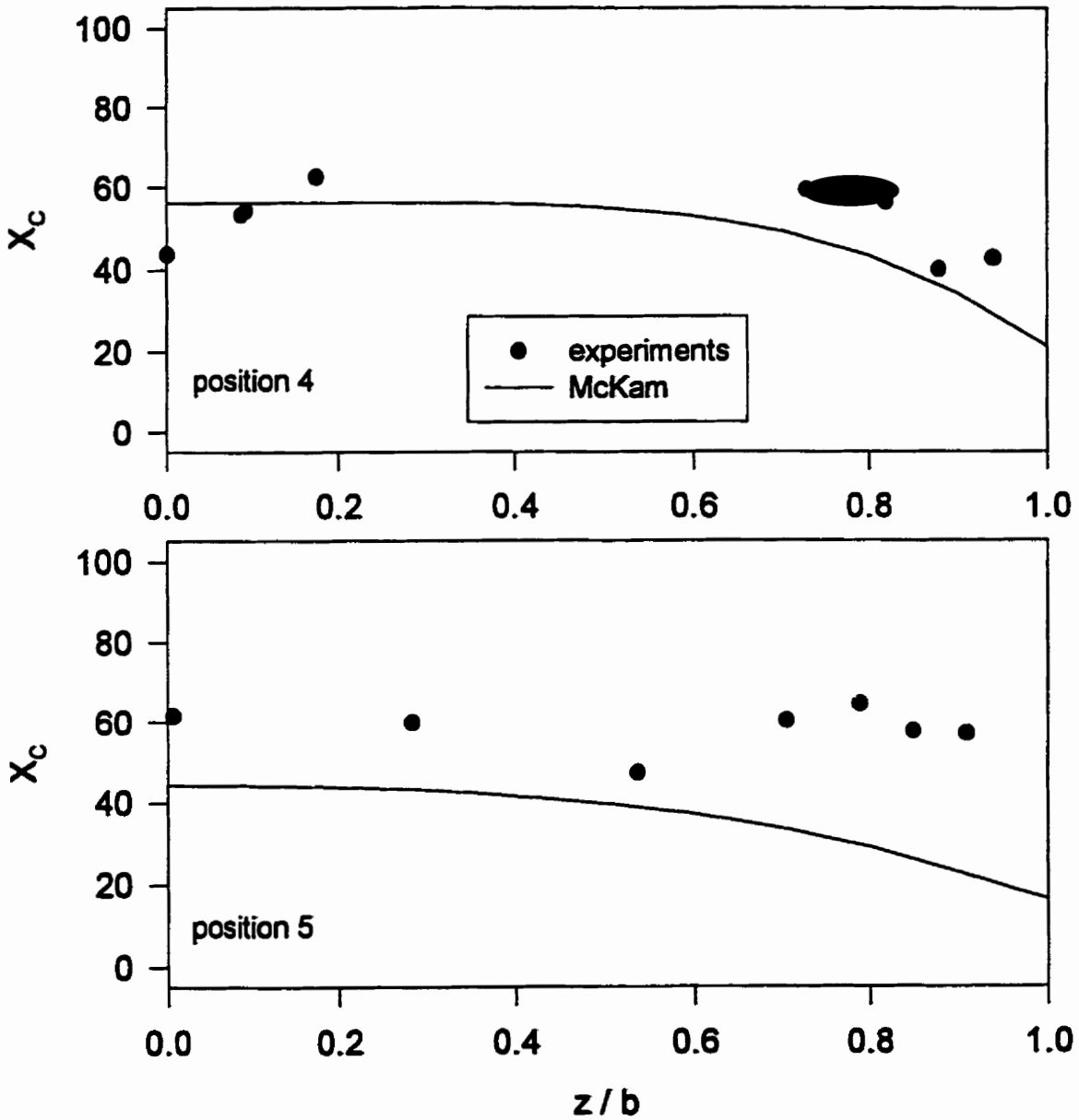

Fig.4.48.Measured and calculated percent crystallinity profiles for positions 4 and 5 in Fig.3.8 (run2 , HDPE)

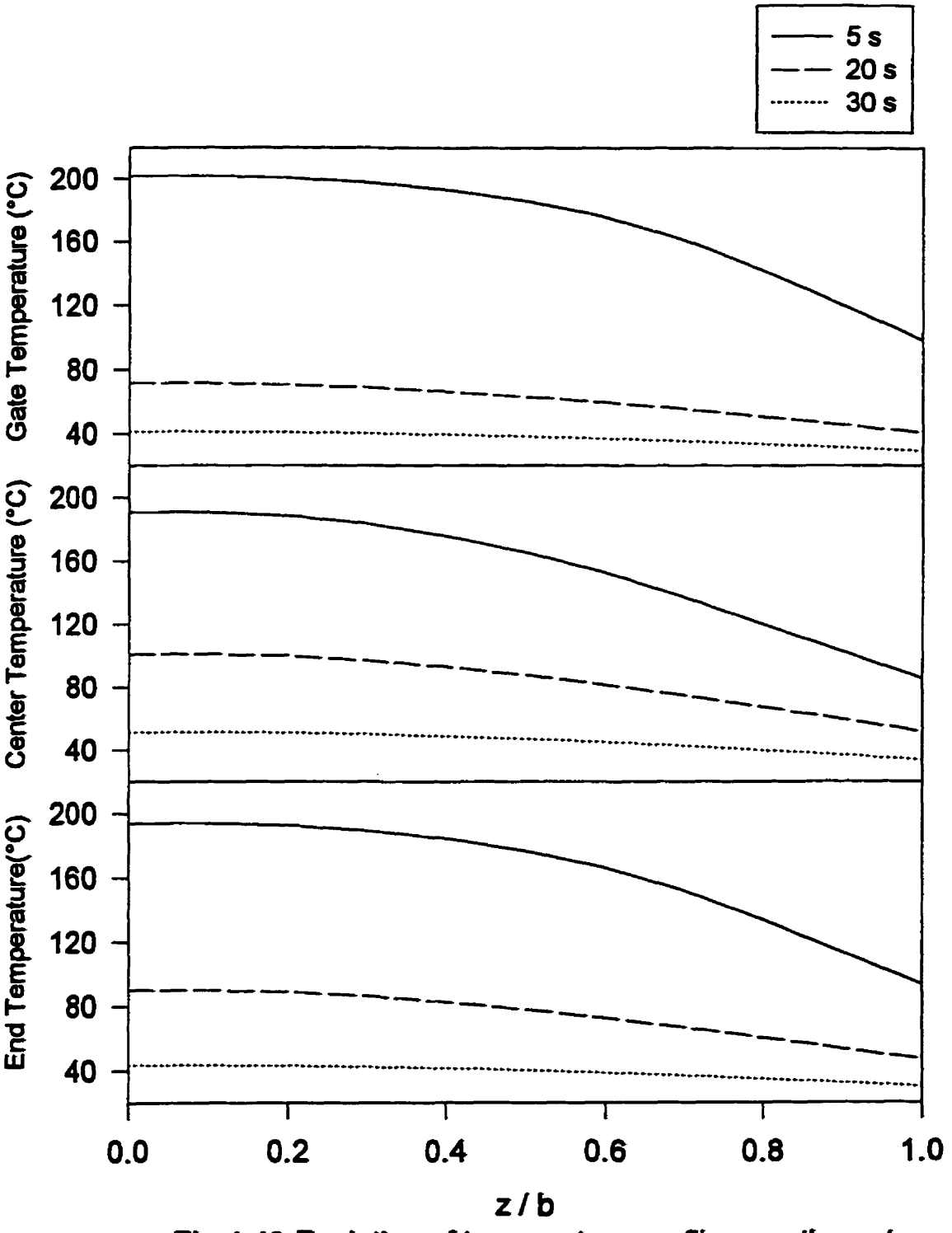

Fig.4.49.Evolution of temperature profile near the gate (l=25), center(l=42), and near the end (l=54) calculated by McKam (J=17, run 2, HDPE)

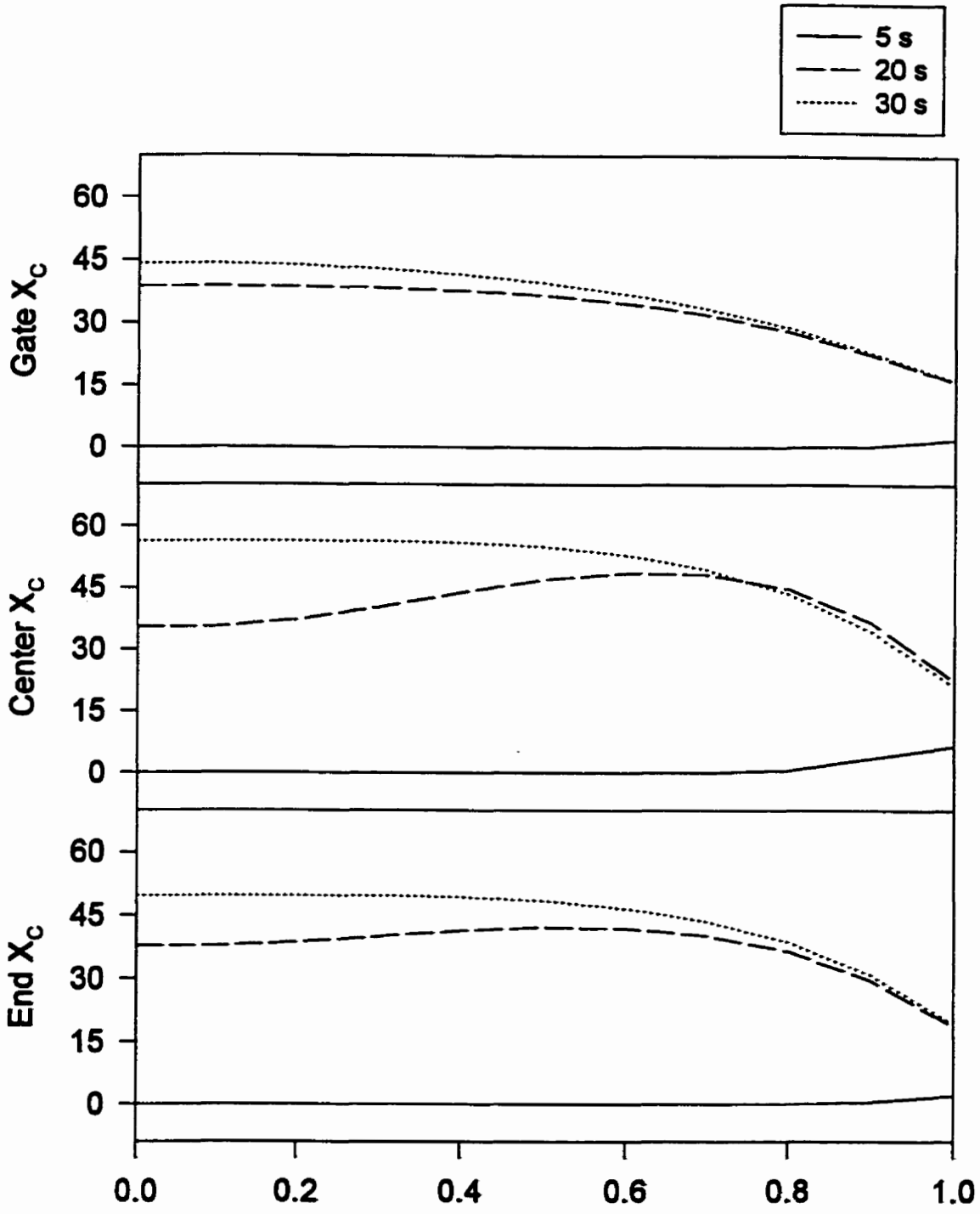

Fig.4.50. Evolution of crystallinity profile for near the gate (l=25), center (l=42), and near the end (l=54) of cavity calculated by McKam(J=17, run 2,HDPE)

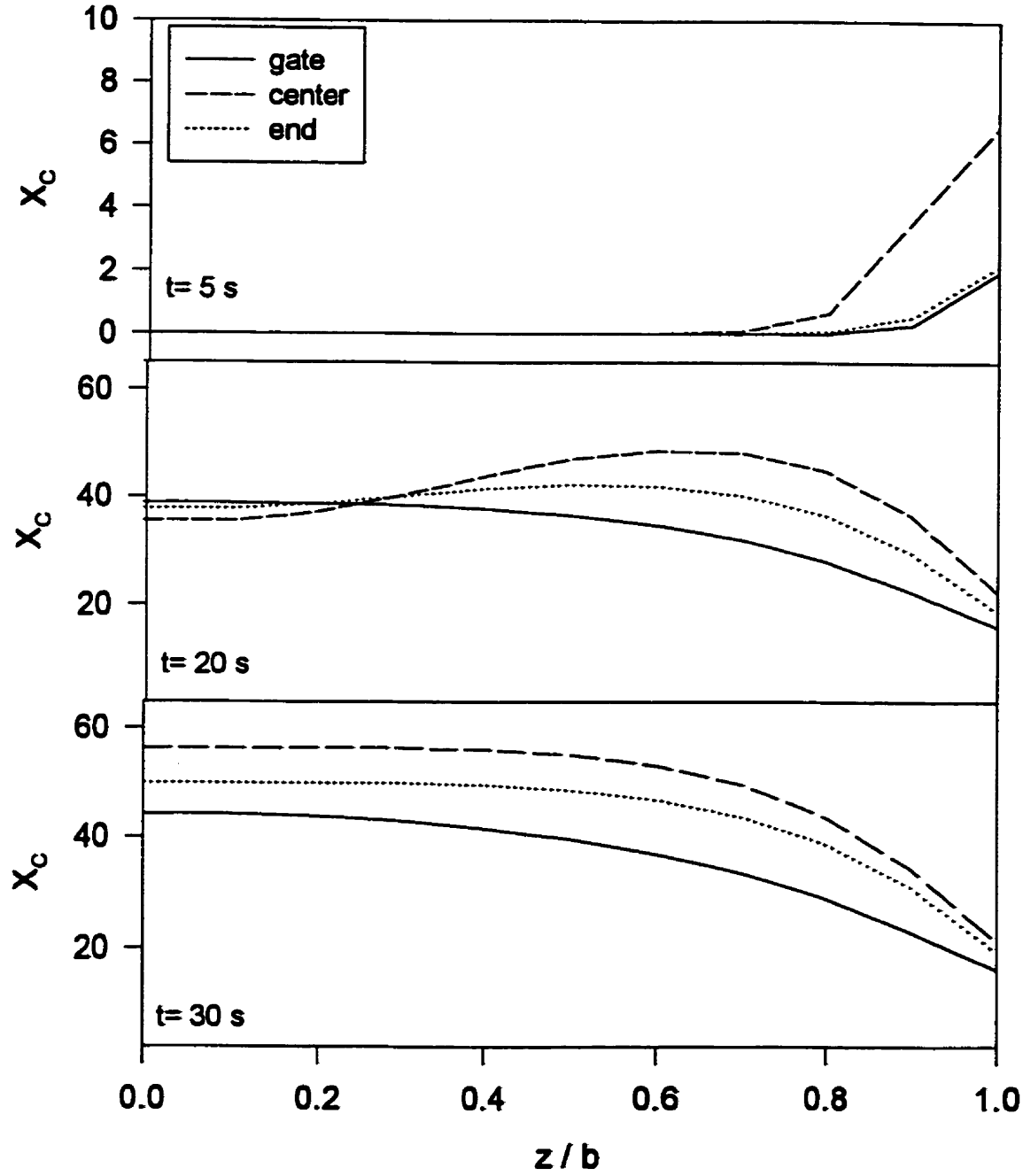

Fig.4.51.Evolution of percent crystallinity X_c for 3 locations in the cavity calculated by McKam (run 2, HDPE)

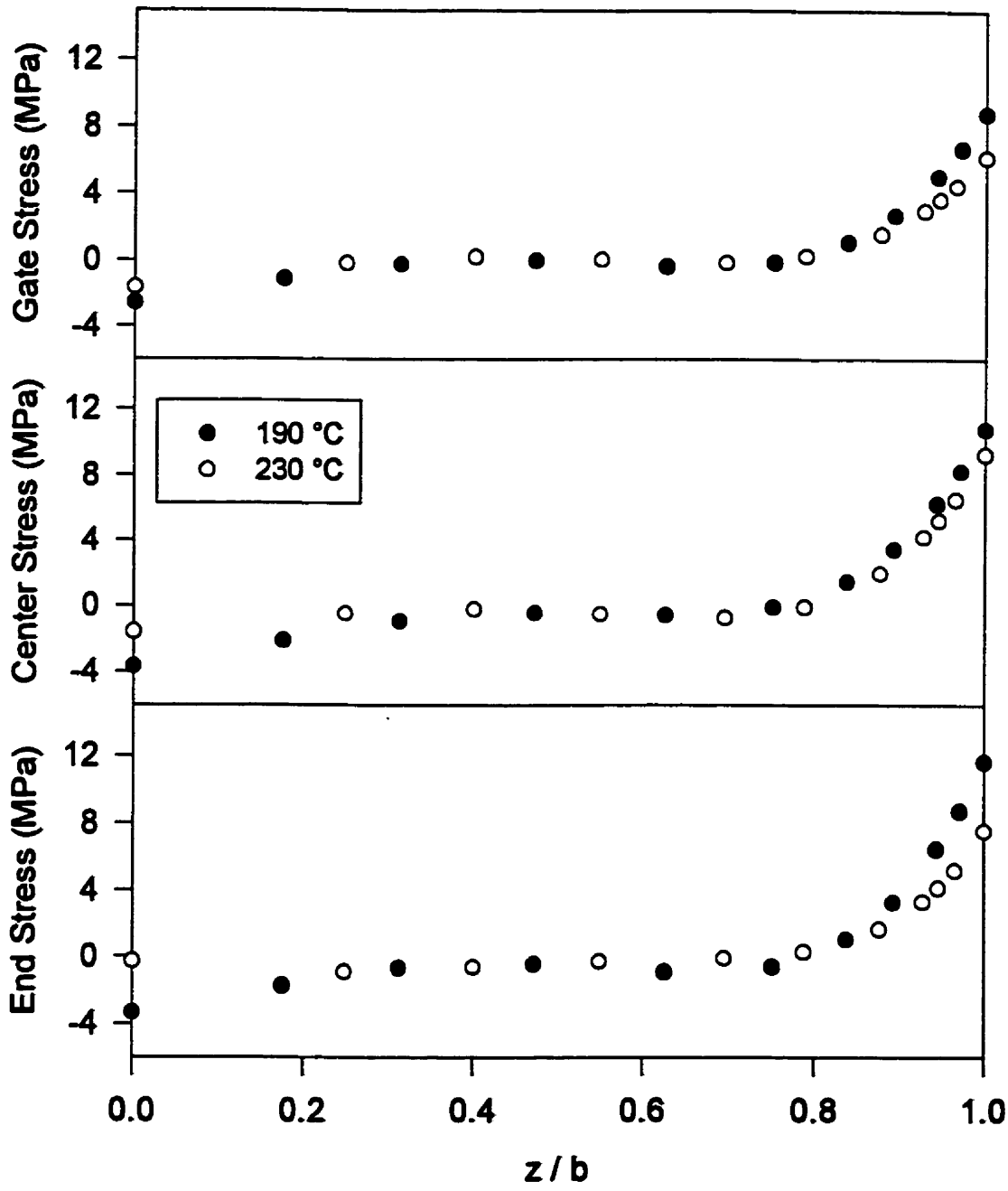

Fig.4.52.Measured residual stress profiles for 3 locations along the flow and 2 melt temperatures(run3, 5, HDPE)

4.1.2.2. Effect of Melt Temperature

Fig.4.52 illustrates the measured residual stress profiles for two different melt temperatures. An increase in the melt temperature consistently decreases the magnitude of the surface and midplane stresses. In the intermediate layers, the stress is not affected. The corresponding pressure histories at the nozzle and near the gate are presented in Fig.4.53 (top). The maximum packing pressure at the gate and the gate-freeze time increase with T_m. Also, a high T_m reduces the filling time.

Fig.4.53 (bottom) shows the solidification pressure and the residual stress profiles calculated using the 2-D FMS model and Biot=0.45. With a large T_m the solidification of the sample is delayed and occurs under lower pressure. Fig.4.54 compares the measurements with the stresses predicted by the 2-D FMS model. The mid-plane compressive stress for T_m=230°C is slightly smaller than T_m=190°C.

The stress profiles calculated by McKam© for these two runs are shown in Fig.4.55. The stresses are largely overpredicted compared to the experiments especially for the higher melt temperature. Also the order obtained in the experiments is not obtained for the effect of melt temperature.

In Fig.4.56, the residual stresses are calculated for four different melt temperatures and a fixed pressure history corresponding to run 1, using the 2-D FMS model. According to these calculations, the stresses on the surface and in the core are reduced by increasing the melt temperature.

4.1.2.3. Effect of Coolant Temperature

As illustrated in Fig.4.57, increasing the coolant temperature also decreases the measured surface and mid-plane stresses, similar to the melt temperature. The decrease of the stress in the core is less important near the gate. As illustrated by Fig.4.58, the gate-freeze time is larger for the higher coolant temperature and the maximum packing is also slightly higher. The pressure drop between the nozzle and the gate is smaller for this case. Using these pressure histories, the solidification pressure and the residual stress profiles are calculated using the 2-D FMS model as presented in Fig.4.58 (bottom) and Fig. 4.59, respectively. Fig.4.60 shows the stresses calculated by McKam©. The calculated trend is

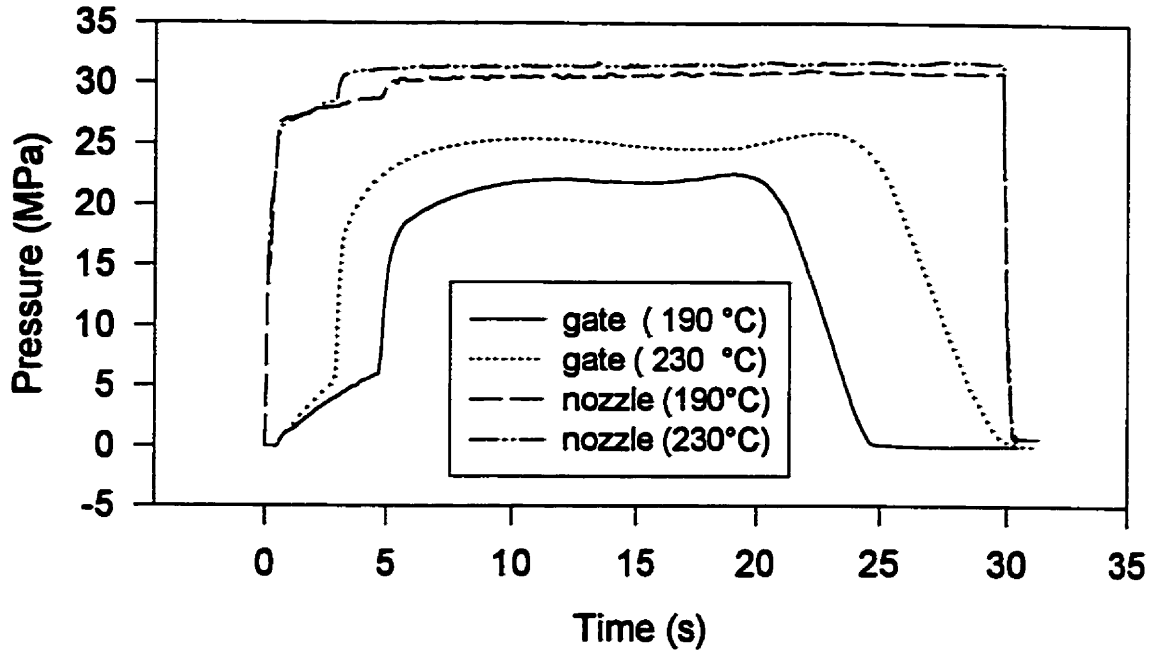

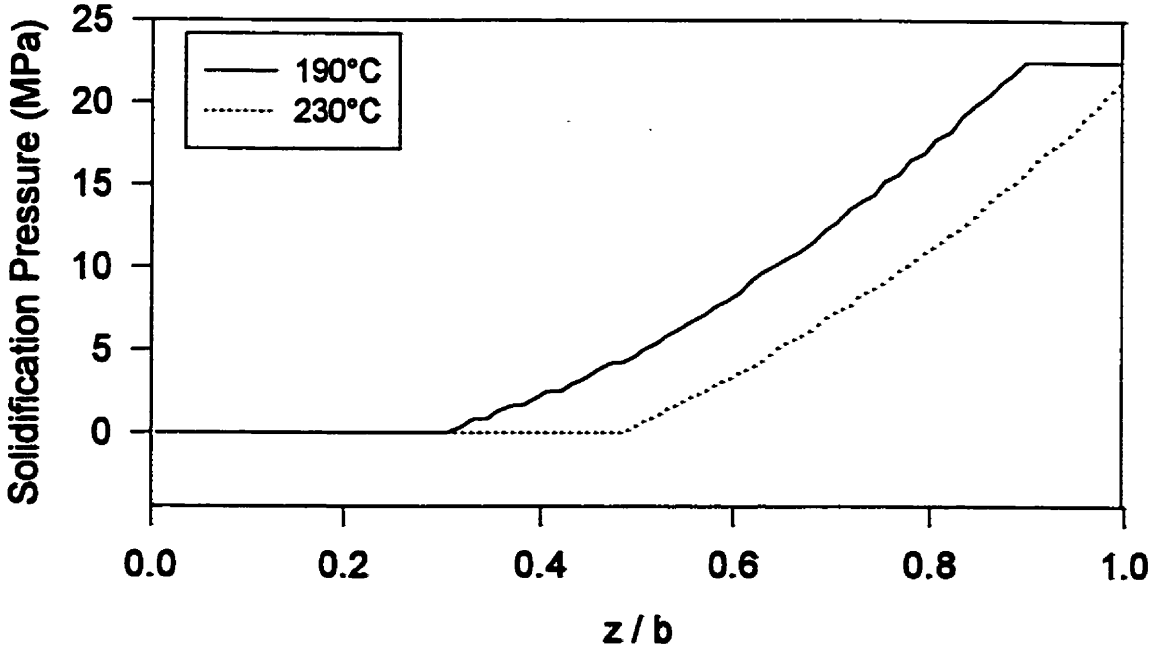

Fig.4.53.Measured pressure histories (top) and calculated solidification pressures (bottom) using 2-D FMS, for 2 melt temperatures (runs 3,5, HDPE)

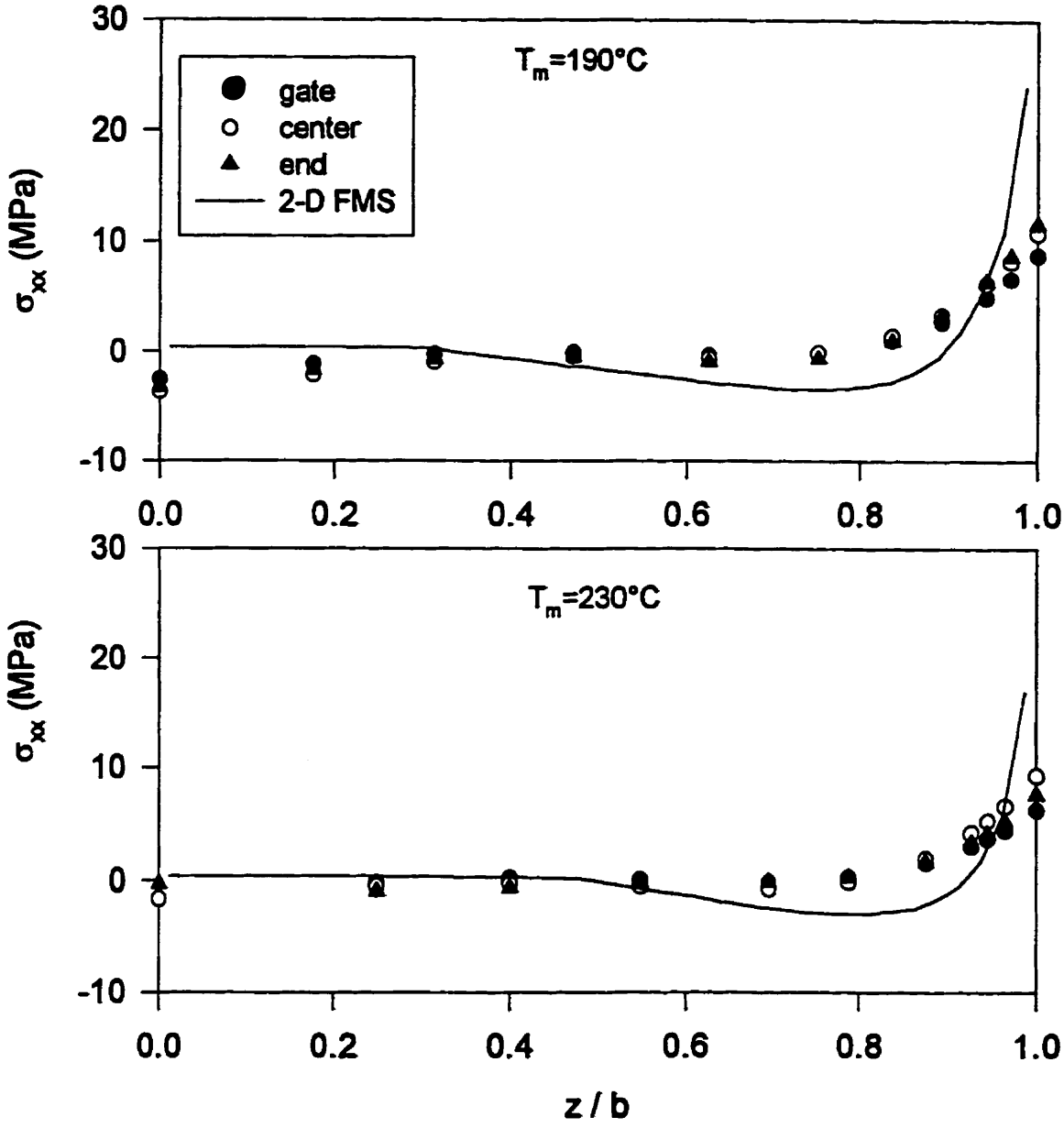

Fig.4.54. Residual stress profiles measured and calculated using 2-D FMS model for 2 melt temperatures (runs 3, 5, HDPE)

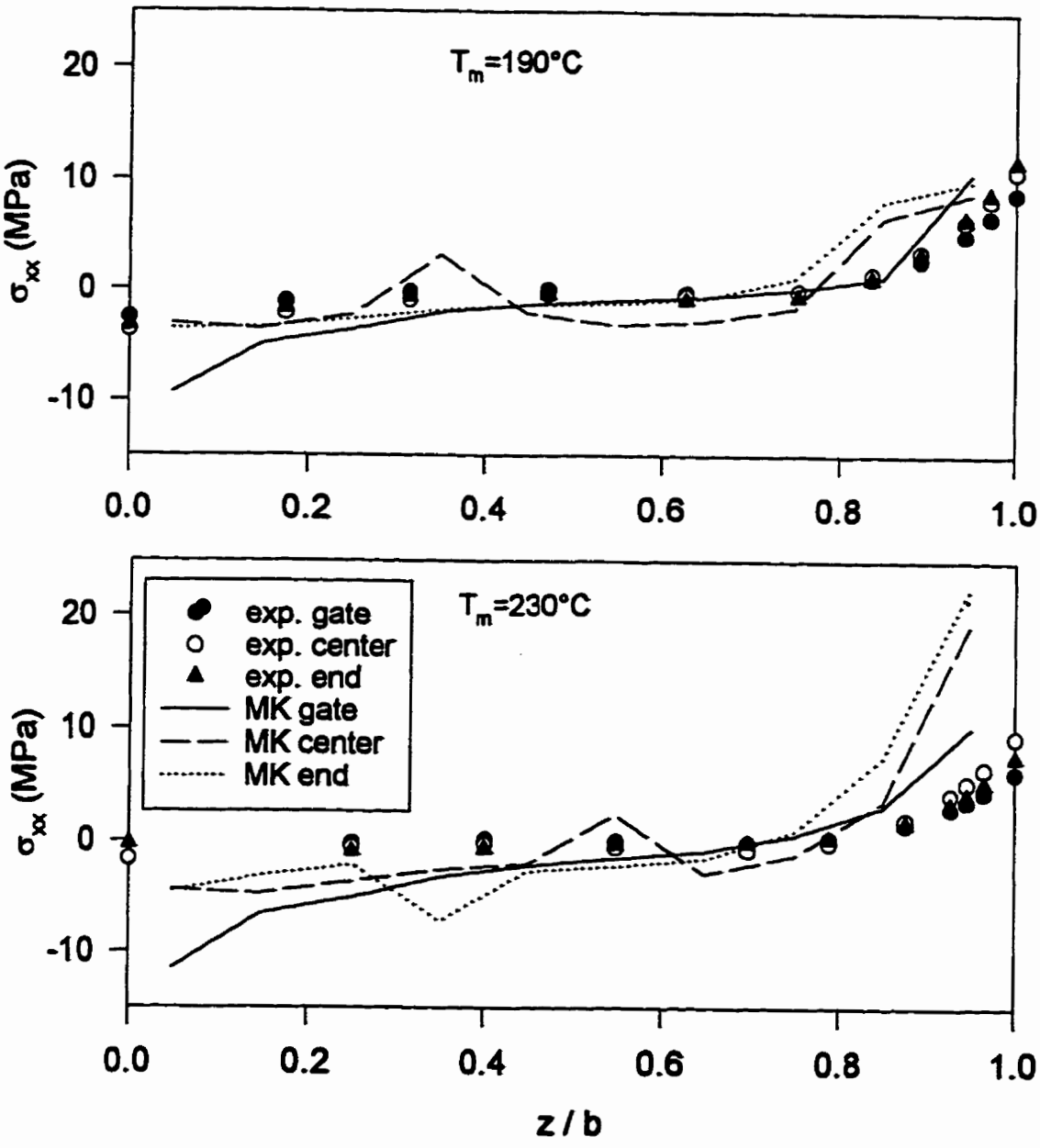

Fig.4.55.Residual stress profiles measured and calculated using McKam for 2 melt temperatures (runs 3, 5, HDPE)

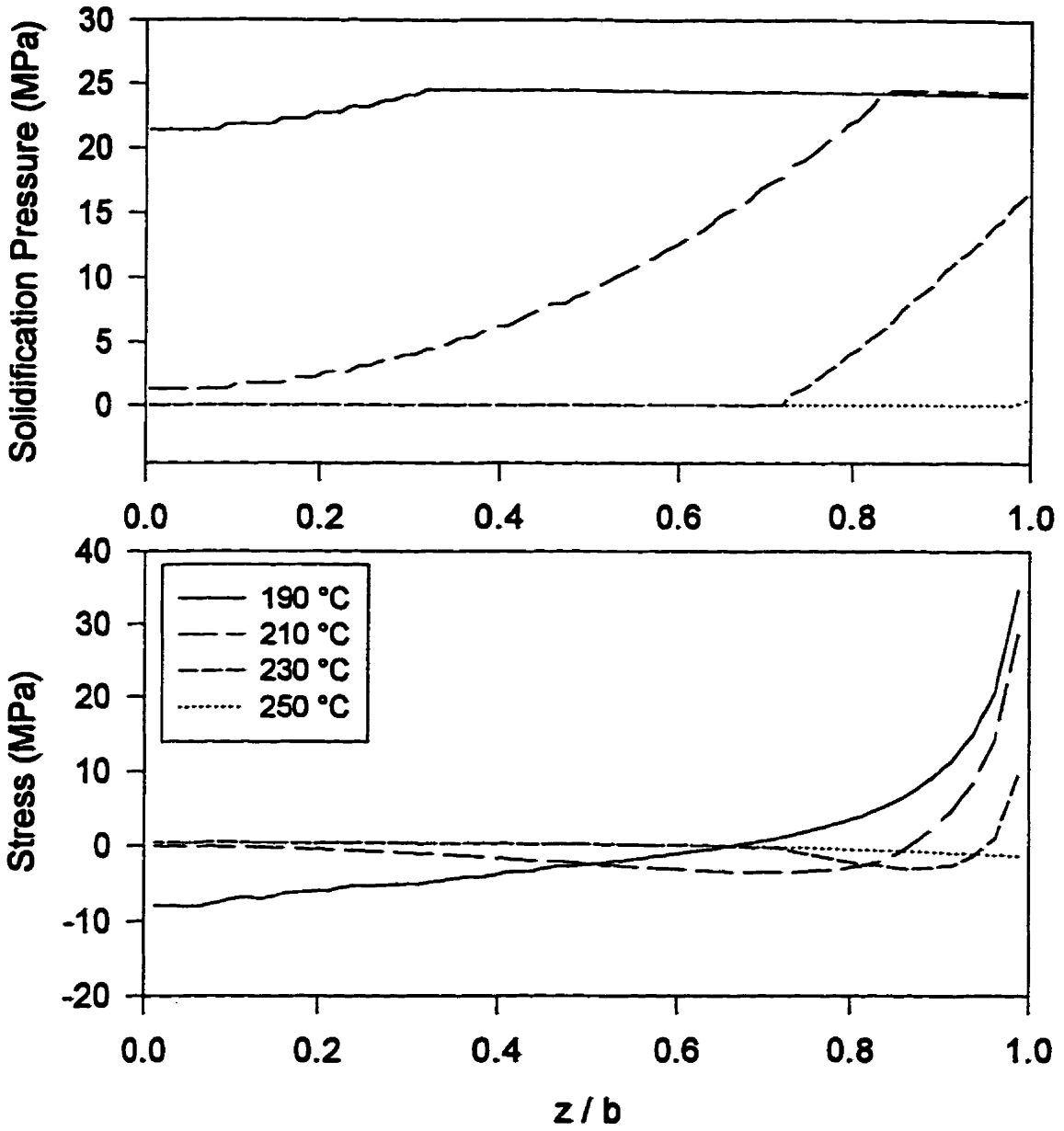

Fig.4.56.Solidification pressure and residual stress profiles for different melt temperatures and the same pressure history using 2-D FMS model (HDPE, run 1, Biot=0.45)

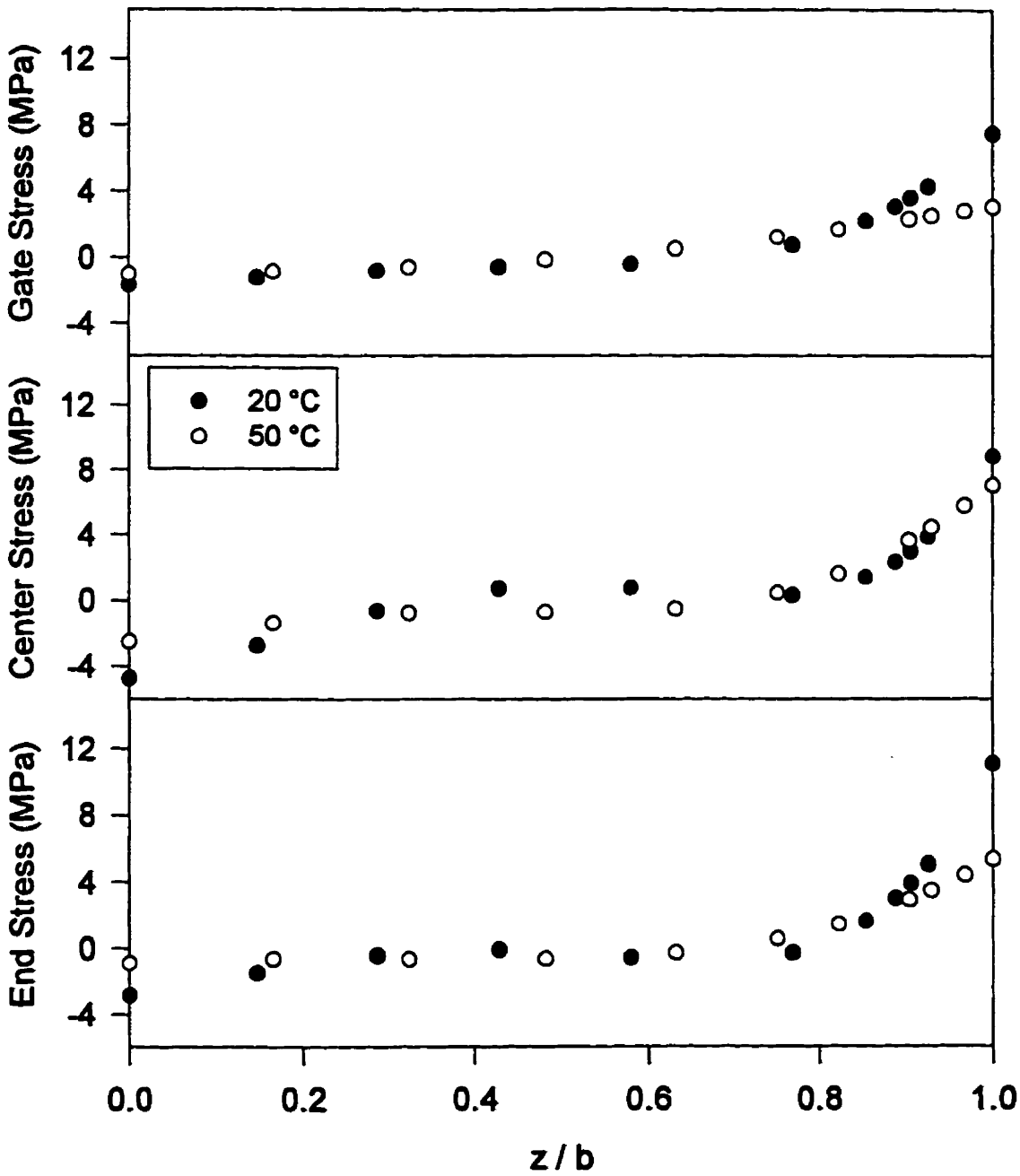

Fig.4.57.Measured residual stress profiles for 3 locations along the flow and 2 coolant temperatures (runs 2, 4, HDPE)

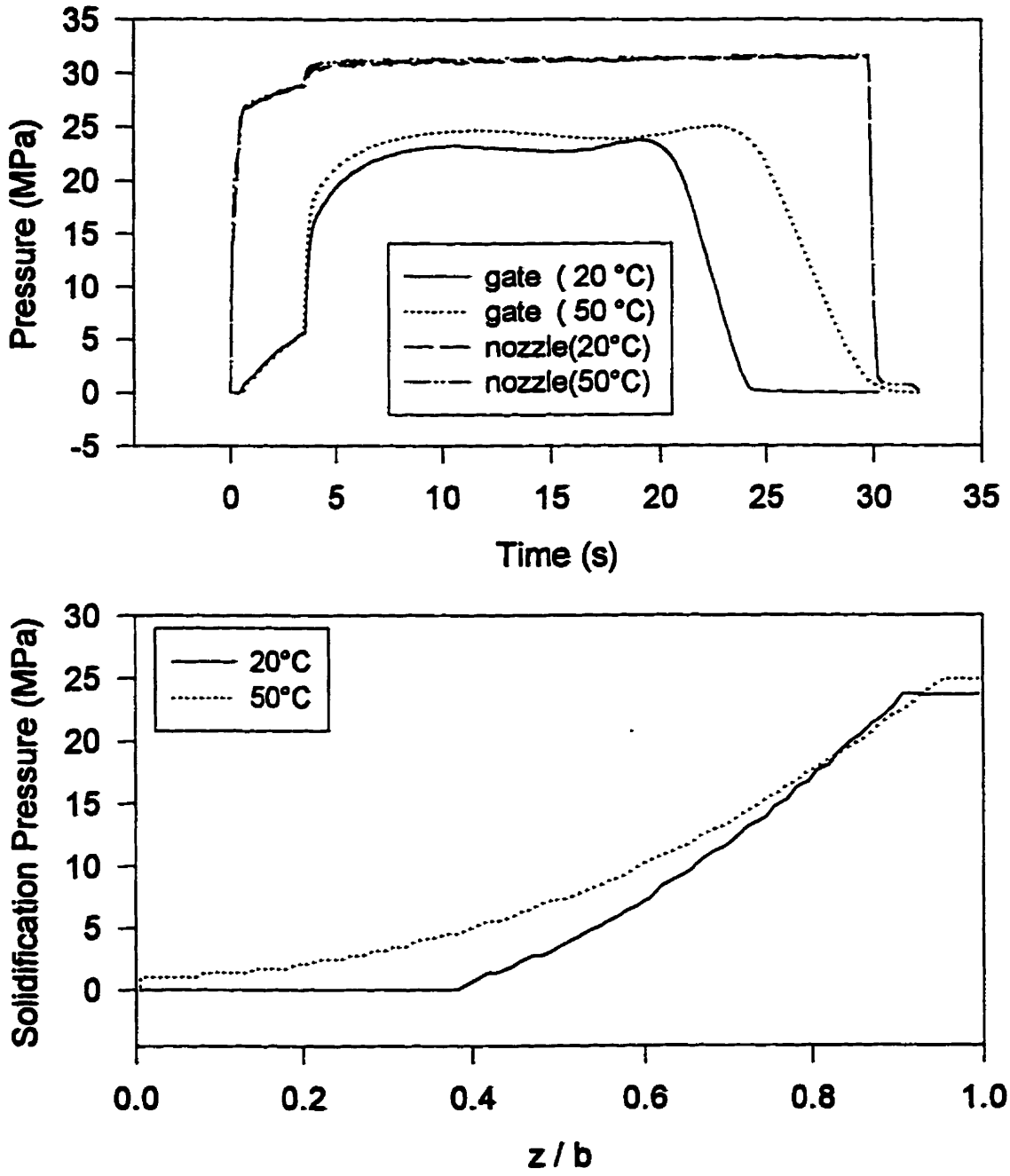

Fig.4.58.Measured pressure histories (top) and calculated solidifcation pressure (bottom) using 2-D FMS, for 2 coolant temperatures (runs 2,4,HDPE)

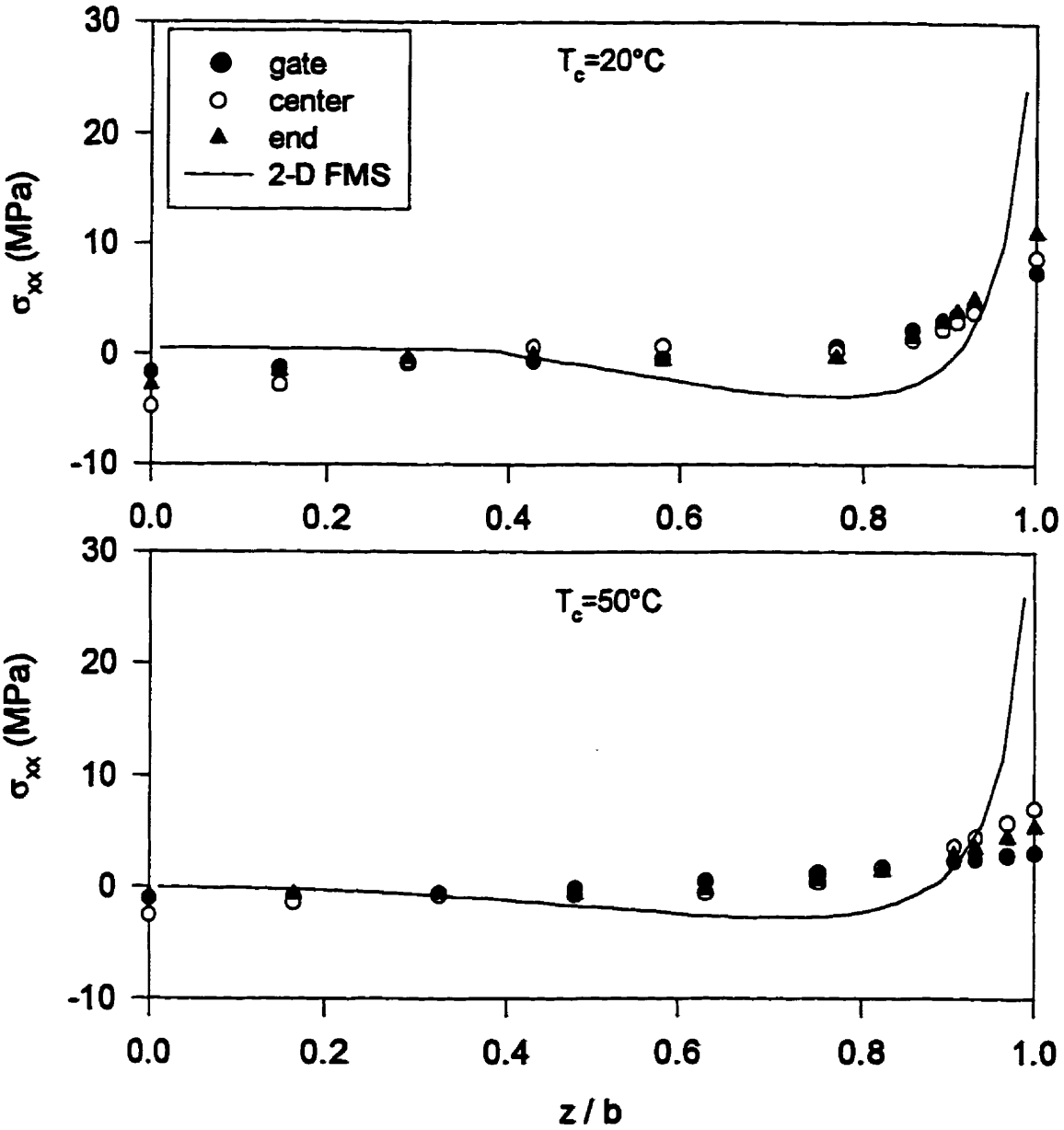

Fig.4.59.Residual stress profiles measured and calculated using 2-D FMS model for 2 coolant temperatures (runs 2,4, HDPE)

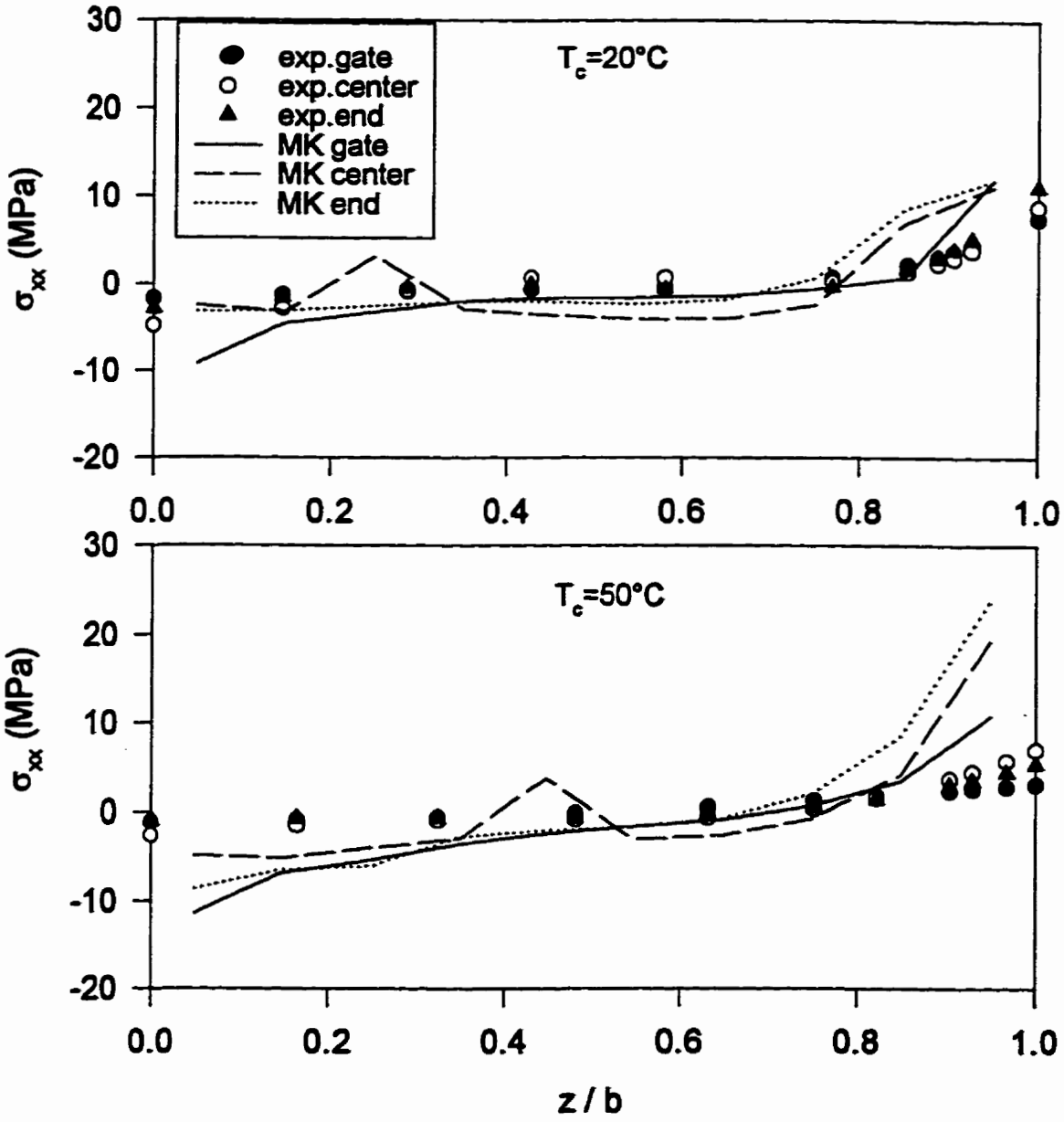

Fig.4.60.Residual stress profiles measured and calculated using McKam for 2 coolant temperatures (runs 2,4, HDPE)

midplane stresses are increased and decreased, respectively, as the coolant temperature is increased.

The calculations presented in Fig.4.61 using the 2-D FMS model and a fixed pressure history show that the surface and midplane stresses decrease by increasing the coolant temperature. In reality, the pressure history can not be constant for variable coolant temperatures.

4.1.2.4. Effect of Holding Time

Fig.4.62 presents the experimental residual stress profiles for holding times (h.t.) of 20 and 35 s. As shown in the measured pressure profiles in Fig.4.63 (top), in the case of h.t.=35s. the actual holding time for the gate position is about 23 s., since the gate solidifies at this time. Therefore, the actual difference in the holding times of the two runs is not significant. Near the gate (Fig.4.62, top), a slightly larger surface tensile stress is observed for the longer holding time. For the center and end positions, however, the order is reversed, especially on the surface.

The calculated P_s profiles in Fig.4.63 (bottom) indicate that more layers solidify under high pressure in the case of the higher h.t. The calculated stress profiles in Fig.4.64 show an increase in the magnitudes of the surface and mid-plane stresses as the holding time is increased. The stresses calculated by McKam in Fig.4.65 do not exhibit a large difference between the two runs.

Fig.4.66 illustrates more clearly the trend in the computed residual stresses for 3 different holding times, using the 2-D FMS model. Since only the holding time varies in the pressure histories, the mid-plane solidification pressure is close to zero for all three cases, resulting in almost identical mid-plane stresses.

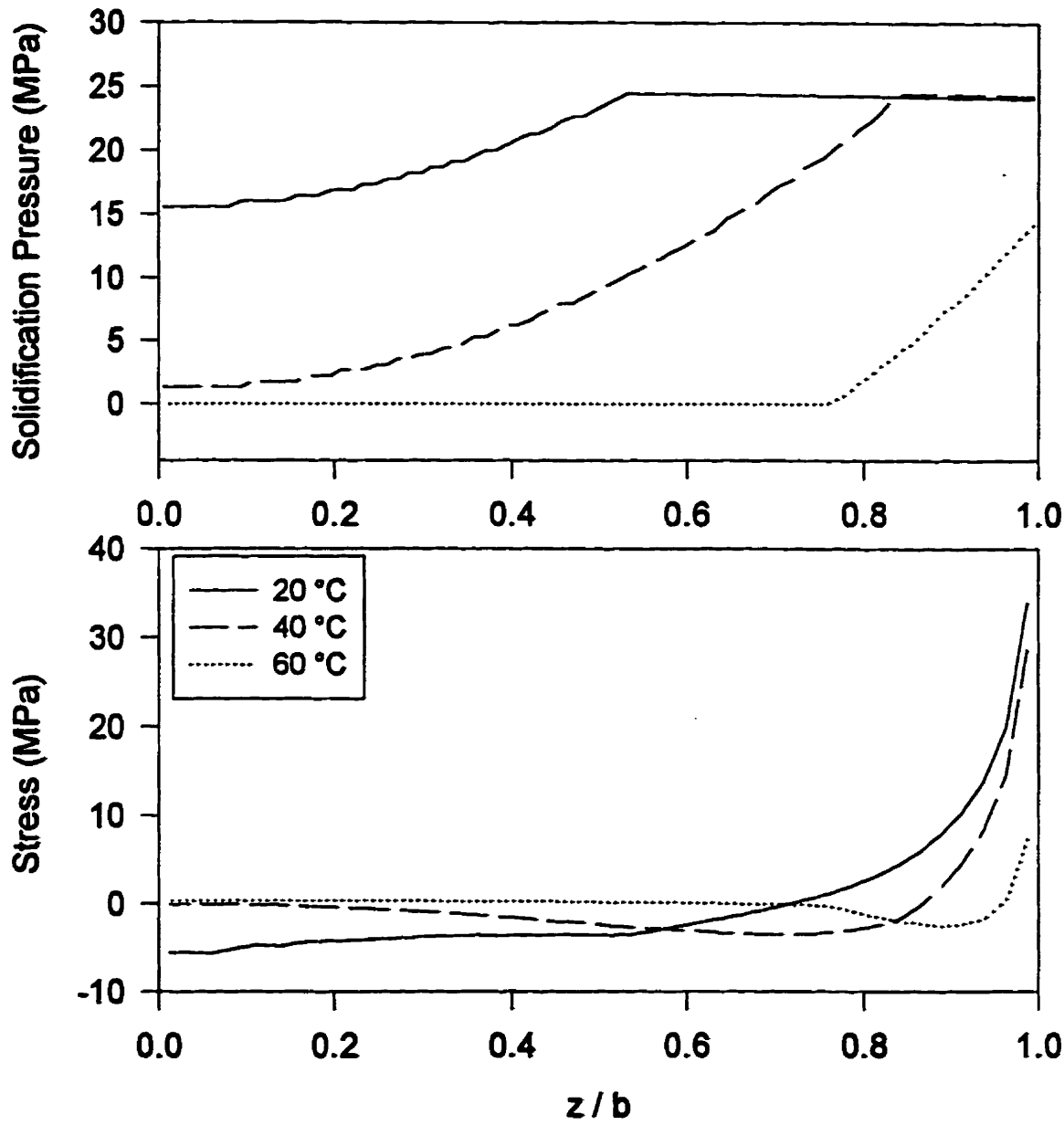

Fig.4.61.Solidification pressure and residual stress profiles for different coolant temperatures and the same pressure history using 2-D FMS (run 1,HDPE)

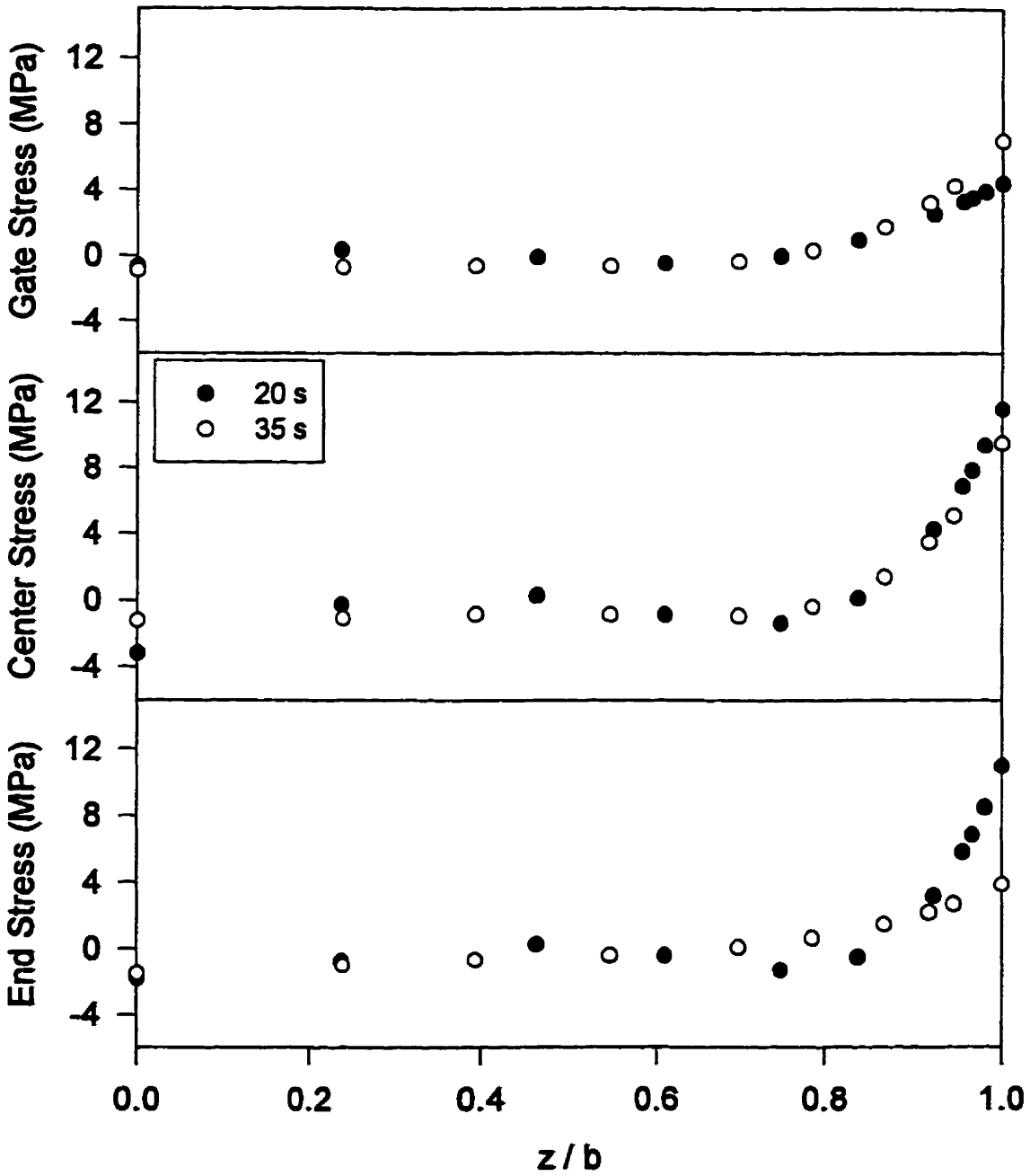

Fig.4.62.Residual stress profiles for 3 locations along the flow and 2 holding times (runs 6,7, HDPE)

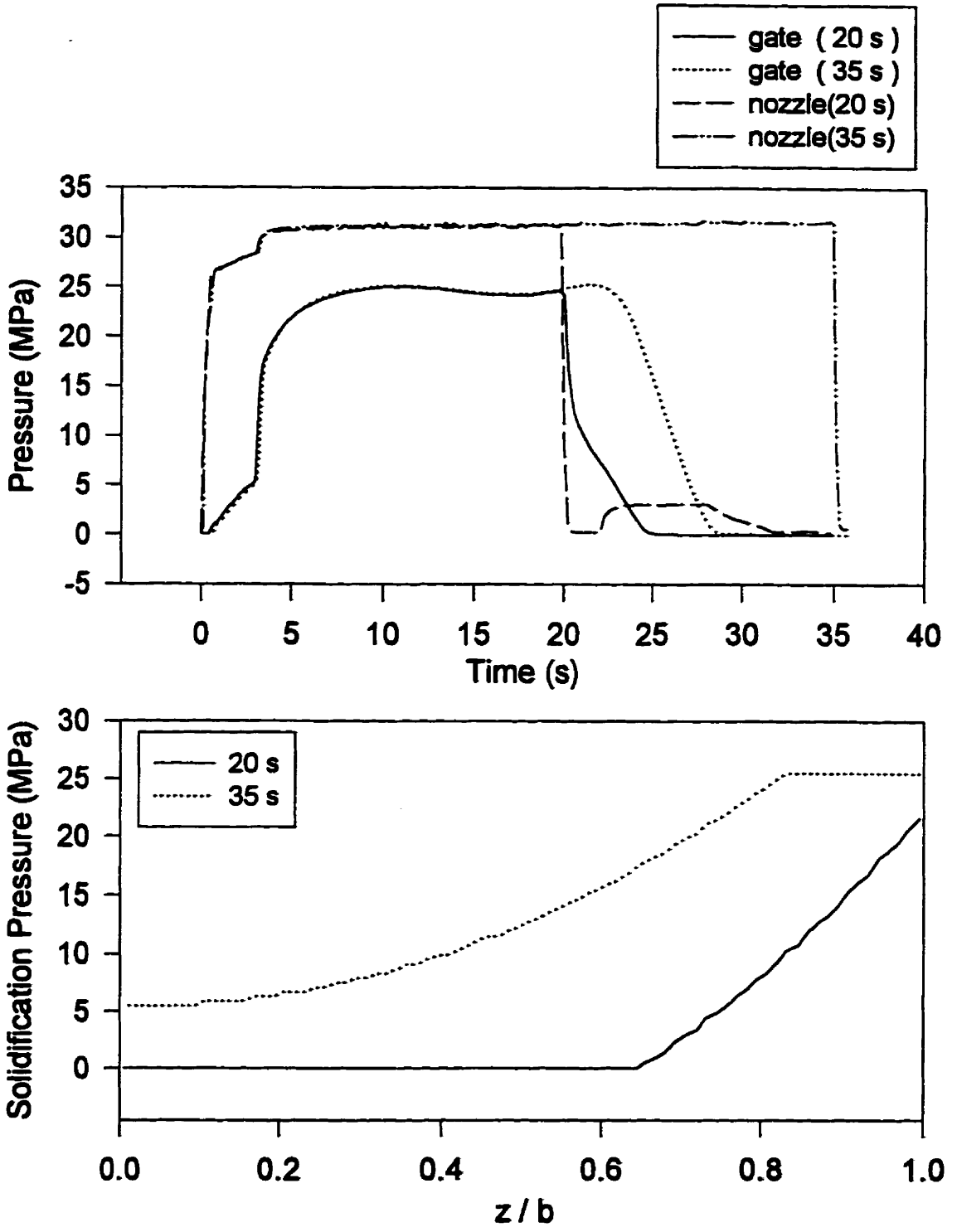

Fig.4.63.Measured pressure histories (top) and calculated solidification pressures (bottom) using 2-D FMS, for 2 holding times (runs 6, 7, HDPE)

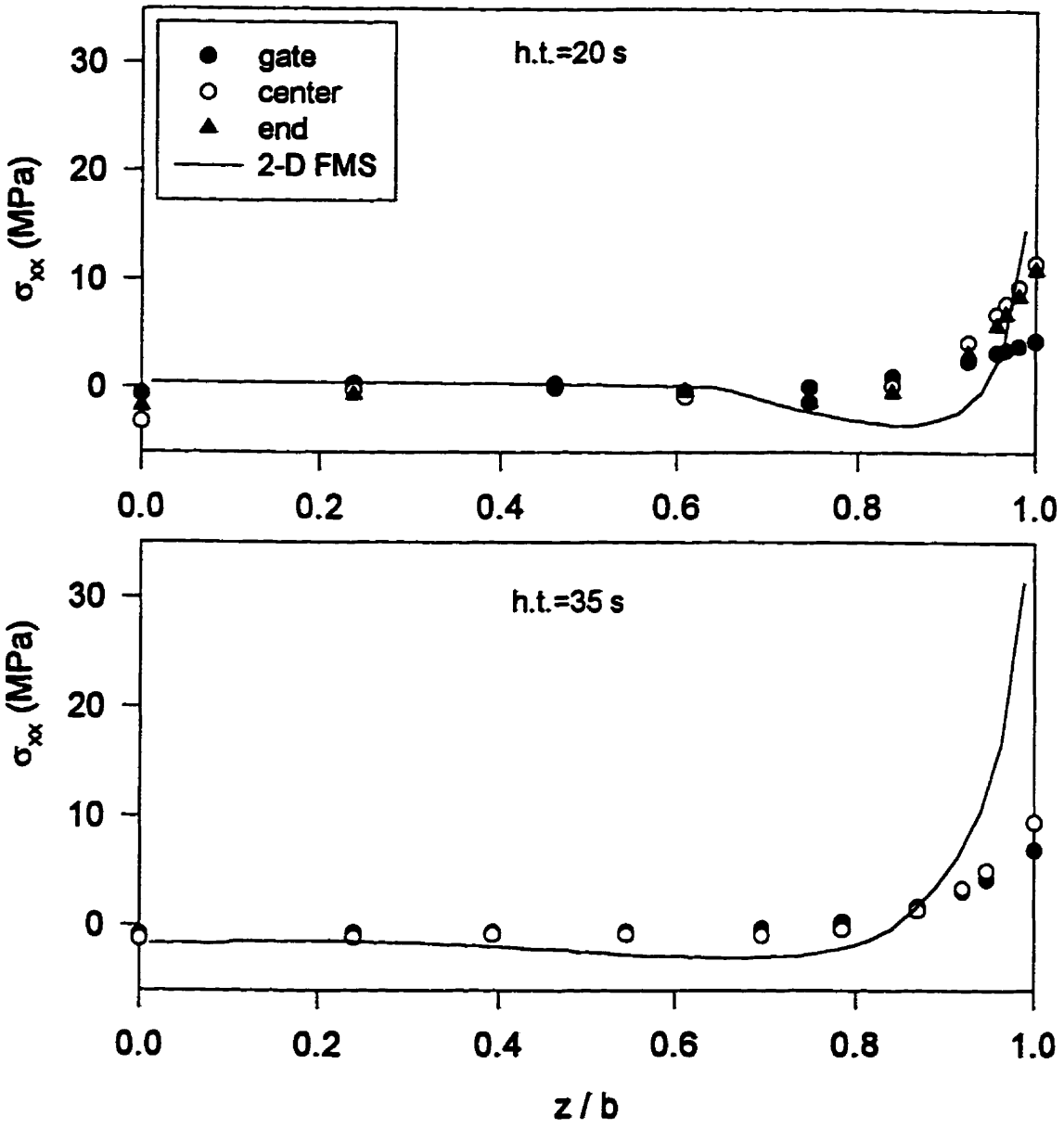

Fig.4.64.Residual stress profiles measured and calculated using 2-D FMS model for 2 holding times (runs 6, 7, HDPE)

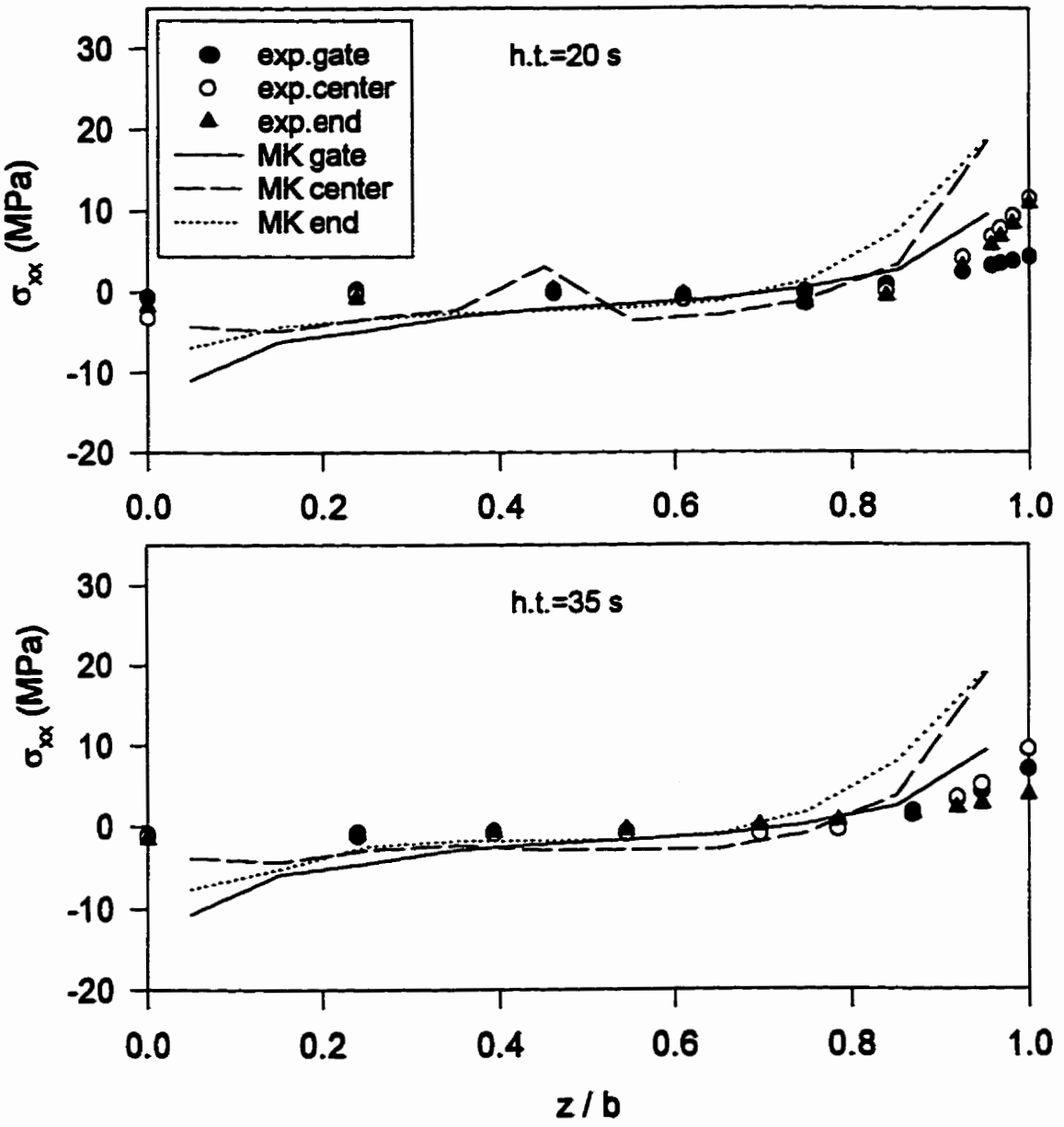

Fig.4.65.Residual stress profiles measured and calculated using McKam for 2 holding times (runs 6,7,HDPE)

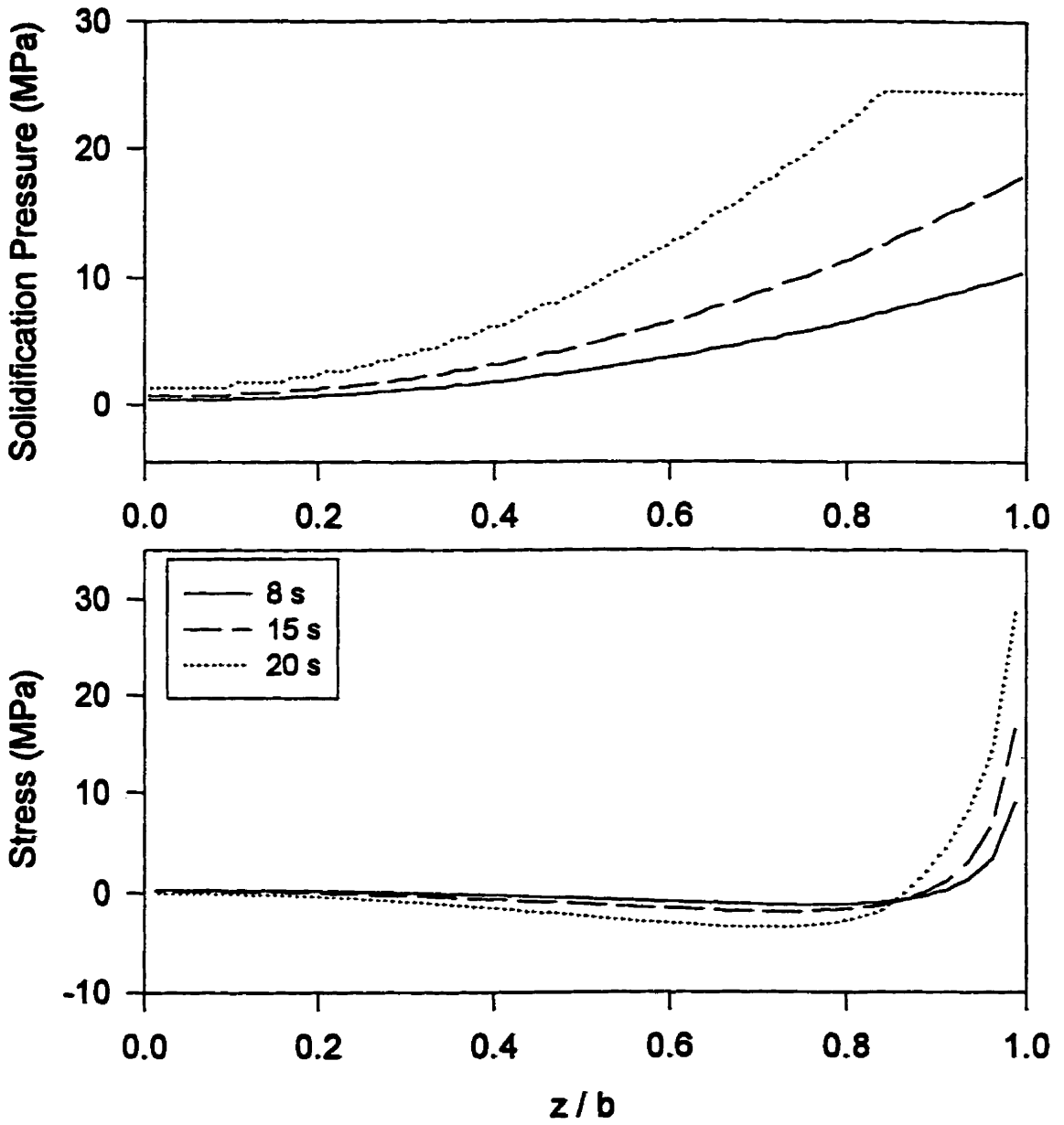

Fig.4.66.Solidification pressure and residual stress profiles for different holding times and the same pressure history using 2-D FMS model (HDPE, run 1)

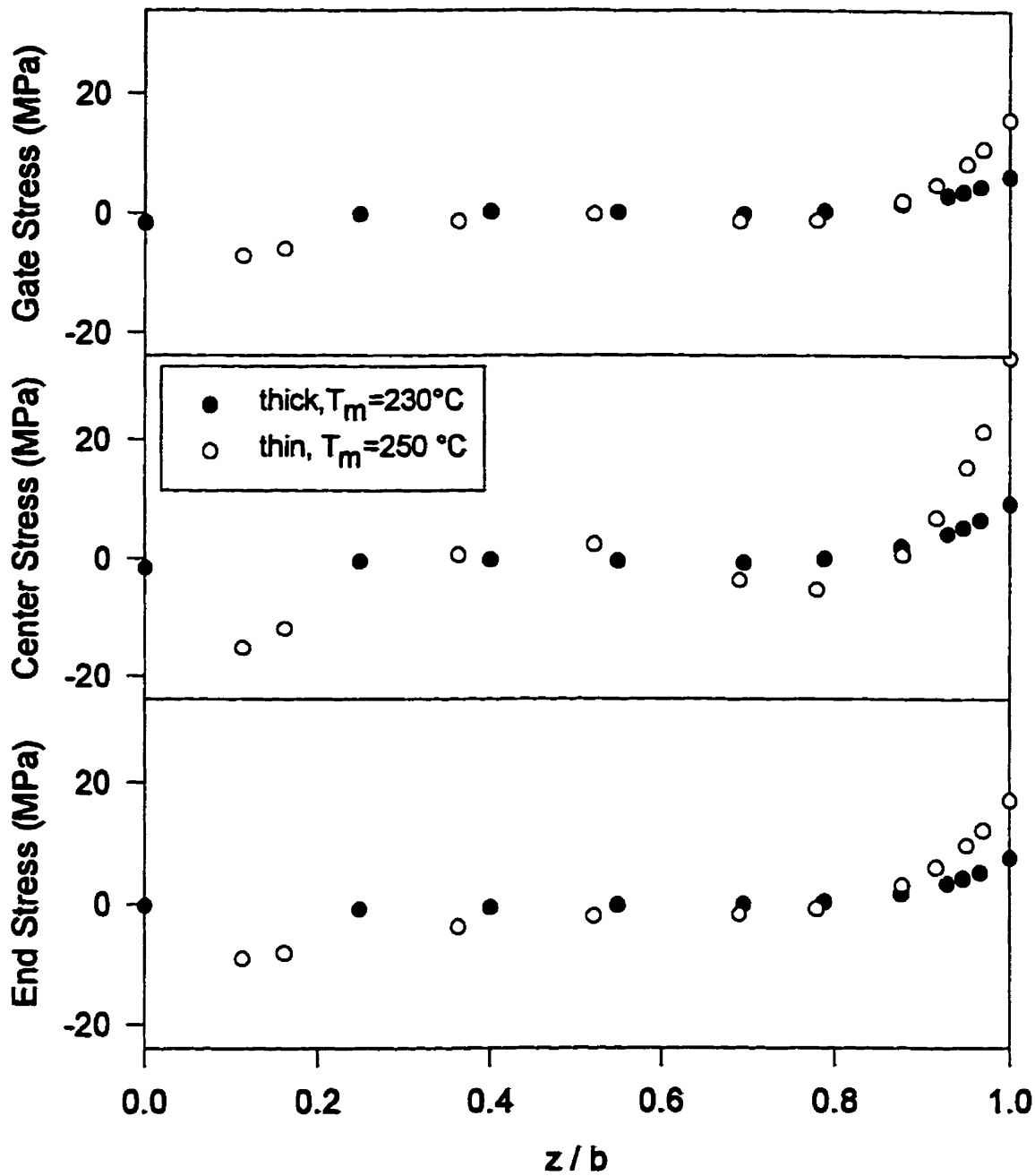

Fig.4.67.Residual stress profile for 3 locations along the flow and 2 mold thicknesses (runs 5,11 HDPE)

4.1.2.5. Effect of Mold Thickness

It was not possible to isolate the effect of mold thickness alone. When the thin mold (1.5 mm) was used, the melt temperature had to be raised from 230°C to 250°C to prevent the polymer melt from solidifying before filling the cavity (short shot). The measured residual stress profiles are presented in Fig.4.67. The surface and midplane stresses are larger in the thin mold compared to the thick one. This effect is more pronounced in the center of the cavity. Part of the increase of the stresses in the thin mold is counteracted by a higher melt temperature, since the latter reduces the stresses on the surface and in the core, as observed earlier. The corresponding pressure histories are given in Fig.4.68 (top). The filling time is much shorter in the thin mold. Also, the solidification of the gate and of the complete sample is significantly faster in this mold. During packing, the pressure drop between the nozzle and the gate is smaller for the thin mold. The calculated solidification pressure in Fig.4.68 (bottom) shows that all layers of the sample solidify under the maximum pressure in the thin mold. The stresses calculated by 2-D FMS and McKam[©] are presented in Fig.4.69 and 4.70, respectively. Although the calculations from both models overpredict the stresses, they show a trend consistent with the experiments.

Calculations were also performed for molds with four different thicknesses using a fixed pressure history. Since the pressure history changes substantially with mold thickness, the results of such calculations were not found useful to include here and were omitted.

4.1.2.6. Effect of Packing Pressure

Two runs with the thin mold were selected to investigate the influence of the packing pressure. The measured stress profiles are shown in Fig.4.71. As shown by the measured pressure histories in Fig.4.72 (top), the difference in the packing pressure was not large. The stresses show no significant difference except for the center location, where the stresses for the high packing run are larger. In both of these two runs with thin molds, all the layers of the sample solidify under high pressure, as illustrated by Fig.4.72 (bottom). The stresses calculated by the 2-D FMS model and McKam[©] show slightly

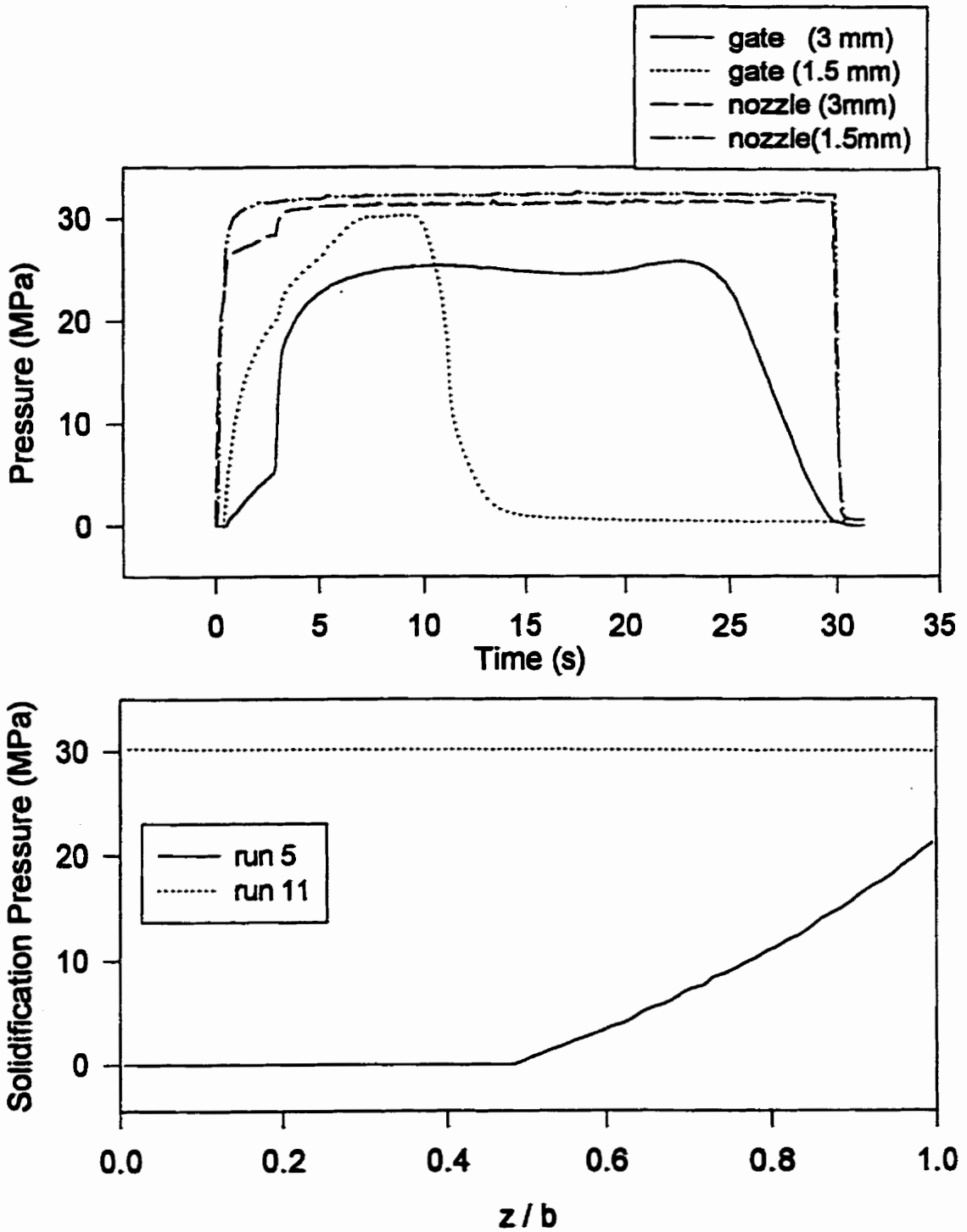

Fig.4.68. Measured pressure histories (top) and calculated solidification pressures (bottom) using 2-D FMS, for 2 mold thicknesses (run 5: thick, T_m=230°C ; run11: thin, T_m=250°C, HDPE)

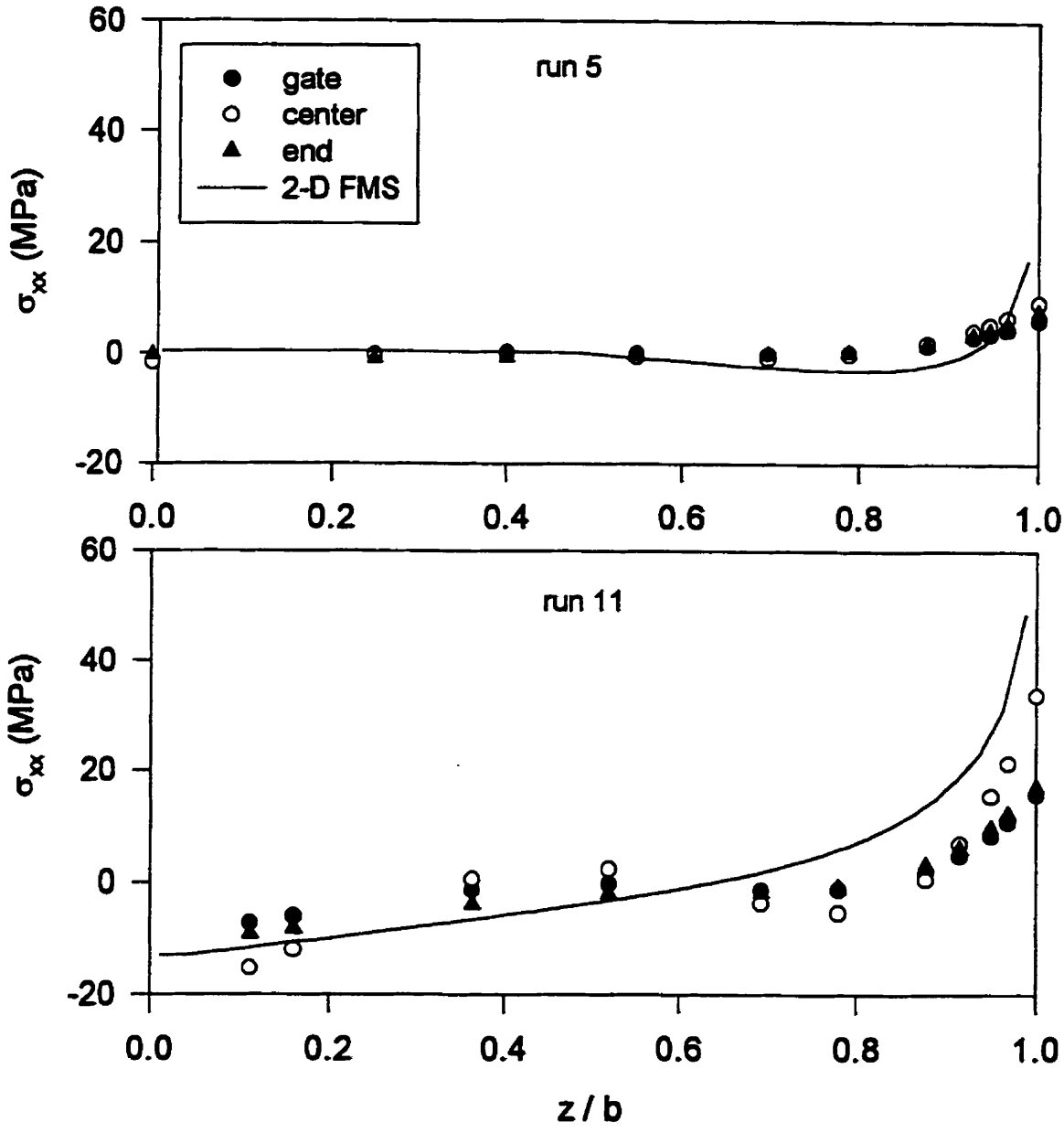

Fig.4.69.Residual stress profiles measured and calculated using 2-D FMS model for 2 mold thicknesses (runs 5, 11, HDPE)

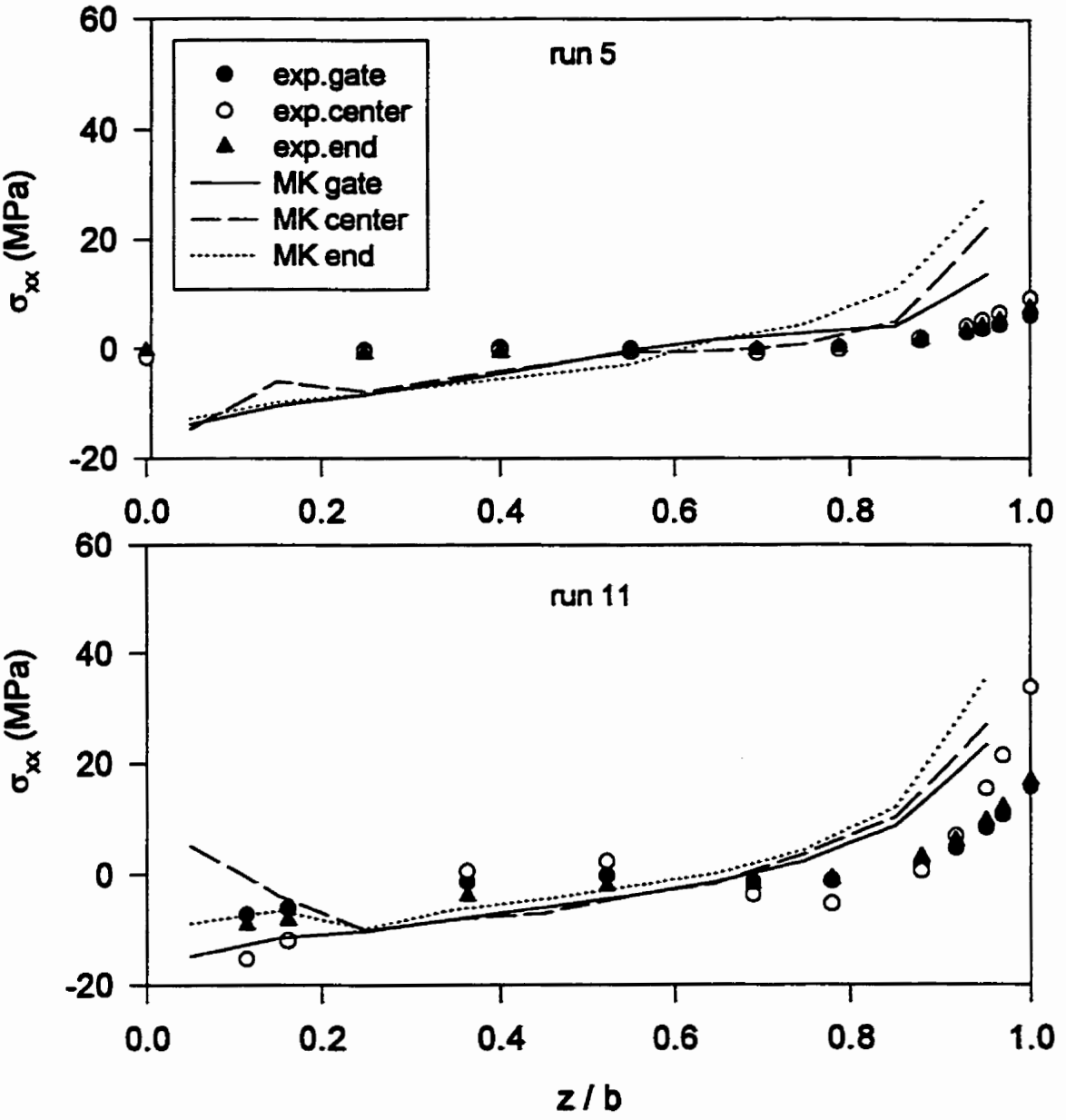

Fig.4.70.Residual stress profiles measured and calculated using McKam for 2 mold thicknesses (runs 5, 11, HDPE)

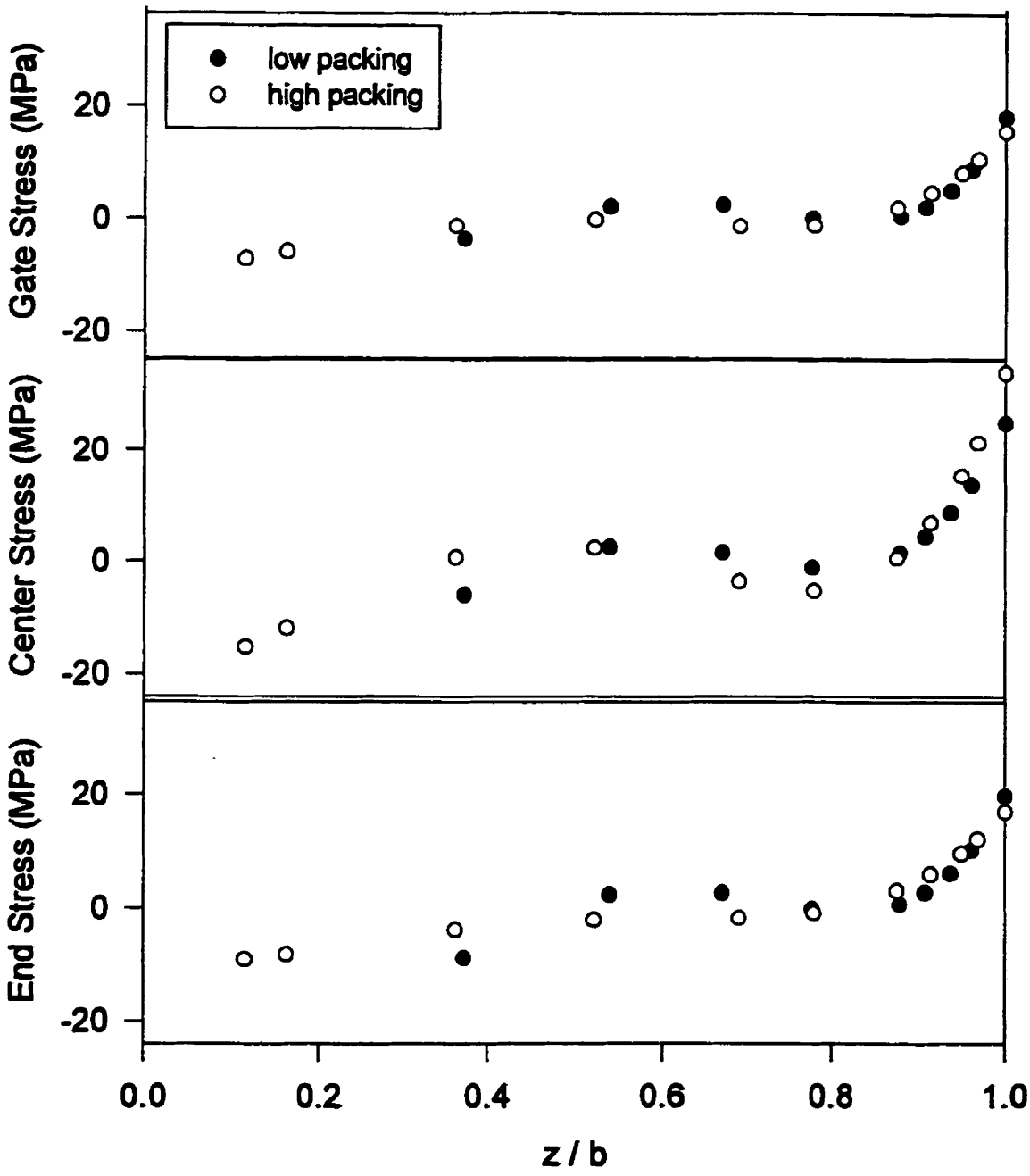

Fig.4.71.Residual stress profiles for 3 locations along the flow and 2 packing pressures (runs 10,11,HDPE)

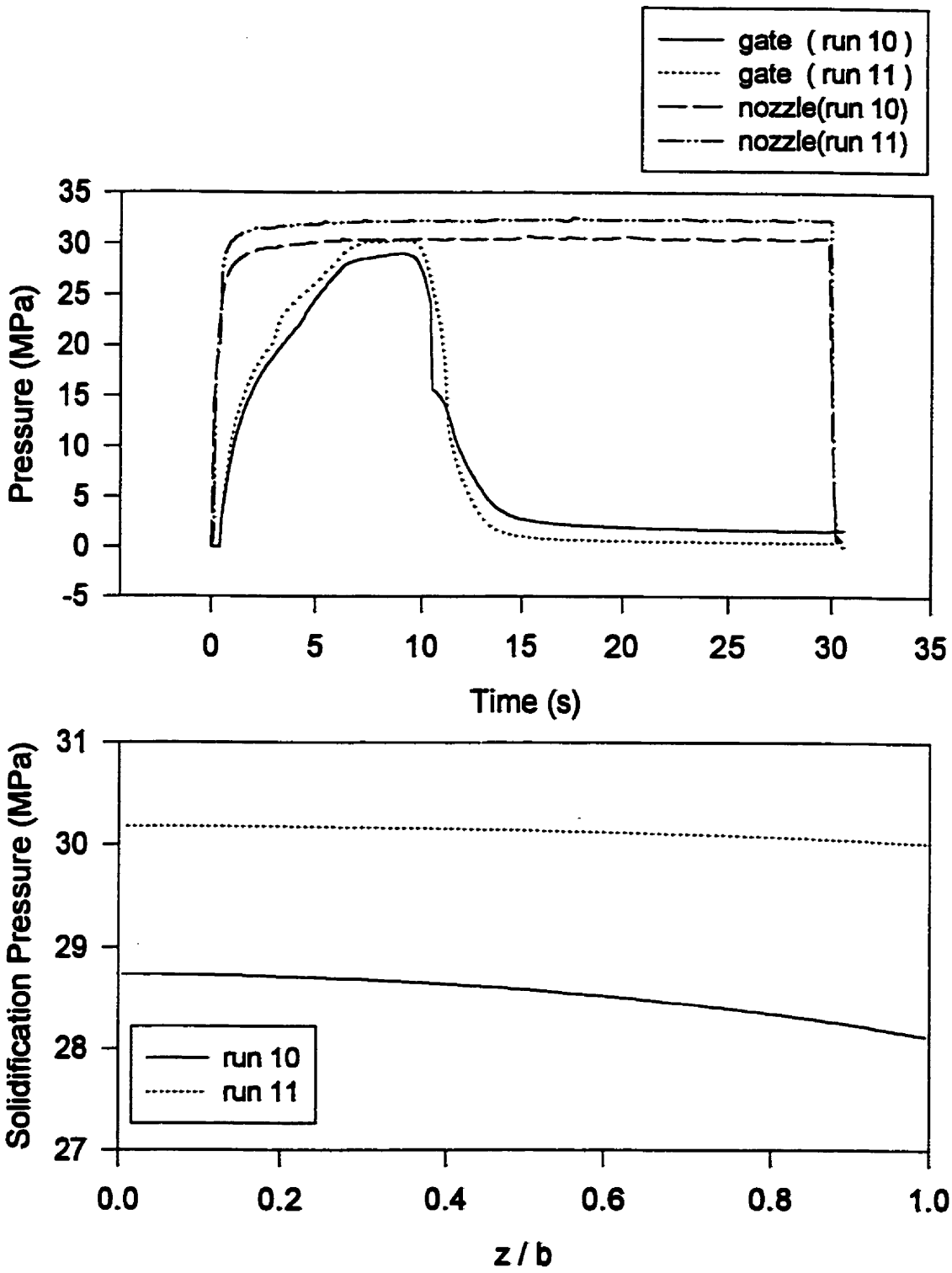

Fig.4.72.Measured pressure histories (top) and calculated soldification pressures (bottom) using 2-D FMS, for 2 packing pressures in thin molds (runs 10,11, HDPE)

higher stresses for the high packing run (Fig.4.73 and 4.74). The stresses obtained from McKam©, however, are smaller and closer to experiments, in spite of the discrepancy between the calculated and experimental pressure histories. Predicted profiles in Fig.4.75 show that, if everything else is kept constant, a decrease in the packing pressure from 30 to 10 MPa causes the surface stress to decrease from 38 to 12 MPa.

4.1.3. INVERSE PROBLEMS

Fig.4.76 presents the measured (18) and calculated residual stresses (51, 52) used to develop and test the inverse methods in this section. The symbols in this figure show the measured residual stress distribution and the corresponding pressure history reported by Menges et al. (18) for injection molding of PS with initial melt temperature of 235°C and mold temperature of 20°C (condition I in Table 2.1). Menges et al. did not report the exact pressure-time cycle. The profile shown in Fig.4.76 (top) and suggested by Brucato et al. (52) is consistent with the maximum pressure and holding time in their experiment. Here, solidification starts at the end of filling and the pressure is assumed zero before that instant. The figure also shows the predictions of the CMS (52) and the 1-D FMS (51) models for the stresses. These models have been described in Chapter 2. The CMS model seems to predict the reported experimental stresses more closely.

4.1.3.1. Unknown Pressure History

The aim is to estimate the pressure history required to generate a specific residual stress profile.

Constrained Mold Shrinkage Model (CMS)

Testing with the Direct Solution

The inverse method was first tested taking the solution of the direct CMS model (Fig.4.76) as the prescribed stress profile. This solution was obtained using the experimental pressure history. The pressure history calculated by the inverse method is depicted by the filled circles in Fig.4.77. Both the initially assumed pressure history to

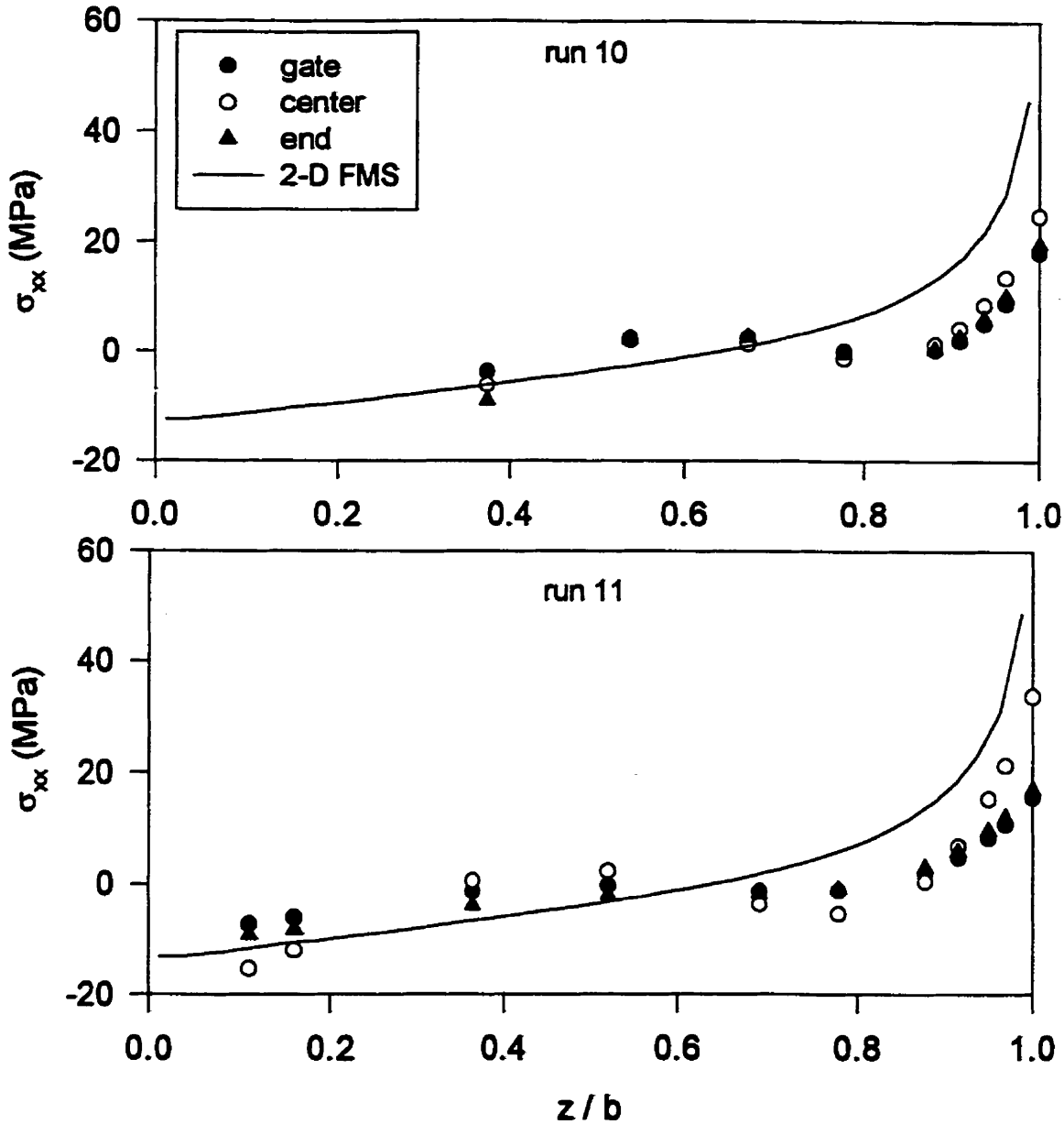

Fig.4.73.Residual stress profiles measured and calculated using 2-D FMS model for 2 packing pressures in thin molds (runs 10, 11, HDPE)

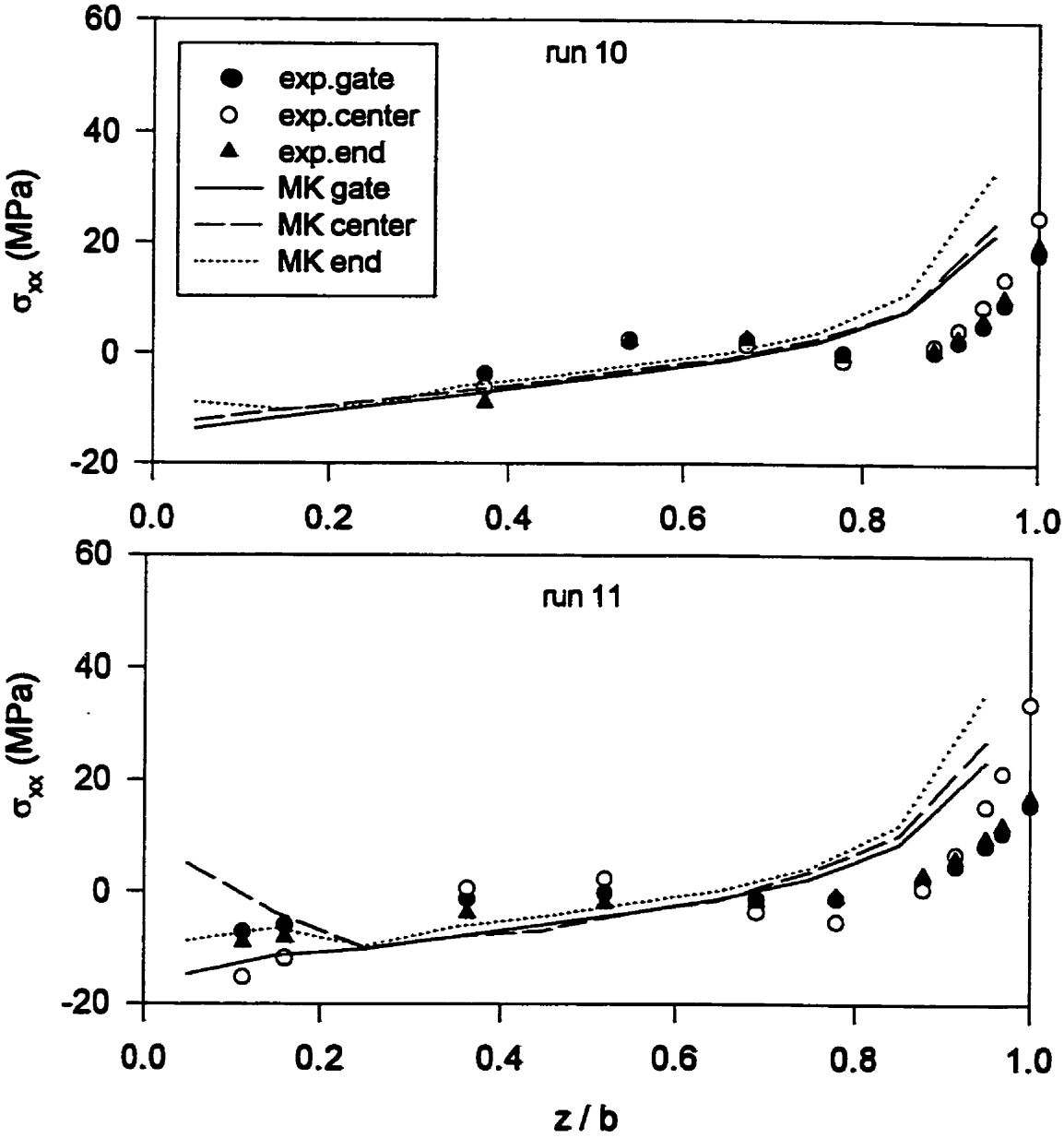

Fig.4.74.Residual stress profiles measured and calculated using McKam for 2 packing pressures in thin molds (runs 10, 11, HDPE)

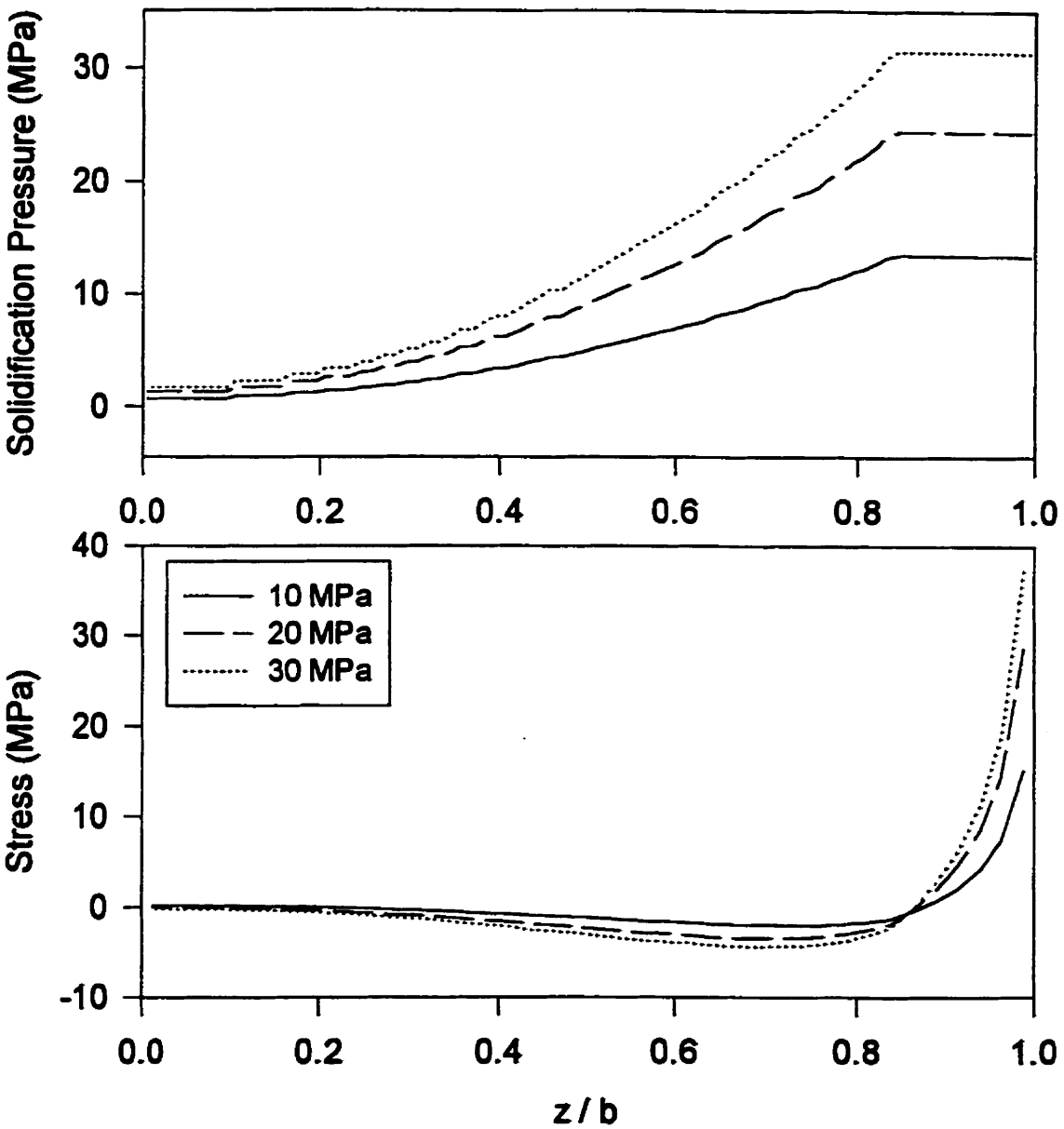

Fig.4.75.Solidification pressure and residual stress profiles calculated for 3 packing pressures using 2-D FMS (HDPE, Biot=0.45)

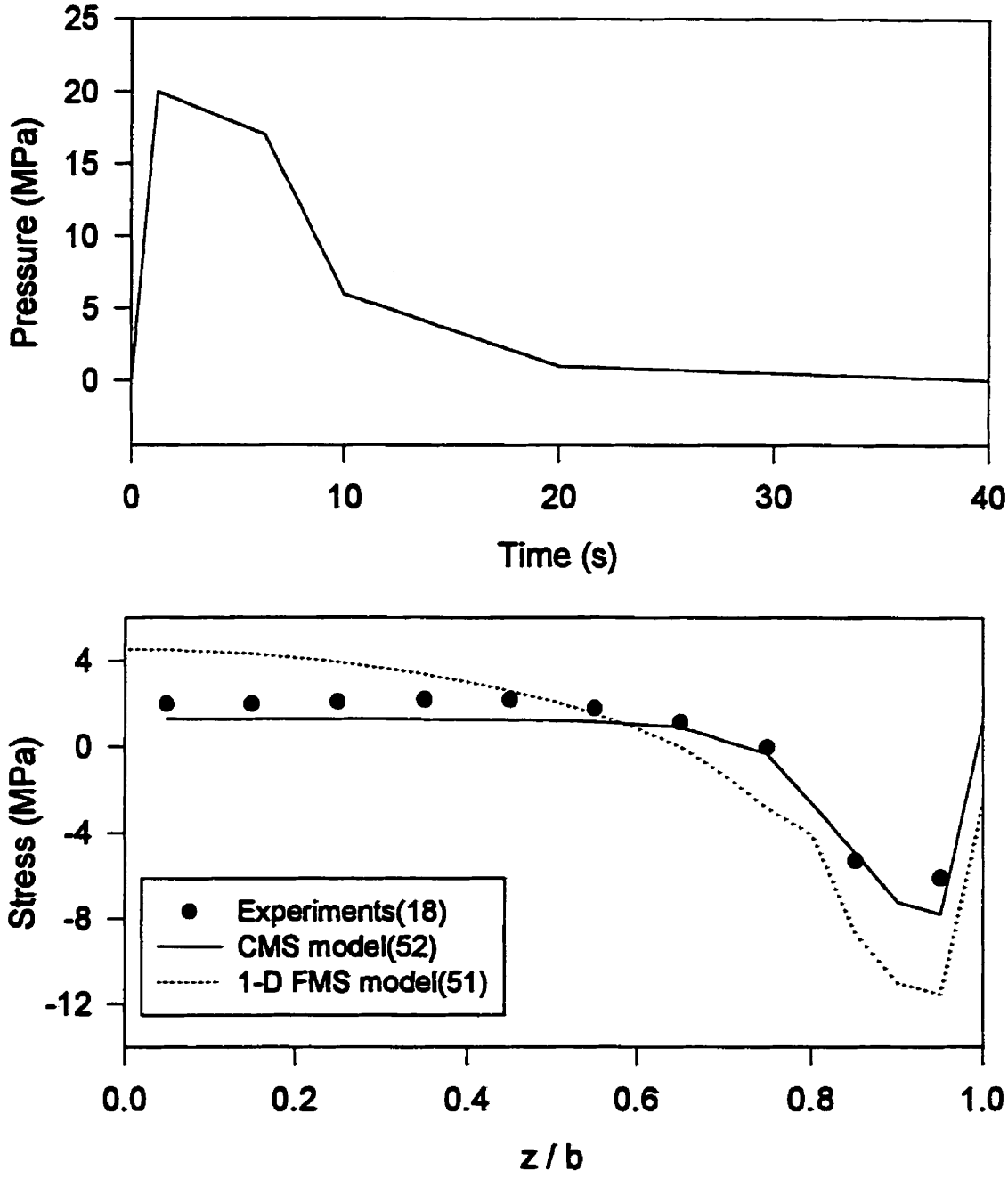

Fig.4.76.Residual stress profiles measured and calculated using different models for PS and conditions I in Table 2.1 .

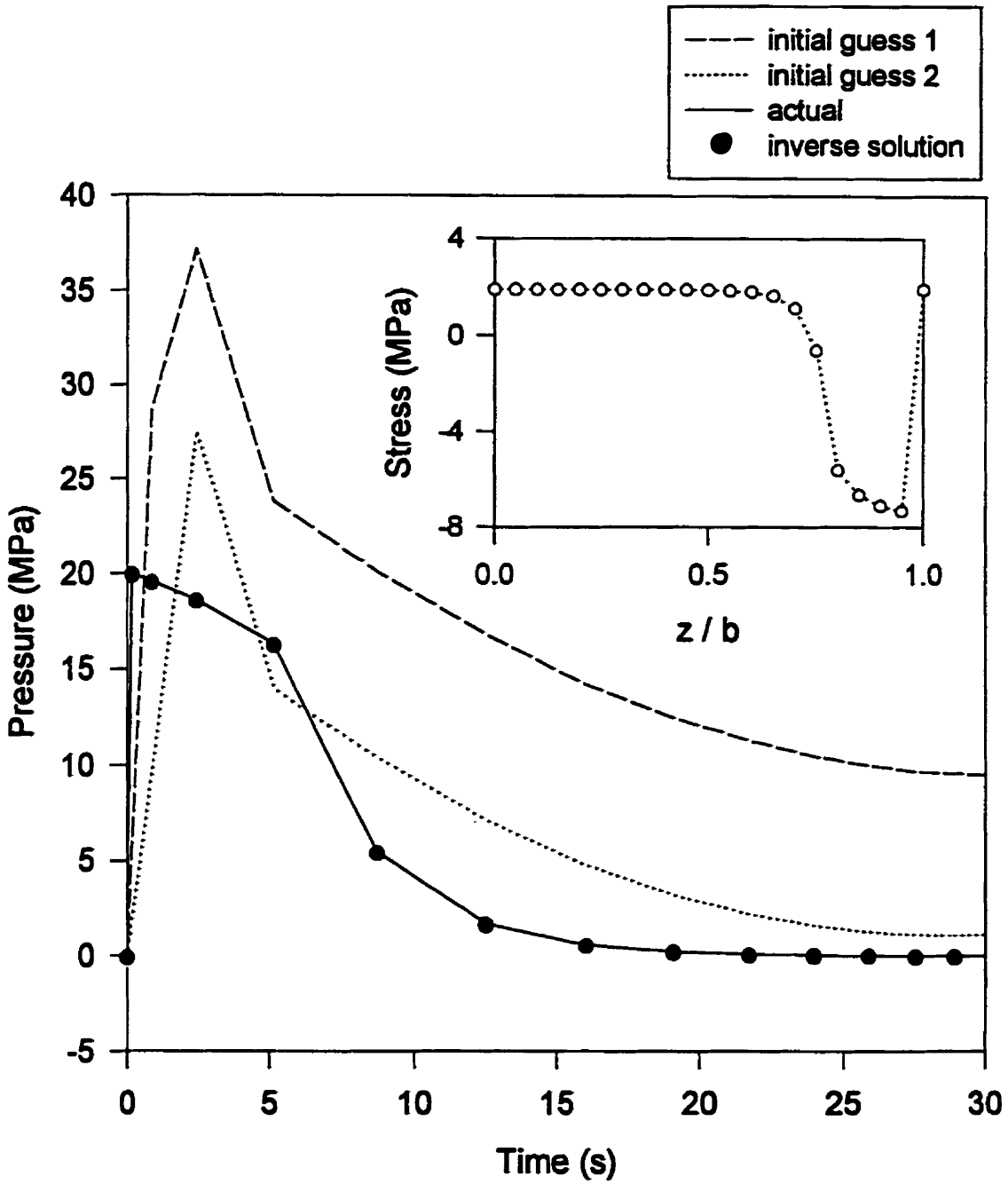

Fig.4.77.Actual pressure history, two initial guesses, and the inverse solution using the stress data from CMS model, a parabolic initial temperature, and conditions I in Table 2.1 for PS

calculate the stress data (actual) and two different initial guesses for the minimization procedure are also shown in Fig.4.77. Starting from any initial guess, the actual pressure is reproduced very closely and with no difficulty, by the inverse method.

Effect of Added Errors

Real experimental measurements are subject to errors. Therefore, an important criterion for the performance of an inverse method is its sensitivity to errors. In order to simulate experimental errors, random errors were generated numerically (102) and added to the "exact" stress data. These stress data were then used as the prescribed stresses along the thickness. Fig.4.78 demonstrates the effect of noise in the residual stress data on the estimated pressure history. The stress data with added errors of different magnitudes are also shown in this figure. It appears that the inverse method is sensitive to errors, and the introduction of noise in the stress data leads to an overprediction of the pressure. Also, as the magnitude of the noise increases, the predicted profile tends to move further from the actual pressure profile represented by the line. However, the general features of the pressure profile are predicted with reasonable accuracy. It is interesting to note that the predicted pressure rises again at the end of the cycle, unlike the actual pressure. This may be related to the oscillatory character of the tensile stress data with added errors in the core. Since the pressure is constrained to physically acceptable positive values, these oscillations in the stress data lead to a rise in the pressure at the end. Another observation is that the magnitude of the errors in the estimated pressure is much larger than in the prescribed stress data. Random errors of ±0.5 MPa in the stress cause a maximum error of 3 MPa in the pressure.

Testing With Experimental Results

Experimental data for residual stresses reported by Menges et al. (18) presented in Fig.4.76 were used to test the above inverse method. Fig.4.79 shows the pressure history calculated by this inverse method. The reported holding pressure and holding time of the injection molding experiment were 20 MPa and 5 s., respectively. The maximum pressure is underpredicted by the inverse method. This was somewhat expected, considering that

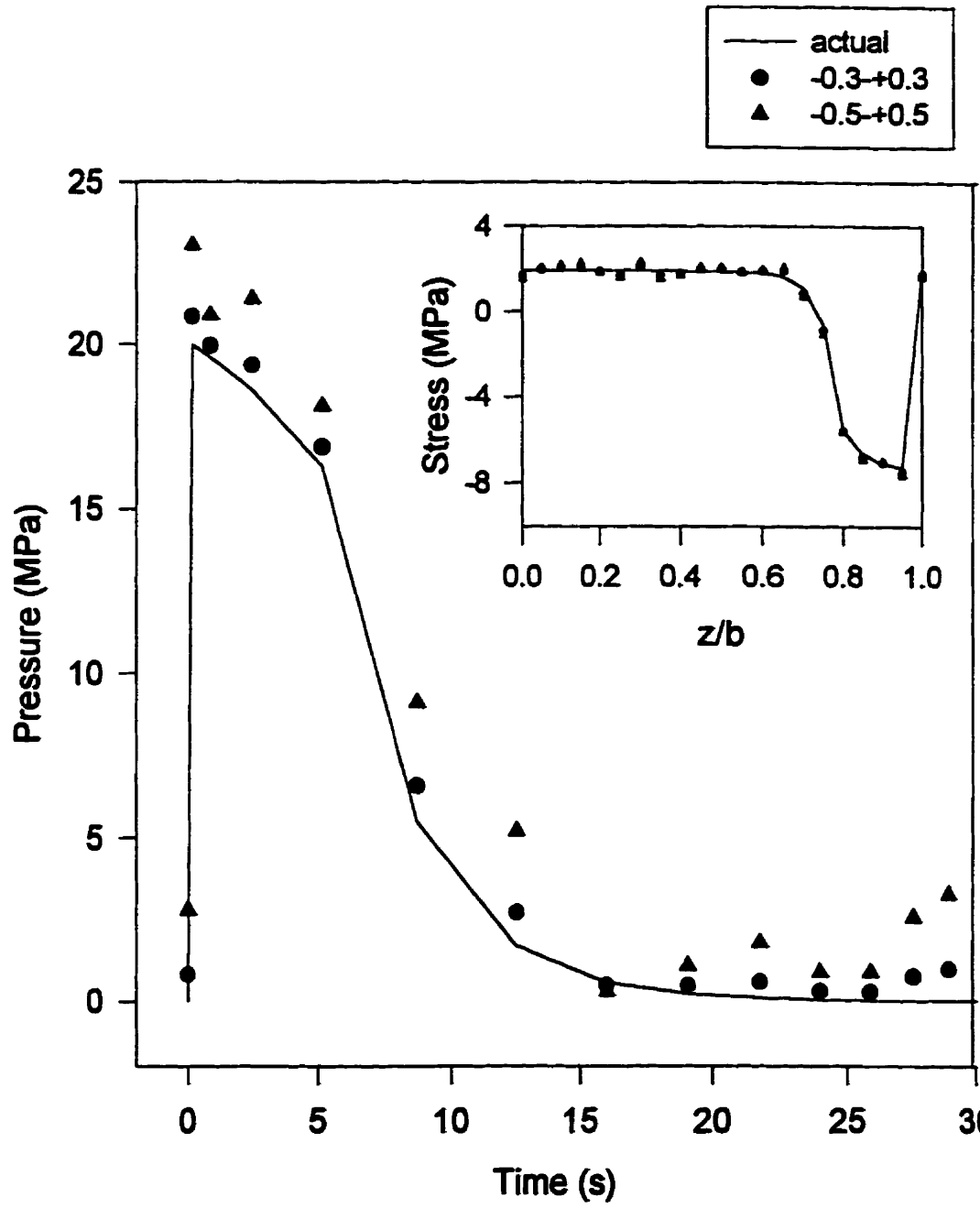

Fig.4.78.Pressure history calculated from inverse model, using the stress distribution from CMS model with added random errors.

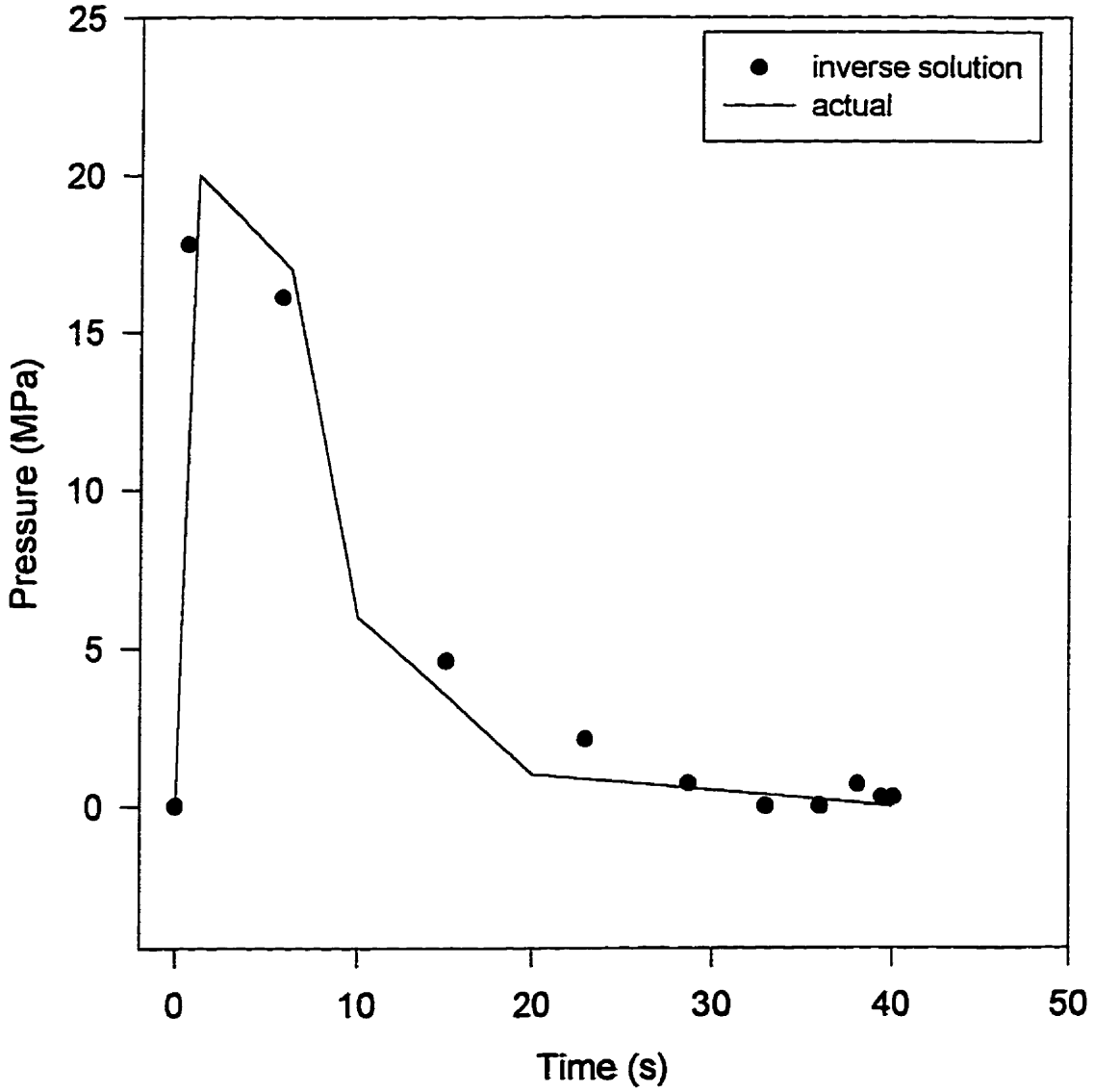

Fig.4.79.Experimental testing of the CMS inverse method using stress data from reference (18)

the maximum pressure corresponds to the compressive region in the stress profile. As shown in Fig.4.76, the maximum compressive stress is overpredicted by the direct CMS model using the experimental pressure history. Therefore, going backwards from the measured stresses, it is reasonable to obtain a lower maximum pressure. In Fig.4.76, in the tensile stress region in the core, there is not a large difference between the predictions of the pressure-induced model and the measurements. Similarly, the predicted pressure history in Fig.4.79 seems to be closer to the experimental profile at the end of the cycle.

One-dimensional Free Mold Shrinkage (1-D FMS) Model

Testing with the Direct Solution

The method was tested in conjunction with residual stresses calculated from the forward problem using the 1-D FMS model (52) and the experimental molding conditions reported by Menges et al. (18) (conditions I, Table 2.1). The pressure history indicated in this reference and detailed by Titomanlio et al. (52) was employed. Fig.4.80 shows the stress data calculated from the direct 1-D FMS model and used in the inverse problem as the prescribed stress profile to estimate the pressure. Fig.4.80 also compares the calculated pressure history using this method to the actual pressure history. Very good agreement is obtained.

Effect of Added Errors

As in the previous case, the above analysis was repeated, adding random errors to the stress data used as the prescribed stress profile. The pressure history resulting from the noisy data is shown in Fig.4.81. As expected, the larger the magnitude of the errors, the further the predicted pressure is from the actual pressure. However, the shape of the pressure profile is correctly predicted even when the error in the stress data is ±1.0 MPa. The sensitivity to the errors is actually smaller in this case than with the CMS inverse method.

Testing with Experimental Results

The 1-D FMS inverse method was tested with the experimental residual stress data from Menges et al. (18). The symbols in Fig.4.82 represent the pressure history calculated from the 1-D FMS inverse method for three different values of final shrinkage δ_f, and the line shows the pressure history corresponding to the experiments (51). The total final shrinkage δ_f is needed to calculate the pressure history by this method. This value may be measured experimentally. Since in this case, no experimental value was reported by the authors, δ_f was varied as a parameter around the calculated value from the direct model for δ_f. It was found that, as the magnitude of the shrinkage increases, the predicted pressure decreases. This may be explained as follows: Pressure counteracts the shrinkage, therefore a larger shrinkage (in magnitude) means there was a smaller pressure to restrain the shrinkage.

Fig.4.82 also shows that the estimated pressure approaches a constant value of ≈2.8 MPa at the end of the cycle, regardless of the magnitude of δ_f. In fact, examining Fig.4.76 we observe that, using the actual pressure in the 1-D FMS model results in a calculated mid-plane stress, which is larger than twice the measured value. Therefore, the use of the measured (smaller mid-plane) stress means a stronger pressure effect (larger pressure) at the end of cycle since the mid-plane layers solidify at this time.

4.1.3.2. Unknown Initial Melt Temperature Profile

In this example, it is desired to estimate the initial temperature profile of the melt that would result in a prescribed residual stress profile. The pressure history is known and the CMS model (52) is used.

Testing of the Inverse Method

Conditions II in Table 2.1 (4) for cooling of a PS sample in the mold are considered here. The residual stress profiles were obtained using the direct CMS model for two cases: a linear and a parabolic initial temperature profile, respectively. Fig.4.83 illustrates the corresponding pressure history and the calculated stress profiles for these cases. Conditions II lead to a three-region profile, including a constant tensile stress

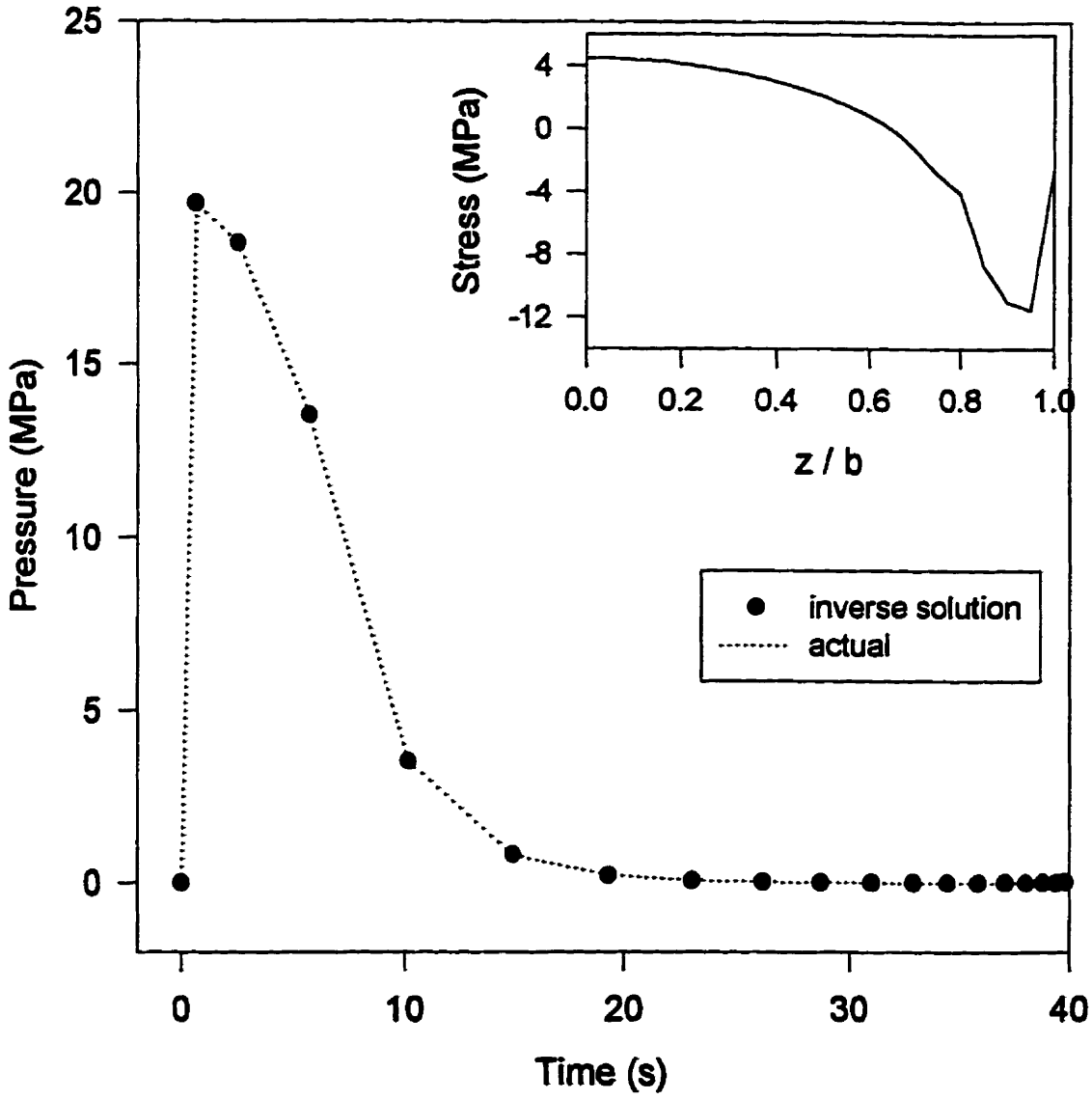

Fig.4.80.Pressure history calculated from the1-D FMS model using the exact stress data obtained from the direct 1-D FMS model and conditions I in Table 2.1

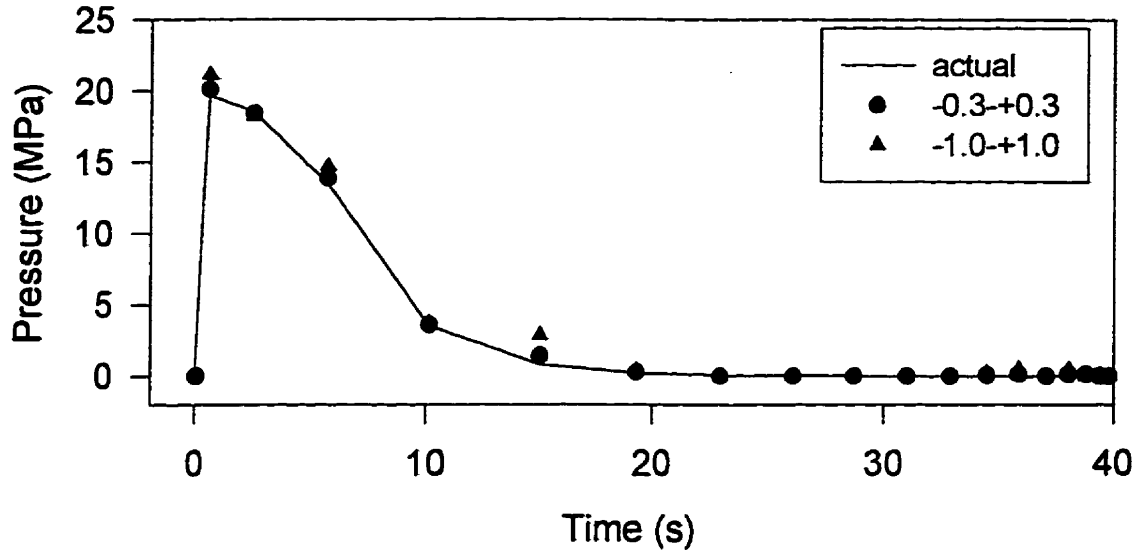

Fig.4.81.Pressure history calculated from the inverse 1-D FMS method using the direct stress data with added errors

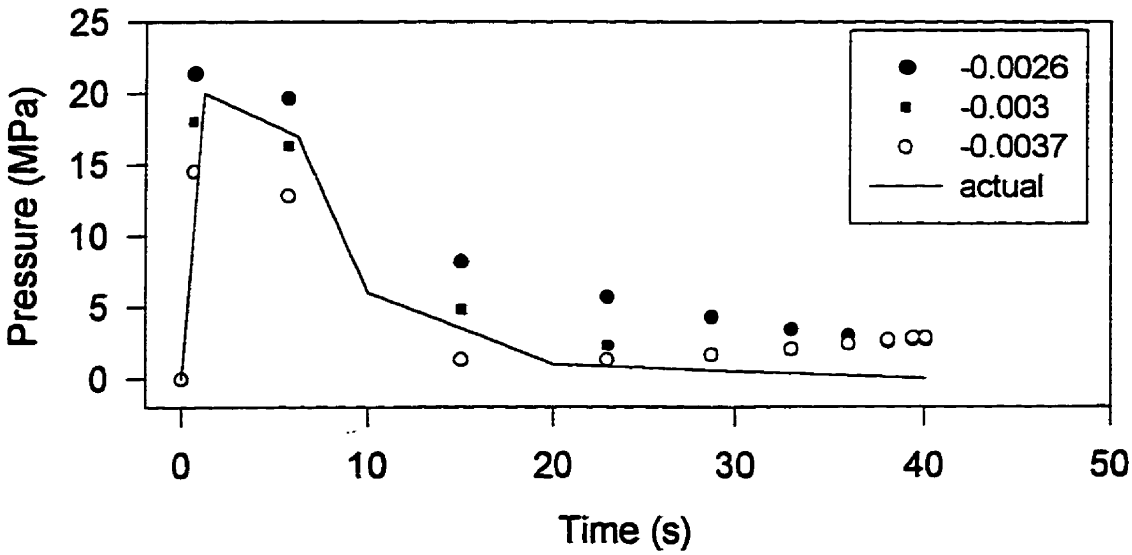

Fig.4.82.Pressure history calculated from the inverse 1-D FMS model using experimental stress data from (18)

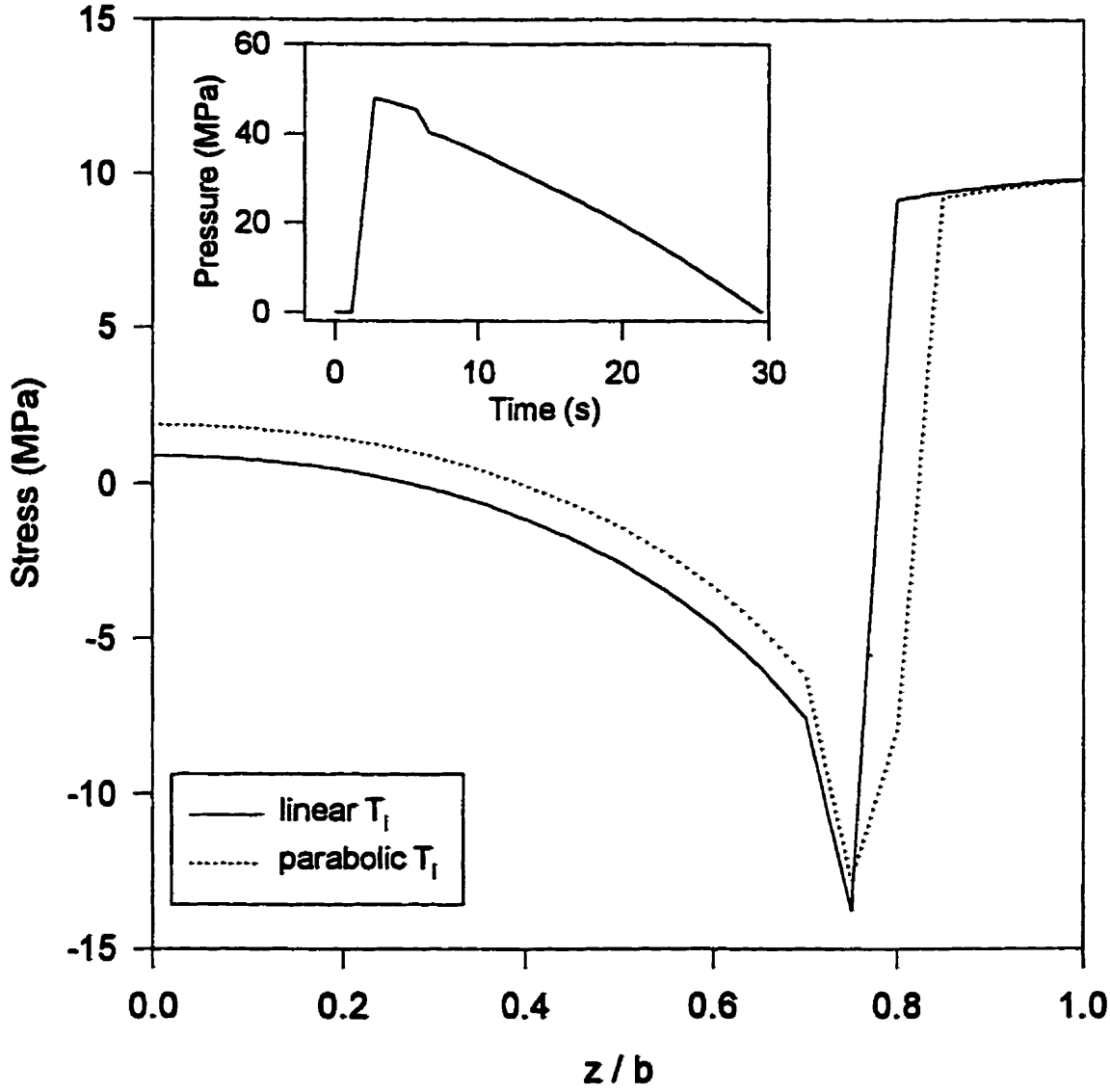

Fig.4.83.Residual stress distribution calculated from CMS model,with conditions II (Table 2.1) and experimental pressure history, for two types of melt temperatures

region on the surface, followed by a narrow compressive, and finally relatively small mid-plane tensile regions. The constant stress on the surface (z/b=1) is due to taking the zero time as the beginning of filling. The pressure is assumed to be zero during this stage when the surface layers solidify.

In case of uniform initial temperature, Brent's method with first derivatives may be used for one-dimensional minimization (102) to calculate the constant T_i with no difficulty. For the case of non-uniform profiles, the multi-dimensional Variable Metric method (102) was used to compute the melt temperature at different positions along the thickness. Fig.4.84 shows a comparison between the actual and the calculated linear and parabolic temperature profiles obtained from the stress data by the inverse method, as it converges to the solution with a decreasing minimum sum of squared residuals $R.R^T$. Fig.4.84 also shows the parabolic initial guess for minimization. In the initial guess, the wall temperature was 100°C and the midplane temperature was taken to be 300°C. Due to the low sensitivity of the residual stress profile to the initial temperature and multiple local solutions for the minimization problem, second order regularization was used. The optimum parameters for the linear and parabolic cases were found to be 0.5 and 0.1, respectively. It can be seen that the profile obtained from the inverse method, using second order regularization, is in good agreement with the actual profile.

Fig.4.85 demonstrates the effect of the value of the regularization parameter on the inverse solution in the case of the parabolic profile. As may be observed from this figure, λ_2=0.01 and λ_2= 1.0 leads to profiles far from the actual one, whereas λ_2=0.1 produces a solution similar to the actual profile.

4.2. DISCUSSION

If the flow stresses are neglected, the residual stress profile in injection molded parts depends, on the one hand, on the evolution of the temperature profile and the position of the solid-melt interface, and, on the other hand, on the pressure history. In the absence of pressure and other constraints, the residual stresses are due to differential contraction (thermal effect) and are equivalent to free quenching (FQ) stresses. The parameter variations that increase the gradient of temperature in the sample, contribute to

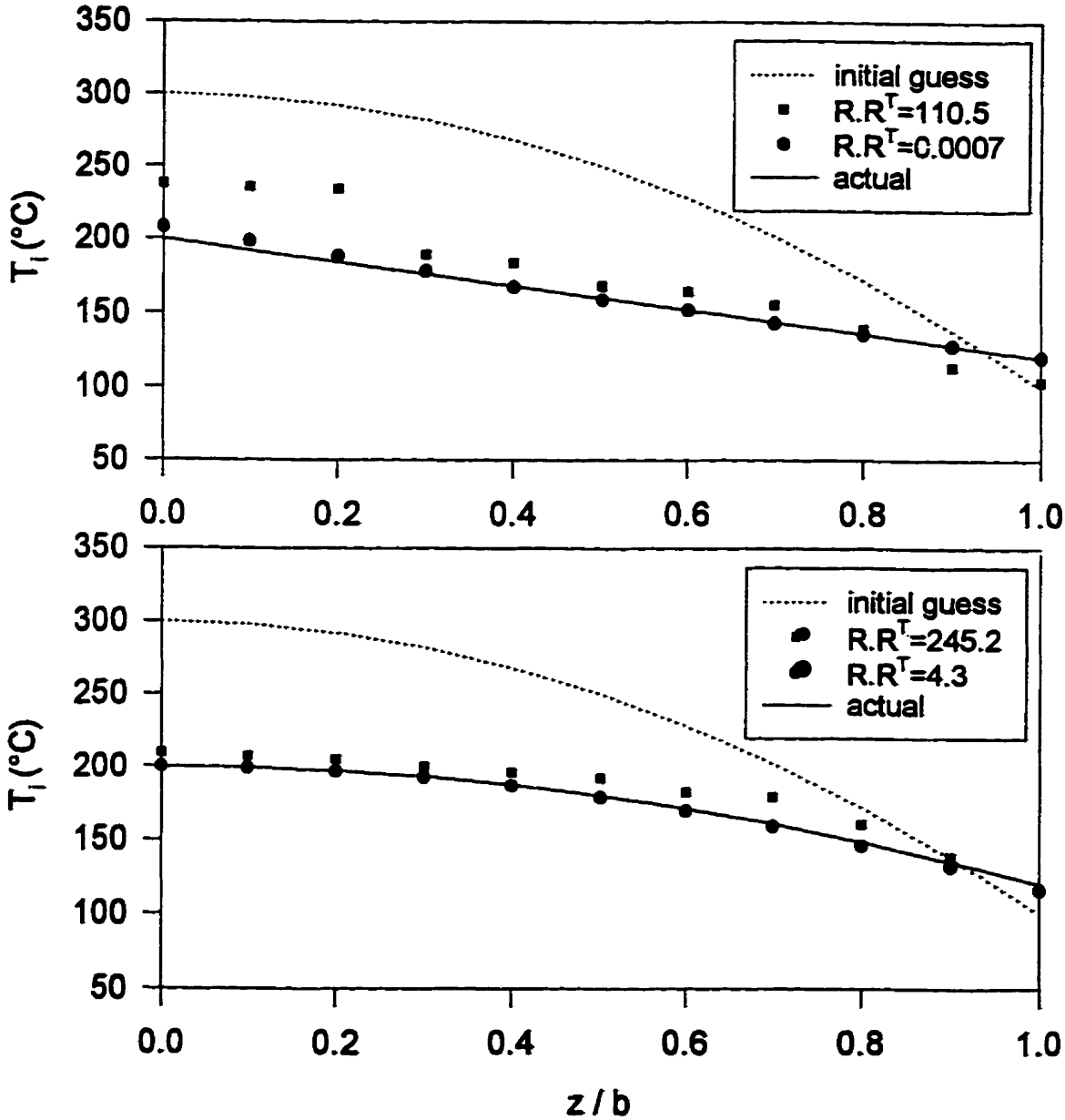

Fig.4.84.Calculation of linear and parabolic T_i using the CMS inverse model and second order regularization parameters of 0.5 and 0.1

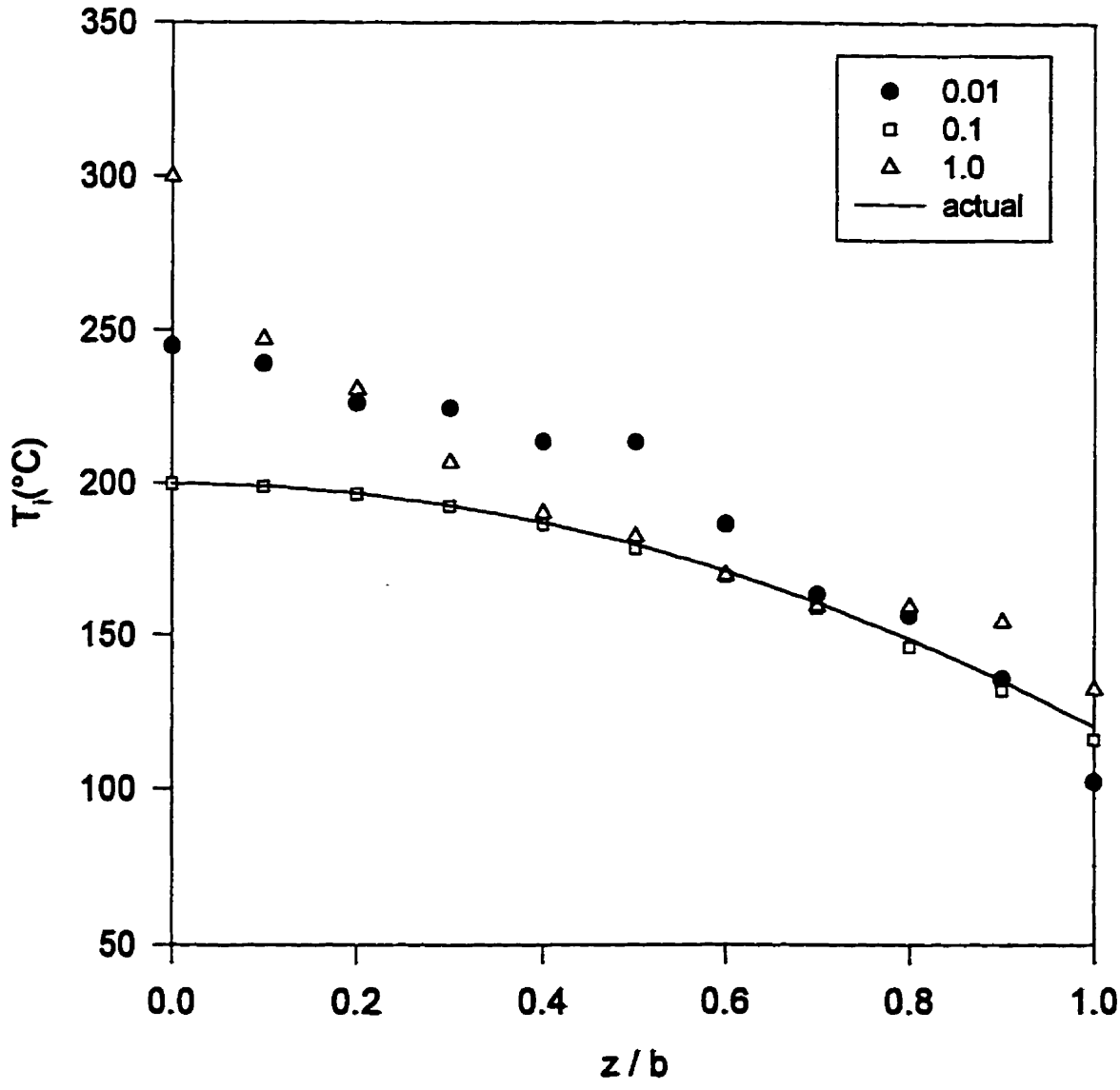

Fig.4.85.Effect of different values of the second order regularization parameter on the inverse solution

an increase in FQ stresses. The most important of these parameters are a high cooling rate, a low coolant temperature, and a thin mold. In the presence of pressure, another factor plays an important role: the solidification pressure (pressure effect). This is the pressure under which each element of the material solidifies. The pressure effect is enhanced by a high packing pressure, high holding time, and large gate-freeze time.

As shown in Fig.4.7-4.10, the thermal effect leads to a two-region profile: compressive stress on the surface and tensile stress in the core. This type of profile has been previously obtained both experimentally and theoretically by other investigators (3, 16). Following the simplified model of Struik (16), the occurrence of this profile may be explained in the following way. The thickness of the sample may be divided into two part: the skin and the core. In the first stage, the layers in the skin shrink as a result of cooling and solidification. Since the core is still molten, this deformation is not restricted and no stress is generated. In the second stage, the contraction of the core is partly restrained by the solid skin leading to tensile stress in the core and compressive stress in the skin. The occurrence of solidification is crucial for residual stresses. In fact, if not for the drastic increase in the modulus due to solidification, the stresses generated in the two stages would cancel out. In a more realistic model, the sample is formed of N layers along the thickness. During each time step, the contraction of each layer i depends on its temperature drop during this time. Each layer is surrounded by two layers: one closer to the surface and one further from it. The layer near the surface has a smaller thermal strain and induces a tensile stress. The layer closer to the core has a larger thermal strain and thus produces a compressive stress in the layer i. Thermal stresses are, thus, caused by differential contraction in the solidifying sample. As illustrated in Fig.4.7-4.10, at low Biot numbers, the temperature difference between the surface and the core of the sample is small. As a result, the differential contraction and the generated stresses are small. The surface stress is more affected by Biot number than the midplane stress. This may be explained by examining the temperature profiles and by considering the following equation derived from equations (2.103) and (2.105) for free quenching:

$$\Delta\sigma(z,t)=\left(\frac{E}{1-\upsilon}\right)\left[\frac{\int_{z_s}^{b}\Delta\varepsilon_T(z,t)dz}{(b-z_s)}-\Delta\varepsilon_T(z,t)\right] \tag{4.1}$$

According to this equation, if the thermal strain $\Delta\varepsilon_T = \int \alpha_l \, dT$ (or ΔT, if the linear thermal expansion coefficient α_l is constant) in the layer z during the time step Δt is smaller than the average thermal strain in the solidified layers, the generated stress is compressive and vice versa. Note that $\Delta\varepsilon_T$ and ΔT are negative in cooling. For large Biot numbers (see Fig.4.9 and 4.10), the surface solidifies and its temperature drops to close to its final value almost instantly. As other layers solidify, since their contraction is restrained by the surface with near zero deformation, they impose large compressive stresses on the surface. For the same reason, tensile stress is imposed on these layers. In intermediate layers, tensile stress is generated until solidification of more layers closer to the core causes the average temperature drop to be larger than their temperature drop. At this time, compressive stress is generated in these layers. The final stress in each layer is the sum of the incremental stresses. Furthermore, the total compressive stress near the surface increases with Biot number because the differential contraction between the surface and the core is increased. It may be seen from the temperature profiles that the Biot number mainly affects the surface temperature where the temperature gradient increases significantly at large Biot numbers. The gradient in the core is small (resulting a constant stress region in the core) and increases only slightly with increasing the Biot number (resulting in a small increase in the tensile stress in the core).

The strain caused by pressure is positive, as shown by equation (2.89). The material in the molten phase is under pressure and causes the adjacent solidifying layer in the solid-melt interface to expand. Therefore, the main effect of the pressure is at the time of solidification. If the pressure effect is very strong compared to the thermal effect, the FQ stress profile is reversed. This may be explained as follows: the initial expansion of the surface layer is not restrained by the molten core. When adjacent layers closer to the core solidify under pressure, their expansion is restricted by the surface, resulting in tensile stress in the surface and compressive stress in the core. Therefore, in injection molding, the final stress is the result of two competing factors: the thermal effect (FQ) and the pressure effect (solidification pressure, P_s). Depending on the relative strength of the thermal and pressure effects, various residual profiles are obtained.

In injection molded polystyrene (PS) samples, we obtained both experimentally and theoretically, a three-region profile in most cases. Variation of some parameters lead to a FQ profile. The stress profiles calculated by the 2-D FMS model may be used to better understand the results. The tensile stress on the surface is clearly a pressure effect. The magnitude of the tensile stress depends on the magnitude of the solidification pressure obtained from the pressure history and the solidification front (Fig.4.16). For Biot=30, P_s for intermediate layers is larger than the surface. Therefore, a larger tensile surface stress is introduced in the surface layers, compared to Biot=3.

Later on, the solidification of the core under zero pressure generates a compressive stress near the surface, thus decreasing the surface stress. The magnitude of the superposed compressive stress depends on the thermal effect. The FQ surface stress increases with Biot number. This explains why the final surface stress drops to a negative value for Biot=100 (Fig.4.16, top). As illustrated by Fig.4.17 and 4.18, the calculated stresses in the core are identical to the FQ stresses. The calculated P_s profiles in Fig.4.16 (bottom) show clearly that the z/b at which the stress profile joins the FQ profile coincides with the point at which P_s becomes zero. This explains the shift of the zero-stress point towards the core and, thus, a broader compressive region, as the Biot number increases. As the zero-stress point approaches the core, the superposed FQ stress becomes more tensile (see FQ curves in Fig.4.17-4.18). Consequently, the maximum compressive residual stress decreases (Fig.4.16).

In polyethylene (HDPE) injection molded samples, measurements and calculations led to a two-region residual stress profile, opposite to FQ profiles, in all cases: large tensile stress on the surface and small compressive or, in some cases, small tensile stress, in the core. As suggested by the typical pressure history for HDPE in Fig.4.33, the stress profile is caused by a strong pressure effect, especially near the surface. In fact, using the measured pressure history, the 2-D FMS model can capture relatively well the obtained two-region profile without including crystallization (Fig.4.41). This allow us to conclude that the main reason for the drastic difference in the residual stress profiles in PS and HDPE is the strong pressure effect in the latter case. It is interesting to note that, using a

different pressure history with a shorter holding time in the calculation with 2-D FMS, leads to a three-region profile similar to PS.

The residual stress profile depends on the Biot number, as expected. As shown in Fig.4.42-4.43, the stress profiles obtained with smaller Biot numbers (0.4, 0.45, and 1) exhibit a tensile stress on the surface as a result of a weak thermal effect and a strong pressure effect in this region. As shown by the solidification pressure profile, as the Biot number is increased, solidification occurs faster and the P_s profile shifts towards the first part of the pressure cycle. Including the heat of crystallization would help obtain a P_s profile that covers the complete pressure cycle. For Biot=100 in Fig.4.43, the superposed compressive FQ stress on the surface becomes more important, on the one hand, and P_s near the surface decreases, on the other hand. Both of these factors contribute to the reduction of the surface tensile stress and lead to a slightly compressive stress.

Residual stress profiles for HDPE samples were also calculated by McKam©. In this case, the complete injection molding cycle is considered and the crystallization and variable thermal properties are taken into account. The pressures calculated by McKam© are presented in Fig.4.45. The applied pressure at the nozzle during the experiments (31MPa for run 1) must be specified as an input to the program. A comparison between Fig.4.33 and 4.45 indicates that unlike the measurement that show a pressure drop of 7 MPa between the nozzle and the gate, the calculated gate pressure is identical to the nozzle pressure. In fact, during packing, the calculated velocities between these two points approach zero leading to a zero pressure drop. It was first speculated that this may be due to neglecting the effect of pressure on viscosity in McKam©. The elevated pressure during packing would increase the viscosity. The small velocities due to the addition of material into the cavity would then produce a larger pressure drop. The effect of pressure on the viscosity was incorporated using Nyun's data (105). The effect was not significant. The reason for the discrepancy may be an under-prediction of the ΔP due to the cavity entrance or of the volume of the material flowing into the cavity and thus of the velocity, during packing. This point needs to be further clarified. It must be noted that the pressure drop in the measured pressure histories decreases for a higher melt temperature and a thinner mold (see Fig.4.21,4.29,4.53,4.68).

The measured and calculated final crystallinity profiles are in good agreement considering the errors involved in both (Fig.4.47, 4.48).The final crystallinity does not vary significantly along the thickness of HDPE, according to both measurements and McKam calculations. This confirms that the value used for the heat transfer coefficient (h=600 W/(m^2.K)) in the McKam© temperature calculations was appropriate. This parameter should ideally be determined experimentally. Fig.4.50 and 4.51 show the evolution of crystallinity as calculated by McKam©. The shape of the final crystallinity is similar for different locations in the cavity. The final crystallinity is the largest in the center of cavity and the smallest near the gate. This may be understood by examining Fig.4.49. Although the temperature drop from the initial temperature (210°C) in the center of the cavity is the largest after 5 s (highest cooling rate), it is the smallest after 20 s (lowest cooling rate). It may be seen in the top graph in Fig.4.51 that, after 5 s, the degree of crystallinity at this location is the largest, resulting in a larger heat of crystallization. The latter reduces the cooling rate. Therefore, the material at this position spends more time at crystallization temperatures and as shown in the bottom graph of Fig.4.51, reaches a higher final crystallinity. The elastic modulus used to calculate the stresses increases with crystallinity. Since the variations of the percent crystallinity X_c along the thickness are not important, their effect on the elastic modulus does not largely influence the final stress profile.

The surface stresses are overpredicted by McKam©. Examination of Fig.4.46 shows two main reason for that: overprediction of the maximum packing pressure in the cavity and relaxation of the surface stress in the specimen. The discrepancy in the gate-freeze time does not affect the residual stresses significantly. The positive flow stresses and the effect of orientation of the molecules may also have an effect. In fact, the measured transverse surface stresses are smaller, as indicated by Fig.4.40.

The effect of processing parameters on the residual stresses may also be understood by considering the relative strength of the thermal and pressure effects. The predictions of the models are consistent with the measurements in most cases. A higher Biot number or heat transfer coefficient for PS compared to HDPE produced stresses more consistent with experiments.

Increasing the melt temperature has several effects. In the pressure histories shown in Fig.4.21 and 4.53, the pressure at the nozzle is slightly higher for the larger T_m. This is due to a smaller pressure drop before the nozzle at higher temperature since the viscosity is lower. The pressure near the gate exhibits an even larger value for the large T_m, for the same reason. The complete solidification of the gate is delayed for this case. In case of PS (Fig.4.21), however, a short holding time ends packing at the same time for both melt temperatures. The solidification pressure profiles for PS (Fig.4.21, bottom) show a stronger pressure effect at higher T_m. In fact, the surface stresses increase with T_m except near the end of cavity. For HDPE, P_e shows a weaker pressure effect at higher T_m, due to a delay in the solidification. This is consistent with the experimental results shown in Fig.4.52. It must be noted that, according to the calculations, the FQ stresses are independent of T_m. This is in agreement with Struik (16). The stresses calculated by the 2-D FMS model for different melt temperatures indicate (Fig.4.23 and 4.60) that, keeping everything else constant, increasing the melt temperature decreases the surface stress.

The stress profiles measured for different coolant temperatures, T_c (Fig.4.57) show a decrease in the tensile surface stress and an increase in the compressive surface stress, with T_c. This suggest a larger thermal effect at higher T_c. The calculated trend is opposite to the experimental findings. A possible explanation for the results follows. At low T_c, solidification is faster, thus, most of the material solidifies during packing under a high pressure. At high T_c, solidification is delayed and occurs under a decaying pressure. The result is a stronger pressure effect for low T_c. This situation occurs in the calculated stresses for HDPE as illustrated by Fig.4.61.

It is expected that a smaller holding time (h.t.) would lead to a weaker pressure effect and a decrease in the surface tensile stresses. In fact, in Fig.4.24, the stresses fall to a negative value for h.t.=2.5s and the profile approaches a FQ curve. The surface stress for h.t.=5 s is, however, slightly larger than h.t.=8.5s. This may be associated with experimental errors, considering the scatter obtained in the curvature data for these two runs. A more careful inspection of Fig.4.25 (top) indicates that for h.t.=8.5s., the nozzle pressure during filling is larger than the other holding times. Also, the pressure drop between the nozzle and the gate during packing is larger compared to the other two cases.

These observations suggest that either the coolant temperature or the melt temperature was not controlled properly and was lower for this run (h.t.=8.5s.). According to the predictions (Fig.4.22 and 4.59), either of these factors lowers the surface stress. This may be the reason for the surface stress in Fig.4.24 to be smaller than expected, in this case.

For HDPE, a larger h.t. increases the surface stress near the gate (Fig.4.62), as expected. The order is reversed at the other locations. The actual pressure at these locations may be different from the gate pressure in Fig.4.63 (top) or this result may be due to experimental errors.

Stresses calculated by 2-D FMS follow the expected trend: a decrease in the tensile surface stress for a lower h.t. (Fig.4.26, 4.27 for PS and 4.64, 4.66 for HDPE). Note that the holding times for HDPE were not effectively varied due to the gate solidification after 23 s. for h.t.=35 s.

Using a thinner mold has opposite effects on PS and HDPE. In PS (Fig.4.28), it enhances the thermal effect, while in HDPE (Fig.4.67), it causes the pressure effect to become more pronounced. A thin mold increases FQ stresses, producing large compressive stress on the surface. However, the effect on the stresses also depends on the solidification pressure profiles shown in Fig.4.29 for PS and Fig.4.68 for HDPE. In fact, for PS, P_s near the surface is relatively small, thus, the thermal effect is dominant. In HDPE. The pressure effect for run 11 (thin mold) is much stronger than run 5. In fact, the packing pressure is higher for run 11 (Fig.4.68) and the material solidifies faster in the thin mold. Fig.4.68(bottom) shows a larger solidification pressure profile for run 11. This explains the large tensile stress on the surface and compressive stress in the core for this run. If the melt temperatures were the same in HDPE, it is expected that the effect of mold thickness would be similar to PS.

Decreasing the maximum packing pressure decreases the tensile surface stress and causes the residual stress profile to approach the FQ profile. This effect may be seen in the stress profiles in Fig.4.32 and 4.75, calculated for large variations of packing pressure. The measured stresses near the gate and in the center of cavity (Fig.4.71) do not exhibit a significant change. This may be due to an insufficient variation of the packing pressures (Fig.4.72 top).

Chapter 5

CONCLUSIONS

In this chapter, a general summary, the most important conclusions, and the original contributions of the thesis are presented.

5.1. SUMMARY AND CONCLUSIONS

A combined theoretical and experimental analysis of the generation of thermal stresses in injection molded products was carried out. Residual stress profiles along the thickness were measured in polystyrene and high density polyethylene samples for various processing conditions. These materials were selected in order to explore the effect of crystallinity on residual stresses. The measured stress profiles were, in fact, found to be significantly distinct in the two polymers. In polystyrene samples, three regions were obtained in most cases: tensile stress on the surface and in the core, and a compressive region in between. Variation of some molding conditions modified the surface stress from tensile to compressive leading to a two-region profile, similar to free quenching. In polyethylene molded samples, on the other hand, two-region stress distributions were obtained in all the investigated range of conditions: a large tensile surface stress and a small compressive mid-plane stress. Such a distribution corresponds to a reversed free quenching profile. The surface stress was found to relax with time despite storage at low temperature (-34.8°C).

Subsequent theoretical investigations provided more insight into the interpretation of these findings. If the flow stresses are neglected, the final stress profile is found to emerge from the superposition of two major effects: one is of purely thermal nature caused by non-uniform contraction during cooling, and the other factor is the pressure

under which the material solidifies. This pressure, called the solidification pressure, is determined by the simultaneous thermal and pressure histories during cooling and depends on the position. The ratio: pressure/thermal effect, called pressure index, is thus the determining factor. The limiting case of a negligible pressure index results in a free quenching stress profile composed of a compressive surface stress and a tensile center stress. In the case of a large pressure index, the resulting profile consists of tensile stress on the surface and compressive stress in the core of the sample. Intermediate values of this parameter lead to combined profiles such as the three-region profile obtained for polystyrene.

Tensile stresses on the surface have been associated with a larger sensitivity of the molded part to stress cracking. Furthermore, sharp changes in the stress along the thickness can also have a negative effect on the mechanical strength of the product by promoting crazing and stress cracking. The results of this thesis regarding the pressure index can provide a practical tool for controlling the residual stress distribution using processing parameters.

The thermal and pressure effects are not, however, completely independent: what affects one in one way, may change the other in the opposite direction and the acquired goal of control of the stresses may not be achieved.

Based on the results of this thesis, the following conclusions are drawn regarding the effect of processing parameters. Reducing the tensile surface stress in a molded product may be accomplished by enhancing the thermal effect and weakening the pressure effect (decreasing the pressure index). This may be achieved by increasing the melt or the coolant temperature, decreasing the holding time, or decreasing the maximum packing pressure. The effect of coolant temperature seems to be opposite to the one expected. The thickness of the mold can also have a variable effect. For further discussion on this issue, see the discussion section in Chapter 4.

The effect of gate size was not investigated, but according to the above considerations, a larger gate delays the gate-seal time, thus increasing the holding time. As a result, the pressure index is increased and we expect to increase the surface tensile stress (or decrease a compressive surface stress). The heat released and the large volume change

during the crystallization of a polymer have a similar effect: it postpones the solidification of the gate, prolonging the high pressure region in the pressure history. The pressure index is consequently increased, as is the case for polyethylene in this study.

The conclusions are listed in a more concise manner in Table 5.1. As illustrated in Table 5.1, the direction of the variation of parameters must be reversed when the initial sign of the stress is changed. For cases in this table where a definite conclusion is not presented, the reader is referred to the relevant section in Chapter 4.

to reduce:		to reduce:		
Surface stress		**Center stress**		
TENSILE	COMPRESSIVE	TENSILE	COMPRESSIVE	
increase	decrease	decrease	increase	melt temperature
increase	decrease	decrease	increase	coolant temperature
increase	decrease	decrease	increase	cooling rate
decrease	increase	increase	decrease	holding time
decrease	increase	–	–	packing pressure
–	–	–	–	mold thickness
decrease	increase	increase	decrease	gate size

Table 5.1. Summary of the effect of molding parameters on the final stresses

Residual stresses were predicted using two models: the two-dimensional free mold shrinkage (2-D FMS) model and McKam©. In the 2-D FMS model only the packing and cooling stages are considered and the experimental pressure history is used. In spite of large simplifications, this model captures the main features of the residual stresses. It may be considered a useful tool in quick estimation of the stresses and the effect of parameters on them. It also provides insight into the mechanism of generation of thermal stresses and the shape of their final profiles. Simplistic temperature calculations, neglecting the stress relaxation and crystallization effects contribute to discrepancies between predictions of this model and the measurements.

McKam© simulates the complete injection molding, taking into account the fountain flow and crystallization effects and calculating pressure at different stages. Although, in most cases, the predictions include the main characteristics of the measured profiles, the stresses are generally overpredicted. Two main reasons were suggested: the cavity packing pressure is overpredicted and the stress relaxation is neglected. The latter was found to be important in polyethylene samples. The discrepancy in the predicted pressure during packing may be due to an incorrect calculation of the pressure drop at the cavity entrance or of the mass of the material entering the cavity during packing. A source of error in the pressure calculations may be the use of equilibrium PVT data; the conditions during the rapid cooling in injection molding seem far from equilibrium. It must be noted that experimental errors in the stress measurements may also contribute to this problem.

The final crystallinity distribution, calculated by McKam© is in good agreement with experiments. This suggests that temperature calculations are realistic.

Three inverse methodologies were developed to estimate the temperature distribution or the pressure profile required to obtain a prescribed residual stress profile. Because of the weak sensitivity of the stresses to the initial temperature, finding a unique solution is more difficult in this case. Regularization and imposing physical constraint were employed to facilitate convergence towards the solution. The 1-D FMS inverse method for calculation of pressure history was found to be less sensitive to errors in the stress data and gave more accurate results. The direct 1-D FMS model, however, tends to overpredict the stresses when compared with experiments. This induces relatively larger errors when testing with experimental results.

5.2. RECOMMENDATIONS FOR FUTURE WORK

A number of suggestions are presented for future experimental work, as follows:

1. The order of the polynomial fitting the curvature profile has a large effect on the magnitude of the measured stresses. This polynomial function is subsequently used to calculate the integral and the derivative of the curvature. Numerical integration and

derivation should be tried instead. The accuracy of the procedure will then depend on the number of data points. In the present study, 10-12 layers were removed leading to 10-12 data points over the thickness. The number of data points should be increased. The effect of data points should be verified by increasing the number of data points for the same run and evaluating the effect on the stress profile.

2. In the measurement of the deflection of the specimen after removal of each layer, it was observed that this quantity varies with time due to the viscoelastic behavior of the polymer. This was especially important in case of polyethylene. This time-dependence may be measured and accounted for, using an empirical correction.

3. The injection molding conditions should be varied over a wider range, in order to obtain more conclusive results about their effect on the final stress profiles. In case of polyethylene, it would be interesting to see if an imposed short holding time would result in a three-region stress profile similar to polystyrene.

4. Measurement of the residual stresses in freely quenched, compression molded, extruded, and injection molded samples with similar cooling conditions can help separate the free quenching stresses, the flow stresses, and the effect of pressure. Flow stresses are present in extruded and injection molded parts. Solidification under an applied pressure occurs in injection and compression molding.

5. Measurement of temperature and pressure at several locations inside the cavity can provide useful information for interpretation of the obtained stress profiles and for the evaluation of model predictions.

6. Residual stresses should be measured in other polymeric materials to study the effect of material properties. Composite samples and liquid crystalline polymers should be considered.

7. Optical experiments such as birefringence measurements on freely quenched, extruded, and injection molded samples can help elucidate the effect and importance of orientation and flow stresses.

8. Warpage of non-symmetrically cooled samples should be measured and compared with predictions.

To extend the theoretical investigation on the residual stresses, the following procedures are proposed for future work:

1. Modification of the 2-D FMS model to calculate the pressure from the PVT data during packing and cooling instead of using the experimental pressure history.
2. Using a two-dimensional temperature gradient variable in the thickness (z) and flow (x) directions in the 2-D FMS model.
3. Calculation of warpage due to a non-symmetric temperature distribution. The complete thickness of the sample should be considered instead of half of it.
4. Using a viscoelastic rheological constitutive equation in McKam© and calculating the flow stresses and their relaxation. Also calculating the residual birefringence and comparing with experiments.
5. Including the anisotropy due to orientation in the calculations. Properties such as the modulus, thermal expansion coefficient, and thermal conductivity will be affected.
6. Developing an inverse method based on the 2-D FMS model and testing it with actual experiments.
7. Using a viscoelastic stress-strain relationship for stress calculations.
8. Development of a 3-D stress analysis.
9. Taking into account the thermal stresses developed in the solidified layer formed on the surface during filling (McKam©).
10. Including non-equilibrium PVT information in McKam© calculations in order to obtain more accurate density and pressure calculations during packing and cooling. The thermal and pressure strains may then be determined from these data as proposed in Chapter 2.
11. Extending the calculation of residual stresses to other processes such as compression molding.
12. Extending the calculations to thermoset polymers taking into account the reaction kinetics and the heat of reaction.
13. Extending the calculations to composite materials.

5.3. ORIGINAL CONTRIBUTIONS

In general, the present study may be regarded as a step towards a better understanding of residual stresses and the effect of various parameters on them. More specifically, the original contributions may be listed as follows:

1. Inverse methods were developed to calculate an unknown pressure from a prescribed residual stress profile in an injection molded sample.

2. An inverse method was derived to estimate the melt temperature profile at the end of the filling stage from a prescribed residual stress profile. These inverse methods may be applied to compression molding, as well.

3. A combined experimental and theoretical study of the residual thermal stresses was accomplished for an amorphous and a semi-crystalline material.

4. Most detailed integrated experimental and computational study of the effect of pressure on thermal stresses in injection molding.

5. Most detailed integrated experimental and computational study of the effect of crystallinity on thermal stresses in injection molding.

6. Three major shapes have been obtained previously and in the present study for the residual stress profiles. Theoretical concepts were applied to physical phenomena in this thesis in order to elucidate the occurrence of these profiles and the transition between them.

7. Stress analysis was incorporated into the complete simulation of the injection molding cycle (McKam©) including the effect of fountain flow, crystallization, and pressure.

8. Practical conclusions were drawn and directions were provided to control residual stresses, especially on the surface. The latter can play an important role in the mechanical strength of the molded product.

REFERENCES

(1) Tadmor, Z., Gogos, C. G., Principles of Polymer Processing, John Wiley & Sons, Inc., N.Y. (1979)

(2) Chu, E. F., PhD. thesis, McGill University, Montreal, Canada (1992)

(3) Isayev, A. I., Crouthamel, D. L. : Polym. J. Plast. Technol. Eng. 22 (2), 177 (1984)

(4) Douven, L. : PhD thesis, Technische Universiteit Eindhoven, The Netherlands (1991)

(5) Wimberger-Friedl, R. , PhD. thesis, Technische Universiteit Eindhoven, (1991)

(6) Lilburn, G.A., Handbook of Measurement of Residual Stresses, (1996)

(7) Treuting, R. G., Read, W. T., J. Appl. Physics, 22 (2), 130 (1951)

(8) Thakkar, B.S. and Broutman, L.J., SPE Tech. Papers, 25, 554 (1979)

(9) Hastenberg, C. H. V., Wildervanck, P. C., Leenen, A. J. H., Polym. Eng. & Sci., 32 (7), 506 (1992)

(10) Siegmann, A., Narkis, M., Rosenzweig, N., Polym. Eng. & Sci., 19, 223 (1979)

(11) So, P., Broutman, L. J., Polym. Eng. & Sci., 16, 785 (1976)

(12) Matsuoka, S., Polym. Eng. & Sci., 21, 907 (1981)

(13) Siegmann, A, Buchman, A., Kenig, S., Polym. Eng. & Sci., 22 (9), 560 (1982)

(14) Patterson, M. W. A., White, J. R., J. Mater. Sci., 24, 3521 (1989)

(15) Struik, L. C. E., Polym. Eng. & Sci., 18 (10), 799 (1978)

(16) Struik, L. C. E. : Internal Stresses, Dimensional Instabilities and Molecular Orientation in Plastics, John Wiley & Sons, England (1991)

(17) Mandell, J. F., Smith, K. L., Huang, D. D., Polym. Eng. & Sci., 21, 1173 (1981)

(18) Menges, G., Dierkes, A., Schmidt, L., Winkel, E., SPE Tech. Papers., 26, 300 (1980)

(19) Schennink, G. G. J., Master's thesis, Twente University of Technology (1990)

(20) Farhoudi, Y., Kamal, M. R., ANTEC Proceedings, 521 (1997)

(21) Coxon, L. D., White, J. R., J. Mater. Sci., 14, 1114 (1979)

(22) Coxon, L. D., White, J. R., Polym. Eng. & Sci., 20, 230 (1980)

(23) Pham, H.T., Bosnyak, C.P., Sehanobish, K., Polym. Eng. & Sci., 33, 1634 (1993)

(24) Thompson, M., White, J.R., Polym. Eng. & Sci. 24 (4) 227 (1984)

(25) Iacopi, A.V., White, J.R., J. Appl. Polym. Sci., 33, 607 (1987)

(26) Isayev, A. I., Polym. Eng. & Sci., 23, 271 (1983)

(27) Shyu, G.D., Isayev, A.I., ANTEC (1995)

(28) Wales, J. L. S., van Leeuwen, J., van der Vijgh, R., Polym. Eng. & Sci., 12, 358 (1972)

(29) Kamal, M. R., Tan, V., Polym. Eng. & Sci., 19, 558 (1979)

(30) Pearson, J. R. A., Mechanical Principles of Polymer Processing, Pergamon Press, Oxford (1966)

(31) Kamal, M. R., Kenig, S., (Part I), Polym. Eng. & Sci., 12, 294 (1972)

(32) Kamal, M. R., Kenig, S., (Part II), Polym. Eng. & Sci., 12, 302 (1972)

(33) Kamal, M. R., Kuo, Y., Doan, P. H., Polym. Eng. & Sci., 15, 863 (1975)

(34) Kamal, M. R., Lafleur, P. G., Polym. Eng. & Sci., 22, 1066 (1982)

(35) Lafleur, P. G., Kamal, M. R., Polym. Eng. & Sci., 26, 92 (1986)(part I)

(36) Kamal, M. R., Lafleur, P. G., Polym. Eng. & Sci., 26, 103 (1986)(partII)

(37) Kamal, M.R., Frydrychowicz, W., Ansari, I., ACS Symposium Series No. 603, California, p.82 (1994)

(38) Isayev, A. I., Hieber, C. A., Rheol. Acta, 19, 168 (1980)

(39) Leonov, Rheol. Acta, 15, 85 (1976)

(40) Stickforth, , Rheol. Acta, 25, 447 (1986)

(41) Baaijens, F. P. T., Rheol. Acta, 30, 284 (1991)

(42) Nowacki, W., Thermoelasticity, Pergamon Press, England (1986)

(43) Bartenev , J. Tech. Phys. 18, 383 (1948)

(44) Bartenev , J. Tech. Phys., 19, 1423 (1949)

(45) Indenbom, V. L., J. Tech. Phys., 24, 925 (1954)

(46) Aggarwala, B. D., Saibel, E., Phys. Chem. Glasses, 2, 137 (1961)

(47) Muki, R., Sternberg, E., J. Appl. Mech., trans. of ASME, June, 193 (1961)

(48) Lee, E. E., Rogers, T. G., J. Appl. Mech., 30, 127 (1963)

(49) Rigdahl, M., Intern. J. Polym. Mater., 5, 43 (1976)

(50) Kabanemi, K. K., Crochet, M. J., Intern. Polym. Process., VII(1), 60 (1992)

(51) Titomanlio, G., Brucato, V., Kamal, M. R., Intern. Polym. Process., 1(2), 55 (1987)

(52) Brucato, V. M. B., Piccarolo, S., Titomanlio, G., paper presented at the 2nd Int. Conf. on Engineering Materials EM'88, Italy (1988)

(53) Boitout, F., Agassant, J. F., Vincent, M. Intern. Polym. Process. X (3), 237 (1995)

(54) Denizart, O., Vincent, M., Agassant, J. F., J. Mater. Sci., 30, 552 (1995)

(55) Rezayat, M., ANTEC Proceedings, 341 (1989)

(56) Rezayat, M., Stafford, R. O., ANTEC Proceedings, 584 (1990)

(57) Bushko, W. C., Stokes, V. K., (part 1) Polym. Eng. & Sci., 35 (4), 351 (1995)

(58) Bushko, W. C., Stokes, V. K., (part 2) Polym. Eng. & Sci., 35 (4), 365 (1995)

(59) Bushko, W. C., Stokes, V. K., (part 3) Polym. Eng. & Sci., 36 (), 322 (1996)

(60) Bushko, W. C., Stokes, V. K., (part 4) Polym. Eng. & Sci., 36 (5), 658 (1996)

(61) Bushko, W. C., Stokes, V. K., ANTEC (1996)

(62) Santhanam, N., PhD thesis, Cornell University, Ithaca, N. Y. (1992)

(63) Crouthamel, D. L., Master of Science thesis, Cornell University, N. Y. (1983)

(64) Ghoneim, H., Hieber, C.A., Polym. Eng. & Sci., 37 (1), 219 (1997)

(65) Jansen, K. M. B., Titomanlio, G., Polym. Eng. & Sci., 36(15), 2029 (1996)

(66) Titomanlio, G., Jansen, K. M. B., Polym. Eng. & Sci. 36 (15) 2041 (1996)

(67) Jansen, K.M.B., Intern. Polym. Processing IX (1), 82 (1994)

(68) Chapman, T.J., Gillespie, J.W. JR, Pipes, R.B., J. Composite Mater., 24, 616 (1990)

(69) Kubo, S., JSME Intern. J., Series I, 31 (2), 157 (1988)

(70) Hadamard, J., Lectures on Cauchy's Problem in Linear Partial Differential Equations. Yale University Press, New Haven, CT (1923)

(71) Dimri, V., Deconvolution and Inverse Theory, Elsevier Science Publishers B. V., The Netherlands (1992)

(72) Stolz, G. Jr., J. Heat Trans., 82, 20 (1960)

(73) Beck, J. V., AVCOTechnical Report RAD-TR-60-38 (part II), AD 267 195, March (1961)

(74) Alifanov, O. M., J. Eng. Phys., 26 (4), 682 (1974)

(75) Hensel, E. D. J., PhD thesis, New Mexico State University, New Mexico (1986)

(76) Flach, G. P., Ozisik, M. N., J. Heat Trans., 114, 5 (1992)

(77) Beck, J. V., Blackwell, B., Clair, C. St. Jr., Inverse Heat Conduction, Wiley-Interscience, N. Y. (1985)

(78) Tikhonov, A. N., Arsenin, V. Y., Solution of Ill-posed Problems, W. H. Winston & Sons, Washington, D. C. (1977)

(79) Cohen, A., Modeling of Polymer Processing, Isayev, A. I. (Ed.), Hanser Publishers, Munich (1991)

(80) Legat, V., Marchal, J.-M., Int. J. Num. Meth. Fl., 16, 29 (1993)

(81) Kang, S., Hieber, C.A., Wang, K.K., ANTEC Proceedings, 991 (1995)

(82) Farhoudi, Y., Kamal, M. R., Intern. Polym. Processing XI (2), 167 (1996)

(83) Tschoegl, N. W., The Phenomenological Theory of Linear Viscoelastic Behavior, Springer-Verlag, Berlin (1989)

(84) Landau, L. D., Lifshitz, E. M. , Theory of Elasticity, Pergamon Press, Oxford (1986)

(85) Nye, J. F. Physical Properties of Crystals, Clarendon Press, Oxford (1985)

(86) Boley, B. A., Weiner, J. H., Theory of Thermal Stresses, John Wiley & Sons Inc., N.Y. (1960)

(87) Larson, R. G., Constitutive Equations for Polymer Melts and Solutions, Butterworths, MA (1988)

(88) Bird, R. B., Armstrong, R. C., Hassager, O., Dynamics of Polymeric Liquids, vol. 1, John Wiley & Sons, Inc., N.Y. (1977)

(89) Osswald, T. A, Menges, G., Materials Science of Polymers for Engineers, Hanser Publishers, Munich (1996)

(90) Nakamura, K., Katayama, K., Amano, T., J. Appl. Polym. Sci., 17, 1031 (1973)

(91) He, J., Pd.D. Thesis, University of Colorado, Boulder (1992)

(92) Boresi, A.P., Sidebottom, O.M., Seely, F.B., Smith, J.O., Advanced Mechanics of Materials, John Wiley & Sons, N.Y. (1978)

(93) Ozisik, M.N., Boundary Value Problems of Heat Conduction, Dover Publications, Inc., N.Y. (1989)

(94) Kamal, M.R., Ansari, I., McKam4[e], Software Package for the Simulation of Injection Molding Processes (1997)

(95) Rodgers, P.A., J. Appl. Polym. Sci., 48, 1061 (1993)

(96) Chan, T. W., Isayev, A. I., Polym. Eng. & Sci., 34 (6), 461 (1994)

(97) Ogale, A.A., McCullough, R.L., Composites Sci. & Tech., 30, 185 (1987)

(98) Lapidus, L., Pinder, G.F., Numeric Solution of Partial Differential Equations in Science and Engineering, John Wiley & Sons, Inc., N.Y. (1982)

(99) Finlayson, B.A., Nonlinear Analysis in Chemical Engineering, McGraw-Hill Inc., USA (1980)

(100) Weaver, W. Jr., Johnston, P.R., Finite Elements for Structural Analysis, Prentice-Hall Inc., Englewood Cliffs, N. J. (1984)

(101) Smith, I.M., Griffiths, D.V., Programming the Finite Element Method, John Wiley & Sons, Inc., N.Y. (1988)

(102) Press, W.H., Teukolsky, S.A., Vetterling, W.T., Flannery, B.P., Numerical Recipes, Cambridge University Press (1992)

(103) Samara, M., PhD thesis, McGill Univsersity, Montreal, Canada (in preparation)

(104) Moy, F., PhD thesis, McGill Univsersity, Montreal, Canada (1980)

(105) Nyun, H., Ph.D. Thesis, McGill University, Montreal, Canada (1973)

APPENDIX I

Derivation of the curvature equation (3.14):

Equation (3.14), used to relate the deflection of the specimen to its curvature is derived here. Consider Fig.A.I.1 below.

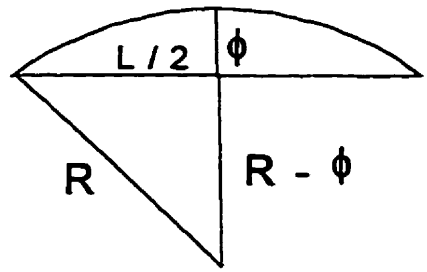

Fig.A.I.1

From the above figure we can write:

$$R^2 = \frac{L^2}{4} + (R-\varphi)^2 \qquad \text{(A.I.1)}$$

where R is the radius of curvature, L is the length of the chord, and φ is the deflection. After some algebra, we obtain:

$$R = \frac{L^2 + 4\varphi^2}{8\varphi} \qquad \text{(A.I.2)}$$

Noting that the curvature is the inverse of the radius, the curvature is obtained, as follows:

$$\kappa = \frac{1}{R} = \frac{8\varphi}{L^2 + 4\varphi^2} \qquad \text{(A.I.3)}$$

Validity of equation (3.15) in the stress measurements:

Equation (3.15) was derived by Treuting and Read (7) for the layer removal technique with the following assumptions: isotropic material, elastic response in the range considered, pure bending, properties (E and υ) constant along the thickness, and no directional effect in the plane of the specimen (curvatures equal in x and y directions). Due to these assumptions, the use of this equation to calculate the stress may introduce errors.

The anisotropy caused by orientational effects along the thickness, in the molded part, may violate the assumption of isotropy. The tensile moduli of typical PS and HDPE molded samples were measured and they did not vary significantly along the thickness. Also, the measured crystallinity profiles in Fig.4.47 and Fig.4.48 do not exhibit a large variation in the z direction. Therefore, the assumption of constant properties seems to be reasonable.

The polymer melt flows in the x direction to fill the cavity. The material flows also in the y direction, especially in filling the first half of the cavity. As a result, the curvature in the x and y directions may not be identical and should ideally be measured and used in the more general form of the equation (7).

Finally, viscoelasticity is important in a polymeric material above its T_g, as is the case for HDPE, at room temperature. In fact, it was observed that after removing each layer, the deflection of the specimen continues to change with time due to creep. The short term response of the material may be considered elastic. Since equation (3.15) relates the elastic deformation to the stress, the time between removing the layer and measuring the deflection was minimized (5-6 min.).

Care must be taken for the removed layer to have a uniform thickness. This becomes more difficult as more layers are removed and the remaining specimen warps. During the experiment, the warped sample was held flat while removing the layer. The stress distribution was assumed symmetrical across the thickness and only half the thickness was cut. If the temperature of the mold differs on the two sides, however, the stress distribution will not be symmetrical. A test was done on a typical PS sample and the profile was found to be symmetrical.

APPENDIX II

Some general properties of the resins used in this thesis (Styron 685 D and Sclair 2908) are provided by the companies and are attached here.

PRODUCT DATA SHEET

STYRON* 685D

POLYSTYRENE RESINS

MELT FLOW RATE 1.6 g/10 min.

- General purpose polystyrene, high heat for oriented sheet, containers, hot and cold drink cups, lids, extruded profiles, and housewares.
- Sheet extrusion, thermoforming, injection molding, and injection blow molding.
- High heat resistance, clarity, toughness and property retention.
- VICAT SOFTENING POINT 108°C (227°F).

Property	ASTM Method	Units SI (Imperial)	Molded Compression	Molded Injection
Yield tensile strength	D638	MPa (psi)	42.7 (6200)	56.5 (8200)
Ultimate tensile strength	D638	MPa (psi)	42.7 (6200)	56.5 (8200)
Ultimate elongation	D638	%	1.5	2.4
Tensile modulus	D638	MPa (psi)	3240 (470,000)	3350 (485,000)
IZOD impact strength (notched) @ 23°C (73°F)	D256	J/M (ft.-lb/in)	13.3 (0.25)	24.0 (0.45)
Deflection temperature (annealed) @ 1.82 MPa (264 psi)	D648	°C (°F)	103 (217)	
Vicat softening point	D1525 (rate B)	°C (°F)	108 (227)	
Melt flow rate	D1238 (cond. G)	g/10 min.	1.6	
Specific gravity	D792	--	1.04	

See "Handling Considerations", reverse side.

NOTICE: The values presented are typical laboratory averages and are intended to serve as guides only. They are not sales specification limits and no warranty is given as to the accuracy of the data or its intended use. Freedom from any infringement of patents is not to be inferred.

Bulk density ..... 37 lb/ft³ (non lubricated)
Mold shrinkage ..... .003-.007 in/in

Revised: August 1992

We don't succeed unless you do.

DOW

Dow Plastics

DOW CHEMICAL CANADA INC.

General Pysical Properties of Sclair 2908 (2)

Physical Properties

M_w, g/mole	7.45×10^4
M_n	2.23×10^4
M_w/M_n	3.33
Density, g/cm³ solid	0.962
Melt Index, g/10 min	7.40
Melting Range, °C	113 - 146

Average Specific Heat, cal/g.°C

C_p solid	0.607
C_p melt	0.587

Average Thermal Conductivity, cal/cm.°C.s

κ solid	8.24×10^{-4}
κ melt	6.25×10^{-4}

Average Thermal Diffusivity, cm²/s

α solid	18.9×10^{-4}
α melt	12.9×10^{-4}